Seismic vibration control of structures using nonlinear dampers with supporting elements

Submitted July 2022, in partial fulfillment of the conditions for the degree of
Doctor of Philosophy

Siyuan Li

University of Nottingham

Abstract

Passive control devices such as fluid viscous dampers (FVDs) are frequently adopted to enhance energy dissipation capacity of civil engineering structures; however, seismic performance of many passive control devices with a nonlinear viscous damping characteristic remains unclear, especially when they work in conjunction with supporting elements. This thesis aims to investigate the effectiveness of different nonlinear dampers with supporting elements on improving dynamic performance of building structures; approaches to achieve effective designs of the dampers in certain types of buildings are also presented. The investigated passive control configurations include the conventional damper-brace system, and a novel truss-damper assembly proposed for seismic vibration control of atrium buildings. In addition to the FVDs, an inerter-based device termed nonlinear inertial mass damper (IMD) is also introduced and studied. The observations made in this research are expected to provide an insight into the practical design of the passive control systems with nonlinear characteristics.

A numerical time-history method is first developed in this thesis to compute the seismic response of a structure with nonlinear FVDs and supporting braces, of which the correctness and accuracy are verified through comparative studies. Based on the proposed numerical method, the effects of different design parameters of the nonlinear damper-brace system are investigated. Results indicate that a minimum brace stiffness is required to achieve a preset structural performance, and for a given brace stiffness, the velocity exponent has an insignificant effect on the maximum structural performance once the dampers are optimally designed. The robustness and reliability of the optimal damper-brace systems are evaluated by incremental dynamic analysis (IDA).

Buildings with atria can be commonly found in most cities. For seismic response mitigation of an atrium building, this study develops an approach to utilize a truss-damper configuration and a core structure inside the atrium to form a novel energy dissipation mechanism. FVDs and nonlinear IMDs are adopted as the passive control devices in the configuration; the effectiveness of these truss-damper systems is evaluated through parametric studies. Results indicate that the truss-damper systems can effectively suppress the seismic vibration of atrium buildings, and the truss-IMD systems generally outperform the truss-FVD systems.

A simplified truss-IMD-core structure model is also proposed in this thesis to further investigate the effect of the core structure stiffness on the seismic performance

of atrium buildings. A multi-objective optimization approach is developed for the simplified model to minimize the peak interstory drift and story acceleration of a building simultaneously under multiple earthquakes. Numerical results from a simple structural model and a six-story building suggest superior performance of the truss-IMD system in mitigating different dynamic responses of atrium buildings.

Acknowledgements

First and foremost I would like to express my sincere gratitude to my supervisor, professor Yung-Tsang Chen, who has given me invaluable support and continuous encouragement since November 2017. His guidance not only helped me in my research work, but also shaped my attitude towards academic research. It would be impossible for me to finish this thesis without his persistent help. I would also like to thank my co-supervisor, professor Bo Li, who has been supportive throughout my PhD study and has given me insightful comments and suggestions. Besides my supervisors, my sincere thanks also go to professor Rob Y. H. Chai for his insightful comments on my research work.

I am also deeply grateful to the University of Nottingham Ningbo China for supporting me to complete my study. My appreciation also goes to my friends and colleagues, especially Cheng Zhang, Yipeng Tian, Nan Wang, Xinyu Shen, and Yuan Jiang, who have been supportive in every way.

I would like to express my deepest gratitude to my parents for their unconditional support all these years. A special thanks goes to my amazing wife, Liping Guo, my spiritual prop and the love of my life. She has cherished with me every good moment and supported me whenever I need it. The great love and support from my family kept me going during these years.

Contents

List of Figures

List of Tables

List of acronyms

DM	damage measure
DOF	degree-of-freedom
FVD	fluid viscous damper
GA	genetic algorithm
IMD	inertial mass damper
IDA	incremental dynamic analysis
IM	intensity measure
MCE	maximum considered earthquake
MDOF	multi-degree-of-freedom
NSGA	non-dominated sorting genetic algorithm
ODE	ordinary differential equation
PGA	peak ground acceleration
PEER	Pacific Earthquake Engineering Research Center
PSD	power spectral density
RK	Runge-Kutta
SF	scale factor
SDOF	single-degree-of-freedom
TMD	tuned mass damper

Nomenclature

α	stiffness ratio of supporting element, first used in Eq. (5.3)
$\boldsymbol{\delta}_j$	interstory drift time-history under j-th earthquake, first used in Eq. (5.19)
$\ddot{x}_g$	ground acceleration, first used in Eq. (3.1)
Δ	total deformation of a damper-brace system or a truss-damper system, first used in Eq. (4.3)
δ	interstory drift, first used in Eq. (5.1)
Δ_b	brace deformation, first used in Eq. (4.1)
Δ_d	damper deformation, first used in Eq. (1.1)
$\Delta_e(t)$	total deformation of truss and core structure, first used in Eq. (7.2)
Δ_I	inerter deformation, first used in Eq. (1.2)
Δ_t	truss deformation, first used in Eq. (6.4)
δ_y	yielding interstory drift of bilinear structure, first used at Page 98
η	equivalent stiffness ratio of truss and core structure, first used in Eq. (7.10)
γ	stiffness ratio of core structure, first used in Eq. (6.12)
$\mathbf{1}$	unit vector, first used in Eq. (5.11)
$\mathbf{A_0^*}$	discrete system matrix, first used in Eq. (5.16)
$\mathbf{A}^*$	system matrix, first used in Eq. (5.15)
$\mathbf{A}_j$	story absolute acceleration time-history under j-th earthquake, first used in Eq. (5.20)
$\mathbf{B_0^*}$	instant discrete damper force distribution matrix, first used in Eq. (5.16)
$\mathbf{B}^*$	damper force distribution matrix, first used in Eq. (5.15)
$\mathbf{C_a}$	damping matrix of atrium building, first used in Eq. (6.25)
$\mathbf{C_c}$	damping matrix of core structure, first used in Eq. (6.25)
$\mathbf{C_s}$	damping matrix of SDOF atrium building system, first used in Eq. (6.1)
$\mathbf{C}$	damping matrix, first used in Eq. (5.11)
$\mathbf{E_0^*}$	instant discrete ground acceleration distribution vector at step [k], first used in Eq. (5.16)

$\mathbf{E_1^*}$	instant discrete ground acceleration distribution vector at step [k + 1], first used in Eq. (5.16)
$\mathbf{E}^*$	ground acceleration distribution vector, first used in Eq. (5.15)
$\mathbf{F_d}$	damper force vector, first used in Eq. (5.11)
$\mathbf{F_{d,s}}$	damper force vector of SDOF atrium building system, first used in Eq. (6.1)
$\mathbf{I}$	identity matrix, first used at Page 88
$\mathbf{K_a}$	stiffness matrix of atrium building, first used in Eq. (6.25)
$\mathbf{K_c}$	stiffness matrix of core structure, first used in Eq. (6.25)
$\mathbf{K_s}$	stiffness matrix of SDOF atrium building system, first used in Eq. (6.1)
$\mathbf{K}$	stiffness matrix, first used in Eq. (5.11)
$\mathbf{M_a}$	mass matrix of atrium building, first used in Eq. (6.25)
$\mathbf{M_c}$	mass matrix of core structure, first used in Eq. (6.25)
$\mathbf{M_s}$	mass matrix of SDOF atrium building system, first used in Eq. (6.1)
$\mathbf{M}$	mass matrix, first used in Eq. (5.11)
$\mathbf{V}_j$	base shear force time-history under j-th earthquake, first used in Eq. (5.21)
$\mathbf{x_a}$	displacement vector of atrium building, first used in Eq. (6.25)
$\mathbf{x_c}$	displacement vector of core structure, first used in Eq. (6.25)
$\mathbf{x_s}$	displacement vector of SDOF atrium building system, first used in Eq. (6.1)
$\mathbf{x}$	displacement vector, first used in Eq. (5.11)
$\mathbf{X}_j$	story displacement time-history under j-th earthquake, first used in Eq. (5.18)
$\mathbf{z_0}$	structural response vector of SDOF model, first used in Eq. (3.2)
$\mathbf{z_s}$	response vector of SDOF atrium building system, first used in Eq. (6.2)
$\mathbf{z}$	structural response vector, first used in Eq. (5.15)
Δt	sampling period, first used at Page 44
k	current time step, first used in Eq. (3.6)
w	total number of earthquakes, first used in Eq. (5.18)
μ	mass ratio of core structure, first used in Eq. (6.12)

ν	velocity exponent, first used in Eq. (1.1)
ω	circular frequency, first used in Eq. (1.3)
ω_1	fundamental circular frequency of structure, first used in Eq. (5.4)
ω_g	fundamental circular frequency of ground surface soil deposit, first used in Eq. (3.16)
ξ	inherent structural damping ratio, first used at Page 73
ξ_g	damping ratio of ground surface soil deposit, first used in Eq. (3.16)
a	absolute story acceleration, first used in Eq. (3.13)
b	inertance coefficient, first used in Eq. (1.2)
c	damping coefficient of structure, first used in Eq. (3.1)
c_c	story damping coefficient of core structure, first used in Eq. (6.1)
c_d	damping coefficient of damper, first used in Eq. (1.1)
f_d	damper force, first used in Eq. (1.1)
f_I	inerter force, first used in Eq. (1.2)
K	slope coefficient of Runge-Kutta recursion formula, first used in Eq. (3.7)
k	story lateral stiffness, first used in Eq. (3.1)
k_b	brace stiffness, first used in Eq. (4.1)
k_c	story lateral stiffness of core structure, first used in Eq. (6.1)
k_E	elastic stiffness of bilinear structure, first used at Page 98
k_e	equivalent stiffness of truss and core structure, first used in Eq. (7.1)
k_t	truss stiffness, first used in Eq. (6.5)
k_{PE}	post-elastic stiffness of bilinear structure, first used at Page 98
m	mass, first used in Eq. (3.1)
m_c	story mass of core structure, first used in Eq. (6.1)
M_1	model mass of the first vibration model of building, first used in Eq. (7.10)
PI_A	performance index in story acceleration, first used in Eq. (3.13)
PI_S	performance index in story displacement, first used in Eq. (3.12)
PI_V	performance index in base shear force, first used in Eq. (5.5)

$PI_{D,c}$	interstory drift performance index of a core structure, first used at Page 117
PI_D	performance index in interstory drift, first used in Eq. (5.1)
PI_{mD}	performance index in maximum story drift, first used in Eq. (5.7)
PI_{mV}	performance index in maximum base shear force, first used in Eq. (5.8)
RR_A	response reduction in story acceleration, first used in Eq. (3.15)
RR_D	response reduction in interstory drift, first used in Eq. (5.2)
RR_mD	response reduction in maximum interstory drift, first used in Eq. (5.9)
RR_mV	response reduction in maximum base shear force, first used in Eq. (5.10)
RR_S	response reduction in story displacement, first used in Eq. (3.14)
RR_V	response reduction in base shear force, first used in Eq. (5.6)
$RR_{D,c}$	interstory drift response reduction of a core structure, first used at Page 117
S_0	constant white-noise PSD of bedrock excitation, first used in Eq. (3.16)
$S_a(T_1, 5\%)$	5% damped spectral acceleration at structure's fundamental period T_1, first used at Page 48
t	time, first used in Eq. (1.1)
T_1	fundamental period of structure, first used at Page 48
V_s	base shear force, first used in Eq. (5.5)
x	displacement in horizontal direction, first used in Eq. (3.1)
x_c	horizontal displacement of core structure, first used in Eq. (6.3)
$\mathbf{A}$	– system matrix of SDOF model, first used in Eq. (3.2)
	– system matrix of SDOF atrium building system, first used in Eq. (6.2)
$\mathbf{A_0}$	– discrete system matrix of SDOF model, first used in Eq. (3.6)
	– discrete system matrix of SDOF atrium building system, first used in Eq. (6.3)
$\mathbf{B}$	– damper force distribution vector of SDOF model, first used in Eq. (3.2)
	– damper force distribution matrix of SDOF atrium building system, first used in Eq. (6.2)
β	– damping ratio of damper, first used in Eq. (5.4)

– damping ratio of equivalent model, first used in Eq. (7.10)

$\mathbf{B_0}$ – instant discrete damper force distribution matrix of SDOF model, first used in Eq. (3.6)

– instant discrete damper force distribution matrix of SDOF atrium building system, first used in Eq. (6.3)

$\mathbf{E}$ – ground acceleration distribution vector of SDOF model, first used in Eq. (3.2)

– ground acceleration distribution vector of SDOF atrium building system, first used in Eq. (6.2)

$\mathbf{E_1}$ – instant discrete ground acceleration distribution vector at step $[k+1]$ of SDOF model, first used in Eq. (3.6)

– instant discrete ground acceleration distribution vector at step $[k+1]$ of SDOF atrium building system, first used in Eq. (6.3)

$\mathbf{E_0}$ – instant discrete ground acceleration distribution vector at step $[k]$ of SDOF model, first used in Eq. (3.6)

– instant discrete ground acceleration distribution vector at step [k] of SDOF atrium building system, first used in Eq. (6.3)

f – fitness function, first used in Eq. (7.11)

λ – inertial mass ratio of IMD, first used in Eq. (6.21)

– inertial mass ratio of equivalent model, first used in Eq. (7.10)

Chapter 1 Introduction

1.1 Background

Excessive or undesirable dynamic response could cause human discomfort, extreme deformations, fatigue, and immediate local or global collapse of structures (Skinner et al. 1974, Ibarra et al. 2005). Therefore, the structural capability in resisting the vibrations induced by different external disturbances, earthquakes in particular, is generally recognized as an important consideration in the design of building structures. As the earthquake-induced structural damage and collapse is attributed largely to the inadequate energy dissipation paths in a structure (Roque et al. 2019), to suppress undesirable vibrations and enhance structural safety during earthquakes, various types of seismic control systems have been developed to increase the damping of the structures. The seismic control systems can be broadly categorized into four groups (Zuo et al. 2020), namely passive, active, semi-active and hybrid; among which the passive control system is most widely used in civil engineering applications due to its simplicity, low cost, high stability and independence of additional power supply (Preumont 2011, Lazar et al. 2014, Wu et al. 2020, Ma et al. 2021*b*). When properly designed and installed, high performance passive control devices, such as viscous dampers, viscoelastic dampers, metallic yield dampers, friction dampers and tuned mass dampers, can dissipate a considerable amount of input energy during earthquakes and increase the resilience of the structures (Soong and Spencer Jr 2002, Symans et al. 2008, Parulekar and Reddy 2009).

Fluid viscous dampers (FVDs) are well established passive energy dissipation devices that have been frequently adopted in mechanical and civil engineering applications. The robustness and reliability of such devices have been proven after decades of usage during the Cold War, especially in the fields of aerospace and military hardware, which motivated the later applications of FVDs in the retrofitting or reinforcing of buildings and infrastructures (Soong and Spencer Jr 2002, Taylor 2013). From the late 1980s to the late 1990s, to prove the applicability of the viscous dampers in civil structures, many research and engineering institutes, such as National Center for Earthquake Engineering Research (renamed to Multidisciplinary Center for Earthquake Engineering Research in 1998), have conducted numerous experimental and analytical investigations (Lin et al. 1988, Tsopelas et al. 1994, Reinhorn et al. 1995, Constantinou et al. 1998). These studies became important references to produce technical specifications for the practical application of the FVDs. With the world-

wide promotion and development of the energy dissipation technology, research on the analysis and design of viscous dampers in civil engineering is constantly evolving.

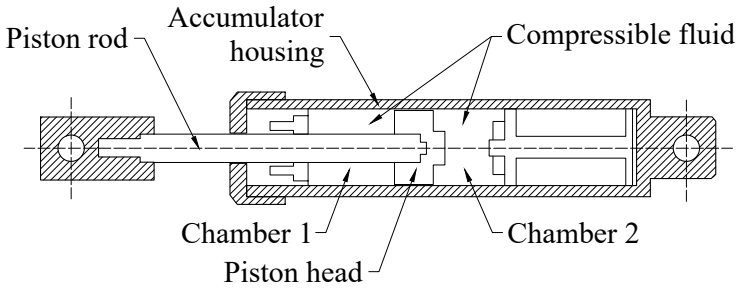

Figure 1.1: Construction of a typical fluid viscous damper (Constantinou and Symans 1993).

A typical fluid viscous damper consists of a stainless-steel piston and an accumulator housing, as shown in Figure 1.1. The housing is divided into two chambers by the piston head; a compressible hydraulic oil (usually silicon oil) is filled in the chambers and can pass from one chamber to the other through orifices (hydraulic circuits) in the piston head. Once there is a relative motion between the two ends of the viscous damper, the input energy will be transformed to heat during the 'oil flowing through orifices' process and dissipates into the atmosphere (Constantinou and Symans 1993, Symans and Constantinou 1998, Soong and Spencer Jr 2002). The analytic model of a FVD can be expressed using a dashpot with damping coefficient c_d, as shown in Figure 1.2.

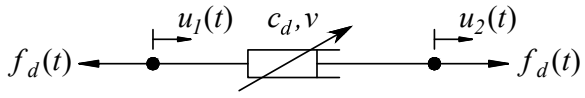

Figure 1.2: Analytic model of a fluid viscous damper.

The force in the FVD can be expressed mathematically as:

$$f_d(t) = c_d|\dot{\Delta}_d(t)|^{\nu} sgn(\dot{\Delta}_d(t)) \tag{1.1}$$

where $\dot{\Delta}_d(t)$ is the relative velocity between the two ends of the damper, namely $\dot{u}_2(t) - \dot{u}_1(t)$, and $sgn(\cdot)$ denotes the signum function. Notably, ν is a positive exponent for the damper velocity, of which the magnitude depends on the design of hydraulic circuits (De Domenico and Ricciardi 2019), and the viscous dampers can be classified into two groups based on the value of ν, namely linear and nonlinear. When ν equals one, the dampers exhibit linear force-velocity relationship and can

thus be categorized as linear ones; for nonlinear dampers the velocity exponents are not equal to one.

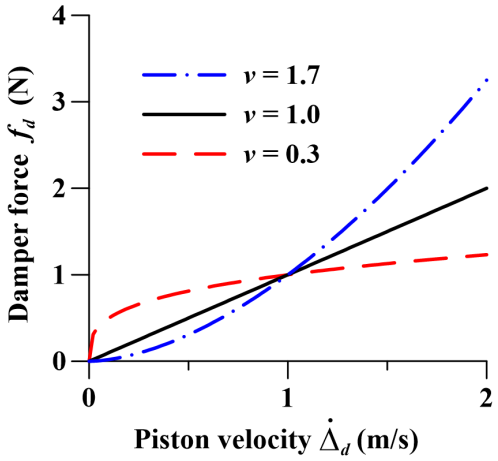

Figure 1.3: Variation of damper force with piston velocity for dampers with different velocity exponents (c_d = 1 N·(s/m)$^{\nu}$)

Previous studies have reported that the nonlinear FVDs with a velocity exponent less than one can limit the peak damper force generated at large structural velocities during extreme events without reducing the supplemental damping provided to the structure, as compared with linear dampers (Lin and Chopra 2002, Martinez-Rodrigo and Romero 2003, Symans et al. 2008, Lin et al. 2008, Zhang and Xi 2012, Bahnasy and Lavan 2013, Tubaldi and Kougioumtzoglou 2015). This could be demonstrated using Figure 1.3, which shows the force-velocity curves of viscous dampers with the same value of damping coefficient and different velocity exponents. It can be seen from the figure that the nonlinear damper with the velocity exponent less than unity provides the largest damper force among the three dampers when piston velocity is smaller than 1 m/s. However, when the piston velocity is larger than 1 m/s, the damper force is limited for the viscous damper with ν less than one, unlike a linear increase in force for ν equals one or an exponential increase for ν larger than one. Therefore, excessive damper force induced by intense velocity can be controlled by this type of nonlinear damper, and possible structural damage due to large damper force, especially at the connection regions and supporting braces, can be avoided or reduced. In addition, as the manufacturing cost of a fluid viscous damper depends heavily on the peak force in the damper during its operation (Pollini et al. 2018), using dampers with a velocity exponent smaller than one may also have cost advantages. Recognizing the benefits, considerable research interests in the seismic applications of nonlinear viscous dampers have arisen in recent years (De Domenico and Ricciardi 2019, Moslehi Tabar and De Domenico 2020), and the velocity exponents frequently

used in civil structures were summarized in some studies. In general, typical values of velocity exponent for seismic applications are in the range of $0.35 - 1$ (Lin and Chopra 2002), with the most common range of $0.4 - 0.5$ (Taylor 2013). For wind applications, the frequently used velocity exponents are in the range of $0.5 - 1$ (Taylor 2013).

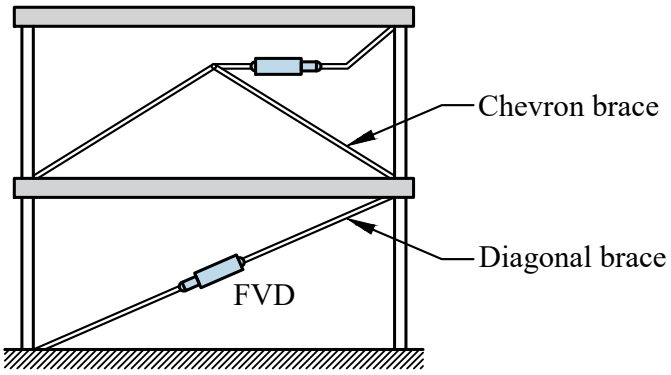

Figure 1.4: Fluid viscous dampers installed with diagonal and Chevron braces.

In building applications, interstory drift is the most commonly used structural motion for activating the FVDs (Soong and Dargush 1997), and the dampers are often installed between stories with supporting braces. Different configurations of braces can be used to transmit the structural interstory drifts and convert them into axial motions between the two ends of the FVDs, with the diagonal and Chevron (inverted-V) configurations among the most common, as shown in Figure 1.4. The conventional story-wise installed damper-brace systems have proven their effectiveness in practical applications (Nakamura et al. 2014). In addition to the brace configurations that utilize the relative motion between adjacent stories, some schemes of braces or other supporting elements that adopt other structural motions to activate a passive control system have been developed in the literature. For instance, Smith and Willford (2007) introduced a damped outrigger system for alleviating wind response of high-rise buildings, which utilized the relative vertical velocity between the perimeter column of external tube structure and the core inside the tube structure to activate the viscous dampers. Lai and Mahin (2015) proposed a strongback mast system to facilitate the development of uniform story drift over the height of a multi-story frame-type building. A damper connecting the strongback system and the ground can thus dissipate energy using the uniform structural vibration during earthquakes. The large relative motion through multiple stories, or between an upper floor and the ground, has also been used in many passive control systems. Some examples can be found in the literature, e.g., Pietrosanti et al. (2017), Kaveh et al. (2020)

and Petrini et al. (2020). Therefore, using structural motion other than interstory drift to activate the FVDs may also be a feasible way for using dampers in building applications.

The damping performance of an energy dissipation device like a FVD can be enhanced when it has an inherent or extrinsic negative stiffness characteristic (Li et al. 2008, Ou and Li 2010, Høgsberg 2011, Di et al. 2021), as the negative stiffness allows the device to generate a force to assist the motion instead of opposing it (Ma et al. 2021*a*), which amplifies the relative motions between the two ends of the system and thus enhance the overall energy dissipation capacity. Negative stiffness is a common characteristic in active and semi-active vibration control systems (Iemura and Pradono 2005, Ou and Li 2010); to introduce this useful feature to passive control systems, some passive negative stiffness devices that are independent of external energy supply have been developed in the last decade (Pasala et al. 2013, Chen et al. 2015, Nagarajaiah and Sen 2020, Zhou et al. 2020, Walsh et al. 2021), which can exhibit negative-slope force-displacement behaviours during their operations. In addition to the negative stiffness devices, previous research suggested that a mechanical element named "inerter" can also increase the damping performance of an energy dissipation device, as the force-displacement relationship of the inerter during cyclic motions has a negative slope (Shi and Zhu 2019, Ma et al. 2021*a*).

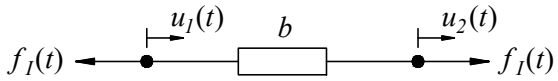

Figure 1.5: Analytic model of an ideal inerter.

Inerter, also termed "gyro-mass" in the literature (Saitoh 2012), is a two-terminal massless mechanical element proposed by Smith (Smith 2002). The concept of inerter was initially developed based on electrical capacitor, which completes the analogy between "inductor-resistor-capacitor" electrical network and "spring-dashpot-inerter" mechanical network (Smith 2002, Chen and Hu 2019). Figure 1.5 shows the analytic model of an ideal inerter, in which the inerter force $f_I(t)$ can be mathematically expressed as:

$$f_I(t) = b(\ddot{u}_2(t) - \ddot{u}_1(t)) = b\ddot{\Delta}_I(t) \tag{1.2}$$

It can be seen from Eq. (1.2) that $f_I(t)$ is proportional to the relative acceleration between the two terminals of the inerter $\ddot{\Delta}_I(t)$ with a constant proportionality b termed "inertance" and measured in the unit of mass. Here, if we assume the deformation of

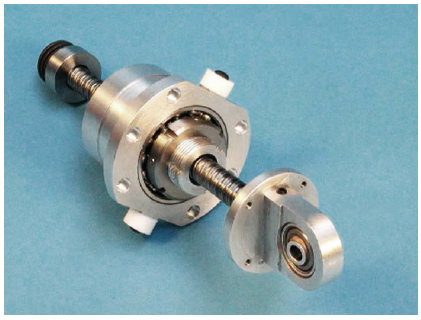

(a) Ball-screw inerter developed by Papageorgiou and Smith (2005) at Cambridge University

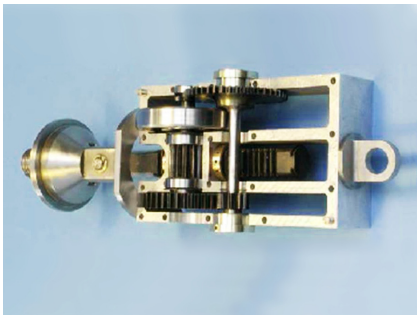

(b) Rack-and-pinion inerter developed by Smith and Wang (2003) at Cambridge University

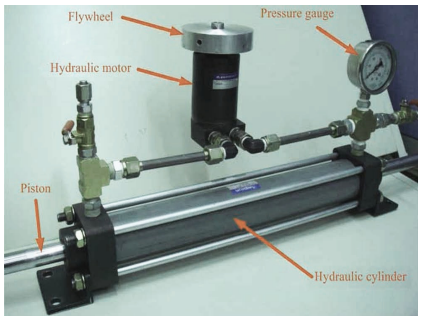

(c) Hydraulic inerter developed by Wang et al. (2011)

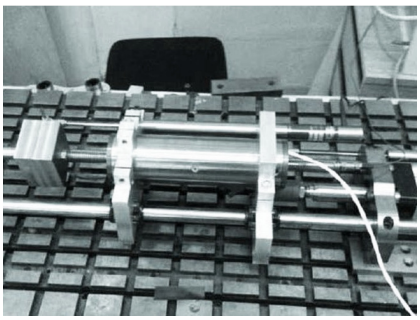

(d) Electromagnetic inerter developed by Gonzalez-Buelga et al. (2015)

Figure 1.6: Examples of inerters.

the device $\Delta_I(t)$ is a harmonic vibration with frequency ω_0, the inerter force can in turn be related to the inerter deformation by:

$$f_I(\omega) = -b\omega_0^2 \Delta_I(\omega) \tag{1.3}$$

where $f_I(\omega)$ and $\Delta_I(\omega)$ are the Fourier transforms of the force and deformation of the inerter, respectively. From Eq. (1.3) it can be seen that, the inerter provides a force that is negatively correlated with its cyclic deformation with a slope of $-b\omega_0^2$ under the harmonic vibration. Therefore, the inerter may exhibit a negative-slope force-displacement relationship during vibration. The ideal inerter can be physically realized through different mechanisms, including rack-and-pinion (Smith and Wang 2003, Papageorgiou et al. 2009), ball-screw (Papageorgiou and Smith 2005, Li et al. 2012), hydraulic (Wang et al. 2011), helical fluid (De Domenico et al. 2019), electromagnetic (Gonzalez-Buelga et al. 2015) and living-hinge (John and Wagg 2019). Some examples of the inerters are shown in Figure 1.6. Since the negative-slope force-displacement relationship of a device can improve the damping capacity of an energy dissipator, many inertial mass dampers (IMDs) that combine an inerter and a viscous damper have been proposed in the literature. These IMDs generally outper-

formed the conventional viscous dampers (Hwang et al. 2007, Nakamura et al. 2014). Rheological representation of an ideal IMD can be made by an inerter arranged in parallel with a dashpot (Ma et al. 2021*a*), in which different types of inerters were adopted in the practically realization of the IMD, with the ball-screw inerters among the most common. In addition to the IMDs that take advantage of the negative-slope feature of the inerter, many inerter-based vibration control systems that utilize other features of the inerter such as the mass amplification effect have been developed in the last two decades (Ma et al. 2021*a*). When one terminal of an inerter is fixed to the ground, the inerter provides an additional mass to the system that equals its inertance, which can be several orders of magnitude larger than the actual mass of the device (Pawlak and Lewandowski 2020, Cao and Li 2022). This feature allows the inerter to be used as an alternative to the auxiliary mass in conventional vibration absorbers like tuned mass dampers (TMDs), and many inerter-based absorbers have been developed in the last two decades, such as tuned inerter dampers (Lazar et al. 2014), tuned mass damper inerters (Marian and Giaralis 2017) and nonlinear energy sink inerters (Zhang et al. 2019). In addition to the vibration absorbers, base isolation and some hybrid control techniques have also adopted inerters (Ma et al. 2020, De Domenico and Ricciardi 2018, De Angelis et al. 2019, Li, Chang, Cao and Huang 2021).

1.2 Statement of research problems

In the past few decades, to evaluate the effectiveness of viscous dampers on enhancing seismic performance of building structures, numerous research has focused on linear FVDs both analytically and experimentally (Constantinou and Symans 1992, Ramirez et al. 2001, Hwang et al. 2005); different design procedures have also been proposed for linear dampers (Lavan and Levy 2005, 2006, Levy and Lavan 2009, Shin and Singh 2014, Del Gobbo et al. 2018). For nonlinear viscous dampers, although relevant design approaches can be found in the literature (Lin et al. 2008, Lang et al. 2013, Fujita et al. 2014, Altieri et al. 2018, De Domenico and Ricciardi 2019), the structural analysis involved in many approaches were based on equivalent linearization technique, in which the nonlinear damping was replaced by an equivalent linear one for the purposes of simplicity. Although the equivalent linearization methods can simplify the design process, the accuracy of the analysis and design results may be reduced; studies on the optimal design of nonlinear dampers that explicitly dealt with their exponential force-velocity relationships remain limited, and some important research, such as the influence of damper nonlinearity on the optimal structural performance, still requires further investigation.

In practical applications, supporting braces are important auxiliary components to connect fluid viscous dampers to a building. Since there are physical connections between the dampers and the braces, it is crucial to incorporate the brace stiffness into the analysis and design of the FVDs. However, in the literature, most of the design methods for fluid viscous dampers, especially those for nonlinear ones, implicitly assumed the braces to be rigid, as the brace stiffness has not been treated as a design variable (Di Paola and Navarra 2009, Tubaldi and Kougioumtzoglou 2015, Xie et al. 2018, Liu et al. 2018, Moradpour and Dehestani 2019). Since the dimension of the braces is often limited due to functional and/or aesthetic considerations, an infinite brace stiffness is difficult to achieve in practice (Park et al. 2004, Losanno et al. 2019). Therefore, the assumption of rigid brace may result in an overestimation of the damping capacity of a damper-brace system (Takewaki and Yoshitomi 1998, McNamara et al. 2000, Singh et al. 2003, Ou et al. 2007, Huang 2009, Fujita et al. 2010). Previous studies showed that the hysteretic behaviour of a damper-brace system with finite brace stiffness exhibited viscoelastic characteristic during external excitation (Constantinou et al. 1998, Castaldo and De Iuliis 2014); however, studies on the interaction between the structural dynamic behaviour and the flexibility of the damper-brace assemblies, particularly those with nonlinear dampers, are still limited. To achieve an optimal design of the nonlinear viscous dampers in building applications, it is essential to investigate the effect of brace stiffness on the seismic performance of structures.

Building with atrium is a common structural type in most of the urban areas in the world; atrium building exhibits several advantages when compared with normal types of buildings without a large interior open space, e.g., a properly designed skylight can introduce natural lighting to the interior of the building (Hung 2003). Solar heat can be retained within the structure, and natural ventilation can also be achieved through solar-driven airflow inside the atrium (Hussain and Oosthuizen 2012). The internal open space extending to the roof gives the atrium building a feeling of light and space (Driscoll 2013), which also makes the internal prominent area particularly suited for social and ceremonial purposes. All these features make atrium buildings popular with users, architects and developers, hence large atrium designs have been adopted in many commercial buildings like hotels, shopping malls and office buildings (Hung 2003, Mohsenin and Hu 2015). When an atrium building is subjected to an earthquake, to suppress undesirable vibration of the building, passive control devices such as viscous dampers can be used, which may be installed between adjacent stories using the conventional damper-brace configurations. However, the damper-brace systems may occupy usable area at multiple floors and affect aesthetic appeal

of the building. Since there is a vertical open space inside the atrium building, an alternative arrangement of the damper-brace assembly that installs the dampers inside the atrium may be feasible. The new arrangement is capable of better utilizing the internal space provided by the atrium building, while maintaining the usable space and aesthetic appeal of the building.

Previous studies have reported that inertial mass dampers that combines the mechanical behaviours of inerters and dashpots generally surpassed conventional dampers in seismic response mitigation of structures (Hwang et al. 2007, Nakamura et al. 2014). The applicability of the IMDs in different civil infrastructure has also been evaluated in the literature, including building structures (Ikago et al. 2012), cable bridges (Lu et al. 2017) and offshore structures (Ma et al. 2019). However, most of the studies used a linear dashpot to simulate the damping characteristic of the device, although the IMDs can exhibit nonlinear damping characteristic in practical applications. The influence of nonlinearity of the IMDs on seismic performance of building structures remains unclear and warrant further exploration.

1.3 Aims and objectives

This thesis aims to investigate the effectiveness of different nonlinear dampers with supporting elements on enhancing seismic performance of building structures, which can provide an insight of the optimal design of the passive energy dissipation devices with nonlinear characteristics and the supporting elements. In addition to the conventional damper-brace assembly for frame-type buildings, a novel truss-damper configuration will be proposed specifically for the vibration control of atrium buildings. The dampers being investigated are the conventional fluid viscous dampers, and inertial mass dampers with nonlinear viscous damping (termed nonlinear IMD in this study). The effects of the stiffness of the supporting elements and the nonlinearity of the dampers on dynamic performance of the buildings under earthquake excitation will be the primary focuses of this study. The thesis also aims to present effective approaches to achieve robust designs of the brace-damper and the truss-damper systems for mitigating the seismic responses of frame-type structures and atrium buildings, respectively.

Due to the different structural forms of the primary buildings, the aims above could be divided into two parts: (i) dynamic response mitigation of shear-type buildings, and (ii) seismic vibration control of atrium buildings. To achieve the first part, the following objectives have been established:

- To develop a numerical time-history method for computing structural response of a shear-type building equipped with one or multiple nonlinear viscous dampers

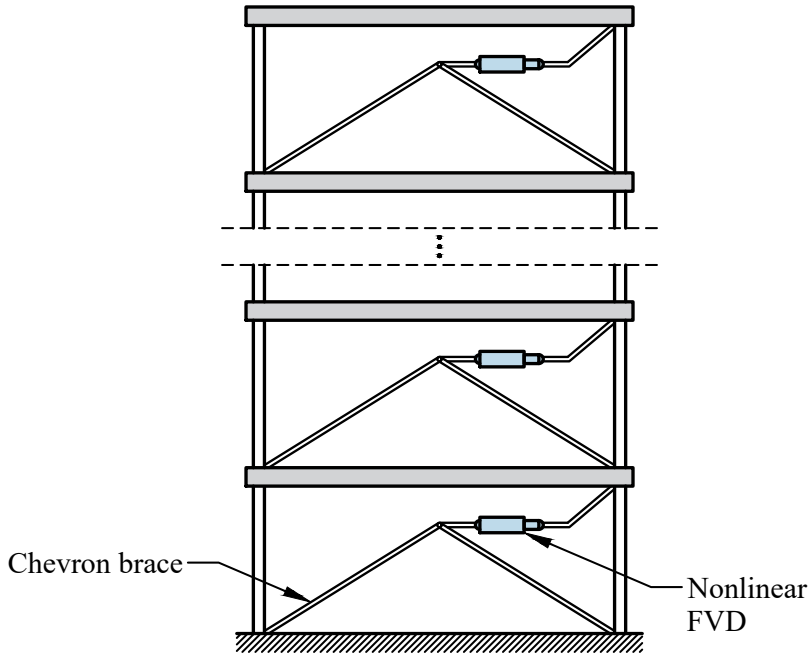

Figure 1.7: A multi-story building equipped with multiple nonlinear damper-brace systems.

with supporting braces, as shown in Figure 1.7, when subjected to an earthquake ground motion.

- To conduct parametric studies on the nonlinear damper-brace system and reveal the effects of different design parameters on seismic performance of building structures.

- To develop an optimization approach for the nonlinear damper-brace system to maximize a specific structural performance under a prescribe earthquake input.

- To evaluate the robustness and reliability of the optimal design approach.

Inspired by the previous studies that adopted structural motion other than inter-story drift to activate the passive control devices (Smith and Willford 2007, Lai and Mahin 2015), a truss-damper configuration is proposed, as shown in Figure 1.8, which utilizes the unsynchronized dynamic response between the tops of an atrium building and a "core structure" inside the atrium to dissipate seismic energy (see Sections 6.1 and 6.2 for detailed truss-damper configurations). Therefore, for the second part of the aims, the following objectives have been formulated:

- To propose a novel approach for vibration control of atrium buildings using a

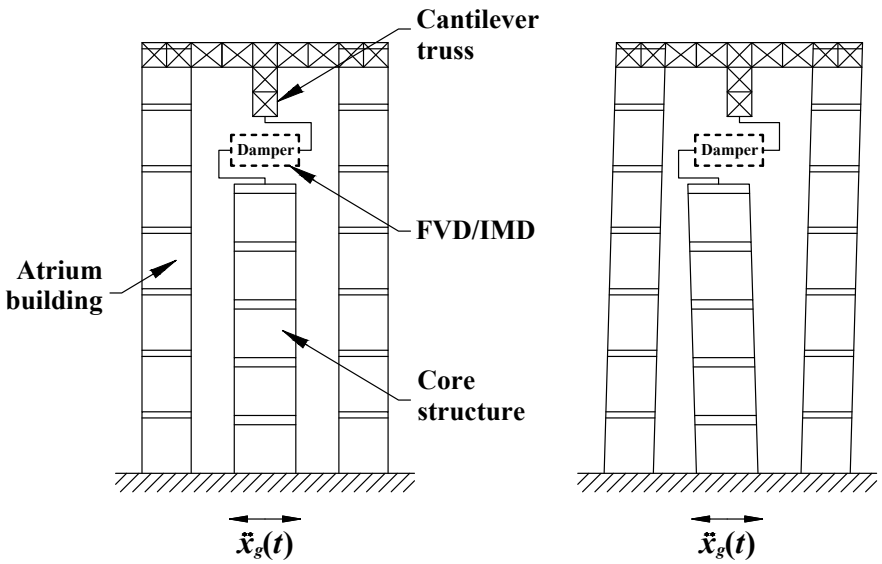

Figure 1.8: Proposed truss-damper configuration for an atrium building.

core structure inside the building in combination with a truss-damper system (a truss-FVD system or a truss-IMD system).

- To develop numerical time-history approaches for calculating the seismic response of an atrium building equipping with a truss-FVD system and a truss-IMD system, respectively.
- To conduct parametric studies on the truss-damper systems and investigate the influences of different design parameters on the seismic performance of the atrium building.
- To develop an optimal design approach for the truss-damper systems to achieve certain performance objectives in an atrium building.
- To evaluate the robustness and reliability of the optimal design approach.

1.4 Thesis outline

Chapter 2 provides detailed literature reviews on the dynamic analysis of structures with nonlinear viscous dampers, seismic design of damper-brace systems in building applications, and the development of inerter-based passive control devices, especially the inertial mass dampers. Seismic control of atrium buildings and some energy dissipation configurations incorporating specific structural elements have also been reviewed.

Chapter 3 introduces the methodologies involved in this research to analyse, design and evaluate the structural systems, including state-space technique and Runge-

Kutta methods for time-history analysis, performance evaluation criteria adopted, genetic algorithms for performance optimization, and earthquake ground motion representations used in this study. Example demonstrations have been provided for the state-space procedure and the spectrum representation method.

Chapter 4 presents the numerical time-history approach for a single-degree-of-freedom (SDOF) structure with a Maxwell-type nonlinear damper-brace system based on the state-space technique. The correctness and accuracy of the proposed approach is evaluated using first the fourth-order Runge-Kutta method, followed by a frequency-domain approach for linear systems.

Chapter 5 investigates the influences of brace stiffness and damper nonlinearity on seismic performance of shear-type buildings. Parametric studies are conducted to assess the effectiveness of the damper-brace assembly on mitigating structural interstory drift and base shear force, using first a SDOF structure, followed by multi-story buildings. Optimizations of the design parameters are performed to maximizing the response reduction capabilities of the nonlinear damper-brace systems. Incremental dynamic analysis is also conducted to evaluate the robustness and stability of the optimal systems in a nonlinear eight-story building.

Chapter 6 introduces the analytic models of an atrium building and a core structure connected by a truss-damper system. Parametric studies are conducted on a truss-FVD system and a truss-IMD system to evaluate their performances in seismic vibration control of atrium buildings. Incremental dynamic analysis is performed to assess the capability and robustness of an optimal truss-damper assembly in a nonlinear SDOF structural system. A 6-story atrium building is also numerically evaluated to compare the seismic performances of the truss-FVD and truss-IMD systems under realistic earthquakes with different vibration characteristics.

Chapter 7 presents a simplified truss-IMD-core structure model that combines a truss-IMD system and a core structure to further investigate the effect of lateral stiffness of the core structure on seismic performance of atrium buildings. A multi-objective optimization approach is developed based on a genetic algorithm to optimize the design parameters of the simplified model for mitigating the interstory drift and story acceleration of an atrium building simultaneously.

Chapter 8 provides an overall conclusion of the thesis and some future research interests.

Chapter 2 Literature review

2.1 Seismic analysis of structures with nonlinear viscous dampers

For seismic analysis of structures with nonlinear viscous dampers, linear approaches such as response spectrum analysis cannot be directly used due to the nonlinear terms in the equations of motion, even with the assumption that the primary structure behaves linearly (Di Paola and Navarra 2009, Moslehi Tabar and De Domenico 2020). Since the nonlinear damping arises mostly from the viscous dampers, to estimate the structural response, approaches that adopted an equivalent linear viscous damping ratio to represent the damping effects of the nonlinear dampers can be found in the literature (Sadek et al. 2000, Lee et al. 2004). Compared with using linear damping ratios, a more popular strategy to linearize the equations of motion is to use equivalent linear viscous dampers to replace the nonlinear ones. For example, Lin and Chopra (2002) used an equivalent linear dashpot to replace a nonlinear damper in a SDOF structure, of which the amount of energy dissipated within one cycle of a harmonic motion is the same as that of the nonlinear damper. The problem is thereby simplified, and linear approaches like frequency-domain methods can be applied. Notably, the maximum displacement experienced by the equivalent dashpot is essential to determine its equivalent damping coefficient, thus iterative procedures are usually required during the linearization process. To avoid the iterations, Diotallevi et al. (2012) proposed an approach to predict the structural response and damper deformation directly. Furthermore, as the harmonic motion cannot really describe earthquake-induced vibration, different stochastic linearization approaches were developed (Di Paola et al. 2007, Di Paola and Navarra 2009, Tubaldi and Kougioumtzoglou 2015), which extended the harmonic motion to random vibrations induced by earthquakes to compute more appropriate linearization results. For instance, De Domenico and Ricciardi (2018) developed an equal-energy non-Gaussian stochastic linearization method to estimate the damping coefficients of the equivalent dampers; the method has been integrated into an optimal design procedure of nonlinear dampers (De Domenico and Ricciardi 2019). A more recent example is a modified stochastic linearization technique proposed by Asadpour et al. (2022) for the analysis of bilinear hysteresis structures with nonlinear FVDs, which linearized the nonlinear damper forces based on optimal non-Gaussian probability density functions obtained using genetic algorithm. In general, the implementation of equivalent linearization approaches can simplify the analysis process of structures

with nonlinear viscous dampers; however, the accuracy of structural response results is generally lower than those computed from numerical time-history methods that explicitly dealt with the damper nonlinearity.

A precise analysis for the seismic response of a structure with nonlinear viscous dampers can be achieved by integrating the nonlinear equations of motion directly (Terenzi 1999, Craig and Kurdila 2006). However, due to the inherent stochastic nature of earthquakes, the seismic-induced ground acceleration is hard to be expressed with rigorous mathematical functions, thus closed-form solutions of the structural response are difficult to obtain. In addition, as the equations of motion of a nonlinear system are nonlinear differential equations, they are usually not possible to be solved analytically (Chopra 2012). In that context, numerical time-history approaches (or time-stepping approaches) that integrate an equation of motion within constant or variable time intervals can be adopted to calculate the seismic response of structures with nonlinear dampers, and the frequently used approaches include Newmark's method (Newmark 1959), Wilson-θ method (Wilson et al. 1972) and Runge-Kutta methods (Lindfield and Penny 2019). A recent example of the numerical approach is that Moslehi Tabar (2019) applied an analytical approximation method, namely perturbation technique, to convert the equation of motion of a nonlinear system into infinite linear equations within each computational time interval, and the accuracy of the presented method depends on the number of linear equations solved. A nonlinear response spectrum analysis technique was also developed based on the perturbation method (Moslehi Tabar and De Domenico 2020), in which a nonlinear spectrum for structures with nonlinear viscous dampers was obtained to facilitate the design of such structures. In general, the numerical time-history methods are considered high precision approaches in the analysis of nonlinear systems and thus could be taken as a baseline in the validation of other approaches.

It is also worth noting that, to simplify the design process of nonlinear viscous dampers, instead of computing the seismic response of the primary structure directly using the aforementioned techniques, some of the design approaches estimated the response intensities of the structure based on the supplemental damping provided by the dampers. For instance, the optimal design method proposed by Lang et al. (2013) established a polynomial relationship between the damping coefficient of the nonlinear dampers and the output frequency responses of the structure based on an output frequency response function concept. The optimal direct displacement-based design procedure developed by Moradpour and Dehestani (2019) adopted an equivalent SDOF system to represent a multi-story structure, and the optimal parameters of the nonlinear dampers can be determined iteratively using a displacement response

spectrum scaled based on the equivalent damping of the dampers. Landi et al. (2014) proposed a direct assessment method to estimate the seismic response of a nonlinear structure with nonlinear viscous dampers based on an estimated damping ratio of the whole structural system, and the method has been modified by Yaghmaei-Sabegh et al. (2020) to analyse structures under pulse-type ground motions. Although these approaches can estimate the structural responses, the complete response-history of the structure is either unobtainable, or of limited accuracy.

2.2 Supporting braces for viscous dampers

In general, the use of a flexible brace will reduce damping performance of a viscous damper especially when the damping coefficient is large, as part of the structural motions will be wasted as brace deformations. Therefore, to ensure a proper damper performance, different requirements on the minimum brace stiffness have been established in the literature and seismic design standards (Silvestri et al. 2010, Zhou et al. 2012, Palermo, Silvestri, Landi, Gasparini and Trombetti 2018, Kitayama and Constantinou 2018, CMC 2010, ASCE 2017), and supporting braces with a stiffness larger than the minimum requirements are considered adequate for ensuring efficiency of the dampers. For instance, Fu and Kasai (1998) conducted parametric studies on different dampers for frame-type structures; the authors reported that a ratio of brace stiffness to story stiffness equals 10 and a ratio of damper loss stiffness to story stiffness in the range of $1-1.5$ are adequate for FVDs and viscoelastic dampers to achieve their optimum performances under harmonic excitation. In the optimal design approach proposed by Singh et al. (2003), braces are considered to be "rigid" if their stiffness is 10 times the story stiffness, and a brace stiffness that is 5 times the story stiffness is considered appropriate to guarantee efficiency of the dampers. Chen and Chai (2011) developed an optimal design procedure for shear-type structures with linear damper-brace systems, and their results showed that as the stiffness of braces equals the first-story stiffness, the optimally designed FVDs mitigated around 90% of structural interstory drift and 80% of story acceleration of a 10-story building.

For better evaluation of the damping performance of viscous dampers in building structures, many researchers suggested to consider the stiffness of supporting braces in the structural analysis, i.e., incorporating the brace elements into the analytic model of the dampers. For example, Hatada et al. (2000) studied the numerical approaches for high-rise buildings with supplementary linear FVDs; the authors reported that for the dampers with large damping coefficient, the equivalent horizontal stiffness of the supporting braces should be incorporated into the analytic model. Park et al. (2004) suggested that the actual peak response of a structure may be much larger

than that estimated by numerical simulations if the flexibility of braces is excluded in the analysis. Huang (2009) conducted parametric studies on a toggle-brace-damper system and claimed that the magnification effect of the brace configuration may be overestimated if the brace stiffness is neglected. Akcelyan et al. (2016) also suggested to include the braces in the analytic model of the viscous dampers to avoid a misestimation of the damper effectiveness.

A damper-brace assembly can be rheologically described using a Maxwell model, which represents the assembly using a dashpot and a spring connected in series. Different design methods for such a damper-brace system have been proposed in the literature to maximize dynamic performance of building structures (Viola and Guidi 2009, Londoño et al. 2013, Losanno et al. 2015, Lavan 2015, Losanno et al. 2018, Pollini et al. 2017, Shen et al. 2020). Notably, to describe the dynamic behaviour of a high-rise building with linear viscous dampers, Hatada et al. (2000) incorporated Maxwell models into a multi-degree-of-freedom (MDOF) structural model; a numerical time-history method was also proposed to obtain the seismic response of the model. Chen and Chai (2011) developed an approach to evaluate the dynamic performance of a shear-type structure with Maxwell model-based brace-damper systems, based on which the effect of brace stiffness on the optimal structural performance was evaluated. Londoño et al. (2013) proposed a method to determine the minimum brace stiffness or the minimum damping coefficient for linear damper-brace assemblies to achieve a target damping ratio in a building. The authors also extended the method to determine the required brace stiffness for satisfying a desired damping performance over a predefined frequency bandwidth (Londoño et al. 2014). To avoid iterative calculations in the design process, Losanno et al. (2018) presented a non-iterative approach to determine the parameters of braces and linear FVDs to achieve a preset damping ratio of the structure. For nonlinear viscous dampers, Pollini et al. (2017) proposed a design approach to minimize the cost of nonlinear dampers in a multi-story structure while maintaining a specific interstory drift performance, and the supporting braces were included in the performance evaluation of the structure. Shen et al. (2020) developed a method for retrofit design of nonlinear damper-brace systems in inelastic structures based on elastic-plastic response reduction curves. Instead of conducting time-history analysis, they established relationships between some proposed response reduction indices and the equivalent period and damping ratio of an analytic model of the structural system. The relationships between the nonlinear damper-brace systems and the achievable optimal performance of building structures have also been investigated in some recent studies (Li et al. 2021).

2.3 Inerter-based passive control devices

2.3.1 Inertial mass dampers

Since the analytic model of an ideal inertial mass damper consists of an inerter and a dashpot, the physical realization of the IMD can be achieved based on different mechanisms of the inerter. In the literature, ball-screw is the most commonly used mechanism for IMDs. For example, Hwang et al. (2007) proposed a rotational inertia viscous damper based on the ball-screw mechanism to transform the interstory drift of a structure into rotary motion of a flywheel, which is immersed in silicon oil to dissipate input seismic energy. The proposed damper has been numerically evaluated using a SDOF structure, and it was reported that the performance of the damper depended heavily on the length of the ball screw lead. Ikago et al. (2012) developed a tuned viscous mass damper that consists of an IMD and a spring connecting the IMD to the structure. The proposed damper exhibited better performance than fluid viscous dampers in shaking table tests of a SDOF structure. Nakamura et al. (2014) proposed an electromagnetic inertial mass damper consisting of a ball-screw inerter and an electric generator, and the inertial force and damping force can be simultaneously generated during external excitation. The seismic performance of the electromagnetic inertial mass damper has been evaluated by shaking table tests, and the damper surpassed conventional types of dampers especially in mitigating the acceleration response of a structure. A recent example of the IMD is the adaptive tuned viscous inertance damper proposed by Ali Sadeghian et al. (2021), of which a continuously variable transmission device has been integrated into the ball-screw inerter to allow adjustment of its inertance. Numerical evaluations showed that the proposed device can significantly increase the damping of a SDOF structure in a vast range of excitation frequency.

Although the above-mentioned studies generally used SDOF structures to assess IMDs, their results nonetheless proved the effectiveness of the IMD in mitigating dynamic response of normal types of buildings. In addition to the building structures, investigations have been made to evaluate the performance of the IMD or its variants on the vibration control of other types of structures in civil engineering. Ma et al. (2019) proposed a hydraulic rotational inertia damper for vibration control of semisubmersible platforms in shallow sea, which churned seawater through rotation of a ball screw device and generated damping force from fluid resistance. The device has been physically manufactured and has proven to be capable of providing a large damping force in the water. Lu et al. (2017) developed a control-oriented model to describe the in-plane motions of a cable-IMD system, based on which the

effectiveness of the IMD on suppressing cable vibration in cable-stayed bridges have been investigated, and their results showed that the IMD reduced a greater amount of root-mean-square response of the cable displacement than FVDs. Lu et al. (2021) assessed the performance of the IMD in the response mitigation of coupled adjacent buildings and proposed some useful guidelines for positioning of the IMDs in such buildings.

2.3.2 Other inerter-based passive control devices

In addition to the inertial mass dampers, extensive research has also been conducted on the development of other types of inerter-based seismic control systems in the last two decades, and those systems can be broadly categorized into two groups, namely inerter-based vibration absorbers and inerter-based vibration isolators (Ma et al. 2021*a*). The conventional vibration absorbers, typified by the tuned mass damper, usually require a large secondary mass to be installed in the primary structure to obtain a desirable dynamic performance, and the effectiveness of the absorber depends greatly on the mass ratio between the secondary mass and the target structure. In that context, inerters can be used to reduce the auxiliary mass and enhance the control effectiveness. Based on the conventional TMDs, Hu and Chen (2015) proposed some inerter-based dynamic vibration absorbers with different configurations, and most of them can achieve a significant improvement in structural performance compared with the traditional TMDs. Marian and Giaralis (2014) proposed a tuned mass damper inerter that can either improve the performance of a TMD with a given mass ratio or reduce the auxiliary mass without a degradation in structural performance. Lazar et al. (2014) developed a tuned inerter damper that can be seen as a special case of the tuned mass damper inerter, i.e., the auxiliary mass equals zero, thus the physical mass of the damper can be reduced, and the workspace may be saved. Other examples of the inerter-based vibration absorbers include the tuned liquid inerter system developed by Zhao et al. (2019) and the nonlinear energy sink inerter proposed by Javidialesaadi and Wierschem (2019). These inerter-based absorbers have proven to be effective vibration supersession devices not only for buildings (Pietrosanti et al. 2017, De Domenico et al. 2019, Shen et al. 2019, Petrini et al. 2020, Wang et al. 2021, Djerouni et al. 2021, Shen et al. 2021), but also for other structures like vehicle suspension (Shen et al. 2016), fluid piping (Duan et al. 2021), and marine shafting systems (Dai et al. 2022).

In addition to the absorbers, many inerter-based vibration isolators have also been presented in the literature to upgrade the conventional base isolation systems. For instance, Hu et al. (2015) proposed five configurations of inerter-based isolators

and demonstrated their superior performances to the conventional isolator. Ma et al. (2020) developed an inerter-based vibration isolation system to control heave motions for semisubmersible platforms, and Shi et al. (2022) proposed an inerter-based nonlinear isolator with geometry nonlinearity produced by incorporating a linear inerter into a diamond-shaped linkage. The effectiveness of different inerter-based isolators has been assessed in some studies (Saitoh 2012, Yang 2016, Yang et al. 2017, Moraes et al. 2018, Yang et al. 2020, Dong, Yang, Zhu, Chronopoulos and Li 2022); some hybrid systems that combined different inerter-based vibration control systems have also presented in recent years (De Domenico and Ricciardi 2018, De Angelis et al. 2019, Li, Chang, Cao and Huang 2021, Cao and Li 2022). Moreover, the applications of inerters in some specific engineering structures have been investigated. For example, Li et al. (2017) evaluated the performance of different shimmy-suppression layouts with inerters in vibration control of aircraft landing gear systems, and Dong, Shi, Yang and Li (2022) proposed a nonlinear passive joint device based on inerters to mitigate vibration transmission in coupled systems; the application of inerters in some special structures or structural components like laminated composite plates (Zhu et al. 2021) and metamaterial structures (Dong et al. 2021, Liu et al. 2022) have also been studied.

2.4 Seismic control of atrium buildings and energy dissipation configurations using specific structural elements

In the literature, very few research was conducted on seismic vibration control of atrium buildings, which may be attributed to the fact that many conventional passive control systems such as the interstory-placed damper-brace assemblies can already provide sufficient damping to structures with atria. However, for better utilization of the internal open space provided by the atrium, some passive control devices can be installed inside the atrium to avoid excessive consumption of the usable space of the building, such as the conventional tuned mass dampers (Lee et al. 2006, Leung et al. 2008, Bekdaş and Nigdeli 2011, Etedali and Rakhshani 2018, Bekdaş et al. 2018) and more recent inerter-based absorbers like the tuned mass damper inerter and tuned inerter damper (Marian and Giaralis 2014, Lazar et al. 2014, Marian and Giaralis 2014, Pietrosanti et al. 2017, Shen et al. 2019, Petrini et al. 2020, Pietrosanti et al. 2020, Deastra et al. 2020, Shen et al. 2021). These devices have been theoretically and experimentally proven to be effective in mitigating the dynamic response of a building when subjected to strong wind or earthquakes, yet a large space inside the building is usually required for successful operations of these devices.

The truss-damper configuration proposed in this study utilizes a core structure to

be a support of the passive control devices, as the core structure is also a structural element that shall be designed to resist earthquake loads. Similar arrangements that incorporated certain structural elements into the seismic control system of a building can be found in the literature, and most of them were proposed for the purpose of enhancing the overall structural performance under external disturbances. For instance, different floors can be connected together using certain passive control devices to alleviate seismic response of the entire building (Marian and Giaralis 2014, Petrini et al. 2020); an adjacent structure can be connected to the primary building with different damping devices to control both structures (Bharti et al. 2010, Bigdeli et al. 2016, Kandemir-Mazanoglu and Mazanoglu 2017, De Domenico et al. 2020, Wang et al. 2021), and some supplemental elements can also be built in the primary building to improve damping capacity of the seismic control devices, such as a strongback system that utilized the uniform story drifts over the height of a building to dissipate energy (Lai and Mahin 2015, Palermo, Laghi, Gasparini and Trombetti 2018), and a damped outrigger system that used the relative vertical displacement between the core and the perimeter columns of a high-rise building (tube-type building preferred) to activate viscous dampers (Smith and Willford 2007, Alhaddad et al. 2020). A recent example of the purpose-built supplemental elements for enhancing damping capacity is a couple wall system proposed by Ji et al. (2021) for high-rise buildings, which consists of two adjacent wall piers extending from the ground to the building roof; multiple tuned viscous mass dampers were arranged between the wall piers in a zigzag configuration, and the relative vertical motion between the two walls inducing by the bending vibration of the building was used to activate the dampers.

Chapter 3 Methodology

3.1 Numerical time-history analysis methods

In this thesis, the mass of a building is idealized as concentrated at the floor levels. For instance, the structural model in Figure 3.1(a) is adopted to represent a single-story structure. The equation of motion of an idealized building with nonlinear viscous dampers can thus be expressed as a second-order ordinary differential equation (ODE), of which the exact analytical solutions are difficult to be obtained. In this thesis, numerical time-history approaches are adopted to solve the governing ODEs directly for given earthquake inputs. The numerical techniques used in this research will be introduced in the following sections.

3.1.1 State-space procedure

A single-story building with a supplemental nonlinear viscous damper installed on top of a Chevron brace, as shown in Figure 3.1(a), is adopted here to demonstrate the state-space technique used in this study.

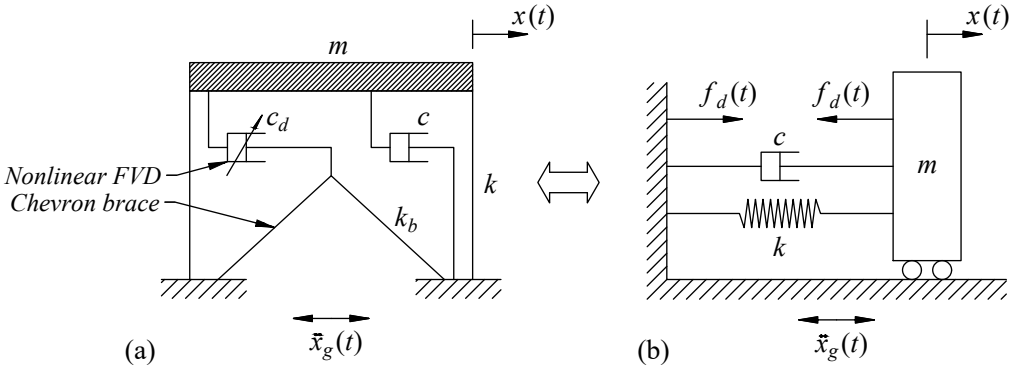

Figure 3.1: (a) Analytic model of a single-story structure with a nonlinear viscous damper (b) an equivalent model.

The analytic model of the SDOF structure can also be represented using Figure 3.1(b), in which the force in the FVD is described as a nonlinear function $f_d(t)$. The equation of motion of the analytic model can thus be expressed as:

$$m\ddot{x}(t) + c\dot{x}(t) + kx(t) + f_d(t) = -m\ddot{x}_g(t) \tag{3.1}$$

where m, c, k and $x(t)$ are the mass, damping coefficient, lateral stiffness, and horizontal displacement of the structure, respectively, and $\ddot{x}_g(t)$ denotes the ground acceleration.

For a structural system with n-degree-of-freedom, the state variables, which describe the motion of the system, can be defined as the structural displacement and velocity, i.e., $x_i(t)$ and $\dot{x}_i(t)$ $(i = 1, 2, ..., n)$. The structural motion can thus be represented in an $2n$-dimensional Euclidean space contains $x_i(t)$ and $\dot{x}_i(t)$, which is also known as the state-space (Meirovitch 1990). When being converted from continuous state to state-space, a second-order differential equation of motion will become a first-order ODE, which simplifies the numerical integration process. The state-space formulation of the equation of motion of the single-story building is:

$$\dot{\mathbf{z}}_\mathbf{0}(t) = \mathbf{A}\mathbf{z}_\mathbf{0}(t) + \mathbf{B}f_d(t) + \mathbf{E}\ddot{x}_g(t) \tag{3.2}$$

where

$\mathbf{z}_\mathbf{0}(t) = \begin{bmatrix} x(t) \\ \dot{x}(t) \end{bmatrix}$ is the response vector of the structure;

$\mathbf{A} = \begin{bmatrix} 0 & 1 \\ -m^{-1}k & -m^{-1}c \end{bmatrix}$ is the system matrix;

$\mathbf{B} = \begin{bmatrix} 0 \\ -m^{-1} \end{bmatrix}$ is the distribution vector of damper force $f_d(t)$;

$\mathbf{E} = \begin{bmatrix} 0 \\ -1 \end{bmatrix}$ is the distribution vector of the ground acceleration $\ddot{x}_g(t)$.

Although the form of equation of motion changes when it is expressed in state-space formulation, the solution of structural response will be the same. The numerical integration approach that solves differential equations using Laplace transformation (Meirovitch 1990) is used in this research. For instance, to calculate Eq. (3.2), Laplace transformation is first applied to the equation, which yields:

$$\mathbf{z}_\mathbf{0}(s) = \mathbf{H}(s)\mathbf{z}_\mathbf{0}(t_0) + \mathbf{H}(s)\mathbf{B}f_d(s) + \mathbf{H}(s)\mathbf{E}\ddot{x}_g(s) \tag{3.3}$$

where $\mathbf{H}(s) = (s\mathbf{I} - \mathbf{A})^{-1}$.

By taking inverse Laplace transformation of Eq. (3.3), the response vector can be described in the time-domain:

$$\mathbf{z}_\mathbf{0}(t) = e^{\mathbf{A}(t-t_0)}\mathbf{z}_\mathbf{0}(t_0) + \int_{t_0}^{t} e^{\mathbf{A}(t-\tau)}\{\mathbf{B}f_d(\tau) + \mathbf{E}\ddot{x}_g(\tau)\}d\tau \tag{3.4}$$

which can be evaluated by the following steps. Within the interval between two consecutive sampling instants, $t_0 = \mathrm{k}\Delta t$ and $t = (\mathrm{k}+1)\Delta t$, where Δt is the sampling period, it is assumed that the force induced by the nonlinear damper-brace system,

$f_d(\tau)$, is piece-wise constant, while the ground acceleration, $\ddot{x}_g(\tau)$, changes linearly within each time step, as described below:

$$\begin{cases} f_d(\tau) = f_d(\mathrm{k}\Delta t) \\ \ddot{x}_g(\tau) = \frac{(\mathrm{k}+1)\Delta t - \tau}{\Delta t}\ddot{x}_g(\mathrm{k}\Delta t) + \frac{\tau - \mathrm{k}\Delta t}{\Delta t}\ddot{x}_g((\mathrm{k}+1)\Delta t) \end{cases} \quad \text{for } \mathrm{k}\Delta t < \tau < (\mathrm{k}+1)\Delta t \tag{3.5}$$

By substituting Eq. (3.5) into Eq. (3.4), the response of the structure can be further developed into a discrete-time state function for two consecutive sampling points [k] and [k + 1]:

$$\mathbf{z_0}[\mathrm{k}+1] = \mathbf{A_0}\mathbf{z_0}[\mathrm{k}] + \mathbf{B_0}f_d[\mathrm{k}] + \mathbf{E_0}\ddot{x}_g[\mathrm{k}] + \mathbf{E_1}\ddot{x}_g[\mathrm{k}+1] \tag{3.6}$$

where
$\mathbf{A_0} = e^{\mathbf{A}\Delta t}$ is the discrete system matrix;
$\mathbf{B_0} = \mathbf{A}^{-1}(\mathbf{A_0} - \mathbf{I})\mathbf{B}$ is the instant discrete damper force distribution matrix;
$\mathbf{E_0} = [\mathbf{A}^{-1}\mathbf{A_0} + \frac{1}{\Delta t}\mathbf{A}^{-2}(\mathbf{I} - \mathbf{A_0})]\mathbf{E}$ is the instant discrete ground acceleration distribution vector at sampling point [k];
$\mathbf{E_1} = [-\mathbf{A}^{-1} + \frac{1}{\Delta t}\mathbf{A}^{-2}(\mathbf{A_0} - \mathbf{I})]\mathbf{E}$ is the instant discrete ground acceleration distribution vector at sampling point [k + 1].

It can be seen from Eq. (3.6) that, for a prescribed ground acceleration-history $\ddot{x}_g$, the next step response vector $\mathbf{z_0}[\mathrm{k}+1]$ can be computed from the response vector at the current step $\mathbf{z_0}[\mathrm{k}]$, once the damper force $f_d[\mathrm{k}]$ is given. The damper force can also be calculated using the state-space technique, as demonstrated in Section 4.2.

3.1.2 Runge-Kutta methods

The Runge-Kutta methods are a family of iterative approaches in numerical analysis, which are one of the most commonly used numerical integration methods for solving initial value problems of ODEs (Cash and Karp 1990, Zheng and Zhang 2017, Lindfield and Penny 2019). The Runge-Kutta methods were first proposed by Carl Runge (Runge 1895) and Martin Kutta (Kutta 1901), which can construct numerical computational formulas with high order accuracy for an ordinary differential equation using the targeting ODE itself.

3.1.2.1 Fourth-order Runge-Kutta method (RK4)

For a differential equation $\dot{y} = f(t, y)$, in which $y(t_0) = y_0$, the fourth-order Runge-Kutta method is defined with the following recursion equation:

$$y_{n+1} = y_n + \frac{1}{6}\left(K_1 + 2K_2 + 2K_3 + K_4\right)\Delta t \tag{3.7}$$

where $\frac{1}{6}\left(K_1 + 2K_2 + 2K_3 + K_4\right)$ is the weighted average slope of the solution; K_1, K_2, K_3 and K_4 are the slope coefficients that are defined as:

$$\begin{cases} K_1 = f\left(t_n, y_n\right) \\ K_2 = f\left(t_n + \frac{\Delta t}{2}, y_n + \frac{\Delta t}{2} K_1\right) \\ K_3 = f\left(t_n + \frac{\Delta t}{2}, y_n + \frac{\Delta t}{2} K_2\right) \\ K_4 = f\left(t_n + \Delta t, y_n + \Delta t K_3\right) \end{cases} \tag{3.8}$$

The local truncation error of the fourth-order Runge-Kutta method is on the order of $O(\Delta t^5)$, and the global accumulated error is on the order of $O(\Delta t^4)$. In this study, RK4 is combined with the state-space method to conduct numerical analysis of nonlinear structural systems with a constant time step size.

3.1.2.2 ODE suite in MATLAB

The MATLAB ODE suite provides different Runge-Kutta programs to solve differential equations. The suite includes `ode45`, `ode23`, `ode113`, `ode78`, `ode89`, `ode15s`, `ode23s`, `ode23t`, `ode23tb` and `ode15i`, among which the `ode45` solver is recommended as the prior choice for solving ODEs (MathWorks 2021). `ode45` is a single-step solver based on the explicit Runge-Kutta (4, 5) pair of Dormand and Prince (1980). The fourth-order and fifth-order of the Dormand-Prince (4, 5) pair can be expressed as:

$$y_{i+1} = y_i + \left(\frac{35}{384}K_1 + \frac{500}{1113}K_3 + \frac{125}{192}K_4 - \frac{2187}{6784}K_5 + \frac{11}{84}K_6\right)\Delta t \tag{3.9}$$

$$\begin{aligned} z_{i+1} = y_i + \Bigg(&\frac{5179}{57600}K_1 + \frac{7571}{16695}K_3 + \frac{393}{640}K_4 - \frac{92097}{339200}K_5 + \\ &\frac{187}{2100}K_6 + \frac{1}{40}K_7\Bigg)\Delta t \end{aligned} \tag{3.10}$$

in which the slope coefficients are defined as:

$$\begin{cases} K_1 = f\left(t_n, y_n\right) \\ K_2 = f\left(t_n + \frac{1}{5}\Delta t, y_n + \frac{1}{5}K_1\right) \\ K_3 = f\left(t_n + \frac{3}{10}\Delta t, y_n + \frac{3}{40}K_1 + \frac{9}{40}K_2\right) \\ K_4 = f\left(t_n + \frac{4}{5}\Delta t, y_n + \frac{44}{45}K_1 - \frac{56}{15}K_2 + \frac{32}{9}K_3\right) \\ K_5 = f\left(t_n + \frac{8}{9}\Delta t, y_n + \frac{19372}{6561}K_1 - \frac{25360}{2187}K_2 + \frac{64448}{6561}K_3 - \frac{212}{729}K_4\right) \\ K_6 = f\left(t_n + \Delta t, y_n + \frac{9017}{3168}K_1 - \frac{355}{33}K_2 + \frac{46732}{5247}K_3 + \frac{49}{176}K_4 - \frac{5103}{18656}K_5\right) \\ K_7 = f\left(t_n + \Delta t, y_n + \frac{35}{384}K_1 + \frac{500}{1113}K_3 + \frac{125}{192}K_4 - \frac{2187}{6784}K_5 + \frac{11}{84}K_6\right) \end{cases} \tag{3.11}$$

In this research, `ode45` is adopted to be a solver of the differential equation between two consecutive computational time steps.

3.2 Performance assessment criteria

3.2.1 Performance indices

Performance-based design has been generally recognized as an ideal strategy for the seismic design of civil engineering structures (Idels and Lavan 2021). According to this design philosophy, the design criteria of the energy dissipation systems in a structure shall be set based on specific structural performance objectives under external disturbances, rather than considering only the additional damping provided by the systems. Therefore, the effectiveness of a supplemental passive control device in a structure can be assessed though evaluating different performance indices set. A performance index reflects the response intensity or damage severity of the entire structure or a certain structural component, which could be defined based on a specific structural response such as roof displacement, interstory drift, story acceleration, and base shear force. For instance, the following indices could be defined to reflect the overall intensities of the story displacement and acceleration under a predefined ground motion:

- The average of the root-mean-square (rms) of story displacement history.

$$PI_S = \frac{1}{n}\sum_{i=1}^{n} rms(x_i) \tag{3.12}$$

  where x_i is the horizontal displacement time-history of the i-th story of a MDOF building.

- The average of the root-mean-square of story acceleration history.

$$PI_A = \frac{1}{n}\sum_{i=1}^{n} rms(a_i) \tag{3.13}$$

  where a_i is the absolute floor acceleration time-history of i-th story, given by $a_i = \ddot{x}_i + \ddot{x}_g$, in which $\ddot{x}_i$ and $\ddot{x}_g$ are the relative floor acceleration and the ground acceleration, respectively.

A larger performance index generally indicates a more intense structural response during the earthquake excitation. In order to numerically determine the improved performance of the structure after the installation of a supplemental control system,

a response reduction criterion is adopted with the following forms:

$$RR_S(\%) = \left(1 - \frac{PI_S}{PI_{S,org}}\right) \times 100 \tag{3.14}$$

$$RR_A(\%) = \left(1 - \frac{PI_A}{PI_{A,org}}\right) \times 100 \tag{3.15}$$

where RR_S and RR_A are the response reductions in story displacement and acceleration, respectively; $PI_{S,org}$ and $PI_{A,org}$ are the corresponding performance indices of the structure in the original state, i.e., without the control system. As the physical meaning of a response reduction is the percentage of a specific structural response that has been eliminated by the supplementary system during the earthquake, a more effective design of the system would result in a larger response reduction.

3.2.2 Incremental dynamic analysis (IDA)

Previous research has revealed that the seismic performance of a structure can be greatly affected by the vibration characteristic of the input ground excitation (Bakhshinezhad and Mohebbi 2020). In order to evaluate the capacity and robustness of a specific design of a seismic control system to the uncertainty of seismic excitation input, multiple realistic earthquake records with different characteristics could be incorporated into the performance assessment of the structure. One of the approaches that has been adopted to tackle this task is the incremental dynamic analysis developed by Vamvatsikos and Cornell (2002).

The IDA is generally recognized as a valuable method to evaluate the dynamic performance of nonlinear structures within the framework of performance-based earthquake engineering (Han and Chopra 2006, Vamvatsikos 2011, Zacharenaki et al. 2014, Soleimani et al. 2018). This method has been widely used in different civil structures, such as buildings (Leng et al. 2020, Talley et al. 2021, Miari and Jankowski 2022), bridges (Gönen and Soyöz 2021, Aldea et al. 2021), and dams (Alembagheri and Ghaemian 2013, Soysal et al. 2016). In this thesis, IDA is adopted to investigate the response intensities of a building structure when it is subjected to different earthquake inputs and different excitation levels, and the average and maximum responses under a set of probable ground acceleration records will be used to evaluate the structural responses.

To conduct an IDA evaluation on a given structural model under a specific ground acceleration, the following definitions should be addressed at the first place:

- Scale Factor (SF), which is a non-negative scalar that multiplies an unscaled

earthquake acceleration time-history to magnify or minify the accelerogram, namely, SF = 1 represents the unscaled acceleration-history, SF < 1 indicates a scaled-down accelerogram, and SF > 1 is a scaled-up one.

- Intensity Measure (IM), or monotonic scalable ground motion intensity measure. IM is a non-negative scalar that describes the intensity of a scaled ground acceleration-history and increases with increasing scale factor SF. The commonly used IMs include peak ground acceleration (PGA), peaking ground velocity and the 5% damped spectral acceleration at the structure's fundamental period ($S_a(T_1, 5\%)$).

- Damage measure (DM), or structural state variable, which is a non-negative scalar that describes response intensity of the structural model when subjected to a prescribed ground excitation input. Possible DMs include peak roof displacement, peak story ductility, maximum interstory drift, story displacement and acceleration.

An IDA curve is the plot of a structural state variable DM calculated or measured in an IDA study against the intensity measures IMs for one or more earthquake inputs, as illustrated in Figure 3.2, which demonstrates the changes in a specific DM, i.e., the maximum structural displacement, under ground acceleration records that are scaled to progressively increasing level of intensity, which can provide an insight into the nature of structural response to a specific earthquake excitation.

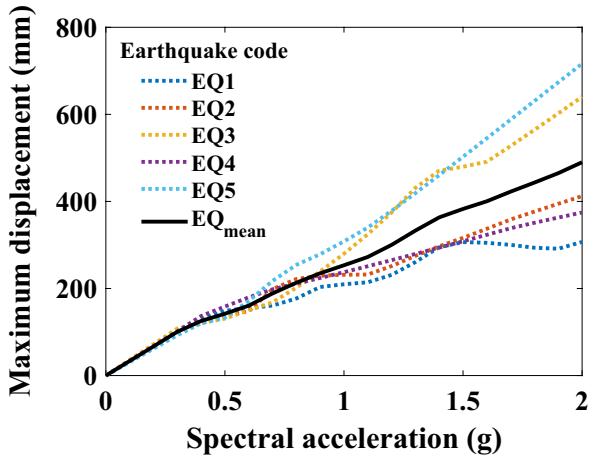

Figure 3.2: IDA curves of a SDOF structure subjected to five different earthquakes.

3.3 Genetic algorithms (GAs) for performance optimization

For maximizing the seismic performance of a structure in terms of structural response reductions, the design parameters of the seismic control systems, i.e., the

Algorithm 1 Pseudocode for the genetic algorithm

```
Define structural properties and excitation inputs
Initialize population (design parameters) POP with size N
Define terminal conditions and maximum iteration number T
Set generation t = 0
while terminal condition not met and t ≤ T do
  for i = 1 to N do
    Evaluate fitness of POP_t by computing target response reduction RR
  end for
  for i = 1 to N do
    Select parents from POP_t
  end for
  for i = 1 to N/2 do
    Crossover and generate new population POP_new
  end for
  for i = 1 to N do
    Perform mutation on POP_new
  end for
  for i = 1 to N do
    Update population POP_{t+1} = POP_new
  end for
  t = t + 1
end while
Return the best solution in POP as the optimal design parameters
Calculate the corresponding maximum response reduction RR_max
```

damper-brace and truss-damper assemblies, shall be optimally determined. To tackle the challenges associated with potentially large number of supplemental systems used in a building, genetic algorithm is adopted in this thesis as a global search engine for the optimal design variables in single-objective optimization tasks. This evolutionary algorithm was first popularized by Holland (1962), and has been extensively used in civil engineering to solve the optimization problems involved in structure design (Tavakolinia and Ch. Basim 2021, Ghasemof et al. 2022), structural model updating (Shabbir and Omenzetter 2016), damage prediction and detection (Daryan and Palizi 2020, Kim et al. 2022), etc. Since GA makes a good balance between achieving a local optimum by exploiting the best solutions and escaping from a local optimum through exploring the solution space (Gen and Cheng 1999), this algorithm is recognized a powerful tool in global optimization (Mishra et al. 2017, Fu et al. 2020, Katoch et al. 2021). Another reason to used GA in this research is that this algorithm is particular suited for solving optimization problems with discrete objective functions (Singh and Moreschi 2002), and the objective functions in this thesis are usually discretized. For instance, in Section 5.1, different response reductions will be served as the objective

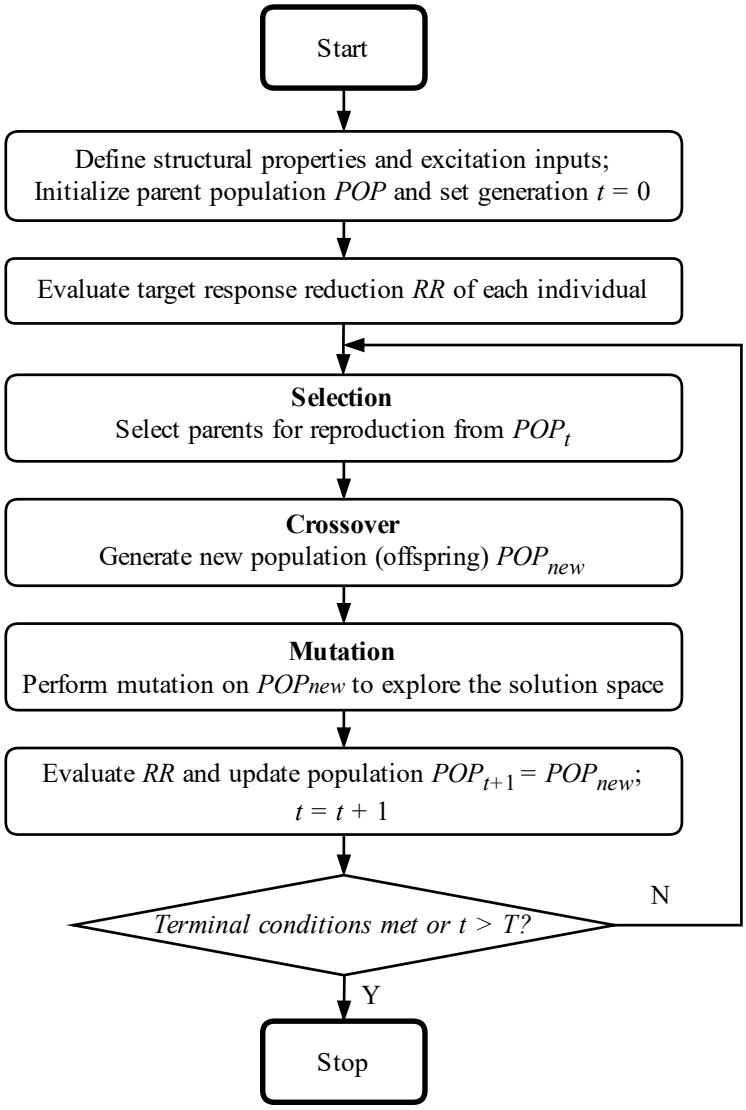

Figure 3.3: Flowchart of genetic algorithm for a single-objective optimization problem.

functions to optimize the damping coefficients of the viscous dampers under a discrete ground accelerogram. As rigorous mathematical expressions of the structural response cannot be obtained, the response reductions are no longer continuous functions of the design parameters but rather discretized. Although GA is a suitable tool for performing global optimizations in this research, it has some general drawbacks. For example, GA usually requires a significant amount of fitness evaluations to obtain an optimum (Ismail 2001) and it is less efficient in reaching an exact local optimum compared with some local optimization algorithms (e.g., gradient decent) (Gen and Cheng 1999); the random selection of parent population (i.e., initial design parameters) may also reduce the quality of solutions at an initial stage (Beg and Islam 2016).

Despite the drawbacks, the algorithm was found to be an effective tool to solve the optimization problems in this thesis. The procedure of the genetic algorithm used in this research is summarized in pseudocode 1; a flowchart of the algorithm is also given, as shown in Figure 3.3.

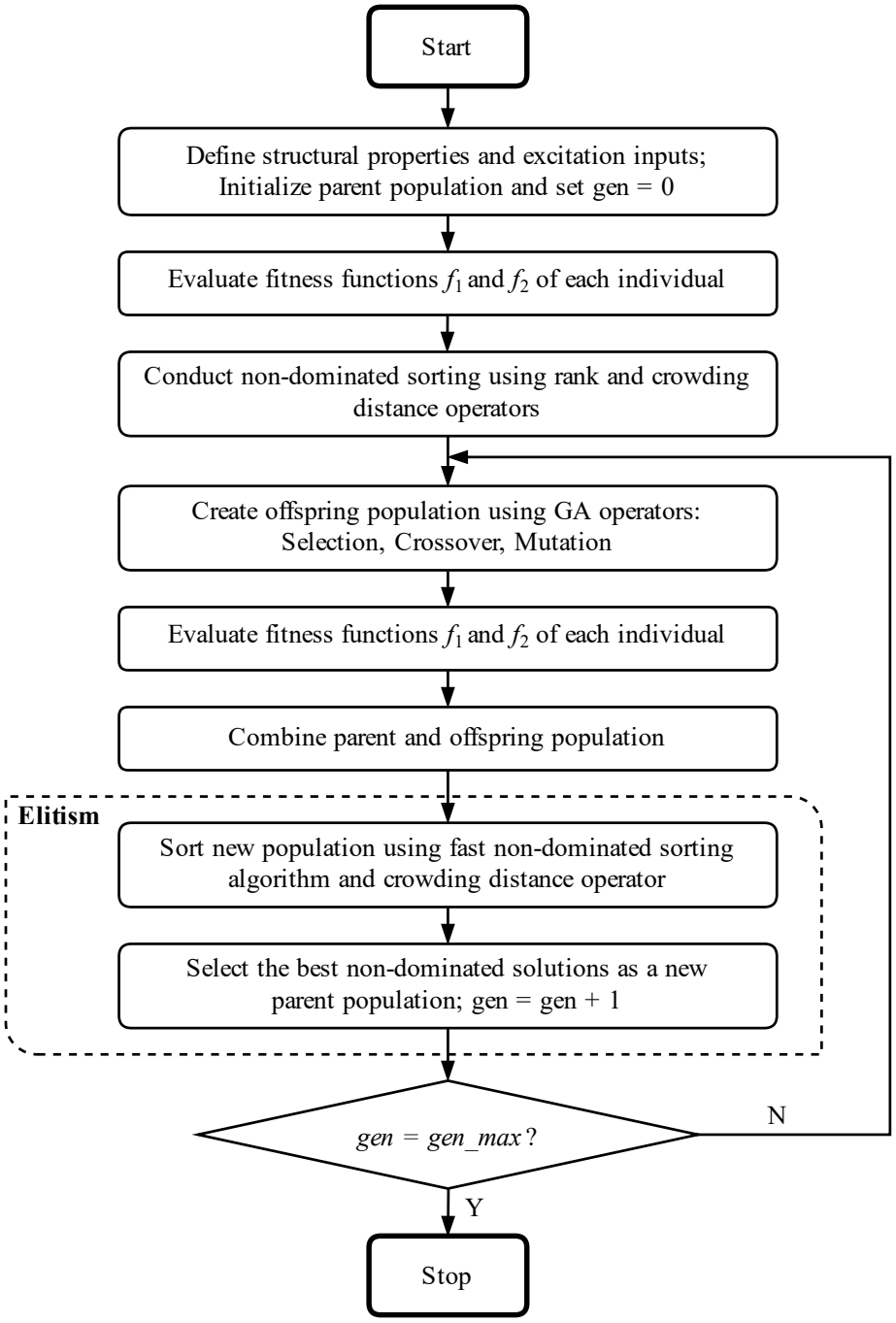

Figure 3.4: Flowchart of NSGA-II algorithm for a multi-objective optimization problem with two fitness functions.

For the single-objective genetic algorithm optimizations performed in this research, the solutions are deemed accurate and tolerable using the following stopping criteria: (i) when the change in the mean value between two consecutive generations is equal to or less than 10^{-4} for a design coefficient (e.g., damping coefficient) and 10^{-6} for a design ratio (e.g., damping ratio) after 100 iterations, or (ii) when the number of iterations reaches 200, i.e., the maximum iteration number T is set to 200. Notably, to reduce the probability of the algorithm being trapped by a local optimum and ensure accuracy of the solutions, in this thesis, the size of population N of the genetic algorithm is set to 20, and each of the optimization problems is optimized at least five times by the algorithm.

Multi-objective optimizations are also conducted to minimize different structural responses of a building simultaneously, e.g., minimizing interstory drift and base shear force at the same time. For multi-objective optimization problems, the performance objectives are usually in conflict with each other, i.e., the improvement of one may lead to degrading of others. Therefore, instead of a single optimal solution, a set of non-inferior solutions, also known as Pareto front or Pareto optimal solutions, should be a more appropriate answer for the optimization problem. In some literature, the multi-objective optimizations can be converted to single-objective optimizations using approaches such as weighted sum (Zadeh 1963) and goal attainment (Gembicki and Haimes 1975). However, these approaches generally require multiple adjustments and simulations to compute some possible optimal solutions at the Pareto front (Bakhshinezhad and Mohebbi 2020). A more efficient way to solve a multi-objective optimization may be to use algorithms that can detect Pareto fronts for the fitness functions, which can find more Pareto optimal solutions at even a single simulation run. For the multi-objective GA optimizations performed in this research, a controlled elitist genetic algorithm `gamultiobj` embedded in MATLAB optimization toolbox is used, which was developed based on an upgraded non-dominated sorting genetic algorithm (NSGA-II) (Deb 2001). Detailed algorithm of NSGA-II can be found in Deb et al. (2002), and a flowchart of the algorithm for a two-objective optimization problem is provided in Figure 3.4.

3.4 Earthquake ground motion representations

The time-variation of ground acceleration-history is recognized as the most effective definition of the ground shaking during an earthquake in seismic engineering (Chopra 2012). The ground acceleration $\ddot{x}_g(t)$ usually appears at the right side of the differential equation (e.g., Eq. (3.1)) that governing the structural seismic response. And time-history analysis for building structures with predefined ground accelero-

grams are usually required by worldwide seismic design standards. For instance, the seismic design code of China (GB50011-2010) (CMC 2010) requires the designers to use historic strong ground motion records and artificial accelerograms simultaneous to conduction time-history analysis of structures. The American code FEMA 356 (ASCE 2000) requires at least three ground acceleration-history sets (two horizontal components plus one vertical component if considered) that are selected and scaled from three or more earthquake events to be used in the time-history analysis. In this research, some realistic earthquake motion records, as well as two artificial accelerograms, i.e., a white-noise model and a Kanai-Tajimi model, will be adopted as the ground excitation inputs. The data extraction approaches for the excitation inputs will be introduced in the following sections.

3.4.1 Realistic earthquake records

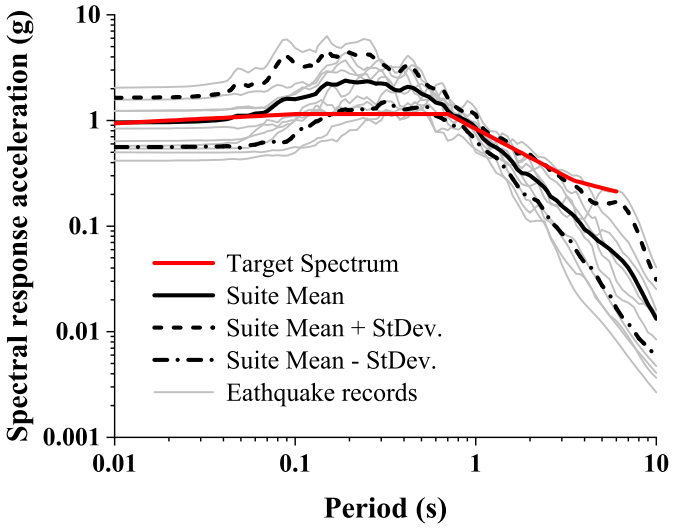

Figure 3.5: Spectral response accelerations of the realistic earthquake records searched and scaled by a user-defined design spectrum with structural damping ratio $\xi = 5\%$ using PEER database.

Acceleration recording instruments like strong-motion accelerographs can record the ground acceleration-histories during an earthquake. The instruments are generally equipped at stations in earthquake-prone regions to record possible ground motions (Chopra 2012). Strong ground shaking records collected at a target region are useful information for seismic design of the building structures located near that region or constructed at sites with a similar ground condition. Some design standards also suggested specific earthquake motion records to be used for designing certain types of buildings with certain site conditions (IEM 2004). The realistic earthquake motion records used in this research are collected from the Pacific Earthquake Engi-

neering Research Center (PEER) ground motion database (PEER 2022). The PEER database provides tools for users to directly search the ground acceleration records by earthquake information like event name, station name and moment magnitude. It also allows the users to search records by a user-defined target design spectrum, as shown in Figure 3.5.

3.4.2 Artificial accelerograms

Apart from the realistic earthquake records and a white-noise ground acceleration, the Kanai-Tajimi earthquake model (Kanai 1960, Tajimi 1960) is also considered in this research as a ground excitation input. The Kanai-Tajimi model idealizes the earthquake ground acceleration as a stationary random process with a power spectral density (PSD) function as follows:

$$S_{\ddot{x}_g}(\omega) = S_0 \frac{\omega_g^4 + 4\xi_g^2\omega_g^2\omega^2}{\left(\omega_g^2 - \omega^2\right)^2 + 4\xi_g^2\omega_g^2\omega^2} \tag{3.16}$$

where S_0 denotes the constant white-noise PSD of the bedrock excitation, ω_g and ξ_g are the fundamental circular frequency and damping ratio of surface soil deposit, respectively, which can be regarded as the parameters of a SDOF linear filter for the bedrock excitation. The above three parameters can be calibrated according to different soil conditions and earthquake magnitudes. Table 3.1 lists the suggested parameters of the Kanai-Tajimi model for different site types and seismic precautionary intensities defined by the seismic design code of China GB50011-2010 (Shen et al. 2021). In GB50011-2010 (CMC 2010), the site conditions are categorized into 4 types by the mean shear wave velocity of foundation soil or rock, namely, types I, II, III and IV. These site types are also associated with the ground soil types, for example, site type I is corresponding to rocks and close-grained gravels. The seismic precautionary intensities VII, VIII and IX are also set by code GB50011-2010 to be corresponded to an effective peak ground acceleration of 0.1-0.15g, 0.2-0.3g and 0.4g, respectively.

Table 3.1: Parameters of Kanai-Tajimi earthquake model.

Site type / Parameter / Intensity	I			II			III		
	ω_g	$\xi_g(\%)$	S_0	ω_g	$\xi_g(\%)$	S_0	ω_g	$\xi_g(\%)$	S_0
VII	33.9	0.38	5.6	23.3	0.43	9.6	17.8	0.46	13.8
VIII	33.9	0.38	22.0	23.3	0.42	36.8	17.9	0.46	52.3
IX	33.9	0.38	85.9	23.3	0.42	141.9	17.9	0.45	200.5

The unit of ω_g is rad/s, the unit of S_0 is $(\mathrm{cm/s^2})^2/\mathrm{Hz}$.

Spectrum representation approach developed by Shinozuka and Deodatis (1991) is used in this research to generate artificial accelerograms from a Kanai-Tajimi earthquake model. For a Kanai-Tajimi model with a PSD function of $S_{\ddot{x}_{g0}}(\omega)$, an artificial stationary stochastic representation of the PSD function, $\ddot{x}_{g0}(t)$, can be generated by the following series as $N \to \infty$:

$$\ddot{x}_{g0}(t) = \sqrt{2} \sum_{j=0}^{N-1} Q_j \cos\left(\omega_j t + \Phi_j\right) \tag{3.17}$$

where

$$Q_j = \sqrt{(2S_{\ddot{x}_{g0}}(\omega_j)\Delta\omega)}, \quad j = 0, 1, 2, \ldots, N-1, \quad Q_0 = 0 \tag{3.18}$$

$$\omega_j = j\Delta\omega, \quad j = 0, 1, 2, \ldots, N-1 \tag{3.19}$$

$$\Delta\omega = \omega_u / N \tag{3.20}$$

Φ_j is a random phase angle for $j = 0, 1, 2, \ldots, N-1$, and ω_u is an upper cut-off frequency that $S_{\ddot{x}_{g0}}(\omega)$ may be assumed to be zero when $\omega > \omega_u$. Since ω_u is a fixed value, according to Eq. (3.20), as $N \to \infty$, $\Delta\omega \to 0$. The following criterion can be applied to estimate ω_u:

$$\int_0^{\omega_u} S_{\ddot{x}_{g0}}(\omega) d\omega = (1 - \epsilon) \int_0^{\infty} S_{\ddot{x}_{g0}}(\omega) d\omega \tag{3.21}$$

where $\epsilon << 1$. For an estimated ω_u, N can be calculated using Eq. (3.20) with a fixed $\Delta\omega$.

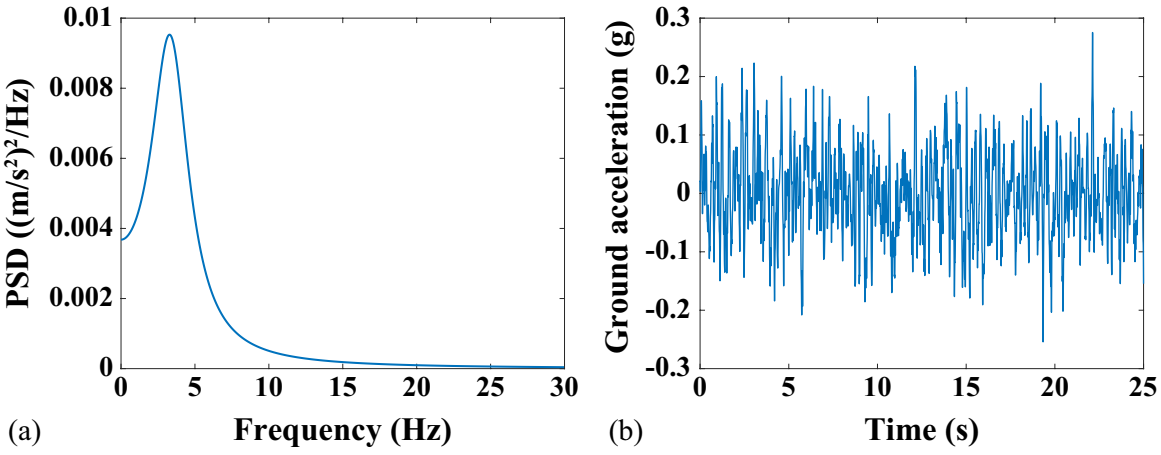

Figure 3.6: (a) PSD function and (b) ground acceleration-history of the Kanai-Tajimi earthquake model (seismic intensity VIII, site type II).

To demonstrate the spectrum representation approach, an artificial accelerogram of a ground motion with seismic intensity VIII and site type II (in which the foundation soil is composed mostly of medium-hard-soil or medium-soft-soil) is generated. The parameters of the corresponding Kanai-Tajimi model, ω_g, ξ_g and S_0, according to Table 3.1, are 23.3 rad/s, 42% and 36.8 $(\text{cm/s}^2)^2/\text{Hz}$, respectively. Figure 3.6(a) shows the PSD of the Kanai-Tajimi model considered, and an artificial accelerogram generated from the PSD function using the spectrum representation approach is shown in Figure 3.6(b). It is worth noting that, as the Kanai-Tajimi model assumes the ground acceleration as a stationary random process and utilizes a white-noise to represent the excitation in bedrock, the excitation amplitude of the accelerogram generated from the Kanai-Tajimi model will not gradually reduce to zero, as shown in Figure 3.6(b), which is different from a realistic earthquake record.

Chapter 4 Dynamic response of a SDOF structure with a nonlinear damper-brace system

In building applications, viscous dampers are often installed between adjacent stories to dissipate seismic energy and increase the resilience of the structure. Since the interstory-placed dampers are connected in series with their supporting braces, it is essential to incorporate the braces into the analytic model of the dampers. In this chapter, a numerical time-history method will be developed to compute the seismic response of a SDOF structure with a nonlinear damper-brace system in the time-domain; the correctness and accuracy of the proposed method will be verified using a numerical comparative study, and the feasibility of the method in evaluating dynamic performance of a building will be further assessed with a comparative case study.

4.1 Mathematical modelling and governing equations

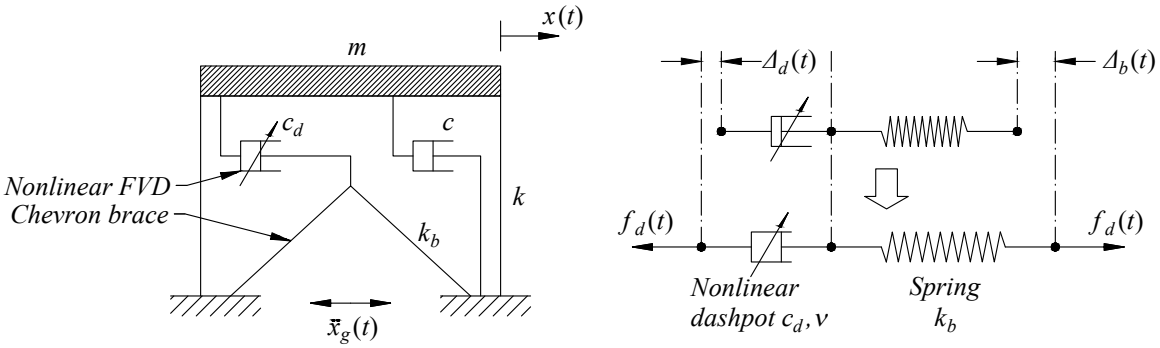

(a) SDOF structure (b) Maxwell model under loading

Figure 4.1: (a) Analytic model of a single-story structure with a nonlinear viscous damper (b) Maxwell model under an external load $f_d(t)$.

A single-story structure equipped with a nonlinear damper on top of a Chevron brace, as shown in Figure 4.1(a), is investigated in this section. The equation of motion of the structure is described in Eq. (3.1). Since the damper and the Chevron brace are connected in series, the damper force will always be equal to the restoring force in the brace. It will be assumed that the damper force obeys the nonlinear power law of Eq. (1.1), while the restoring force in the brace obeys the Hooke's law:

$$f_d(t) = k_b \Delta_b(t) = c_d |\dot{\Delta}_d(t)|^{\nu} sgn(\dot{\Delta}_d(t)) \tag{4.1}$$

where k_b and $\Delta_b(t)$ are the stiffness and the deformation of supporting brace in the

horizontal direction, respectively, c_d and $\dot{\Delta}_d(t)$ are the damping coefficient and the deformation rate of the damper, respectively, ν is the exponent of the damper velocity $\dot{\Delta}_d(t)$, and the signum function $sgn(\cdot)$ is defined as:

$$sgn(\mathrm{x}) = \begin{cases} 1 & \text{for} \quad \mathrm{x} > 0 \\ 0 & \text{for} \quad \mathrm{x} = 0 \\ -1 & \text{for} \quad \mathrm{x} < 0 \end{cases} \tag{4.2}$$

For the Maxwell model shown in Figure 4.1(b), the following kinematic conditions must be imposed for the damper-brace system:

$$\Delta(t) = \Delta_d(t) + \Delta_b(t) \tag{4.3}$$

and

$$\dot{\Delta}(t) = \dot{\Delta}_d(t) + \dot{\Delta}_b(t) \tag{4.4}$$

where $\Delta(t)$ is the total deformation of the damper-brace system.

4.2 Numerical time-history approach for a SDOF structure

The state-space procedure for obtaining the numerical solution of the equation of motion of the single-story building equipped with a single nonlinear damper-brace system is described in Section 3.1.1. When subjected to a ground acceleration input, the discrete-time state expression of the structural dynamic response can be described using Eq. (3.6), yet the force in the damper-brace system remains unknown. Therefore, once the damper force f_d is calculated, the numerical time-stepping method is completed, and the structural response can be computed from Eq. (3.6). To obtain the damper force, Eq. (4.1) is first rewritten as:

$$|\dot{\Delta}_d(t)| sgn(\dot{\Delta}_d(t)) = (\frac{k_b}{c_d})^{\frac{1}{\nu}} |\Delta_b(t)|^{\frac{1}{\nu}} sgn(\Delta_b(t)) \tag{4.5}$$

which can be further expressed as:

$$\dot{\Delta}_d(t) = (\frac{k_b}{c_d})^{\frac{1}{\nu}} |\Delta_b(t)|^{(\frac{1}{\nu}-1)} \Delta_b(t) \tag{4.6}$$

For a single-story structure with a damper supported by a Chevron-type brace as shown in Figure 4.1(a), the story velocity of the structure $\dot{x}(t)$ is equal to the total

deformation rate of the damper-brace system $\dot{\Delta}(t)$, thus Eq. (4.4) becomes:

$$\dot{x}(t) = \dot{\Delta}_d(t) + \dot{\Delta}_b(t) \tag{4.7}$$

The substitution of Eq. (4.6) into Eq. (4.7) yields:

$$\dot{\Delta}_b(t) = A(t)\Delta_b(t) + \dot{x}(t) \tag{4.8}$$

where $A(t)$ is a dependent variable that changes with the horizontal deformation of Chevron brace $\Delta_b(t)$:

$$A(t) = -(\frac{k_b}{c_d})^{\frac{1}{\nu}}|\Delta_b(t)|^{(\frac{1}{\nu}-1)} \tag{4.9}$$

Eq. (4.8) is a first-order differential equation that describes the dynamic response of the damper-brace system when excited by the structural velocity $\dot{x}(t)$. It should be noted that the results of Eqs. (4.6) and (4.9) become infinity at a zero-brace deformation when ν is larger than unity, thus Eqs. (4.6) and (4.8) are valid only for velocity exponents less than or equal to one. Eq. (4.8) can be solved numerically in discrete-time state space by discretization of the independent variable, time t. The dependent variables, namely, the structural velocity $\dot{x}(t)$ and variable $A(t)$ will change with the time step. It is assumed that $A(t)$ is a piece-wise constant and $\dot{x}(t)$ changes linearly within each computational time interval:

$$\begin{cases} A(\tau) = A(\mathrm{k}\Delta t) \\ \dot{x}(\tau) = \frac{(\mathrm{k}+1)\Delta t-\tau}{\Delta t}\dot{x}(\mathrm{k}\Delta t) + \frac{\tau-\mathrm{k}\Delta t}{\Delta t}\dot{x}((\mathrm{k}+1)\Delta t) \end{cases} \quad \text{for} \quad \mathrm{k}\Delta t < \tau < (\mathrm{k}+1)\Delta t \tag{4.10}$$

Apply the Laplace transform on both sides of Eq. (4.8) gives:

$$\Delta_b(s) = G(s)\Delta_b(t_0) + G(s)\dot{x}(s) \tag{4.11}$$

where $G(s) = (s - A(s))^{-1}$.

Take the inverse Laplace transform of Eq. (4.11) while noting the assumptions made in Eq. (4.10), the brace deformation Δ_b can be expressed as the following discrete-time state equation:

$$\Delta_b[\mathrm{k}+1] = A_d[\mathrm{k}]\Delta_b[\mathrm{k}] + E_0[\mathrm{k}]\dot{x}[\mathrm{k}] + E_1[\mathrm{k}]\dot{x}[\mathrm{k}+1] \tag{4.12}$$

where

$A[\mathrm{k}] = -(\frac{k_b}{c_d})^{\frac{1}{\nu}}|\Delta_b[\mathrm{k}]|^{(\frac{1}{\nu}-1)}$;

$A_d[\mathrm{k}] = e^{A[\mathrm{k}]\Delta t}$;
$E_0[\mathrm{k}] = A[\mathrm{k}]^{-1}A_d[\mathrm{k}] + \frac{1}{\Delta t}A[\mathrm{k}]^{-2}(1 - A_d[\mathrm{k}])$;
$E_1[\mathrm{k}] = -A[\mathrm{k}]^{-1} + \frac{1}{\Delta t}A[\mathrm{k}]^{-2}(A_d[\mathrm{k}] - 1)$.
The force provided by the nonlinear damper-brace system at sampling point $[\mathrm{k}+1]$ can thus be calculated by substituting brace deformation $\Delta_b[\mathrm{k}+1]$ from Eq. (4.12) back into Eq. (4.1) to give:

$$f_d[\mathrm{k}+1] = k_b\Delta_b[\mathrm{k}+1] = k_b\left[A_d[\mathrm{k}]\Delta_b[\mathrm{k}] + E_0[\mathrm{k}]\dot{x}[\mathrm{k}] + E_1[\mathrm{k}]\dot{x}[\mathrm{k}+1]\right] \tag{4.13}$$

The substitution of Eq. (4.13) into Eq. (3.6) gives the complete discrete-time state expression of the structural response under the prescribed earthquake. It should be noted that, before an earthquake, the building is assumed to be initially at rest with a horizontal deformation equals zero, i.e., $\mathbf{z_0}[1] = [0 \quad 0]^{\mathbf{T}}$, hence imposing no deformation on the damper-brace system. In other words, the damper force at the first sampling instant, $f_d[1]$, must be set to zero.

4.3 Evaluations of the proposed numerical approach

In this section, the correctness and accuracy of the numerical time-stepping method developed in Section 4.2 will first be examined by the fourth-order Runge-Kutta method, and the feasibility of using the method to conduct structural performance evaluations will then be assessed through a comparative study with a research from Chen and Chai (2011).

4.3.1 Comparative numerical verification

In Eq. (4.5), the term at right side of the equation, $|\dot{\Delta}_d(t)|sgn(\dot{\Delta}_d(t))$, is equal to $\dot{\Delta}_d(t)$. Thus the substitution of Eq. (4.5) into Eq. (4.7) yields:

$$\dot{\Delta}_b(t) = \dot{x}(t) - (\frac{k_b}{c_d})^{\frac{1}{\nu}}|\Delta_b(t)|^{\frac{1}{\nu}}sgn(\Delta_b(t)) \tag{4.14}$$

Since Eq. (4.14) is a first-order ODE that describes the dynamic response of the brace in a nonlinear damper-brace system, Runge-Kutta methods can also be used to solve it numerically and compute the nonlinear damper force with Eq. (4.1). Here, RK4 is adopted to calculate the damper force as well as the structural response under a given ground acceleration, which can be used to evaluate the accuracy of the numerical time-stepping method proposed in Section 4.2. Using RK4, the discrete-time state function of brace deformation for two consecutive sampling steps [k] and

[k + 1] can be expressed as:

$$\Delta_b[\mathrm{k}+1] = \Delta_b[\mathrm{k}] + \frac{1}{6}(K_{b1} + 2K_{b2} + 2K_{b3} + K_{b4})\Delta t \tag{4.15}$$

where

$$\begin{cases} K_{b1} = \dot{x}[\mathrm{k}] - (\dfrac{k_b}{c_d})^{\frac{1}{\nu}} |\Delta_b[\mathrm{k}]|^{\frac{1}{\nu}} sgn(\Delta_b[\mathrm{k}]) \\ K_{b2} = \dfrac{1}{2}(\dot{x}[\mathrm{k}] + \dot{x}[\mathrm{k}+1]) - (\dfrac{k_b}{c_d})^{\frac{1}{\nu}} |\Delta_b[\mathrm{k}] + \dfrac{\Delta t}{2} K_{b1}|^{\frac{1}{\nu}} sgn(\Delta_b[\mathrm{k}] + \dfrac{\Delta t}{2} K_{b1}) \\ K_{b3} = \dfrac{1}{2}(\dot{x}[\mathrm{k}] + \dot{x}[\mathrm{k}+1]) - (\dfrac{k_b}{c_d})^{\frac{1}{\nu}} |\Delta_b[\mathrm{k}] + \dfrac{\Delta t}{2} K_{b2}|^{\frac{1}{\nu}} sgn(\Delta_b[\mathrm{k}] + \dfrac{\Delta t}{2} K_{b2}) \\ K_{b4} = \dot{x}[\mathrm{k}+1] - (\dfrac{k_b}{c_d})^{\frac{1}{\nu}} |\Delta_b[\mathrm{k}] + \Delta t K_{b3}|^{\frac{1}{\nu}} sgn(\Delta_b[\mathrm{k}] + \Delta t K_{b3}) \end{cases} \tag{4.16}$$

Noting that Eq. (4.16) also assumes the structural velocity $\dot{x}(t)$ changes linearly within each computational time interval. The force in the damper-brace system at time step [k + 1] can be computed by substituting the value of $\Delta_b[\mathrm{k}+1]$ calculated by Eq. (4.15) into Eq. (4.1).

To calculate the structural response, the equation of the motion of the SDOF structure, Eq. (3.1), is first rewritten as:

$$\begin{cases} \dot{x}(t) = y(t) \\ \dot{y}(t) = -m^{-1} c\, y(t) - m^{-1} k\, x(t) - m^{-1} f_d(t) - \ddot{x}_g(t) \end{cases} \tag{4.17}$$

The discrete expression of the structural response can thus be expressed as:

$$\begin{cases} x[\mathrm{k}+1] = x[\mathrm{k}] + \dfrac{1}{6}(K_{11} + 2K_{12} + 2K_{13} + K_{14})\Delta t \\ y[\mathrm{k}+1] = y[\mathrm{k}] + \dfrac{1}{6}(K_{21} + 2K_{22} + 2K_{23} + K_{24})\Delta t \end{cases} \tag{4.18}$$

(see next page)

where

$$
\begin{cases}
K_{11} = y[\mathrm{k}] \\
K_{21} = -m^{-1}c\,y[\mathrm{k}] - m^{-1}k\,x[\mathrm{k}] - m^{-1}f_d[\mathrm{k}] - \ddot{x}_g[\mathrm{k}] \\
K_{12} = y[\mathrm{k}] + \dfrac{\Delta t}{2}K_{21} \\
K_{22} = -m^{-1}c\left(y[\mathrm{k}] + \dfrac{\Delta t}{2}K_{21}\right) - m^{-1}k\left(x[\mathrm{k}] + \dfrac{\Delta t}{2}K_{11}\right) - m^{-1}f_d[\mathrm{k}] \\
\qquad\quad - \dfrac{1}{2}\left(\ddot{x}_g[\mathrm{k}] + \ddot{x}_g[\mathrm{k}+1]\right) \\
K_{13} = y[\mathrm{k}] + \dfrac{\Delta t}{2}K_{22} \\
K_{23} = -m^{-1}c\left(y[\mathrm{k}] + \dfrac{\Delta t}{2}K_{22}\right) - m^{-1}k\left(x[\mathrm{k}] + \dfrac{\Delta t}{2}K_{12}\right) - m^{-1}f_d[\mathrm{k}] \\
\qquad\quad - \dfrac{1}{2}\left(\ddot{x}_g[\mathrm{k}] + \ddot{x}_g[\mathrm{k}+1]\right) \\
K_{14} = y[\mathrm{k}] + \Delta t K_{23} \\
K_{24} = -m^{-1}c\left(y[\mathrm{k}] + \Delta t K_{23}\right) - m^{-1}k\left(x[\mathrm{k}] + \Delta t K_{13}\right) - m^{-1}f_d[\mathrm{k}] - \ddot{x}_g[\mathrm{k}+1]
\end{cases}
\tag{4.19}
$$

Noting that the assumptions made in Eq. (3.5) are also adopted by Eq. (4.19), i.e., the damper force is a constant between two adjacent sampling instants, while the ground acceleration changes linearly.

To conduct accuracy assessment for the numerical method, a SDOF structure with a natural period of 1 second is considered. This period is in the period range of 0.5 and 1.5 seconds, which is the range for structures with medium fundamental periods defined by the performance-based seismic design rule of China (CECS 160: 2004) (IEM 2004). The stiffness of the structure is assumed to be 100 kN/m, which is the lateral stiffness used in some literature (De Domenico and Ricciardi 2019) for evaluating SDOF structures. The structural mass can thus be calculated from the natural period and stiffness as 2533 kg, and a 3% damping ratio is assigned to the structure. The seismic inputs are set as a ground acceleration record from the 1940 Imperial Valley earthquake recorded at station El Centro, and the artificial accelerogram generated from the Kanai-Tajimi earthquake model shown in Figure 3.6. Two different nonlinear damper-brace systems are respectively attached to the structure, and the structural responses are computed respectively for each seismic input. The design parameters of the two damper-brace systems are set as: damping coefficient $c_{d,1}$ and velocity exponent ν_1 of damper 1 are 2 kN·(s/m)$^{0.5}$ and 0.5, respectively, damping coefficient $c_{d,2}$ and velocity exponent ν_2 of damper 2 are 10 kN·s/m and 1.0, respectively, and the stiffness of braces for the two dampers are identically set to 100 kN/m. It is worth noting that although the examined parameter combinations

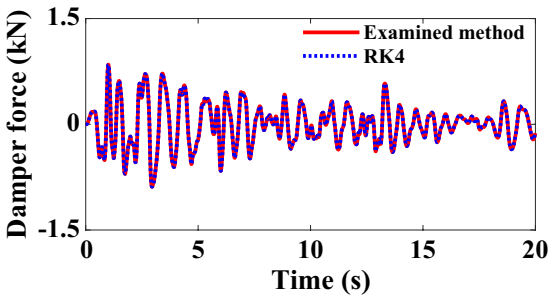

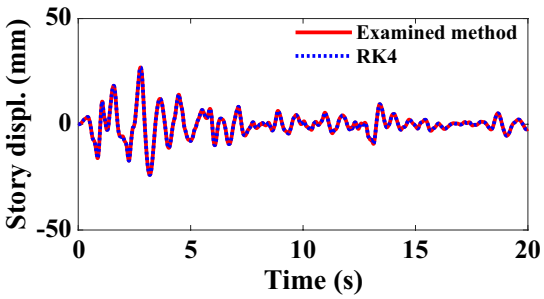

$\text{Mean}_{\text{E.m.}}$: 7.96×10^{-4} kN $\quad \text{StDev}_{\text{E.m.}}$: 0.29058 kN $\quad\quad$ $\text{Mean}_{\text{E.m.}}$: -0.05359 mm $\quad \text{StDev}_{\text{E.m.}}$: 5.9863 mm

Mean_{RK4}: 7.77×10^{-4} kN $\quad \text{StDev}_{\text{RK4}}$: 0.29050 kN $\quad\quad$ Mean_{RK4}: -0.05342 mm $\quad \text{StDev}_{\text{RK4}}$: 5.9919 mm

(a) Numerical response results for damper 1 ($c_d = 2$ kN·(s/m)$^{0.5}$, $\nu = 0.5$).

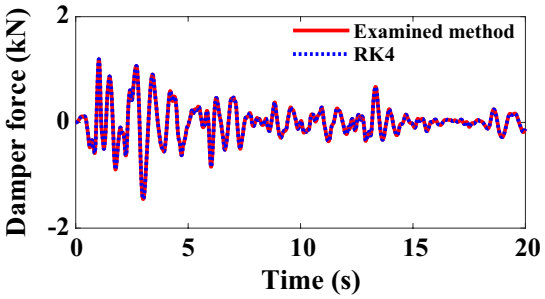

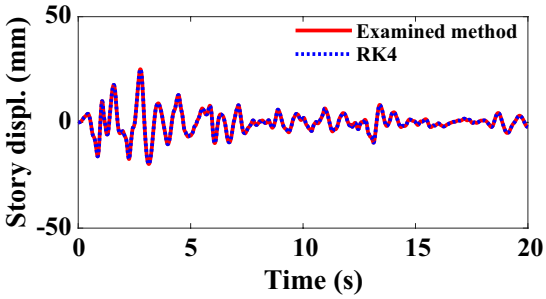

$\text{Mean}_{\text{E.m.}}$: -5.08×10^{-4} kN $\quad \text{StDev}_{\text{E.m.}}$: 0.32580 kN $\quad\quad$ $\text{Mean}_{\text{E.m.}}$: -0.02641 mm $\quad \text{StDev}_{\text{E.m.}}$: 5.5143 mm

Mean_{RK4}: -5.08×10^{-4} kN $\quad \text{StDev}_{\text{RK4}}$: 0.32580 kN $\quad\quad$ Mean_{RK4}: -0.02640 mm $\quad \text{StDev}_{\text{RK4}}$: 5.5143 mm

(b) Numerical response results for damper 2 ($c_d = 10$ kN·s/m, $\nu = 1.0$).

Figure 4.2: Structural responses from different methods under the 1940 Imperial Valley earthquake.

($c_{d,1}$ and ν_1, $c_{d,2}$ and ν_2) do not need to be the optimal ones, they are selected to be not very far from the optimal damper parameters for the SDOF structure to achieve an optimal performance in story drift under white-noise excitation; those optimal damper parameters can be found in Figure 5.2.

Figures 4.2 and 4.3 show the dynamic response results of the structure when subjected to the 1940 Imperial Valley earthquake and the Kanai-Tajimi excitation, respectively. In each figure, the response results, namely, the damper force and the story displacement, are computed respectively using the examined numerical time-stepping method and RK4. Mean value and standard deviation for each of the response histories are also calculated and listed in the figures. It can be seen from Figures 4.2 and 4.3 that, the curves which represent the response results from the examined method and the curves representing the RK4 results are almost precisely the same, which suggests a high accuracy of the numerical method developed in this chapter. Moreover, if the results from RK4 are assumed to be accurate, among all the mean value and standard deviation results, the maximum error in mean value

of the results from the examined method is 2.4%, calculated from the damper force time-history in Figure 4.2(a); the maximum error in standard deviation of the results from the examined method is 0.38%, also calculated from the damper force results in Figure 4.2(a), and all the other errors are below 0.5%. The error evaluation also suggests acceptable accuracy of the proposed numerical method.

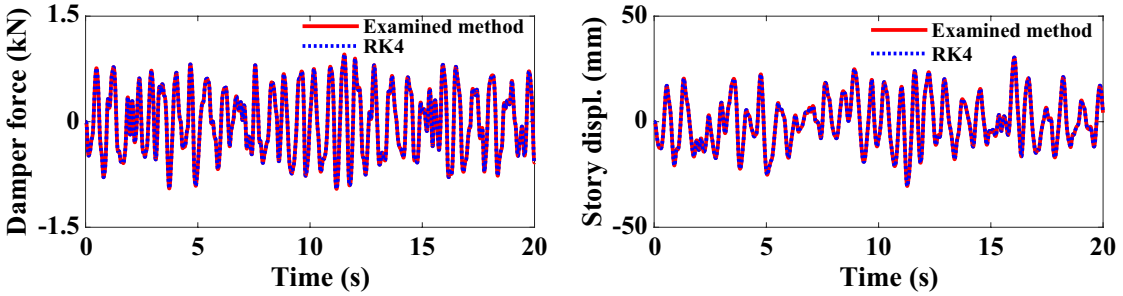

$\text{Mean}_{\text{E.m.}}$: 0.00284 kN $\text{StDev}_{\text{E.m.}}$: 0.46147 kN $\text{Mean}_{\text{E.m.}}$: -0.11932 mm $\text{StDev}_{\text{E.m.}}$: 11.5314 mm

Mean_{RK4}: 0.00286 kN $\text{StDev}_{\text{RK4}}$: 0.46147 kN Mean_{RK4}: -0.11928 mm $\text{StDev}_{\text{RK4}}$: 11.5450 mm

(a) Numerical response results for damper 1 ($c_d = 2$ kN·(s/m)$^{0.5}$, $\nu = 0.5$).

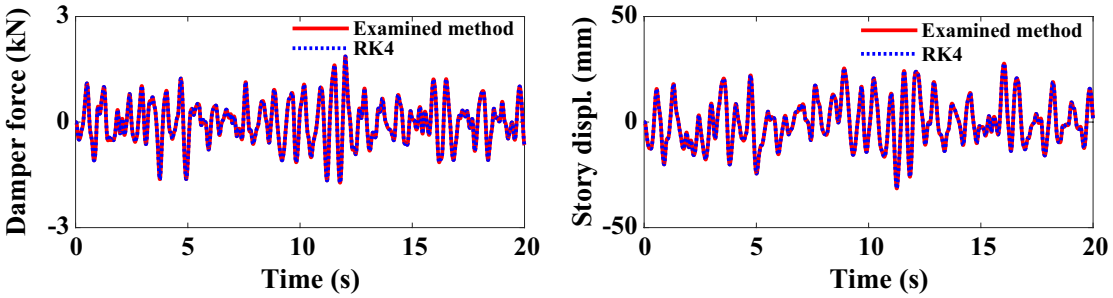

$\text{Mean}_{\text{E.m.}}$: 0.00329 kN $\text{StDev}_{\text{E.m.}}$: 0.60325 kN $\text{Mean}_{\text{E.m.}}$: -0.12398 mm $\text{StDev}_{\text{E.m.}}$: 10.7515 mm

Mean_{RK4}: 0.00329 kN $\text{StDev}_{\text{RK4}}$: 0.60325 kN Mean_{RK4}: -0.12397 mm $\text{StDev}_{\text{RK4}}$: 10.7515 mm

(b) Numerical response results for damper 2 ($c_d = 10$ kN·s/m, $\nu = 1.0$).

Figure 4.3: Structural responses from different methods under the Kanai-Tajimi excitation.

The computation costs of the examined numerical method and the fourth-order Runge-Kutta method are also compared using MATLAB. Table 4.1 shows the computing times consumed by the two methods, and the total amounts of computer memory allocated to the methods, during ten successive runs of a program that computes seismic response of the SDOF structure under the Kanai-Tajimi excitation, when the building is equipped with a nonlinear damper-brace system with the predefined damper parameters, $c_{d,1}$ and ν_1, and brace stiffness equals 100 kN/m. It can be observed from the table that the examined method consumes fewer computing times than the Runge-Kutta method, except in the first run, yet the total computer memories allocated to the examined method are generally larger, especially in the first run.

Table 4.1: Computation costs of the numerical method and RK4 for the SDOF structure with damper parameters $c_{d,1}$ and ν_1 under the Kanai-Tajimi excitation.

	Examined method		RK4	
Number of runs	Total time (s)	Allocated memory (Kb)	Total time (s)	Allocated memory (Kb)
1	0.106	11812	0.093	8800
2	0.064	1108	0.088	8524
3	0.063	1116	0.092	1660
4	0.062	0	0.095	2388
5	0.075	1156	0.094	1656
6	0.072	1272	0.092	596
7	0.072	68	0.091	64
8	0.077	1116	0.094	592
9	0.073	1156	0.097	0
10	0.074	1108	0.097	228

It is also found that the longer computation time for the examined method in the first run is mainly due to a children function `expm` called for defining the discrete system matrix that relates only to the properties of primary building and the sampling period, as shown in Eqs. (3.2) and (3.6), and the proposed approach spends less time on computing damper force than the Runge-Kutta method. As the instant memory being occupied by the program is well below the computer's capacity, the total time consumed is more reflective of the computation cost of a method, thus the proposed approach has an advantage in computing time. However, as mentioned in Section 4.2, the proposed method only valid for velocity exponents less than or equal to one, while RK4 works well for most of the commonly used velocity exponents, hence the applicability of the proposed method is lower than the Runge-Kutta method.

4.3.2 Comparative structural performance evaluation

In the research work conducted by Chen and Chai (2011), the seismic performance of a SDOF structure equipped with a linear viscous damper on top of a Chevron brace, as shown in Figure 4.4, were evaluated; an optimization procedure was also presented to find the optimal parameters for maximizing the structural performances in story displacement and acceleration. Since linear viscous dampers were adopted, frequency-domain analysis was performed to find the closed-form solutions for the optimal structural performances under a white-noise ground excitation. The feasibility of the numerical method proposed in this chapter can thus be examined by comparing the corresponding optimal performance results with those of the closed-form solutions. The mathematical procedures introduced by Chen and Chai (2011) to obtain the

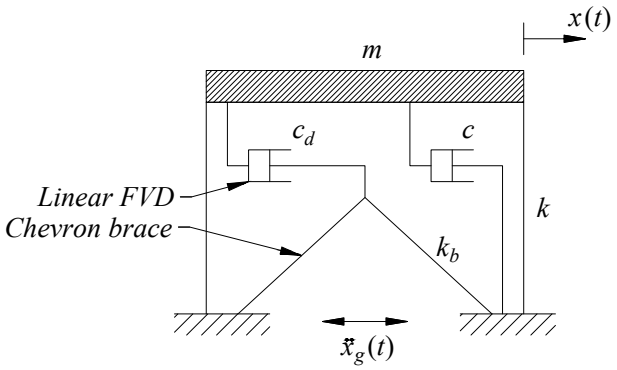

Figure 4.4: Analytic model of a single-story structure with a linear FVD.

optimal performances in story displacement and acceleration of a SDOF structural system are described below:

The damper force in the linear damper-brace system can be described using the following first-order differential equation:

$$f_d(t) + \frac{c_d}{k_b}\dot{f}_d(t) = c_d\dot{\Delta}(t) \tag{4.20}$$

Eq. (4.20) can be substituted into Eq. (3.1) to obtain the equation of motion of the structure. By taking the Fourier transform for each term in the equation of motion, the story displacement in the frequency-domain, $x(\omega)$, was described as a function of the Fourier transform of the ground acceleration, $\ddot{x}_g(\omega)$:

$$x(\omega) = H(\omega)\ddot{x}_g(\omega) \tag{4.21}$$

where $H(\omega)$ is the transfer function with the following expression:

$$H(\omega) = \frac{-mc_d^2\omega^2 - mk_b^2}{-c_d^2 m\omega^4 + jc_d^2 c\omega^3 + \left(c_d^2 k_\mathrm{b} + c_d^2 k - k_b^2 m\right)\omega^2 + j(c_d k_b^2 + ck_b^2)\omega + k_b^2 k} \tag{4.22}$$

where j denotes the imaginary constant. To evaluate the seismic performance in story displacement of the SDOF structure, the mean square value of the story displacement was defined as a displacement index:

$$J_s = \delta^2 = \int_{-\infty}^{\infty} |x(\omega)|^2 \, d\omega \tag{4.23}$$

A zero-mean white-noise with a constant power spectral density of S_0 was assumed to be the seismic input. By substituting Eq. (4.21) into Eq. (4.23), the story

displacement performance index J_s can be calculated as:

$$J_s = \pi S_0 \frac{4\xi\alpha_b\beta_d + \alpha_b^2 + 4\beta_d^2}{\omega_1^3\left(8\alpha_b\beta_d\xi^2 + 2\left(\alpha_b^2 + 4(\alpha_b+1)\beta_d^2\right)\xi + 2\alpha_b^2\beta_d\right)} \tag{4.24}$$

where $\alpha_b = k_b/k$ and $\beta_d = c_d/(2m\omega_1)$ are the dimensionless brace stiffness ratio and damping ratio for the damper-brace system; ω_1 and ξ denote the natural circular frequency and inherent damping ratio of the SDOF structure. To achieve an optimal structural performance in story displacement, Eq. (4.24) should be minimized with respect to both α_b and β_d. However, since the brace should be designed with a limited stiffness coefficient in practice, a minimized performance index $J_{s,opt}$ can be achieved by solving $\partial J_s/\partial\beta_d = 0$ for a set brace stiffness ratio α_b. The mathematical expressions of the minimum performance index $J_{s,opt}$ and the optimal damping ratio $\beta_{d,s,opt}$ are:

$$J_{s,opt} = \pi S_0 \frac{2\left(1-\xi\right)}{{\omega_1}^3\left(\alpha_b + 4\left(\xi - \xi^2\right)\right)} \tag{4.25}$$

and

$$\beta_{d,s,opt} = \frac{\alpha_b}{2\left(1-2\xi\right)} \tag{4.26}$$

To calculate the improved story displacement performance after the installation of the viscous damper with an optimal damping ratio $\beta_{d,s,opt}$, a target reduction ratio TR_s was adopted with the following expression:

$$TR_s = 1 - \frac{J_{s,opt}}{J_{s,org}} = \frac{\alpha_b}{\alpha_b + 4\left(\xi - \xi^2\right)} \tag{4.27}$$

where $J_{s,org}$ is the displacement performance index of the original structure, which can be obtained by setting β_d to zero in Eq. (4.24).

In addition to the structural performance in story displacement, the performance in story absolute acceleration was also considered by Chen and Chai (2011). The story absolute acceleration of the SDOF system $a(t)$ is given by:

$$a(t) = \ddot{x}(t) + \ddot{x}_g(t) \tag{4.28}$$

Taking the Fourier transform for Eq. (4.28) yields the following equation:

$$a(\omega) = \left(1 - \omega^2 H(\omega)\right)\ddot{x}_g(\omega) \tag{4.29}$$

To evaluate the structural acceleration performance, a story acceleration index J_a was defined as the mean square of the story acceleration in the frequency-domain:

$$J_a = \sigma_a^2 = \int_{-\infty}^{\infty} |a(\omega)|^2 \, d\omega \tag{4.30}$$

Similar to TR_s, the target reduction in story acceleration, TR_a, was calculated as:

$$TR_a = 1 - \frac{J_{a,opt}}{J_{a,org}} = \frac{\alpha_b \left(1 - 2\xi\right)^2}{\left(\alpha_b + 4\left(1 - \xi\right)\xi\right)\left(1 + 4\xi^2\right)} \tag{4.31}$$

where $J_{a,opt}$ and $J_{a,org}$ are the optimal story acceleration performance index and the index of the original structure without the damper-brace system, respectively. The corresponding optimal damping ratio for achieving the target reduction was expressed as:

$$\beta_{d,a,opt} = \frac{\alpha_b \left(1 - 2\xi\right)}{2(\alpha_b + 1)} \tag{4.32}$$

To assess the feasibility of the numerical time-history method in Section 4.2 in the evaluation of structural seismic performances, the target reductions and the optimal damping ratios are recalculated in the time-domain using the numerical method. A single-story building with the same mass and stiffness properties as the structure studied in Section 4.3.1 is adopted here. A linear damper-brace system is installed in the building, and two different damping ratios, i.e., 2% and 5%, are assigned to the structure, respectively. It can be observed from Eqs. (4.26), (4.27), (4.31) and (4.32) that the optimal results, i.e., TR_s, TR_a, $\beta_{d,s,opt}$ and $\beta_{d,a,opt}$, are independent of the PSD magnitude of the white-noise excitation S_0, thus S_0 could be any value for generating a white-noise accelerogram. However, it is found that a white-noise time-history with an infinite frequency bandwidth is hard to be produced; a white-noise

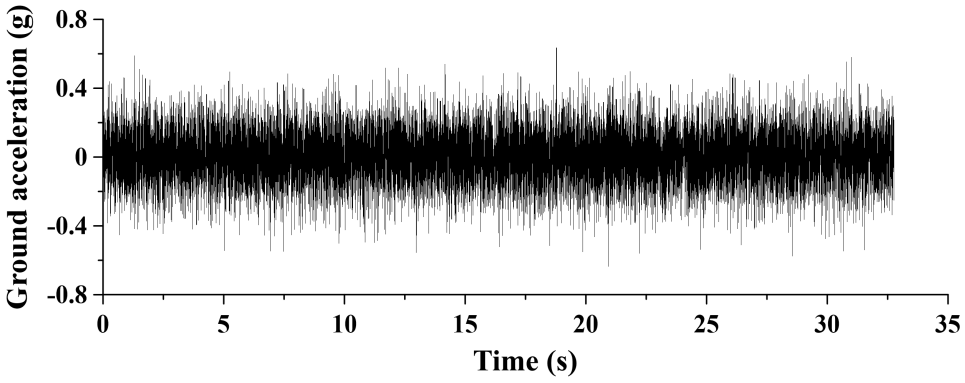

Figure 4.5: Time-history of a zero-mean white-noise ground acceleration.

time-history with a constant PSD at limited frequency bandwidth is thus adopted here as the ground acceleration input, as shown in Figure 4.5.

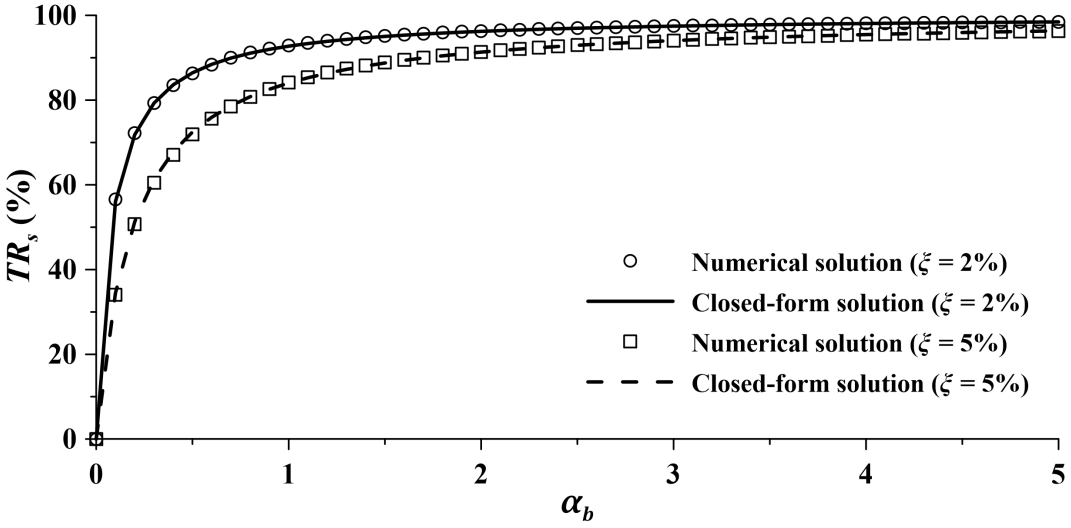

Figure 4.6: Target displacement reduction versus brace stiffness ratio for the SDOF structure under white-noise ($\nu = 1$).

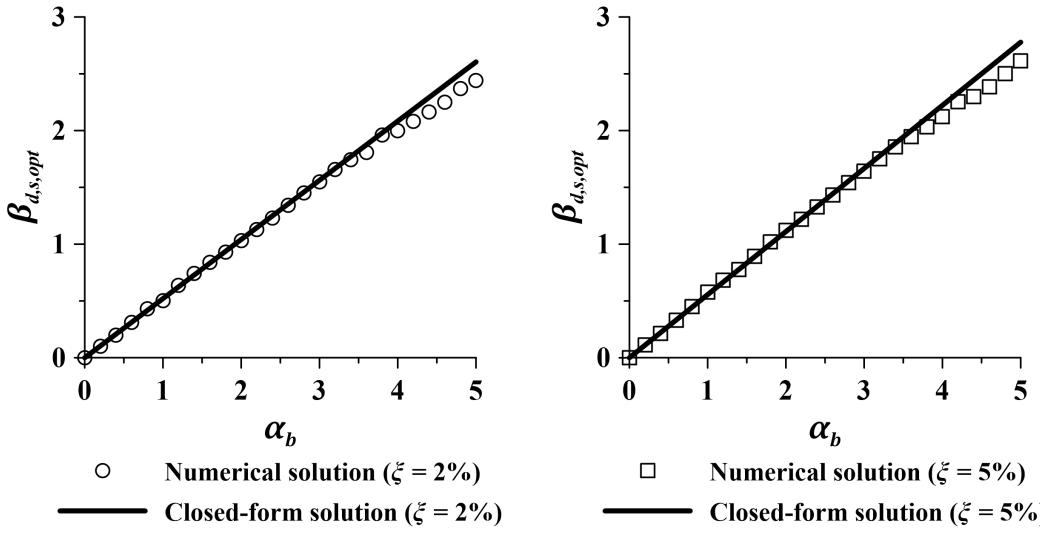

Figure 4.7: Optimal damping ratio for displacement performance versus brace stiffness ratio for the SDOF structure under white-noise ($\nu = 1$).

The time-histories of story displacement and acceleration can be computed using the numerical time-stepping method, and the performance indices can thus be calculated in the time-domain. For a given set of design parameters, namely for given α_b and β_d, the corresponding performance indices, J_s and J_a, can be calculated by taking the mean-square values of the time-histories of story displacement and story

absolute acceleration of the structure, receptively. By minimizing the performance indices for a given brace stiffness ratio under the white-noise excitation, the optimal performance indices, $J_{s,opt}$ and $J_{a,opt}$, and the corresponding optimal damping ratios, $\beta_{d,s,opt}$ and $\beta_{d,a,opt}$, can be obtained. The target reductions TR_s and TR_a can thus be calculated by Eqs. (4.27) and (4.31). Notably, as only linear viscous dampers are involved the evaluations, the velocity exponent was set to one during the numerical computations.

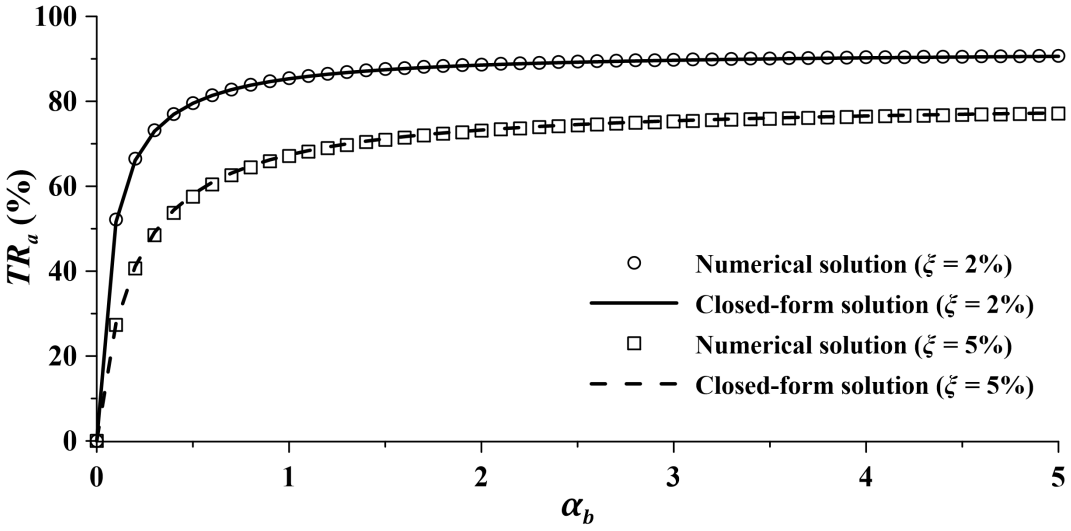

Figure 4.8: Target acceleration reduction versus brace stiffness ratio for the SDOF structure under white-noise ($\nu = 1$).

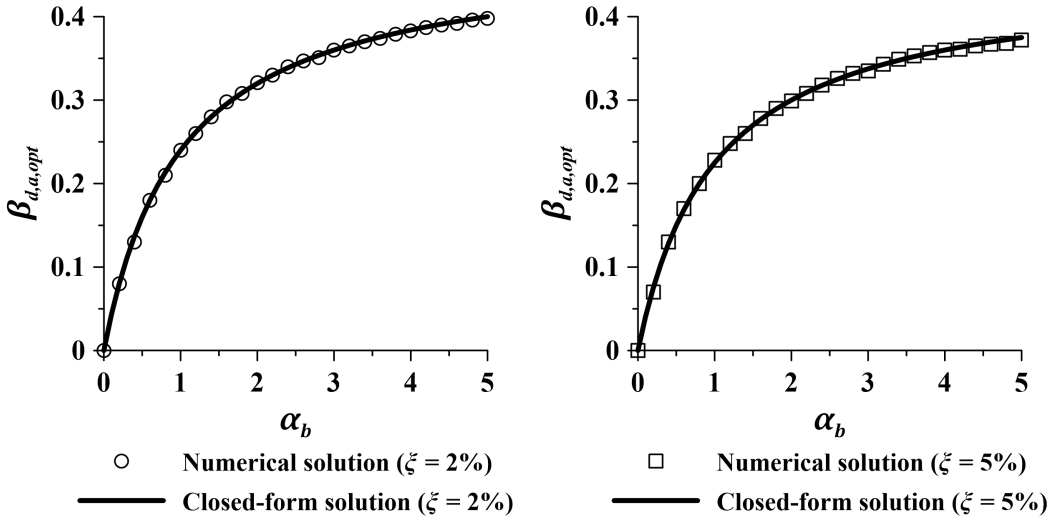

Figure 4.9: Optimal damping ratio for acceleration performance versus brace stiffness ratio for the SDOF structure under white-noise ($\nu = 1$).

The comparative plots of the target reductions in story displacement, TR_s, and the optimal damping ratios, $\beta_{d,s,opt}$, against the brace stiffness ratios for $0 \leq \alpha_b \leq 5$ are plotted in Figure 4.6 and 4.7, respectively, and Figure 4.8 and Figure 4.9 display the corresponding plots for TR_a and $\beta_{d,a,opt}$, respectively. It can be seen from Figure 4.6 and 4.8 that, the target reduction results from the numerical method are generally consistent with those from the closed-form solutions. However, in Figure 4.7, the optimal damping ratios computed from the numerical method deviate a little bit from the closed-form solutions in Eq. (4.26) when α_b is greater than 3.5. It is found that the differences between the numerical results and closed-form solutions mainly come from the different ground excitation inputs, as the numerical computations adopt a white-noise accelerogram generated from a PSD function with limited frequency bandwidth to be the ground acceleration, while the closed-form solutions are based on a white-noise with an infinite bandwidth. The differences may also come from the optimization process of the design parameters, as well as the error accumulated from the assumptions made in Eqs. (3.5) and (4.10) during the numerical computations. Despite the differences, it can be seen from these comparative plots that the closed-form solutions generally agree with the results from the proposed numerical approach, which indicates that the accuracy of the structural seismic response computed from the numerical approach is adequate to evaluate dynamic performance of the structure and compute optimal design parameters.

4.4 Conclusions

In this chapter, a numerical time-history approach was developed for dynamic analysis of building structures with nonlinear damper-brace systems. The proposed approach explicitly dealt with the nonlinearity of the viscous dampers based on state-space technique, which can compute the response time-histories of a SDOF structure with a damper installed on top of a Chevron brace subjected to a ground acceleration. The correctness and accuracy of the developed approach were verified through a numerical comparative study. The results obtained from the proposed approach were consistent with those calculated from the fourth-order Runge-Kutta method. The feasibility of the numerical method for conducting structural performance evaluations has also been evaluated using a comparative case study. The results from the proposed method showed a good agreement with the closed-form solutions.

Chapter 5 Effects of brace stiffness and damper nonlinearity on seismic performance of building structures

Supporting braces for viscous dampers are considered a crucial component for ensuring an efficient energy dissipation in a structure. Despite their importance, limited research has been conducted to investigate the effects of the brace stiffness and the velocity exponent of fluid viscous damper in building applications. In this chapter, based on the numerical time-history approach developed in Chapter 4, the influences of the design variables of a nonlinear damper-brace assembly on the seismic performance of building structures are investigated through parametric studies, using first a SDOF structure, followed by multi-story buildings. Optimizations of the design parameters for maximizing a target structural performance are performed based on genetic algorithm, and the robustness of the optimal design results are evaluated through incremental dynamic analysis.

5.1 Performance assessment of a SDOF structure with a nonlinear damper-brace system

The effectiveness of the damper-brace system under seismic excitation will now be assessed through an evaluation of various performance indices. As noted in Section 3.2.1, the improved performance of the structure may be quantified using a response reduction criterion by comparing the performance indices before and after the installation of the damper-brace systems. In the next two sections, different response reduction ratios will be defined, and the effects of brace stiffness and damper nonlinearity on the overall structural performance will be presented for a SDOF shear-type building.

5.1.1 Minimization of interstory drift

The performance of a multi-story building under earthquake conditions may be assessed using the interstory drifts. In this chapter, the average of the root-mean-square of the interstory drift time-history is taken as the first performance index:

$$PI_D = \frac{1}{n}\sum_{i=1}^{n} rms\left(\delta_i\right) \quad \text{for } n\text{-story structures} \tag{5.1}$$

where δ_i is the interstory drift time-history of the i-th story of a MDOF building. In addition to representing the interstory drift intensity of the structure, the PI_D index

also reflects the extent of structural wall damage during an earthquake (Silvestri and Trombetti 2007).

To evaluate the structural performance after the installation of the supplemental damper–brace systems, a response reduction ratio RR_D is adopted with the following expression:

$$RR_D(\%) = \left(1 - \frac{PI_D}{PI_{D,org}}\right) \times 100 \tag{5.2}$$

where $PI_{D,org}$ is the interstory drift performance index of the structure in the original state, i.e., without the damper–brace systems. Since RR_D represents the percentage reduction in structural interstory drift after installing the braces and dampers, a larger RR_D would indicate a more effective design of the damper-brace system.

For the purposes of design of the structure in Figure 4.1(a), two parameters can be defined for the damper-brace system: (i) a dimensionless brace stiffness ratio, α, relating the brace lateral stiffness to the structure story stiffness, i.e.,

$$\alpha \equiv \frac{k_b}{k} \tag{5.3}$$

and (ii) a damping ratio, β, relating the damping coefficient of the supplemental damper to the mass and vibrational frequency of the structure, i.e.,

$$\beta \equiv \frac{c_d}{2m\omega_1} \tag{5.4}$$

where $\omega_1 = \sqrt{k/m}$ is the natural circular frequency of the primary structure. It is worth noting that since the unit of c_d changes with the velocity exponent ν, the unit of β is $(\text{s/m})^{\nu-1}$.

A parametric study is now conducted to assess the effects of different design parameters on structural performance using the properties defined in Section 4.3 for a SDOF structure: story mass $m = 2533$ kg, story stiffness $k = 100$ kN/m, and inherent damping ratio $\xi = 2\%$. Note that the natural period of the primary structure has been set to 1 second. Different combinations of the design parameters (α, β, and ν) are then assigned to the brace-damper system to quantify the response reduction in the interstory drift of the structure. A white-noise acceleration time-history with a zero-mean is used as the input ground motion.

Figure 5.1 shows the three-dimensional mesh and contour plots of the response reduction in interstory drift RR_D versus brace stiffness ratio α and damping ratio of the supplemental damper β for a velocity exponent ν equals 0.6 and 0.8. The colour of the mesh reflects the magnitude of the response reduction, with greater values of

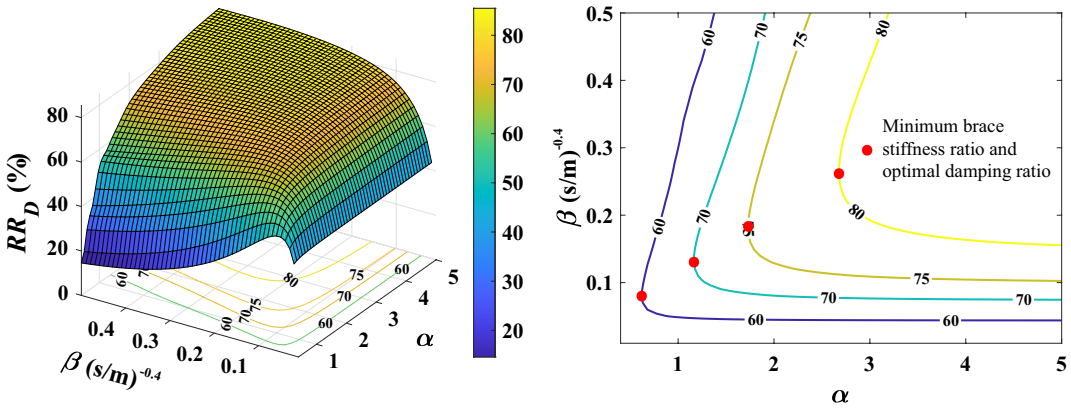

(a) Mesh and contour plots for v equals 0.6.

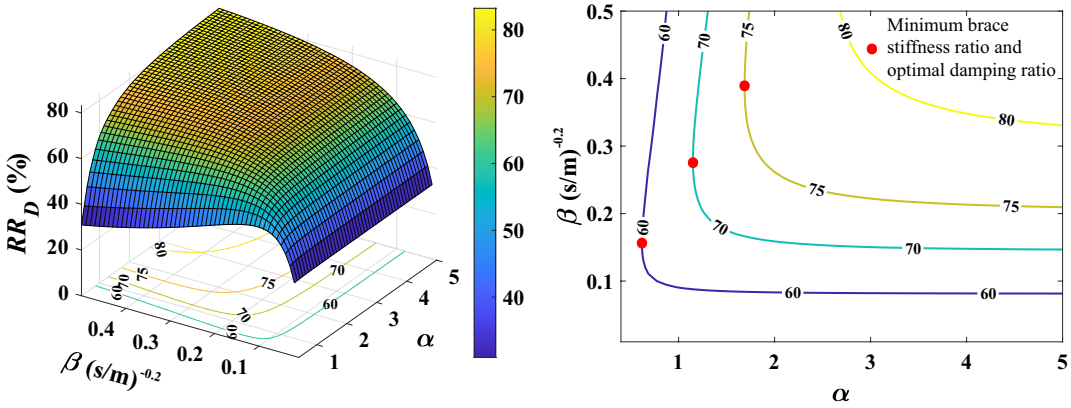

(b) Mesh and contour plots for v equals 0.8.

Figure 5.1: Three-dimensional mesh plot and contour plot of response reduction in interstory drift versus brace stiffness ratio and supplemental damping ratio for the SDOF structure under white-noise excitation.

RR_D implying smaller interstory drift response and hence a more effective and desirable design of the damper and the brace. It can be seen from Figure 5.1(a) that for a velocity exponent of ν equals 0.6, a larger brace stiffness and a larger damping coefficient of the supplemental damper result in better structural performance in terms of interstory drift reduction. However, there exists an infinite combination of the design parameters for a given targeted response reduction. Importantly, it can be seen from the contour plot in Figure 5.1(a) that, for a specified response reduction, there exists a minimum brace stiffness and a corresponding optimum damping coefficient of the viscous damper. Similar observations are made for the case of ν equals 0.8, as shown in Figure 5.1(b). These findings for structures with nonlinear damper-brace systems are consistent with that observed for linear damper-brace systems, as had been reported earlier by Chen and Chai (2011).

Given a target response reduction, the existence of a minimum brace stiffness, as

noted above, suggests that a worthwhile exercise would be to investigate the maximum level of response reduction that can be achieved by the damper-brace system if the brace stiffness is constrained. For the best performance, however, the damping coefficient of the viscous damper c_d also needs to be optimized. To that end, for a given brace stiffness, the damping coefficient is hereby optimized, with the response reduction in interstory drift serving as the objective function, which is to be maximized.

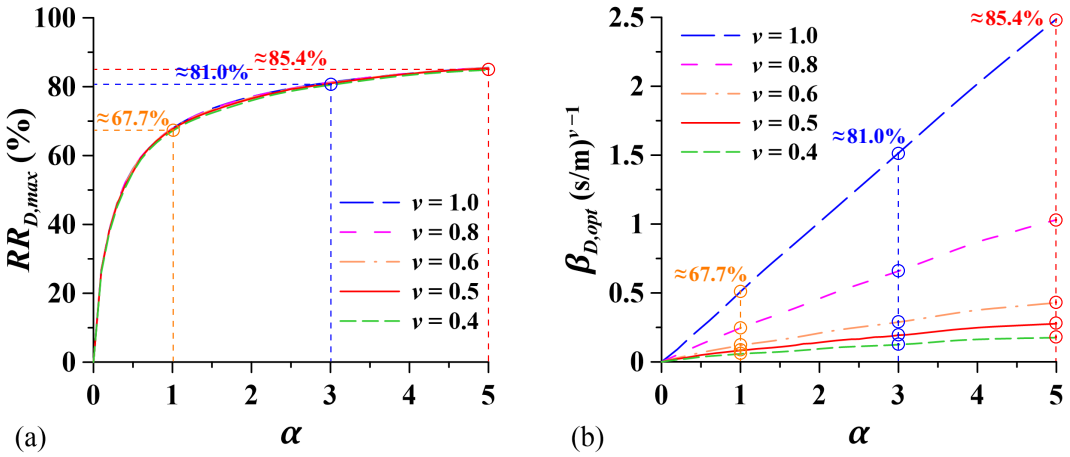

Figure 5.2: (a) Maximum response reduction in interstory drift $RR_{D,max}$ and (b) corresponding optimal damping ratio $\beta_{D,opt}$ against brace stiffness ratio α for the SDOF structure under white-noise excitation.

Figure 5.2 shows the maximum response reduction in interstory drift $RR_{D,max}$ and the corresponding optimal damping ratio $\beta_{D,opt}$ versus the brace stiffness ratio α for velocity exponent ν of 0.4, 0.5, 0.6, 0.8 and 1.0. The examined velocity exponents are selected to cover most of the typically used values for seismic applications, as stated by Taylor (2013) and Lin and Chopra (2002). It can be seen from Figure 5.2(a) that, the maximum response reduction increases rapidly with the brace stiffness in the low stiffness ratio range, say $\alpha < 1$. This sharp increase shows that the maximum response reduction in interstory drift is highly sensitive to the brace stiffness when the stiffness ratio is small, implying that a small increase in brace stiffness can provide a significant performance improvement. However, as the stiffness ratio becomes larger, say $\alpha > 1$, the response reduction still increases but at a reduced rate. It can also be seen from Figure 5.2(a) that the maximum response reduction changes slightly for different velocity exponents, indicating that if there is no constraint on the damping coefficient, and the damping coefficient to be optimized, the velocity exponent of the viscous dampers has almost no influence on the maximum response reduction in interstory drift. Figure 5.2(b) shows the variation of the optimal damping ratio with the brace stiffness ratio. It can be seen from the figure that, given a velocity

exponent for the damper, the optimal damping ratio increases linearly with increasing brace stiffness ratio. It can also be seen that, for a set of brace stiffness ratio, the optimal damping ratio decreases when the velocity exponent decreases from 1 to 0.4. Observations made from Figure 5.2 are instructive as they suggest that to achieve a certain response reduction in interstory drift, a nonlinear damper with velocity exponent less than unity has an advantage over its linear counterpart.

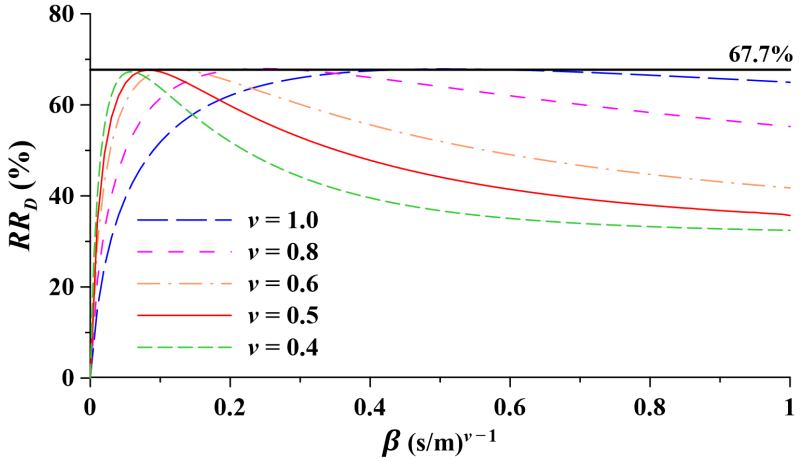

Figure 5.3: Variation of interstory drift response reduction RR_D with damping ratio β for different velocity exponents ν ($\alpha = 1$).

Figure 5.3 further illustrates the fact that nearly the same maximum response reduction can be achieved in the range of velocity exponent between 0.4 and 1. In generating the data for the figure, a brace stiffness equals to the story stiffness is first selected, followed by varying the damping coefficient for each velocity exponent. Figure 5.3 plots the response reduction for interstory drift RR_D against the damping ratio β for velocity exponent in the range of $0.4 \leq \nu \leq 1$. It can be seen from the figure that peak values of the response reduction are close, at about 67.7%, for the selected velocity exponent range, implying that if the damper has been optimally designed and there is no constraint on the damping coefficient, dampers with the velocity exponent in the range of $0.4 \leq \nu \leq 1$ are expected to provide the same improvement in structural interstory drift. Moreover, it can also be seen from Figure 5.3 that, for all the dampers that are optimally designed, a further increase in damping will reduce the effectiveness of the damper-brace system.

For a preset brace stiffness, although the unit of damping coefficient changes with the velocity exponent, it may be worthwhile to evaluate the variation of structural response reduction with the magnitude of damping ratio and velocity exponent. Figure 5.4 shows the three-dimensional mesh plot and contour plot of the variation for the SDOF structure under the white-noise ground acceleration. A "ridge" of the mesh

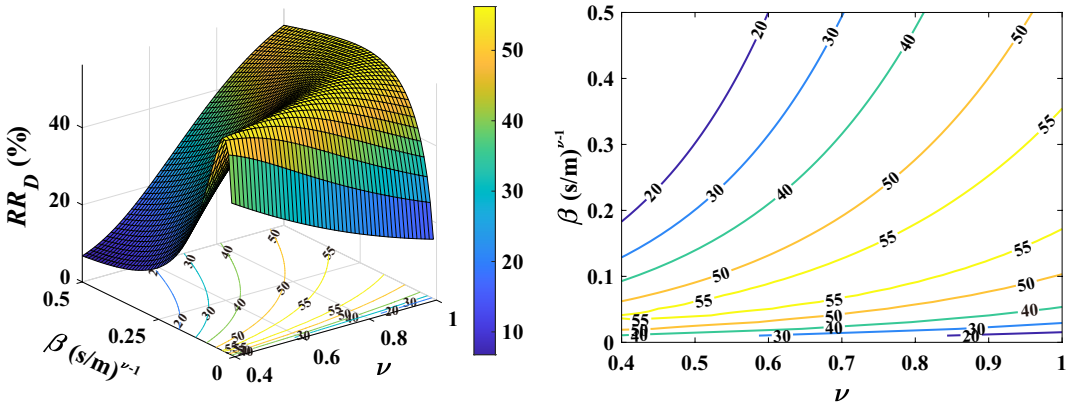

Figure 5.4: Mesh and contour plots of response reduction in interstory drift versus damping ratio and velocity exponent for the SDOF structure under white-noise excitation ($\alpha = 0.5$).

surface can be found in the first plot of Figure 5.4, which shows the achievable "peak" response reductions (i.e., $RR_{D,max}$) of the structure within the examined ranges of β and ν. The peak response reductions at the ridge of surface seem to have similar values, and the magnitude of damping ratio increases with the velocity exponent for obtaining a peak reduction. These trends are similarly noted in the contour plot in Figure 5.4, which further confirm the observation from Figures 5.2 and 5.3 that for a given brace stiffness, similar maximum response reductions can be achieved for different velocity exponents, once the damping coefficient is optimally determined. Therefore, if we optimize both the damping ratio and velocity exponent for a certain brace stiffness ratio, there will be an infinite combination of damper parameters that can obtain similar maximum response reductions.

Table 5.1: Maximum damper forces of the dampers with optimal damping ratios $\beta_{D,opt}$ in the SDOF structure under white-noise excitation.

Brace stiffness ratio α	Maximum damper force (N)				
	$\nu = 0.4$	$\nu = 0.5$	$\nu = 0.6$	$\nu = 0.8$	$\nu = 1.0$
0.2	242	258	273	299	320
0.5	448	468	485	516	540
1.0	656	703	746	822	886
2.0	979	1044	1094	1166	1213
5.0	1798	1983	2098	2242	2321

Although similar maximum response reductions can be achieved by the optimal viscous dampers for different velocity exponents, it is nonetheless important to evaluate the peak force in the dampers during the ground motion. Table 5.1 summarizes the maximum damper forces of the dampers with optimal damping ratios $\beta_{D,opt}$ un-

der the white-noise excitation. It can be seen from the table that as the velocity exponent increases from 0.4 to 1.0, the maximum damper forces generally increase for the examined brace stiffness ratios, which indicates that the use of a smaller velocity exponent can reduce the peak damper force while achieving a similar response reduction of the building. Since the manufacturing cost of the FVD depends heavily on the peak damper force, this observation also suggests that the use of nonlinear dampers with a ν less than one has an economic advantage.

5.1.2 Minimization of base shear force

In addition to interstory drift, an index involving the base shear force is also used as a potential candidate for response reduction. The performance index in base shear force, PI_V, is hereby defined as the root-mean-square of the base shear force time-history V_s:

$$PI_V = rms\left(V_s\right) \tag{5.5}$$

The PI_V index represents the total dynamic load acting on the structure; it also reflects the cost of foundation structures (Silvestri and Trombetti 2007). Based on the base shear force performance index, the reduction in structural shear force can be estimated using the following reduction ratio for the base shear force:

$$RR_V(\%) = \left(1 - \frac{PI_V}{PI_{V,org}}\right) \times 100 \tag{5.6}$$

where $PI_{V,org}$ is the performance index in base shear force of the original structure without the supplemental damper-brace systems.

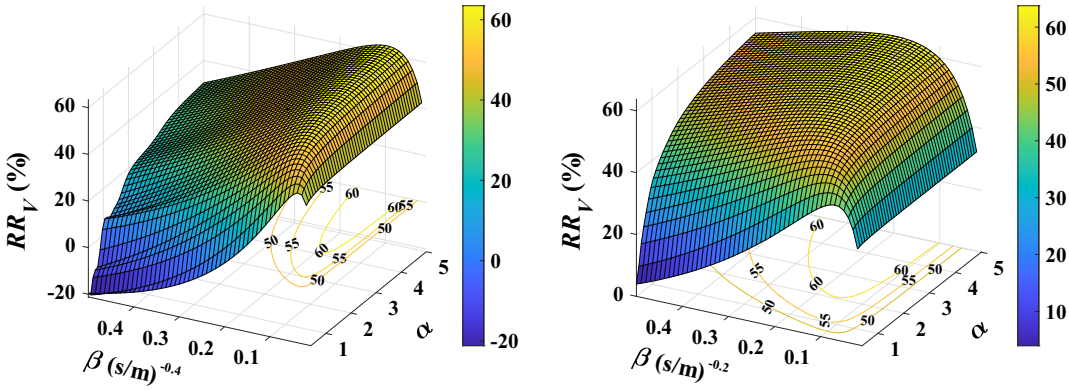

(a) $\nu = 0.6$. (b) $\nu = 0.8$.

Figure 5.5: Three-dimensional mesh and contour plots of response reduction in base shear force versus brace stiffness ratio and damping ratio for the SDOF structure under white-noise excitation.

Design parameters for reducing the base shear force, as signified by the ratio RR_V, are calculated using the same procedure in Section 5.1.1 for interstory drift. Figure 5.5 shows the three-dimensional mesh plot and the contour plot of the RR_V versus the stiffness ratio α and the damping ratio β for the velocity exponents of 0.6 and 0.8. However, unlike the interstory drift reduction presented earlier in Figure 5.1, the mesh plot in Figure 5.5(a) shows that the use of larger brace stiffness and larger damping coefficient does not necessarily result in a greater base shear force reduction. While a larger brace stiffness generally provides a greater response reduction, a larger damping coefficient in the viscous damper may not lead to a greater reduction in the base shear force. It can also be seen from Figure 5.5 that there exist infinite combinations of design parameters to achieve the same reduction in base shear force, and for a given target in response reduction, there exists a minimum brace stiffness and an optimal damping coefficient in the viscous damper.

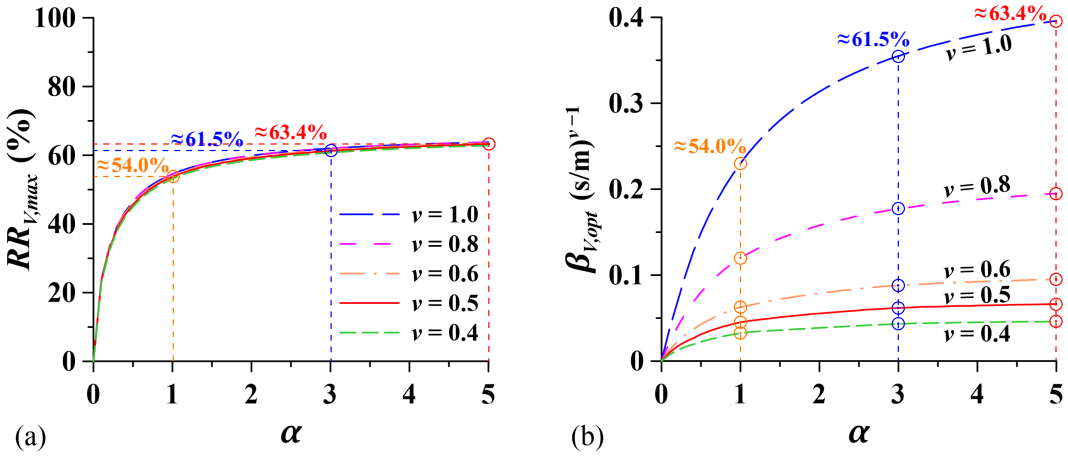

Figure 5.6: (a) Maximum response reduction in base shear $RR_{V,max}$ and (b) corresponding optimal damping ratio $\beta_{V,opt}$ against brace stiffness ratio α for the SDOF structure under white-noise excitation.

Figure 5.6 shows the variation of the maximum response reduction in base shear force $RR_{V,max}$, and the optimal damping ratio $\beta_{V,opt}$ with the brace stiffness ratio α for the velocity exponent in the range 0.4-1. Similar to the trend noted for interstory drift, the plots in Figure 5.6(a) show a sharp increase in base shear response reduction in the small brace stiffness ratio range, and tends toward a diminishing return when the brace stiffness ratio becomes larger, say $\alpha > 1$. The trend is noted regardless of the magnitude of the velocity exponent; thus the tested velocity exponents are expected to provide the same improvement in structural base shear when the damper is optimally designed. It can be seen from Figure 5.6(b) that the optimal damping ratio of the damper shows a nonlinear increase with the brace stiffness, but the growth rate decreases gradually. It can also be observed from the figure that as the

velocity exponent decreases from 1 to 0.4, the amount of damping required for the maximum reduction in base shear force decreases. It is worth noting that the optimal damping ratio for maximum reduction in base shear force is much smaller than that of interstory drift.

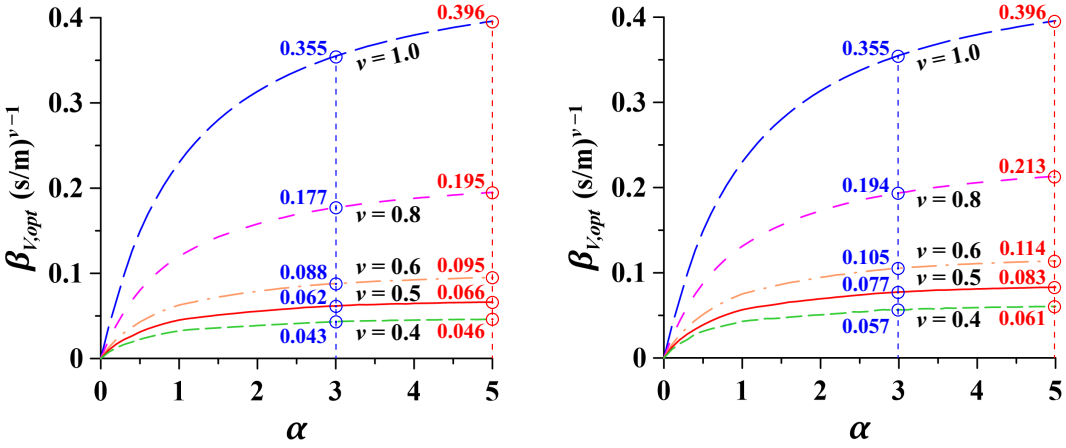

(a) PGA = 0.637 g (b) PGA = 1 g

Figure 5.7: Optimal damping ratios to achieve maximum response reductions in base shear force under white-noise excitation with different intensities.

The optimal parameters above are computed based on a white-noise acceleration time-history with a peak ground acceleration of 0.637 g. However, as nonlinear viscous dampers are used, these optimal parameters may no longer be "optimal" if we change the overall intensity of the ground acceleration, i.e., uniformly scale-up or scale-down the input accelerogram. Figure 5.7(a) shows the optimal damping ratios required to maximize the base shear response reduction under the original white-noise acceleration-history, and Figure 5.7(b) shows the optimal damping ratios under a white-noise that is scaled-up from the original accelerogram to have a PGA equals 1 g. It is worth noting that the optimal parameters for different excitation intensity levels result in the same maximum response reductions (Figure 5.6(a)) for a given set of brace stiffness and velocity exponent. From Figure 5.7 it can be seen that, as the PGA of the ground motion increases from 0.637 to 1 g, the optimal damping ratios for a linear damper, i.e., ν equals one, are identical, yet an optimal damping ratio of a nonlinear damper increases for a given set of α and ν.

5.1.3 Seismic performance of the SDOF structure under realistic earthquakes

The seismic performance of the SDOF structure is also evaluated using the accelerograms of three realistic ground motions. The examined earthquakes are summarized in Table 5.2.

Table 5.2: Earthquake ground motions considered.

Earthquake event	Station	PGA(g)
1940 Imperial Valley	El Centro	0.348
1989 Loma Prieta	Capitola	0.458
1994 Northridge	Canoga Park - Topanga Canyon	0.358

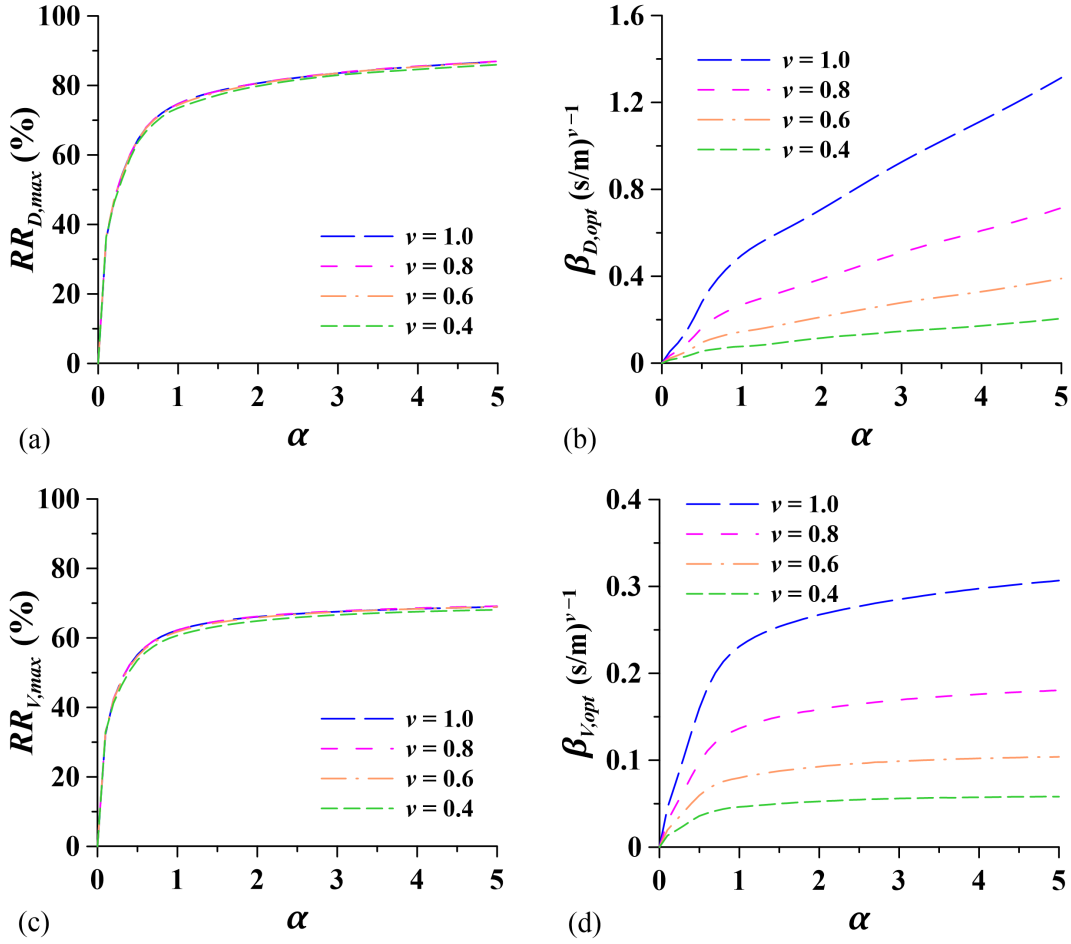

Figure 5.8: (a) $RR_{D,max}$ and (b) $\beta_{D,opt}$ versus brace stiffness ratio α; (c) $RR_{V,max}$ and (d) $\beta_{V,opt}$ versus α for the SDOF structure under the 1940 Imperial Valley earthquake.

The maximum response reductions in interstory drift and base shear force, $RR_{D,max}$ and $RR_{V,max}$, as well as the corresponding optimal damping ratios, $\beta_{D,opt}$ and $\beta_{V,opt}$, against the brace stiffness ratio under the three examined earthquakes are plotted in Figures 5.8, 5.9 and 5.10. It can be seen from Figures 5.8(a),(c), Figures 5.9(a), (c) and Figures 5.10(a), (c) that, the response reductions curves under the realistic earthquakes are similar to those under the white-noise excitation, as shown in Figure 5.2(a) and Figure 5.6(a). However, the achievable maximum response reduction for a

given brace stiffness will change when the structure is subjected to a different ground motion. For instance, when the brace stiffness equals the structural stiffness, i.e., α equals one, the maximum interstory drift response reduction for the building under the Imperial Valley earthquake is approximately 75%, as shown in Figure 5.8(a), while the maximum achievable response reductions under the Loma Prieta earthquake and the Northridge earthquake are around 57% and 69%, respectively. It can also be seen from the response reduction curves that, for a prescribed ground motion input, the maximum achievable response reductions in interstory drift are generally larger than those in base shear force for a given brace stiffness.

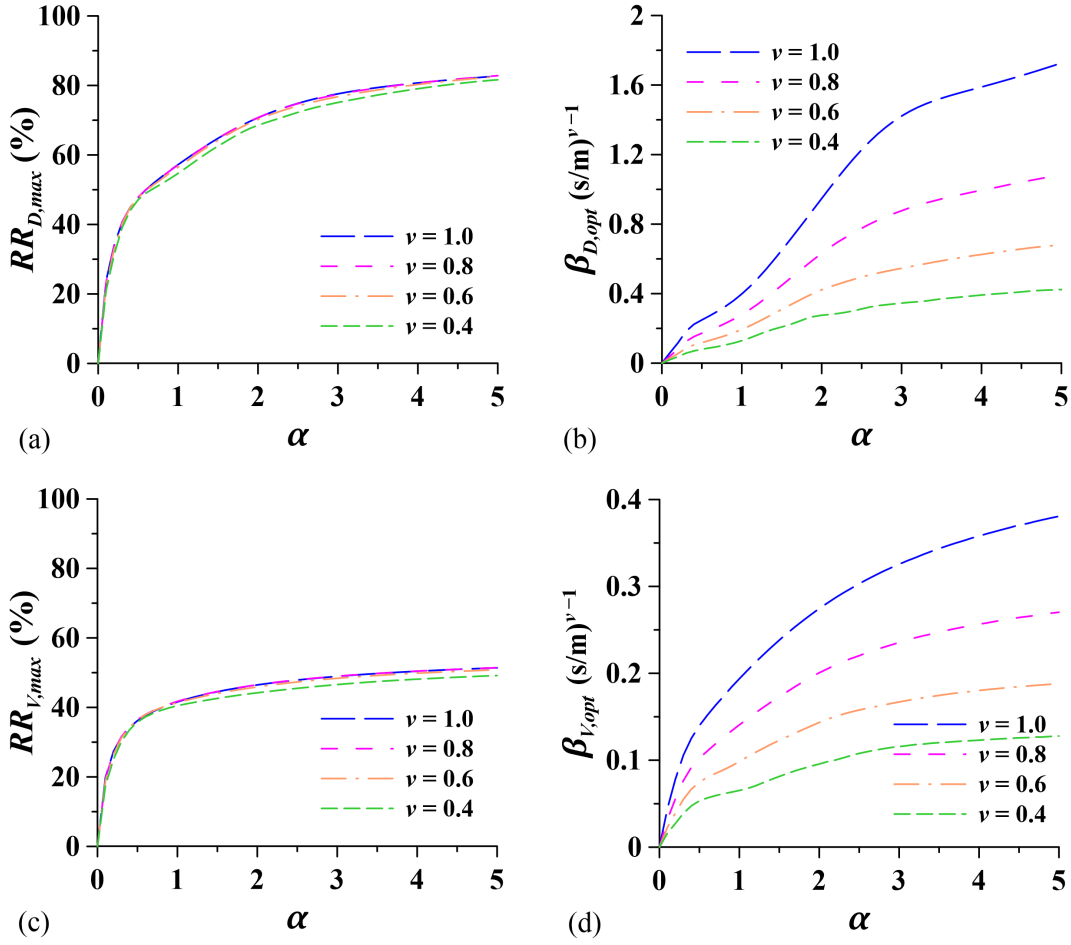

Figure 5.9: (a) $RR_{D,max}$ and (b) $\beta_{D,opt}$ versus brace stiffness ratio α; (c) $RR_{V,max}$ and (d) $\beta_{V,opt}$ versus α for the SDOF structure under the 1989 Loma Prieta earthquake.

Figures 5.8(b), (d), Figures 5.9(b), (d) and Figures 5.10(b), (d) show the optimal damping ratios required from the viscous damper to achieve the maximum response reductions. From the figures it can be seen that, the optimal damping ratios for maximizing a response reduction vary for different earthquakes, which indicates that

the optimal parameters for a specific ground acceleration input may not still be optimal when the excitation changes. In general, the optimal damping ratios increase with increasing brace stiffness for a preset velocity exponent, which agrees with the observations made in Sections 5.1.1 and 5.1.2 for the white-noise ground excitation. It can also be observed from these figures that, for a given brace stiffness ratio, the magnitudes of the optimal damping ratios required to maximized the story drift and base shear force response reductions generally increase with increasing velocity exponent, for all the examined earthquake acceleration time-histories. This observation also agreed with those for the white-noise excitation in the previous sections.

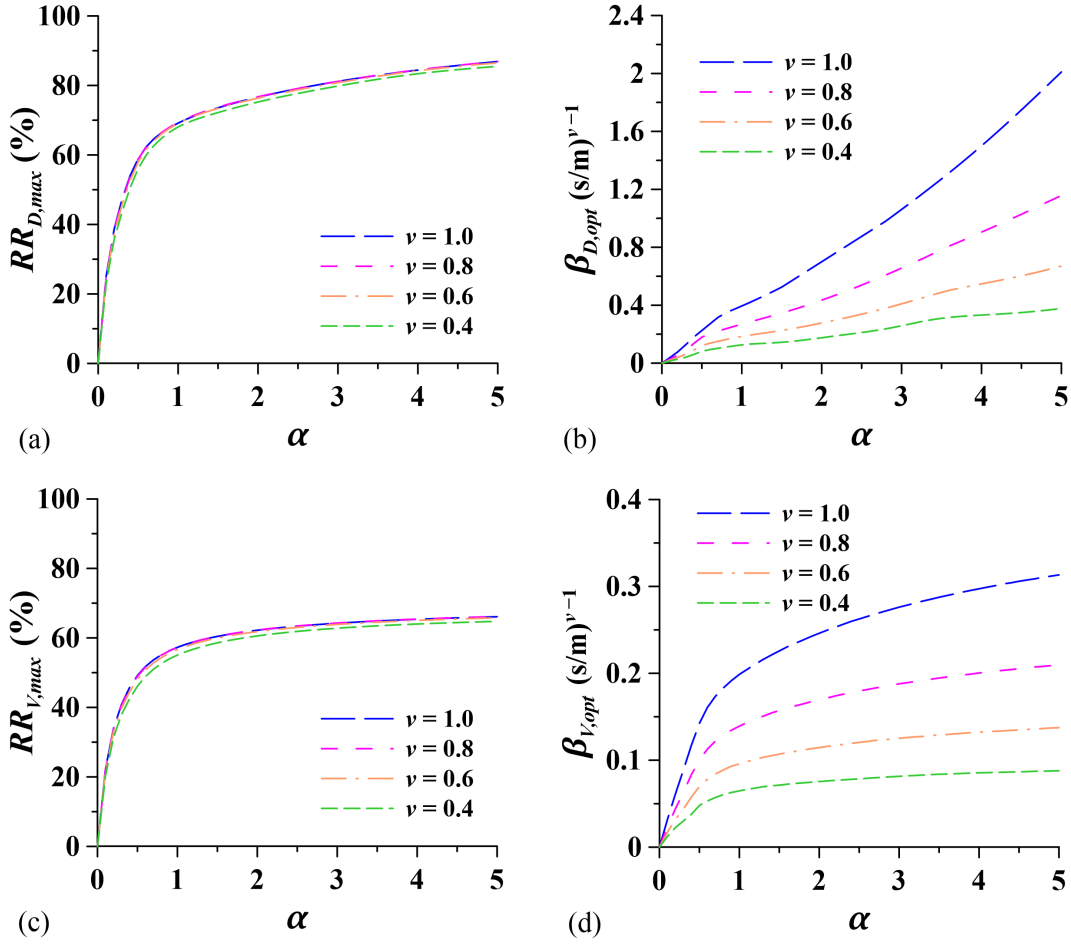

Figure 5.10: (a) $RR_{D,opt}$ and (b) $\beta_{D,opt}$ versus brace stiffness ratio α; (c) $RR_{V,max}$ and (d) $\beta_{V,opt}$ versus α for the SDOF structure under the 1994 Northridge earthquake.

5.1.4 Minimization of peak seismic responses

In addition to the root-mean-square of structural responses, the seismic performance of a building may also be assessed through evaluations of the peak responses. In this section, to evaluate the effectiveness of a damper-brace system in mitigating

peak structural responses, a performance index in peak story drift, and an index in peak base shear force, are respectively defined as:

$$PI_{mD} = max(abs(\delta)) \tag{5.7}$$

and

$$PI_{mV} = max(abs(V_s)) \tag{5.8}$$

where δ and V_s are the time-histories in story drift and base shear force of a SDOF structure, respectively, and the corresponding response reductions can be calculated as:

$$RR_{mD}(\%) = \left(1 - \frac{PI_{mD}}{PI_{mD,org}}\right) \times 100 \tag{5.9}$$

and

$$RR_{mV}(\%) = \left(1 - \frac{PI_{mV}}{PI_{mV,org}}\right) \times 100 \tag{5.10}$$

where $PI_{mD,org}$ and $PI_{mV,org}$ are the performance indices in peak story drift and maximum base shear of the original structure without a damper-brace system, respectively. Based on these peak response reductions, the optimal performances of the SDOF structure described in Section 5.1.1, and the corresponding optimal damper parameters to minimize the peak story drift and peak base shear force of the structure under white-noise excitation, are computed, as shown in Figures 5.11 and 5.13.

Figure 5.11 shows the maximum achievable response reduction in peak story drift $RR_{mD,max}$ and the optimal damping ratio $\beta_{mD,opt}$ against the brace stiffness ratio for velocity exponent equals 0.4, 0.6, 0.8 and 1.0. From Figure 5.11(a) it can be seen that the maximum peak story drift response reduction generally increases with increasing brace stiffness ratio, which is similar to the trend for the maximum story drift response reduction $RR_{D,max}$ in Figure 5.2(a), and the velocity exponent also has no significant influence on the $RR_{mD,max}$. It can be seen from Figure 5.11(b) that, in general, the optimal damping ratio increases with the brace stiffness ratio, but sharp changes in $\beta_{mD,opt}$ can be observed at α around 1.7 and 3, for all the examined velocity exponents. For instance, when α increases from 1.6 to 1.7, there is a sharp increase in $\beta_{mD,opt}$ for a given velocity exponent. However, if we plot the response reduction against the damping ratio for α equals 1.6 and 1.7, as shown in

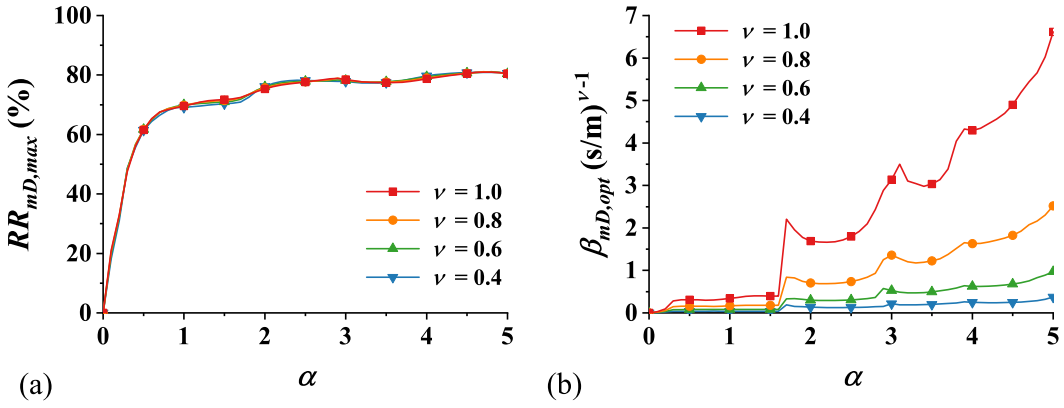

Figure 5.11: (a) Maximum response reduction in peak story drift $RR_{mD,max}$ and (b) corresponding optimal damping ratio $\beta_{mD,opt}$ against brace stiffness ratio α for the SDOF structure under white-noise excitation.

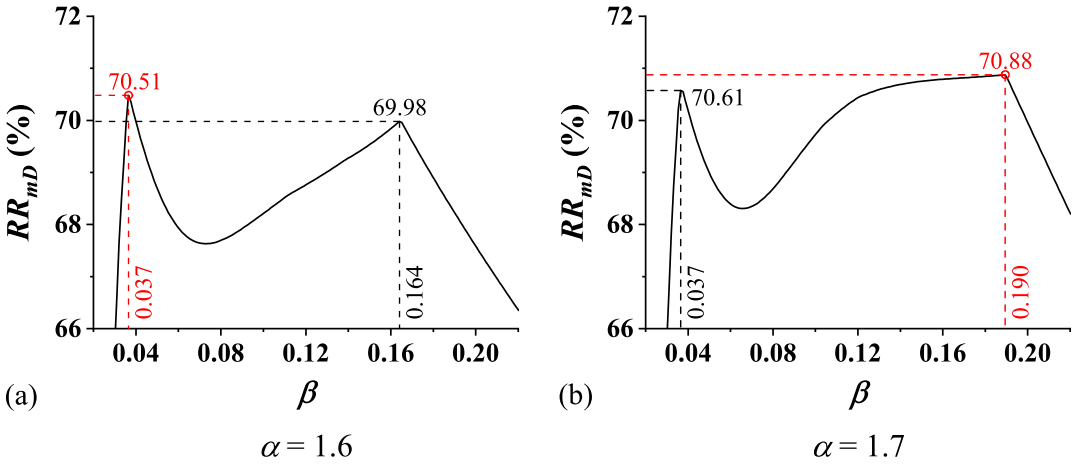

Figure 5.12: Response reduction in peak base shear force RR_{mV} against damping ratio β for α equals 1.6 and 1.7 ($\nu = 0.4$).

Figure 5.12, it can be found that the sudden change in optimal damping ratio is due to the existence of different "peak" response reductions for a given α. Unlike the performance index in story drift PI_D that describes the overall drift intensity of the structure during an earthquake, the PI_{mD} focuses on the peak drift at a certain time instant within the earthquake time-history. The damping required to minimize a peak structural response at two different time instants in an earthquake may be quite different, which causes a sudden change in the optimal damping ratio.

Figure 5.13 shows the maximum achievable response reductions in peak base shear force $RR_{mV,max}$ and the corresponding optimal damping ratios $\beta_{mV,opt}$ for different brace stiffness ratios and different velocity exponents. It can be seen from Figure 5.13(a) that, as the brace stiffness ratio increases, the trends of $RR_{mV,max}$ are similar

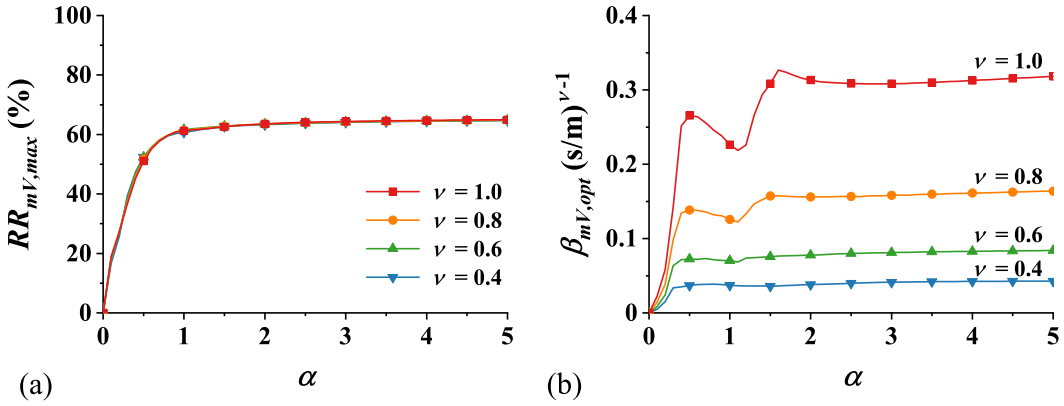

Figure 5.13: (a) Maximum response reduction in peak base shear force $RR_{mV,max}$ and (b) corresponding optimal damping ratio $\beta_{mV,opt}$ against brace stiffness ratio α for the SDOF structure under white-noise excitation.

to those of other maximum response reductions, and for a given brace stiffness, the maximum response reductions in peak base shear force are also very close for different velocity exponents. Sharp changes in the optimal damping ratio can be similarly observed in Figure 5.13(b), and it can also be seen from the figure that, for a given brace stiffness ratio, the magnitude of the optimal damping ratio to minimize the peak base shear force increases with increasing velocity exponent of the damper.

5.2 Performance assessment of a MDOF structure with multiple damper-brace systems

5.2.1 Dynamic response of the structure-damper-brace system

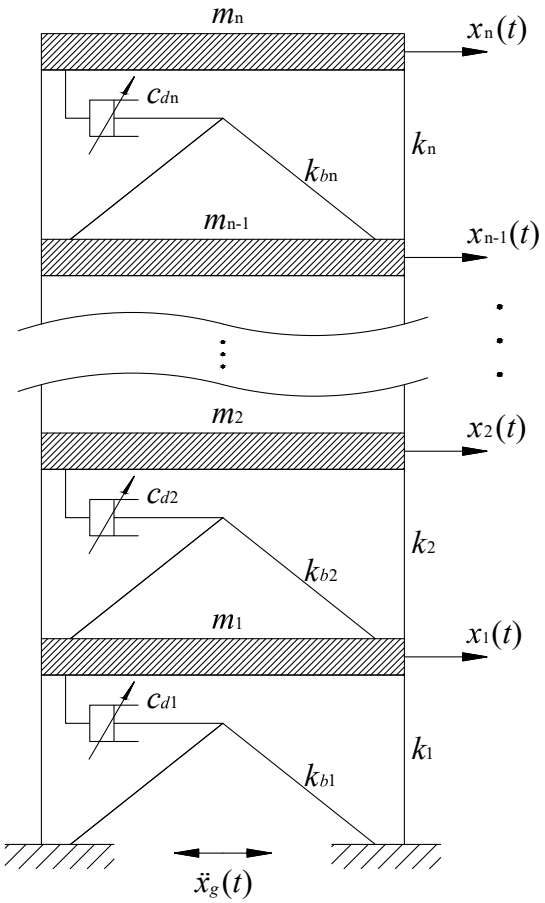

Figure 5.14: A n-story shear-type building with nonlinear FVDs installed on top of Chevron braces.

The equation of motion for a structure with n-degree-of-freedom and controlled by p number of nonlinear viscous dampers installed on Chevron braces, such as that shown in Figure 5.14, can be written as:

$$\mathbf{M}\ddot{\mathbf{x}}(t) + \mathbf{C}\dot{\mathbf{x}}(t) + \mathbf{K}\mathbf{x}(t) + \mathbf{F_d}(t) = -\mathbf{M}\mathbf{1}\ddot{x}_g(t) \tag{5.11}$$

where $\mathbf{M}$, $\mathbf{C}$ and $\mathbf{K}$ are the $n \times n$ mass, damping and stiffness matrices of the structure, respectively, $\mathbf{x}(t) = [x_1(t) \;\; x_2(t) \;\; \cdots \;\; x_n(t)]^{\mathbf{T}}$ is the $n \times 1$ story displacement vector, $\mathbf{1} = [1 \;\; \cdots \;\; 1]^{\mathbf{T}}$ denotes the $n \times 1$ unit vector and $\mathbf{F_d}(t)$ is the $n \times 1$ damper force vector expressed as:

$$\mathbf{F_d}(t) = \begin{bmatrix} f_{d,1}(t) - f_{d,2}(t) \\ f_{d,2}(t) - f_{d,3}(t) \\ \vdots \\ f_{d,n-1}(t) - f_{d,n}(t) \\ f_{d,n}(t) \end{bmatrix} \tag{5.12}$$

where $f_{d,i}(t)$ is the force induced by the nonlinear viscous damper at i-th story; if no damper is installed at i-th floor, $f_{d,i}(t)$ should be set to zero. The activating displacement of the damper-brace system at the i-th floor, $\Delta_i(t)$, is equal to the horizontal relative displacement between the floors (interstory drift), i.e., $\Delta_i(t) = x_i(t) - x_{i-1}(t)$. Steps outlined in Section 4.2 are used to determine the displacement increment in the i-th supporting brace, $\Delta_{b,i}[\mathrm{k}+1]$:

$$\Delta_{b,i}[\mathrm{k}+1] = A_{d,i}[\mathrm{k}]\Delta_{b,i}[\mathrm{k}] + E_{0,i}[\mathrm{k}]\dot{\Delta}_i[\mathrm{k}] + E_{1,i}[\mathrm{k}]\dot{\Delta}_i[\mathrm{k}+1] \tag{5.13}$$

where

$A_i[\mathrm{k}] = -(\frac{k_{bi}}{c_{di}})^{\frac{1}{\nu_i}} |\Delta_{b,i}[\mathrm{k}]|^{(\frac{1}{\nu_i}-1)}$;

$A_{d,i}[\mathrm{k}] = e^{A_i[\mathrm{k}]\Delta t}$;

k_{bi}, c_{di} and ν_i are the brace stiffness, damping coefficient and velocity exponent of the i-th damper-brace system, respectively. The i-th damper force at the next increment can be calculated as:

$$f_{d,i}[\mathrm{k}+1] = k_{bi}\Delta_{b,i}[\mathrm{k}+1] \tag{5.14}$$

To compute the response history of the structure, Eq. (5.11) is rewritten in the following first-order differential equation:

$$\dot{\mathbf{z}}(t) = \mathbf{A}^*\mathbf{z}(t) + \mathbf{B}^*\mathbf{F_d}(t) + \mathbf{E}^*\ddot{x}_g(t) \tag{5.15}$$

where

$\mathbf{z}(t) = \begin{bmatrix} \mathbf{x}(t) \\ \dot{\mathbf{x}}(t) \end{bmatrix}$ is the $2n \times 1$ response vector of the structure;

$\mathbf{A}^* = \begin{bmatrix} \mathbf{0} & \mathbf{I} \\ -\mathbf{M}^{-1}\mathbf{K} & -\mathbf{M}^{-1}\mathbf{C} \end{bmatrix}$ is the $2n \times 2n$ system matrix;

$\mathbf{B}^* = \begin{bmatrix} \mathbf{0} \\ -\mathbf{M}^{-1} \end{bmatrix}$ is the $2n \times n$ damper force distribution matrix;

$\mathbf{E}^* = \begin{bmatrix} \mathbf{0} \\ -\mathbf{1} \end{bmatrix}$ is the $2n \times 1$ external excitation distribution vector.

Similar to the assumptions made in Section 3.1.1, the damper force at i-th floor is assumed to be piece-wise constant between the two consecutive sampling points [k] and [k + 1]. The ground acceleration however is interpolated linearly between these sampling points. Thus the discrete time-state function for the response of the multi-story building under a ground acceleration $\ddot{x}_g$ can be expressed as:

$$\mathbf{z}[\mathrm{k}+1] = \mathbf{A_0^*}\mathbf{z}[\mathrm{k}] + \mathbf{B_0^*}\mathbf{F_d}[\mathrm{k}] + \mathbf{E_0^*}\ddot{x}_g[\mathrm{k}] + \mathbf{E_1^*}\ddot{x}_g[\mathrm{k}+1] \tag{5.16}$$

where the parameters, which are all matrices, $\mathbf{A_0^*}$, $\mathbf{B_0^*}$, $\mathbf{E_0^*}$ and $\mathbf{E_1^*}$ are given by:
$\mathbf{A_0^*} = e^{\mathbf{A}^* \Delta t}$ is the discrete system matrix;
$\mathbf{B_0^*} = \mathbf{A}^{*^{-1}}(\mathbf{A_0^*} - \mathbf{I})\mathbf{B}^*$ is the instant discrete damper force distribution matrix;
$\mathbf{E_0^*} = [\mathbf{A}^{*^{-1}}\mathbf{A_0^*} + \frac{1}{\Delta t}\mathbf{A}^{*^{-2}}(\mathbf{I} - \mathbf{A_0^*})]\mathbf{E}^*$ is the instant discrete ground acceleration distribution vector at sampling point [k];
$\mathbf{E_1^*} = [-\mathbf{A}^{*^{-1}} + \frac{1}{\Delta t}\mathbf{A}^{*^{-2}}(\mathbf{A_0^*} - \mathbf{I})]\mathbf{E}^*$ is the instant discrete ground acceleration distribution vector at sampling point [k + 1].

5.2.2 Numerical example I: a two-story shear building

The 2DOF building studied by Lavan and Levy (2006) is adopted here to investigate whether observations made for SDOF structures can be extended to MDOF structures. The first and second natural periods of the structure are 0.281 and 0.115 seconds, respectively, and the structure is assumed to have an inherent damping ratio of 3% for the two vibration modes. The investigation is also made using the white-noise excitation noted in Section 5.1. The mass and stiffness matrices of the structure are:

$$\mathbf{M} = \begin{bmatrix} 25000 & 0 \\ 0 & 25000 \end{bmatrix} \text{(kg)} \quad \text{and} \quad \mathbf{K} = \begin{bmatrix} 62500 & -25000 \\ -25000 & 25000 \end{bmatrix} \text{(kN/m)} \tag{5.17}$$

For the best performance of the 2DOF structure, damping coefficients of the dampers at the first floor, c_{d1}, and the second floor, c_{d2}, are optimized for the maximum response reduction given the set of equal brace stiffness $k_{b1} = k_{b2} = k_b$ and equal velocity exponent $\nu_1 = \nu_2 = \nu$ using genetic algorithm described in Section 3.3. The optimization is carried out using the dimensionless brace stiffness ratio, α, which is defined here as the ratio of the brace stiffness k_b to the first story stiffness k_1, which is 37500 kN/m in this case.

5.2.2.1 Response reduction in interstory drift

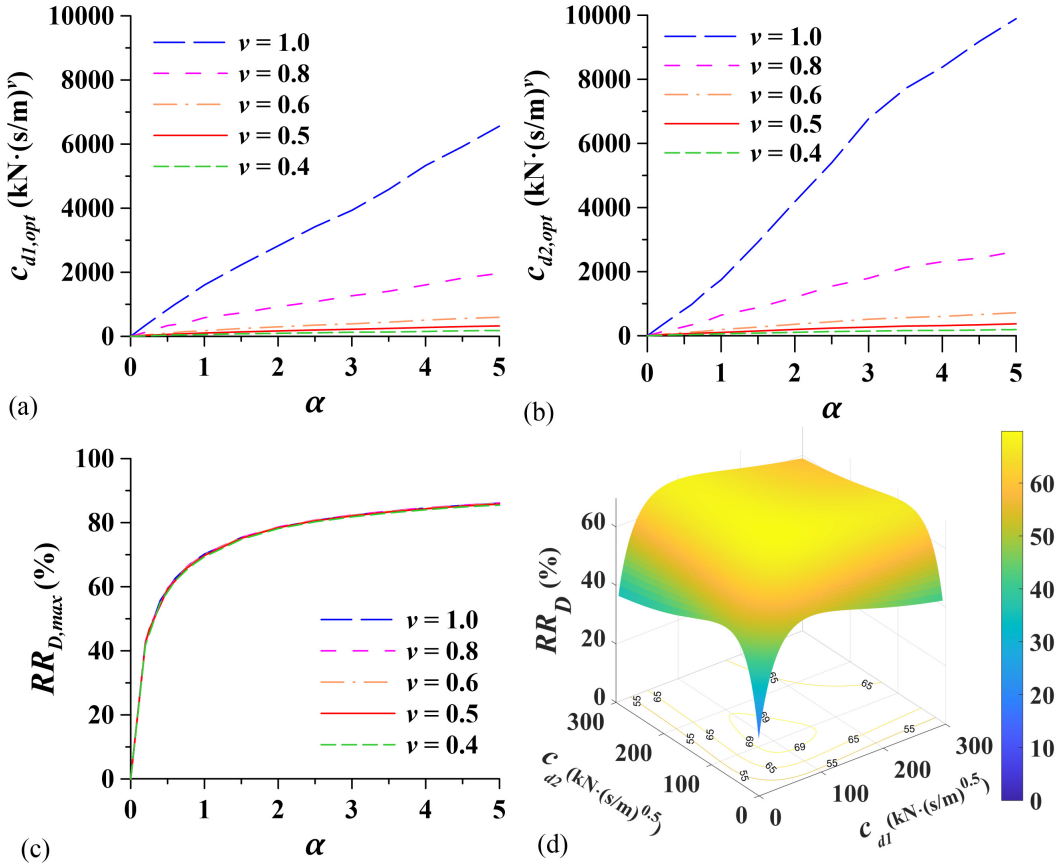

Figure 5.15: (a) Optimal damping coefficient of the damper at 1st story versus brace stiffness ratio; (b) optimal damping coefficient of the damper at 2nd story versus brace stiffness ratio; (c) maximum response reduction in interstory drift versus brace stiffness ratio; (d) response reduction against two damping coefficients ($\alpha = 1$, $\nu = 0.5$).

Figures 5.15(a) and (b) show the plots of the optimal damping coefficients $c_{d1,opt}$ and $c_{d2,opt}$ against the brace stiffness ratio α for velocity exponent from 0.4 to 1. It can be seen from Figures 5.15(a) and (b) that, in general, for the structure to achieve a maximum response reduction, the use of a larger brace stiffness requires a larger damping coefficient, and the optimal damping coefficient decreases as the velocity exponent decreases from 1 to 0.4. It can also be seen by comparing Figures 5.15(a) and (b) that the required optimal damping coefficient of the damper at the first floor is generally smaller than the damper at the second floor given a fixed combination of the brace stiffness and velocity exponent. Figure 5.15(c) shows the variation of the achievable maximum response reduction in the interstory drift with the brace stiffness ratio. Curves similar to that seen in Figure 5.2(a) for the SDOF structure

can also be observed in Figure 5.15(c), where the maximum response reduction grows rapidly as the brace stiffness ratio becomes small and the growth becomes gradual when the brace stiffness is large. Changes in the velocity exponent can be seen to have an insignificant effect on the optimal interstory drift performance of the 2-story structure. Observations from Figure 5.15(c) also reveal that for achieving a target response reduction, there exists a minimum brace stiffness requirement, and the use of nonlinear dampers with velocity exponent less than unity requires a much smaller value of damping coefficient than the linear counterparts.

To verify the accuracy of the results obtained by the genetic algorithm, an exhaustive search is also carried out independently for comparison, in which every set of design parameters lies on the grids within a given search region is examined to find the approximate optimal results. Figure 5.15(d) shows the exhaustive search result of the response reduction in interstory drift versus the two damping coefficients c_{d1} and c_{d2} for the brace stiffness of $\alpha = 1$ and the velocity exponent of $\nu = 0.5$. It can be seen from Figure 5.15(d) that there exists a global maximum in the response reduction in interstory drift. The global maximum $RR_{D,max}$, as obtained by the exhaustive search at a grid size of 1×1 kN·(s/m)$^{0.5}$, is 69.78% with the corresponding damping coefficients of $c_{d1,opt}$ equals 106 kN·(s/m)$^{0.5}$ and $c_{d2,opt}$ equals 104 kN·(s/m)$^{0.5}$. Results obtained by the genetic algorithm for $RR_{D,max}$, $c_{d1,opt}$ and $c_{d2,opt}$ are 69.78%, 106.2 kN·(s/m)$^{0.5}$ and 104.4 kN·(s/m)$^{0.5}$, respectively. The results from exhaustive search agree well with the those from the genetic algorithm, indicating GA is capable of obtaining the global optimal solutions for such a multi-dimensional optimization problem.

5.2.2.2 Response reduction in base shear force

The variations in the optimal damping coefficients and their corresponding maximum reduction in the base shear force with the brace stiffness are shown in Figures 5.16(a)-(c) for different velocity exponents. It can be seen from Figures 5.16(a) and (b) that the optimal damping coefficients for both dampers increase with increasing brace stiffness but with a decreasing growth rate. The diminishing return in the response reduction occurs regardless of the velocity exponent, as can be seen from Figure 5.16(c). It is worth noting that, the required damping for both dampers to achieve a maximum response reduction in base shear force is significantly less than that for interstory drift.

An exhaustive search is also conducted on the two-story structure to confirm the optimal results for base shear force obtained by the genetic algorithm. Figure 5.16(d) shows a plot of the exhaustive search result for base shear force against the

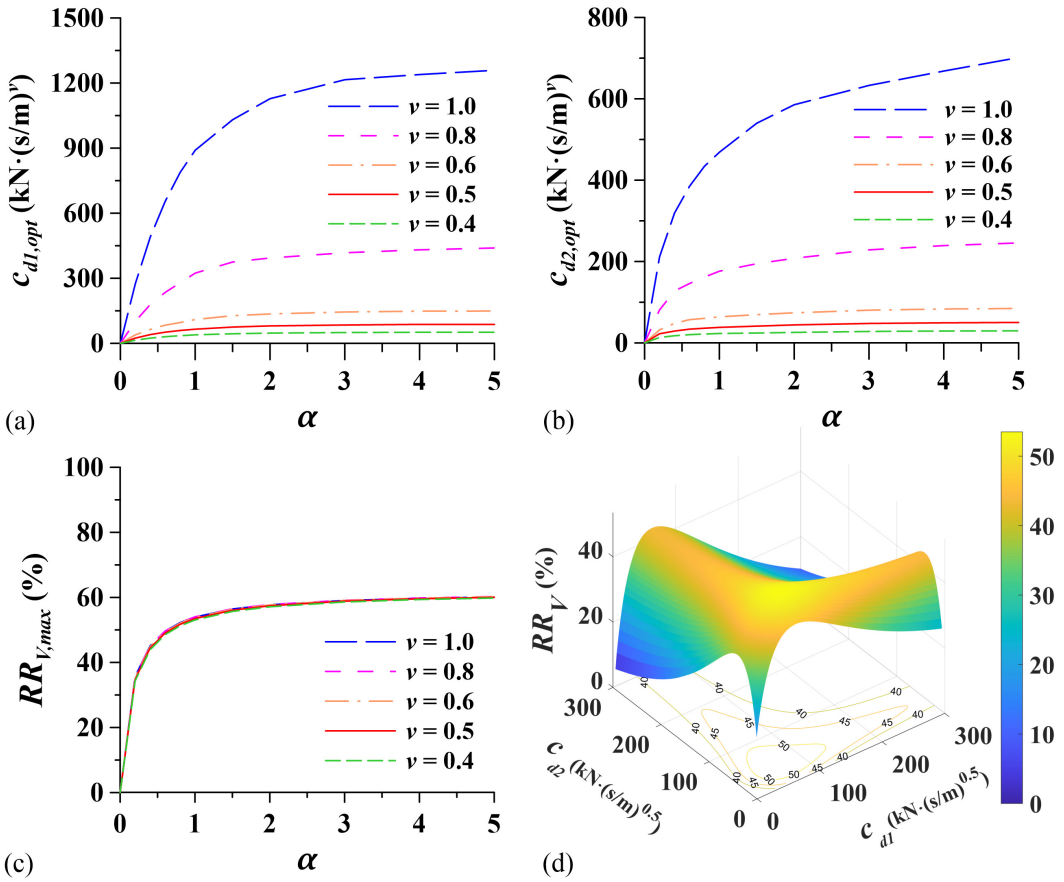

Figure 5.16: (a) Optimal damping coefficient of the damper at 1st story versus brace stiffness ratio; (b) optimal damping coefficient of the damper at 2nd story versus brace stiffness ratio; (c) maximum response reduction in base shear versus brace stiffness ratio; (d) response reduction against two damping coefficients ($\alpha = 1$, $\nu = 0.5$).

two damping coefficients c_{d1} and c_{d2} for the brace stiffness ratio of α equals 1 and velocity exponent of ν equals 0.5. It can be seen from Figure 5.16(d) that, similar to observations made for interstory drift reduction, there also exists a global maximum response reduction for the base shear force. The maximum response reduction obtained by the exhaustive search and the genetic algorithm are both 53.49%, while the optimal damping coefficients are $c_{d1,opt}$ equals 65 kN·(s/m)$^{0.5}$ and $c_{d2,opt}$ equals 38 kN·(s/m)$^{0.5}$ for exhaustive search compared to $c_{d1,opt}$ of 65.5 kN·(s/m)$^{0.5}$ and $c_{d2,opt}$ of 38.2 kN·(s/m)$^{0.5}$.

5.2.3 Numerical example II: a six-story shear building

A six-story shear-type building is included in this study to further investigate the effects of the brace stiffness and velocity exponent on optimal seismic response reduction of MDOF structures. The building is the same as that studied by Takewaki (1997), which has identical story mass and stiffness in each floor, namely, $m_1 = m_2 =$

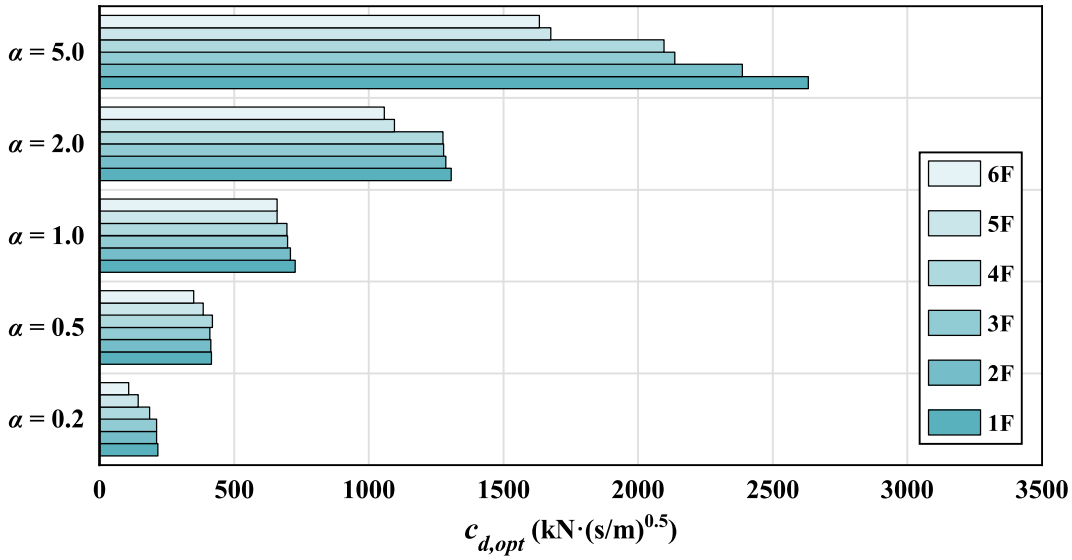

Figure 5.17: Distribution of optimal damping coefficients for different brace stiffness ratios in the 6-story building ($\nu = 0.5$).

$\cdots = m_6 = 80000$ kg and $k_1 = k_2 = \cdots = k_6 = 40$ MN/m. The fundamental period of the building is 1.17 seconds, and a 2% inherent damping is assigned to the structure. It is assumed that each story of the building is equipped with a nonlinear viscous damper installed on top of a Chevron brace. All braces in the building are assumed to be identical (i.e., $k_{b1} = k_{b2} = \cdots = k_b$), while the dampers may have different damping coefficients but with the same velocity exponent (i.e., $\nu_1 = \nu_2 = \cdots = \nu$). Response reduction is investigated using a brace stiffness ratio α of 0.2, 0.5, 1, 2 and 5. The Kanai-Tajimi earthquake model described in Section 3.4.2 is used for optimizing the damper parameters. The building is assumed to be constructed on foundation soil type II, and the seismic precautionary intensity is assumed to be VIII. The artificial accelerogram generated from the PSD function of the Kanai-Tajimi model, as shown in Figure 3.6(b), is adopted as the input ground acceleration-history.

Figure 5.17 shows the distribution of optimal damping coefficients in different stories of the building, and the distribution is obtained by the genetic algorithm for a velocity exponent of ν equals 0.5. It can be seen from Figure 5.17 that a lager brace stiffness generally requires a larger optimal damping coefficient in all stories and that for a given stiffness ratio, larger damping coefficients are generally needed in the lower stories. Figure 5.18 shows the plots of the maximum reduction in interstory drift and the sum of optimal damping coefficients for the velocity exponent of 0.5, 0.7, and 1. It can be seen from 5.18(a) that the maximum response reduction $RR_{D,max}$ increases with increasing brace stiffness ratio but at a decreasing rate. For example, an increase of the brace stiffness ratio from 1 to 2 provides a modest improvement in

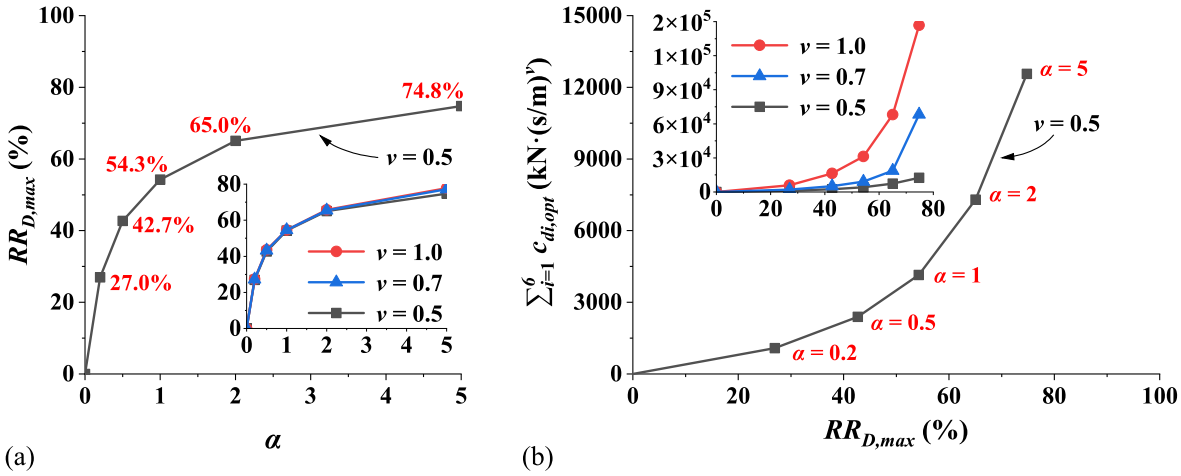

Figure 5.18: (a) Maximum response reduction in interstory drift and (b) summation of optimal damping coefficients for the 6-story building under the Kanai-Tajimi excitation ($\nu = 0.5$).

performance as reflected by a 10.7% increase in $RR_{D,max}$, and an increase in a brace stiffness ratio from 2 to 5 provides 9.8% improvement in performance. It can also be seen in the sub-figure of Figure 5.18(a) that, for optimally designed viscous dampers in the structure, the maximum reductions in interstory drift are nearly the same for different velocity exponents. Figure 5.18(b) shows that the damping required for the structure to reach an optimal performance is not proportional to the value of the maximum response reduction. For example, Figure 5.18(a) shows that an increase in brace stiffness from 2 to 5 times the first story stiffness only results in close to 10% improvement in the interstory drift, but the required sum of the damping coefficients for ν equals 1.0 and 0.7, which is shown in the sub-figure of Figure 5.18(b), is more than doubled. Since the fabrication and installation of the braces and dampers are directly related to the overall cost of the protective system (Park et al. 2004, Pollini et al. 2017), a target structural performance is best set before the design of the nonlinear damper-brace system to achieve a balance between cost and performance. It can also be seen from the sub-figure in Figure 5.18(b) that the use of a larger velocity exponent would result in a larger sum of the damping coefficients, which is consistent with the observations made for the SDOF structure in Section 5.1 and the 2DOF structure in Section 5.2.2.

Since the damping coefficients of the viscous dampers can be optimized for maximizing a response reduction given the brace stiffness and velocity exponent, it is instructive to examine the supplemental damping required of the different structural performance indices. Table 5.3 summarizes the optimal damping coefficients for achieving maximum response reductions of the 6-story structure in terms of in-

terstory drift, base shear force, story displacement, and floor acceleration. Note that results in the table correspond to a brace stiffness that is equal to the first story stiffness and a velocity exponent of 0.5. It can be seen from Table 5.3 that the optimally designed damping coefficients vary depending on the chosen performance index. All four response reductions are greater than 35 percent, and the reductions in interstory drift, story displacement and acceleration are over 50 percent. The required sums of the damping coefficients for interstory drift and story displacement indices are very close, and they are significantly larger than those for base shear force and story acceleration indices.

Table 5.3: Optimal damping coefficients for the 6-story building under four performance evaluation criteria ($\alpha = 1, \nu = 0.5$).

Story	Damping coefficient ($\mathrm{N}\cdot(\mathrm{s/m})^{0.5}$)	Performance index			
		Interstory drift	Base shear	Story displacement	Story acceleration
6F	$c_{d6,opt}$	659335	173797	441635	169306
5F	$c_{d5,opt}$	659597	290040	530455	259615
4F	$c_{d4,opt}$	695665	349989	571366	380044
3F	$c_{d3,opt}$	698386	372328	646693	471202
2F	$c_{d2,opt}$	708474	411482	821899	336071
1F	$c_{d1,opt}$	726320	478571	1188536	195911
	$\sum_{i=1}^{6} c_{di,opt}$	4147776	2076207	4200584	1812149
	Max. Response	$1 - \frac{PI_D}{PI_{D,org}}$	$1 - \frac{PI_V}{PI_{V,org}}$	$1 - \frac{PI_S}{PI_{S,org}}$	$1 - \frac{PI_A}{PI_{A,org}}$
	Reduction	54.25%	38.23%	51.67%	51.79%

Although the nonlinear damper-brace system has been shown to be effective in mitigating structural responses under the Kanai-Tajimi excitation, it is nonetheless important to verify its effectiveness under more realistic earthquakes. The performance-based seismic design of China (CECS 160: 2004) published by IEM (2004) recommends several earthquake ground acceleration records for time-history analysis of buildings with a fundamental period of 0.5-1.5 seconds at site type II. The recommended ground motions of the 1979 Imperial Valley earthquake recorded at station El Centro Array #10 in California (PEER 2022), and the 1952 Kern County earthquake recorded at Taft Lincoln school also in Caifornia (PEER 2022), are considered in this example. Figure 5.19 shows the response envelopes plotted against the building height under the Imperial Valley earthquake using damper parameters optimized for interstory drift index. It can be seen from Figure 5.19 that the structural responses generally decrease with an increase in the brace stiffness ratio, indicating that even though the design damper parameters have not been optimized based on

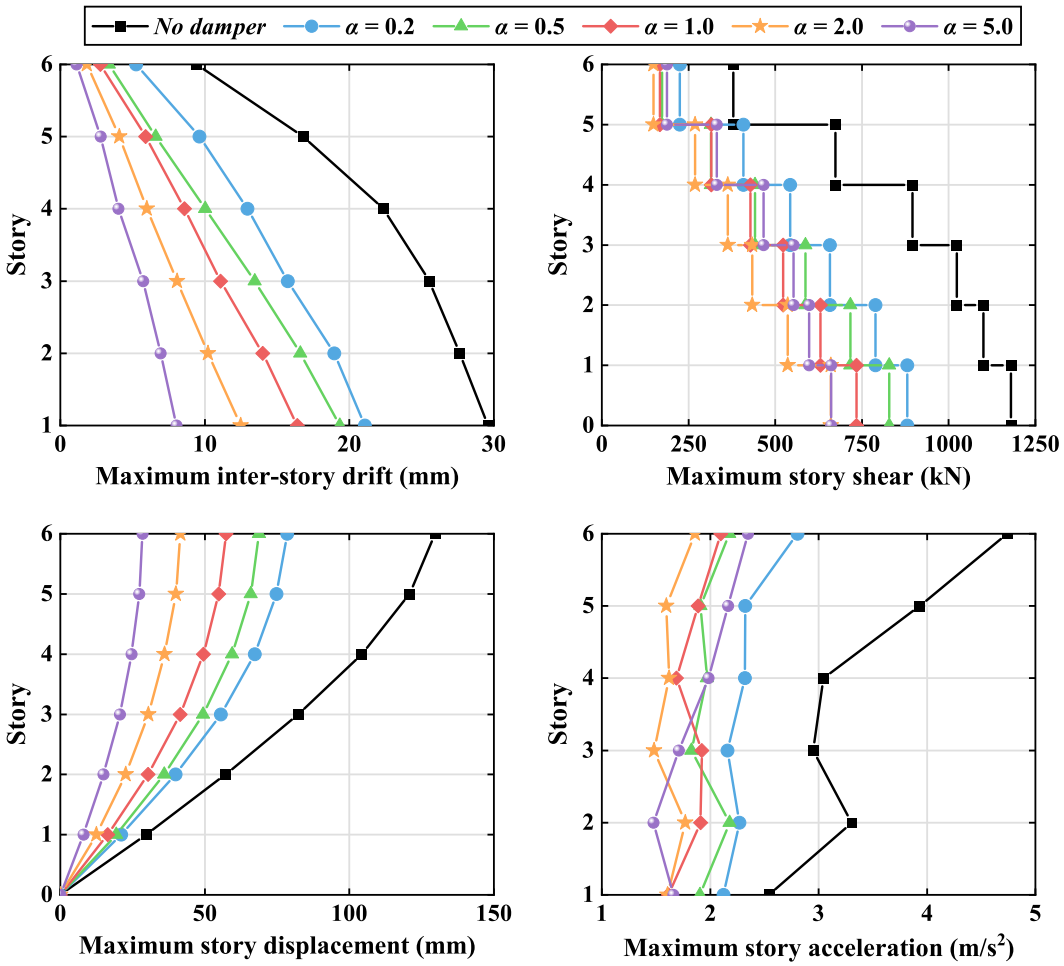

Figure 5.19: Response envelopes of the 6-story building installed with the optimally designed damper-brace systems for interstory drift under the 1979 Imperial Valley earthquake ($\nu = 0.5$).

the actual earthquakes but the Kanai-Tajimi excitation, the brace-damper systems are still capable of providing significant improvement to the seismic performance of the structure. However, it should be noted from the plots of base shear and story acceleration that, when the brace stiffness ratio increases from 2 to 5, the overall maximum base shear and story acceleration both increases. The increases in base shear and story acceleration may be attributed to the fact that the design parameters had been optimized based on the interstory drift performance index rather than by the story acceleration.

From a structural design point of view, the performance of the structure should be assessed by a set of performance indices rather than by a single index alone. In that context, three additional performance indices, pertaining to the base shear force defined in Eq. (5.5), story displacement, as defined in Eq. (3.12), and floor acceleration, as defined in Eq. (3.13), are evaluated under both the 1979 Imperial Valley and the

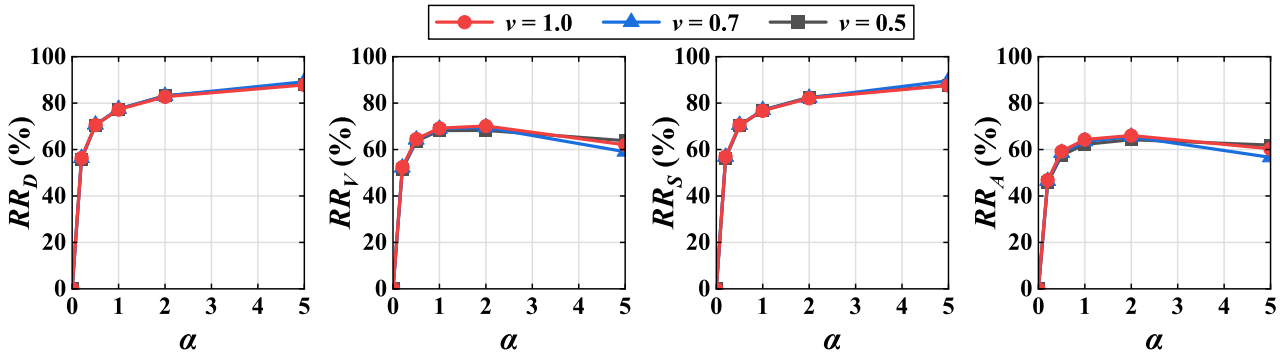

(a) The 1979 Imperial Valley earthquake, El Centro Array #10.

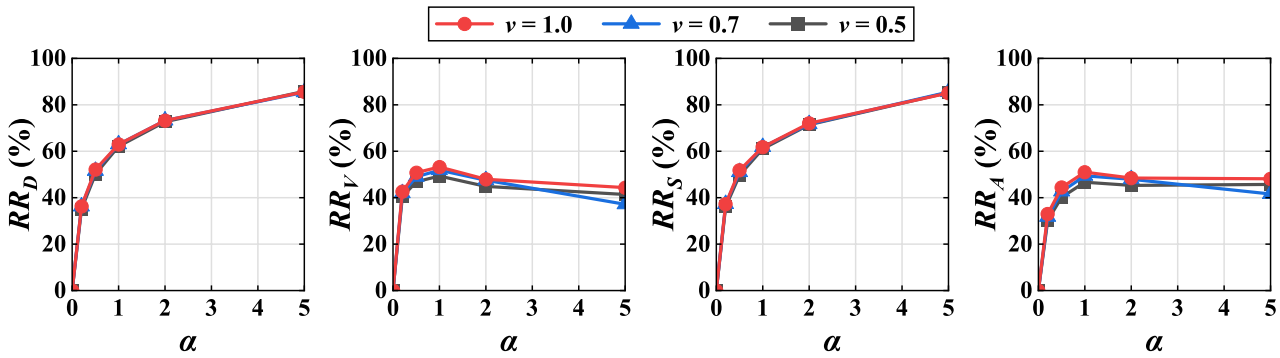

(b) The 1952 Kern County earthquake, Taft Lincoln School.

Figure 5.20: Response reductions for different performance indices of the 6-story building under (a) the 1979 Imperial Valley earthquake and (b) the 1952 Kern County earthquake, using the optimal dampers designed based on RR_D under the Kanai-Tajimi excitation.

1952 Kern County earthquakes using the damper parameters optimally determined from the interstory drift index under the Kanai-Tajimi excitation. Figure 5.20 shows the response reductions for the different performance indices (RR_D, RR_V, RR_S and RR_A) for different nonlinear velocity exponents under the two earthquakes. It can be seen from Figures 5.20(a) and (b) that response reductions in interstory drift and story displacement generally improve with increasing brace stiffness for both earthquakes, while the response reductions in base shear and story acceleration for Imperial Valley earthquake start to decrease when brace stiffness ratio is greater than 2, and for Kern County earthquake the response reductions start to decrease when α is larger than 1. It is evident that the interstory drift and story displacement response reductions tend towards diminishing returns after α equals one (i.e., brace stiffness equals first story stiffness), and the base shear and story acceleration response reductions may reduce when brace stiffness is larger than the first story stiffness. Since previous results also suggested that greater amounts of optimal damping will be required when using a larger brace stiffness, it is not suggested to use an excessive large brace

stiffness for damper-brace assemblies. From Figures 5.20(a) and (b) it can also be seen that, for a given brace stiffness ratio, response reductions are close for different velocity exponents, particularly in the interstory drift and story displacement indices. Results from Figure 5.20 also suggest that, for a given brace stiffness, there exists a maximum achievable response reduction regardless of the value of the velocity exponent, similar to that observed in Figure 5.18(a). If higher performance is desired of displacement-based indices, the brace stiffness should be increased, followed by the optimization of the damper parameters, although this could be at the expense of a decrease in story acceleration and base shear performance indices.

5.2.4 Numerical example III: incremental dynamic analysis of a nonlinear eight-story building

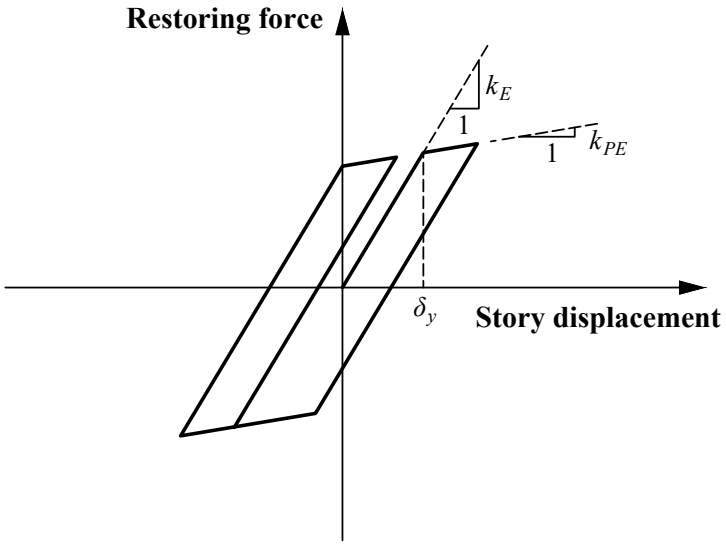

Figure 5.21: Bilinear elastic-plastic stiffness model of the nonlinear structure.

To evaluate the capacity and robustness of the optimally designed nonlinear damper-brace systems to the uncertainty of ground motions, incremental dynamic analysis has been performed on a nonlinear eight-story building under multiple earthquakes with different vibration characteristics. The nonlinear building is a benchmark structure studied by Yang et al. (1988), of which the lateral stiffness of each floor is assumed to be bilinear elastic-plastic, as shown in Figure 5.21, with elastic stiffness $k_E = 340.4$ MN/m, post-elastic stiffness $k_{PE} = 0.1k_E = 34.04$ MN/m and yielding interstory drift $\delta_y = 2.4$ cm. It can be seen from Figure 5.21 that an excessive lateral displacement can yield the floor and may cause permanent deformation in stories. The floor mass and damping coefficient are identical at each story unit, namely $m_1 = m_2 = \cdots = m_8 = 345.6 \times 10^3$ kg and $c_1 = c_2 = \cdots = c_8 = 734.3$ kN·s/m.

Noting that the fundamental period of the building based on its elastic stiffness, T_1, is 1.085 seconds.

Table 5.4: Seismic design parameters.

Parameters	value
Risk/Occupancy category	II
Importance factor	1
Seismic design category	D
Site class	C
MCE[1] spectral response acceleration parameter at short periods S_S (g)	2.866
MCE spectral response acceleration parameter at period of 1 sec S_1 (g)	0.924
Short period site coefficient F_a	1
Long period site coefficient F_v	1.3
Spectral response acceleration parameter at short periods S_{DS} (g)	1.911
Spectral response acceleration parameter at period of 1 sec S_{D1} (g)	0.8
Long-period transition period T_L (s)	8

[1]Maximum Considered Earthquake.

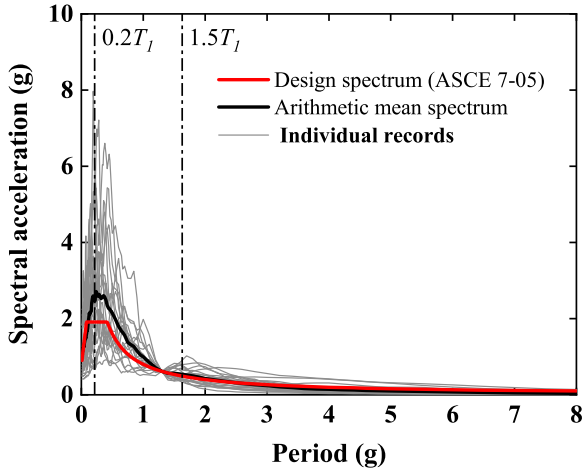

Figure 5.22: Design response spectrum at downtown Los Angeles (based on parameters in Table 5.4) and acceleration response spectrums of the selected earthquakes.

Building structures may be subjected to ground excitation with different vibration properties due to the stochastic nature of earthquakes. Therefore, to assess the robustness of the damper-brace system to the uncertainty of input ground motions, several realistic strong earthquakes have been considered that are selected based on the design ground acceleration spectrum for a specific construction site. In this example, the structure is assumed to be located in downtown Los Angeles in California, USA, on very dense soil and soft rock that is classified as site class C in ASCE 7-05 (ASCE 2005). The occupancy category of the building is assumed to be II, and the corresponding seismic design parameters can be found in ASCE 7-05. Alternatively, the parameters can be determined from the seismic design maps developed

Table 5.5: Selected ground motions used in the numerical example.

Code	Earthquake event	Year	Station	Magnitude	$S_a(T_1, 5\%)$ (g)	PGA (g)
EQ1	Imperial Valley-02	1940	El Centro Array #9	6.95	0.85	0.62
EQ2	Parkfield	1966	Cholame - Shandon Array #5	6.19	0.75	1.29
EQ3	Managua, Nicaragua-01	1972	Managua - ESSO	6.24	0.72	1.11
EQ4	Gazli, USSR	1976	Karakyr	6.80	1.32	0.88
EQ5	Coyote Lake	1979	Gilroy Array #4	5.74	0.98	1.12
EQ6	Imperial Valley-06	1979	Aeropuerto Mexicali	6.53	0.77	0.45
EQ7	Imperial Valley-06	1979	Bonds Corner	6.53	1.10	1.76
EQ8	Imperial Valley-06	1979	Chihuahua	6.53	0.71	0.61
EQ9	Imperial Valley-06	1979	El Centro Array #11	6.53	0.52	0.78
EQ10	Imperial Valley-06	1979	El Centro Differential Array	6.53	0.64	0.88
EQ11	Imperial Valley-06	1979	Holtville Post Office	6.53	0.93	0.63
EQ12	Northridge-01	1994	Canyon Country - W Lost Cany	6.69	0.71	0.95
EQ13	Northridge-01	1994	LA - Saturn St	6.69	1.01	1.74
EQ14	Northridge-01	1994	LA - 7-story Univ Hospital	6.69	0.73	2.09
EQ15	Northridge-01	1994	Newhall - Fire Station	6.69	0.55	0.45
EQ16	Northridge-01	1994	Pacific Palisades - Sunset	6.69	0.85	1.73
EQ17	Northridge-01	1994	Rinaldi Receiving Station	6.69	0.78	0.41
EQ18	Kobe, Japan	1995	Amagasaki	6.90	1.57	0.59
EQ19	Kobe, Japan	1995	KJMA	6.90	0.80	0.52
EQ20	Kobe, Japan	1995	Tadoka	6.90	0.69	1.25

by Structural Engineers Association of California and California Office of Statewide Health Planning and Development (SEAOC and OSHPD 2022), which provide more specific MCE spectral response acceleration parameters (S_S and S_1). The seismic design parameters used are summarized in Table 5.4, based on which a design acceleration response spectrum of the construction site is generated according to ASCE 7-05 (ASCE 2005), as shown in Figure 5.22, and the PEER database is used to search for historic earthquake records. The selected 20 ground motion records are listed in Table 5.5, which have been scaled such that the mean acceleration response spectrum is larger than the design spectrum between periods of $0.2T_1$ and $1.5T_1$, namely 0.217 and 1.673 seconds, as shown in Figure 5.22. In this example, the 5% damped spectral acceleration at the structure's fundamental period, $S_a(T_1, 5\%)$, is adopted as the intensity measure of the ground motions for conducting the IDA, which are summarized in Table 5.5. For a specific earthquake, the scale factor for obtaining a spectral acceleration with an IM of 1 g, $\mathrm{SF}_{S_a=1\mathrm{g}}$, is the multiplicative inverse of $S_a(T_1, 5\%)$, and the SF for a given spectral acceleration is the product of the value of this S_a and $\mathrm{SF}_{S_a=1\mathrm{g}}$. The spectral acceleration considered in this example increases from 0 to 3 g with a step size of 0.1 g, and the following damage measures are defined to describe response intensities of the structure under the prescribed ground excitation inputs, in which Eqs. (5.18)-(5.21) are defined as the average maximum response measures,

and Eqs. (5.22)-(5.25) are the maximum response measures:

$$\text{Average maximum story displacement} = \frac{1}{\mathrm{w}}\sum_{j=1}^{\mathrm{w}} max(abs(\mathbf{X}_j)) \tag{5.18}$$

$$\text{Average maximum interstory drift} = \frac{1}{\mathrm{w}}\sum_{j=1}^{\mathrm{w}} max(abs(\boldsymbol{\delta}_j)) \tag{5.19}$$

$$\text{Average maximum story acceleration} = \frac{1}{\mathrm{w}}\sum_{j=1}^{\mathrm{w}} max(abs(\mathbf{A}_j)) \tag{5.20}$$

$$\text{Average maximum base shear force} = \frac{1}{\mathrm{w}}\sum_{j=1}^{\mathrm{w}} max(abs(\mathbf{V}_j)) \tag{5.21}$$

$$\begin{aligned}\text{Maximum story displacement} = max\{&max(abs(\mathbf{X}_1)),\ max(abs(\mathbf{X}_2)),\ \ldots \\ &\ldots,\ max(abs(\mathbf{X}_{\mathrm{w}}))\}\end{aligned} \tag{5.22}$$

$$\begin{aligned}\text{Maximum interstory drift} = max\{&max(abs(\boldsymbol{\delta}_1)),\ max(abs(\boldsymbol{\delta}_2)),\ \ldots \\ &\ldots,\ max(abs(\boldsymbol{\delta}_{\mathrm{w}}))\}\end{aligned} \tag{5.23}$$

$$\begin{aligned}\text{Maximum story acceleration} = max\{&max(abs(\mathbf{A}_1)),\ max(abs(\mathbf{A}_2)),\ \ldots \\ &\ldots,\ max(abs(\mathbf{A}_{\mathrm{w}}))\}\end{aligned} \tag{5.24}$$

$$\begin{aligned}\text{Maximum base shear force} = max\{&max(abs(\mathbf{V}_1)),\ max(abs(\mathbf{V}_2)),\ \ldots \\ &\ldots,\ max(abs(\mathbf{V}_{\mathrm{w}}))\}\end{aligned} \tag{5.25}$$

where $\mathbf{X}_j$, $\boldsymbol{\delta}_j$, $\mathbf{A}_j$ and $\mathbf{V}_j$ are the time-histories of story displacement, interstory drift, story absolute acceleration and base shear force of the building under j-th earthquake, respectively, w is the total number of the earthquakes considered, and $abs(\cdot)$ is the absolute value function. Noting that for a multi-story building, the response histories of $\mathbf{X}_j$, $\boldsymbol{\delta}_j$, $\mathbf{A}_j$ are the histories of all the floors, rather than the histories of a certain story. For instance, the story displacement time-history of a n-

story building under j-th earthquake is $\mathbf{X}_j = [\mathbf{x}_{1,j}\ \mathbf{x}_{2,j}\ \cdots\ \mathbf{x}_{n,j}]$, where $\mathbf{x}_{i,j}$ denotes the displacement-history of i-th floor.

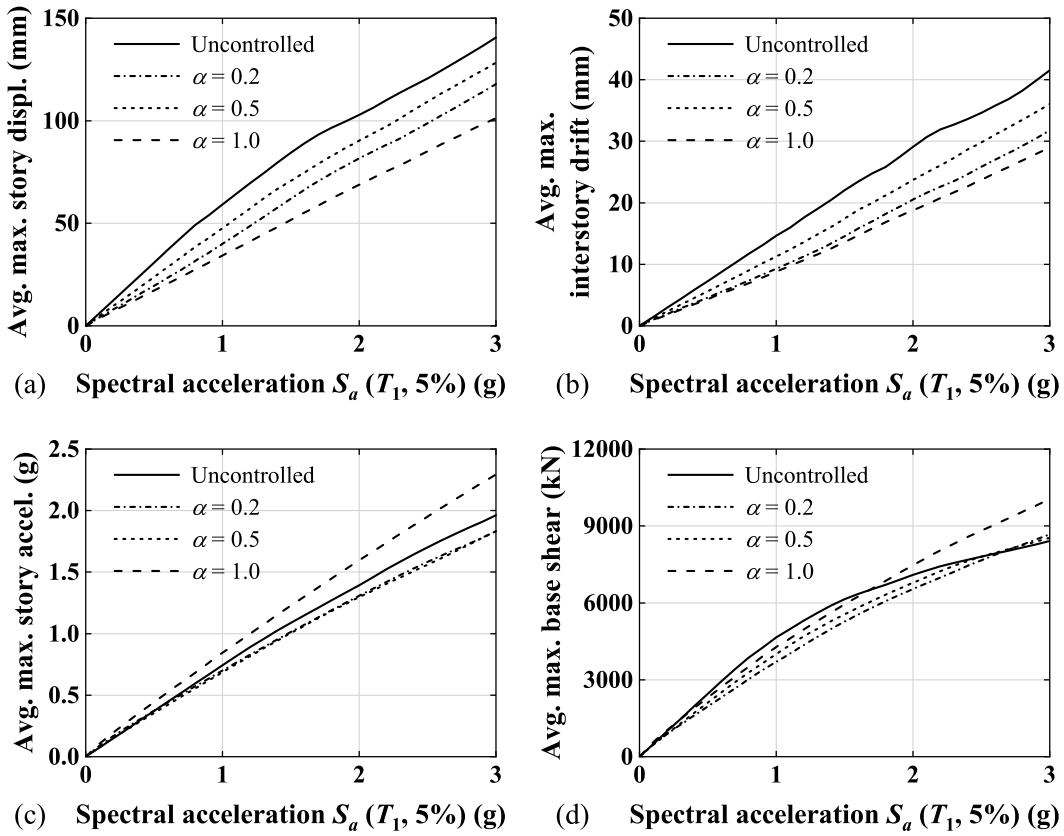

Figure 5.23: IDA curves of average of maximum (a) story displacement (b) interstory drift (c) story acceleration and (d) base shear force for uncontrolled structure and controlled by the optimal damper-brace systems under selected earthquakes ($\nu = 0.5$).

Figure 5.23 shows the IDA curves corresponding to the average maximum displacement, interstory drift, absolute acceleration and bases shear force for the uncontrolled structure and the structure controlled by the optimal viscous dampers for maximizing the interstory drift response reduction under a white-noise ground acceleration time-history. The optimal damping coefficients considered in this example are summarized in Table 5.6. It can be seen from Figures 5.23(a) and (b) that, despite the various earthquake excitation characteristics, the optimal dampers can effectively alleviate the average maximum story displacement and interstory drift of the building at a wide range of excitation intensity ($S_a(T_1, 5\%)$ from 0 to 3 g), and the performance of an optimal damper-brace system with a larger brace stiffness is generally better than that with a smaller stiffness. For the average maximum story acceleration and base shear force, it can be seen from Figures 5.23(c) and (d) that using a larger brace stiffness ratio may not enhance the seismic performance of the building, especially

Table 5.6: Optimal damping coefficients of the 8-story nonlinear building for different brace stiffness ratios under white-noise excitation ($\text{PGA}_{\ddot{x}_g}$= 0.6 g, $\nu = 0.5$).

Story	Damping coefficient (N·(s/m)$^{0.5}$)	Brace stiffness ratio		
		$\alpha = 0.2$	$\alpha = 0.5$	$\alpha = 1$
8F	$c_{d8,opt}$	744485	1566873	16040115
7F	$c_{d7,opt}$	884610	1551727	1966766
6F	$c_{d6,opt}$	1121201	2052859	13110102
5F	$c_{d5,opt}$	1161348	2328036	9298316
4F	$c_{d4,opt}$	1196200	2706469	7814802
3F	$c_{d3,opt}$	1220828	2745907	4005069
2F	$c_{d2,opt}$	1369470	2190080	3853896
1F	$c_{d1,opt}$	1383215	2480578	6899300
	$\sum_{i=1}^{6} c_{di,opt}$	9081356	17622530	62988367
	$RR_{D,max}$	61.30%	74.52%	81.47%

when α increases from 0.5 to 1. The large accelerations and base shear forces are caused by the large damper force in the viscous dampers; these responses could be alleviated by using an acceleration-based performance index to optimize the damper parameters. It is also worth noting that, all the IDA curves exhibit a linear region when the IM, i.e., $S_a(T_1, 5\%)$, is small. This is caused by the elastic behaviour of the building at small displacements, and the linear elastic region of an IDA curve ends when any structural element reaches the end of its elastic phase (Vamvatsikos and Cornell 2002). In this example, the terminate of the initial linear region of an IDA curve indicates the first yield of at least one story of the building.

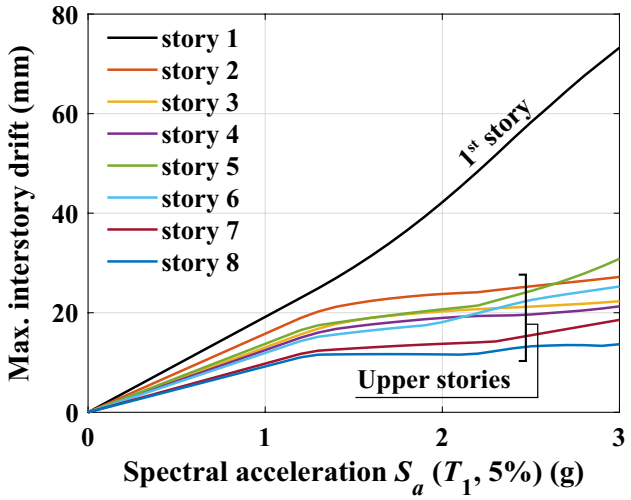

Figure 5.24: IDA curves of peak interstory drifts for each story of the uncontrolled structure under the EQ7 Imperial Valley earthquake.

"Hardening" in the IDA curves can be observed from Figures 5.23(a) and (d), especially from the curves of the uncontrolled structure, which show a gradual reduce in the growth rate of the DMs with increasing spectral acceleration. It seems counter-intuitive that the growth speed of the structural response has not been accelerated after yielding of the structure; however, this hardening phenomenon can be commonly seen in the incremental dynamic analysis, and it is not only due to the excitation intensity, but also because of the pattern and the timing of structural vibration (Vamvatsikos and Cornell 2002). For multi-story structures, strong earthquakes may cause early yielding of one story, which in turn alleviates the responses of other floors, as illustrated in Figure 5.24 that the "softening" of the first story results in "hardening" of upper floors. Even a SDOF structure that yields in an earlier vibration cycle may relieve its response in later cycles and thus exhibit a small DM value under an intense ground motion (Vamvatsikos and Cornell 2002).

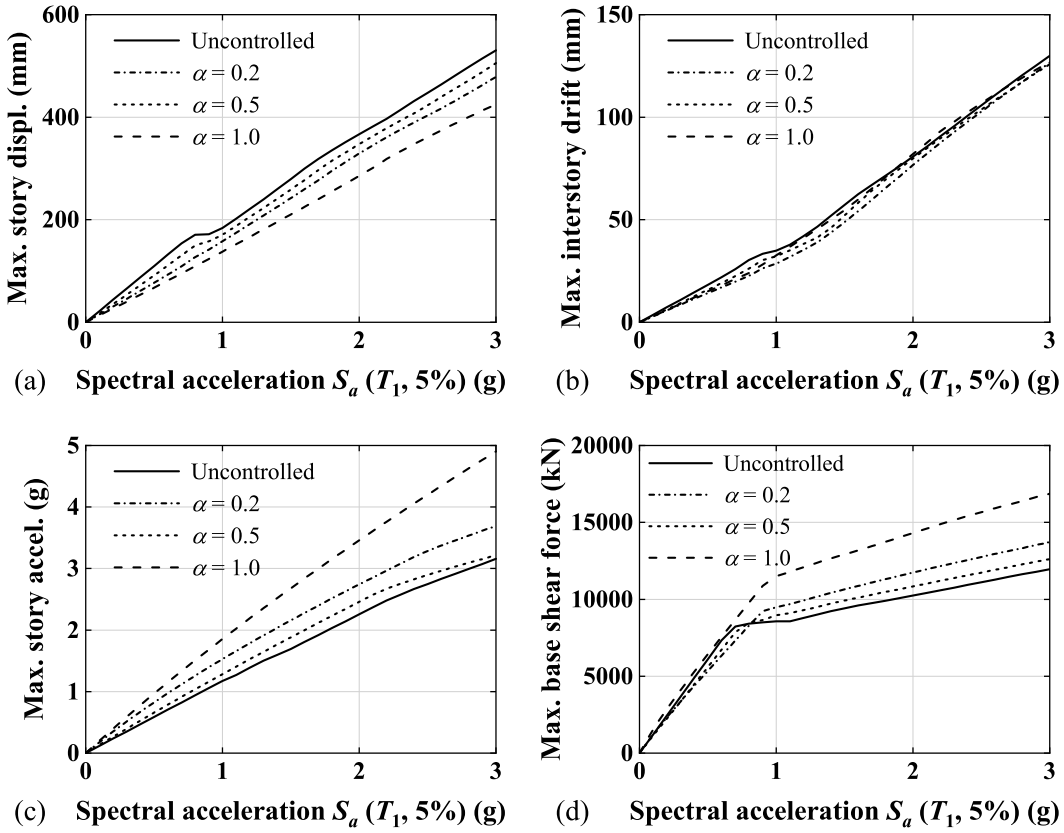

Figure 5.25: IDA curves of maximum (a) story displacement (b) interstory drift (c) story acceleration and (d) base shear force for uncontrolled structure and controlled by the optimal damper-brace systems under selected earthquakes ($\nu = 0.5$).

Figure 5.25 plots the IDA curves of the maximum displacement, interstory drift, absolute acceleration and base shear force for the uncontrolled structure and that

controlled by the optimal dampers under the 20 selected earthquakes. It can be seen from Figures 5.25(a) and (b) that, the optimally designed damper-brace systems can generally mitigate the peak story displacement and interstory drift of the building within the prescribed intensity range of ground motions, although the maximum interstory drift of the controlled structure for α equals one is larger than that of the uncontrolled building when 1.8 g $< S_a <$ 2.6 g. For the uncontrolled structure in Figure 5.25(a), the first slope change of the IDA curve can be found at a spectral acceleration around 0.7 g, indicating the initial yielding of the structure; however, the post-elastic behaviour of the structure seems to be delayed a little bit when equipped with a damper-brace system. For the story acceleration and base shear force, it can be seen from Figures 5.25(c) and (d) that the peak responses of the controlled structure under the 20 earthquakes are generally larger than the uncontrolled building, indicating the optimal dampers designed based on the interstory drift performance index may not reduce the peak acceleration-related responses in extreme earthquake events; the viscous damper shall be designed based on an acceleration-related index (e.g., story acceleration and base shear indices) to alleviate these peak responses. However, it can be seen from Figure 5.25(d) that compared with the uncontrolled building, the first slope change in the IDA curve is postponed by around 0.2 g when using an optimal damper-brace system, indicating the elastic phase of the structure has been extended by the supplemental dampers.

To illustrate the dynamic behaviour of the nonlinear building with the optimal damper-brace systems, Figures 5.26 and 5.27 are plotted, in which Figure 5.26 shows the interstory drift time-histories of the first four floors of the uncontrolled structure and the structure with the optimal dampers for α equals 0.5 under the scaled Northridge earthquake (EQ12) with $S_a(T_1,\ 5\%) = 3$ g, while Figure 5.27 displays the corresponding time-histories in story absolute acceleration. Although the yielding displacement relative to the ground changes during the inelastic deformation of the structure, the initial yielding drifts are marked in Figure 5.26 using dashed lines to highlight the first yielding of a story. From Figure 5.26 it can be seen that, the use of the optimal damper-brace systems generally mitigates the interstory drifts of the building during the earthquake, and the inelastic deformations of the structure caused by excessive interstory drifts are also reduced. For example, the large horizontal drifts in the first 5 seconds result in an approximately 20 mm's permanent deformation in the first story of the uncontrolled building, while the supplemental viscous dampers reduce the final floor deformation to around 4 mm; the second and fourth stories also yield during the ground motion and develop unrecoverable deformations after the earthquake, yet the interstory drifts of these floors are kept within

the elastic range of the story stiffness when equipped with the optimal damper-brace systems. It can be seen from Figure 5.27 that, the optimal dampers can also mitigate story acceleration during the earthquake, especially at the third and fourth floors. Due to the additional damping provided by the dampers, the examined structural responses are quickly suppressed after 5 seconds, which demonstrates the increased resilience of the structure after the installation of the dampers.

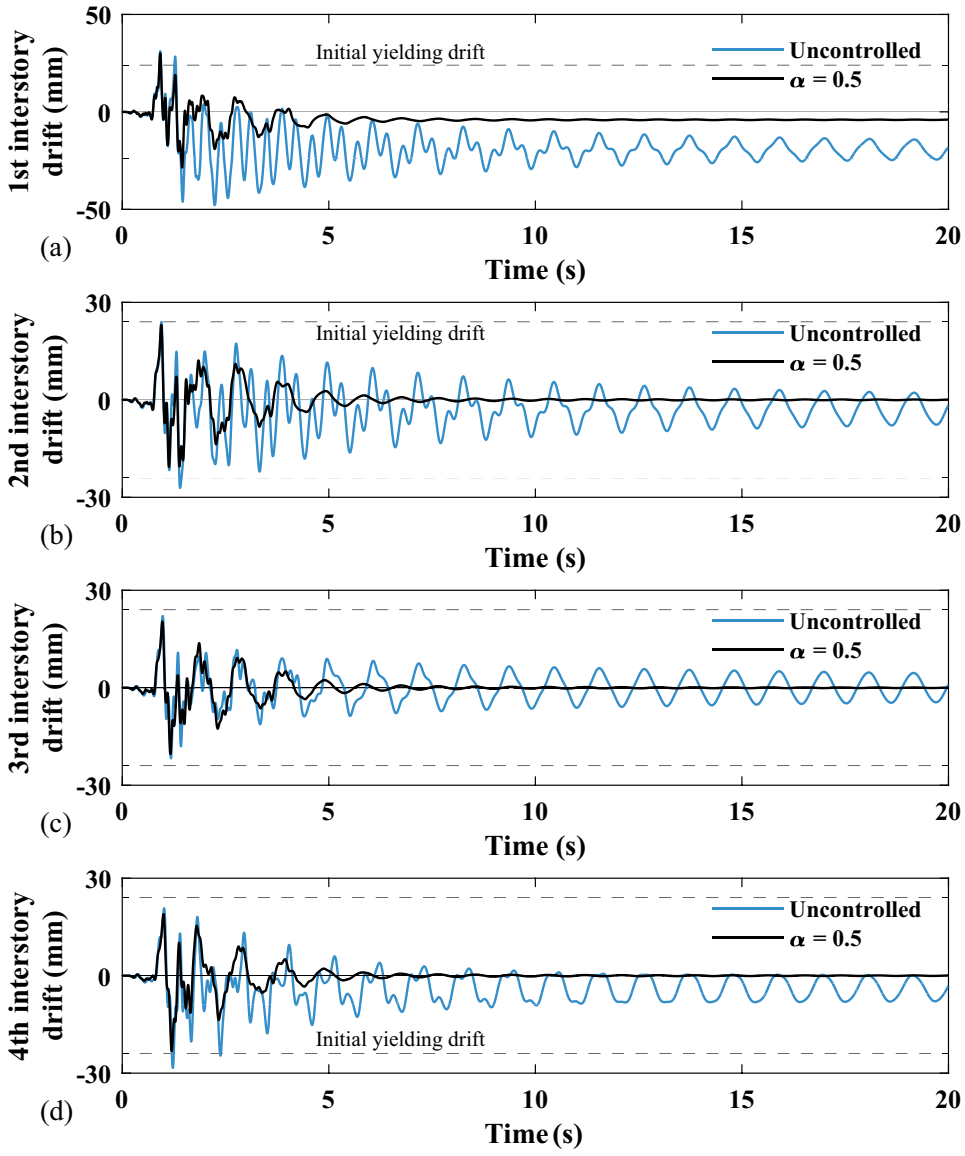

Figure 5.26: Interstory drift time-histories of first four stories of the uncontrolled structure and equipped with optimal dampers for $\alpha = 0.5$ under the scaled EQ12 Northridge earthquake with $S_a(T_1,\ 5\%) = 3$ g ($\nu = 0.5$).

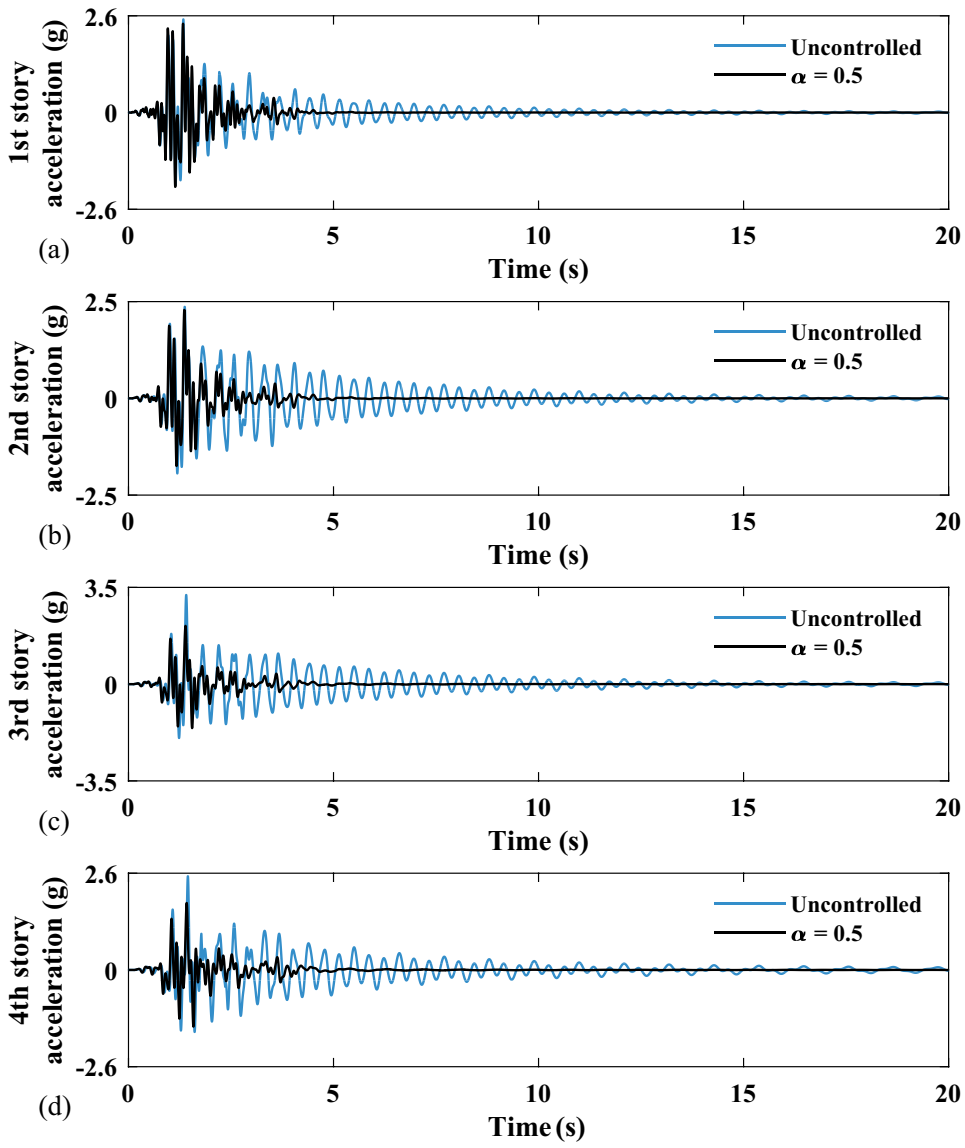

Figure 5.27: Story acceleration time-histories of first four stories of the uncontrolled structure and equipped with optimal dampers for $\alpha = 0.5$ under the scaled EQ12 Northridge earthquake with $S_a(T_1,\ 5\%) = 3$ g ($\nu = 0.5$).

To illustrate the hysteretic behaviour of the nonlinear structure during an earthquake, the hysteretic curves of the shear walls that provide lateral restoring force to the structure at the first four floors under the EQ2 Northridge earthquake are plotted in Figure 5.28. As can be seen from the figure, compared to the uncontrolled structure, the maximum achievable interstory drifts of the building can be reduced by equipping the optimal damper-brace systems, even in the case of pure elastic interstory drift (Figure 5.28(c)). The areas enclosed by the hysteretic loops of the uncontrolled structure are generally larger than those of the building controlled by

the damper-brace systems, which indicates that a significant amount of input seismic energy is dissipated by the supplemental viscous dampers. In general, the nonlinear damper-brace systems designed by the presented optimization approach exhibit good performance in mitigating both the elastic and post-elastic deformations of the structure.

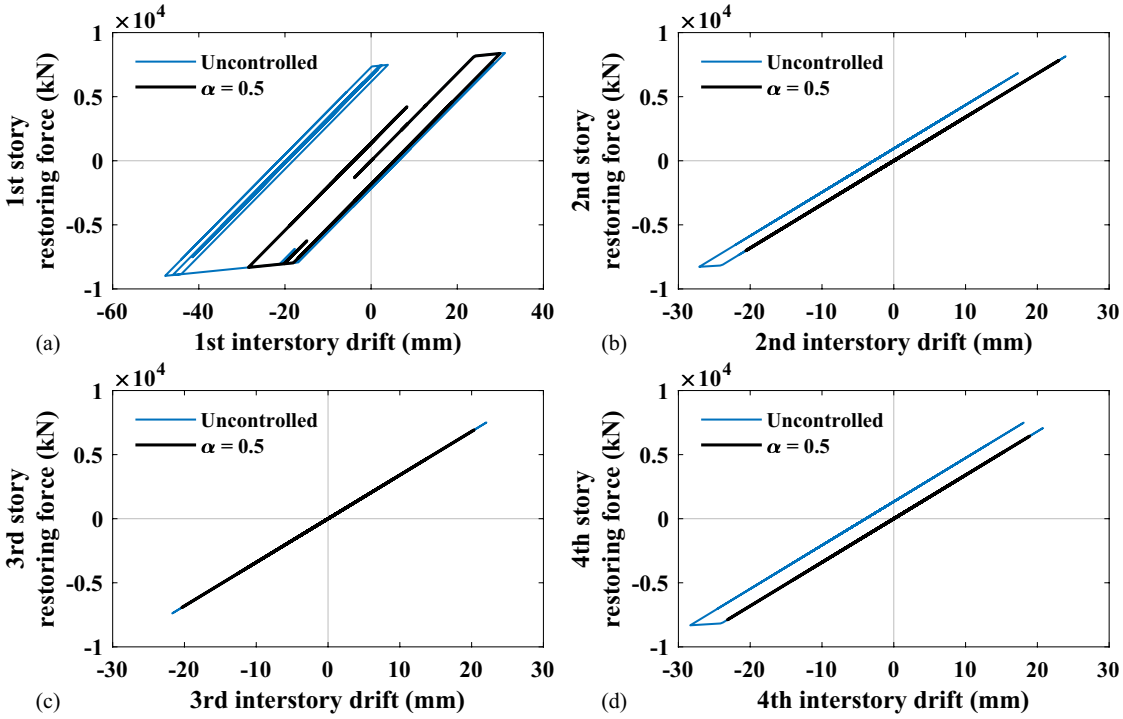

Figure 5.28: Restoring force-story drift relationships of first four stories of the uncontrolled structure and equipped with optimal dampers for $\alpha = 0.5$ under the scaled EQ12 Northridge earthquake with $S_a(T_1,\ 5\%) = 3$ g ($\nu = 0.5$).

Figure 5.29 shows the mean story ductility of the nonlinear building due to an ensemble of the scaled 20 earthquakes with $S_a(T_1,\ 5\%)$ equals 3 g, in which the ductility factor of i-th floor under j-th earthquake is defined as:

$$\text{Ductility factor of } i\text{-th floor under } j\text{-th earthquake} = \frac{\delta_{max(i,j)}}{\delta_y} \tag{5.26}$$

Eq. (5.26) normalizes the maximum absolute interstory drift between $(i-1)$-th and i-th floors due to j-th earthquake, $\delta_{max(i,j)}$, relative to the yielding interstory drift of the building, δ_y. From Figure 5.29 it can be seen that the optimal damper-brace systems can effectively reduce the ductility of the building under the examined earthquakes. It can also be seen from the figure that the story ductility is generally large at lower floors, indicating the lower stories, especially the first and second stories, exhibit more inelastic behaviours during the earthquakes, and thus dissipate more seismic energy

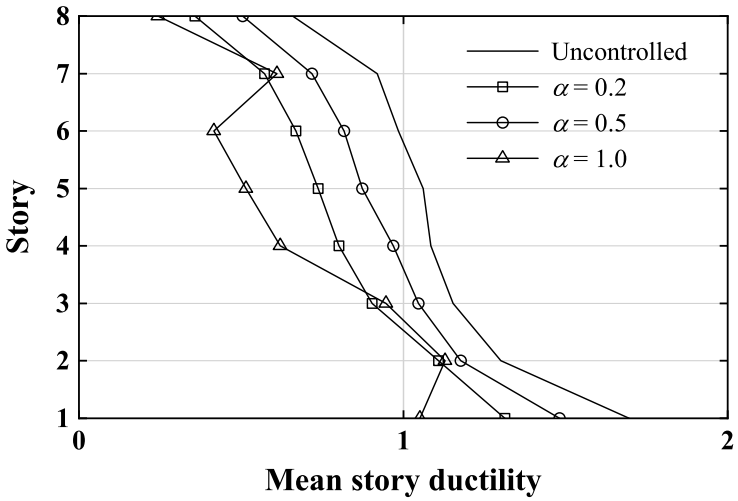

Figure 5.29: Mean story ductility of the 8-story building under the scaled 20 earthquakes with $S_a(T_1,\ 5\%) = 3$ g ($\nu = 0.5$).

and in turn reduce the post-elastic deformations of upper floors. In general, the use of optimal dampers with a larger brace stiffness ratio α result in smaller story ductility, although the ductility of the building with the optimal dampers for α equals 1 is slightly larger than that of the structure with the optimal dampers for α equals 0.5 at 2nd, 3rd and 7th floors.

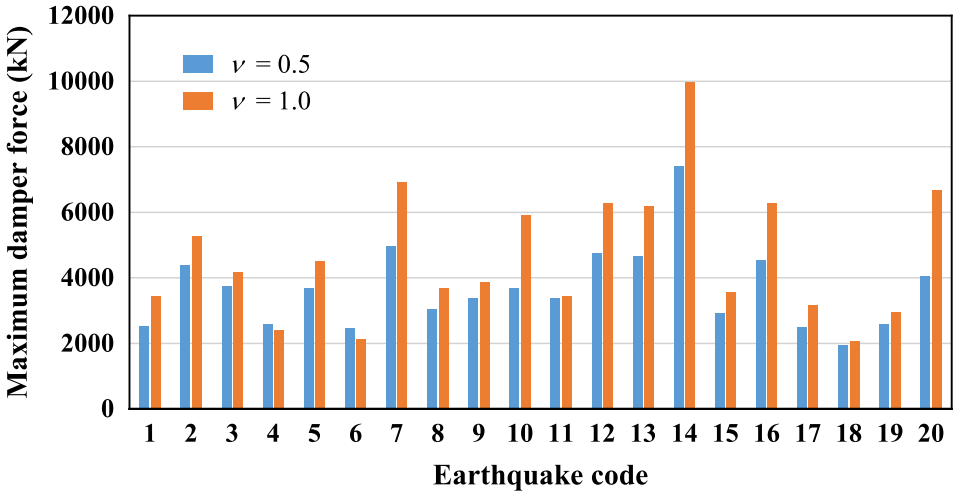

Figure 5.30: Maximum damper forces of the optimal dampers in the 8-story building under different scaled earthquakes with $S_a(T_1,\ 5\%) = 3$ g ($\alpha = 1$).

The observations made in Section 5.1.1 suggested that the use of viscous dampers with a smaller velocity exponent can effectively reduce the peak damper force while maintaining a similar level of structural response reduction. To evaluate the peak force in the dampers with different velocity exponents during some intense ground

motions, Figure 5.30 is plotted, which shows the maximum damper forces of optimal viscous dampers in the 8-story building under the selected earthquakes that are scaled to have a $S_a(T_1,\ 5\%)$ of 3 g. Two sets of optimal dampers for a given brace stiffness ratio (α equals 1) are evaluated, which have different velocity exponents, i.e., ν equals 0.5 and 1; both the optimal damper sets can achieve a maximum response reduction $RR_{D,max}$ of around 82%. From Figure 5.30 it can be seen that, different earthquakes result in different peak damper forces, and the maximum forces of the dampers with ν equals 0.5 are generally smaller than those of the dampers with ν equals 1, although the linear dampers have slightly smaller peak damper forces in earthquakes 4 and 6. Therefore, compared with using linear dampers, the use of nonlinear ones with a smaller velocity exponent can alleviate the peak damper forces induced by some strong earthquakes, which can also lower the manufacturing cost of the dampers and reduce the structural damages related to large damper forces.

5.3 Conclusions

In this chapter, the potential for satisfactory seismic performance of shear-type buildings as protected by nonlinear viscous dampers and braces was investigated. The viscous dampers were assumed to be installed on top of Chevron-type braces that are responding elastically. Based on the numerical time-stepping method developed in Chapter 4, the seismic performance of a building before and after the damper installation was evaluated. Results from single- and two-story example structures indicated that an infinite combination of parameters was possible for the damper-brace system given a performance objective or specific response reduction; however, a minimum brace stiffness together with a corresponding set of damping coefficients can be optimally determined to achieve the target performance. Results also indicated that nonlinear viscous dampers with velocity exponent less than unity generally require smaller values of the damping compared to their linear viscous damper counterparts, and importantly, the velocity exponent of the viscous dampers has no significant effect on the maximum response reduction when the dampers are optimally designed. Results from a six-story example building confirmed the observations made in single- and two-story buildings, which also suggested that a large brace stiffness is not necessary to achieve an acceptable level of response reduction. For a given brace stiffness, there existed a maximum response reduction for performance indices involving interstory drift, base shear force, floor displacement, and floor acceleration. If higher performance is desired of displacement-based performance indices, the brace stiffness may be increased accordingly, followed by appropriate optimization of the damper parameters. Incremental dynamic analysis was conducted to evaluate the capacity

and robustness of the damper-brace systems using a nonlinear eight-story benchmark building under multiple earthquakes. Results indicated that the optimally designed dampers were effectively robust to the uncertainty of ground motions.

Chapter 6 Seismic vibration control of atrium buildings with a truss-damper system

In this chapter, a passive control approach that utilizes a core structure inside an atrium building in combination with a truss-damper system to achieve a novel path for seismic energy dissipation is presented. The analytic models of a truss-FVD system and a truss-IMD system are introduced, and their corresponding numerical approaches for conducting time-history analysis are presented. Parametric studies are performed to assess and compare the vibration control effectiveness of the truss-damper configurations, and the seismic capacity and robustness of the optimally designed control systems are evaluated under multiple earthquake records.

6.1 A truss-FVD system for vibration control of atrium buildings

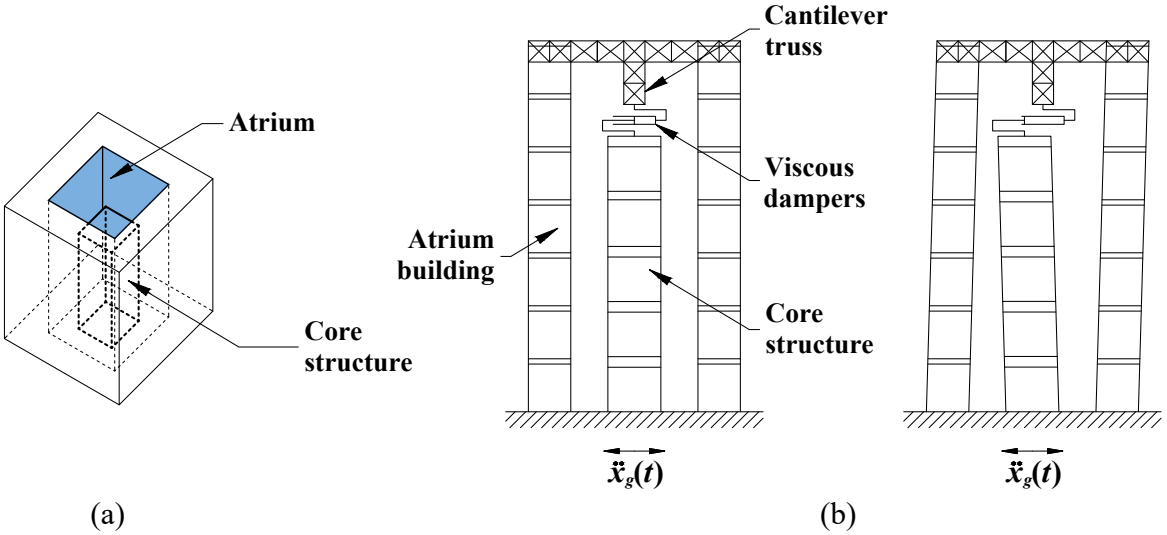

Figure 6.1: (a) A centralized atrium building with a core structure (b) proposed truss-FVD system.

A truss-FVD system that incorporates a cantilever truss and fluid viscous dampers into an atrium building and a core structure to mitigate their seismic responses is first introduced in this section. The investigated atrium has a centralized type, as illustrated in Figure 6.1(a). The core structure, which could be an existing construction, as shown in Figure 6.2, or a purpose-built structure for the global control system, is located inside the centralized atrium. A truss structure extending from the building roof to the top of the core structure is built first. Unlike conventionally been done in buildings where viscous dampers are placed between stories, it is proposed to install

the dampers in between the bottom of the overhang truss and the top of the core structure, as shown in Figure 6.1(b). Such a 'truss-damper' configuration utilizes the unsynchronized dynamic motions of the two structures to improve the overall efficiency of the dampers, hence the proposed truss-damper setup is deemed suitable for the atrium building. In the next two sections, a numerical time-history method will be developed to compute the seismic responses of the atrium building and the internal core structure. Based on the numerical approach, the effectiveness of the truss-FVD system will be assessed through an evaluation of the response reduction in interstory drift under seismic excitation.

(a) Suria KLCC at Petronas towers, Kuala Lumpur, Malaysia.

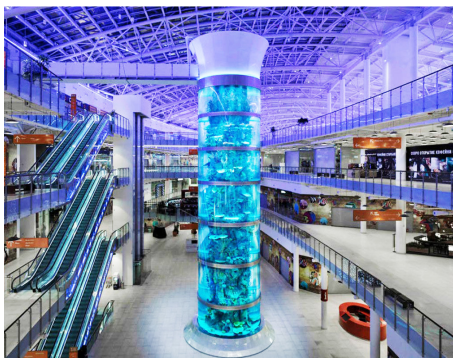

(b) Avia Park mall, Moscow, Russia.

Figure 6.2: Internal core structure examples (Kenny 2014, Praime construction 2015).

6.1.1 Analytic model of a simple atrium building and a core structure connected by a truss-FVD system

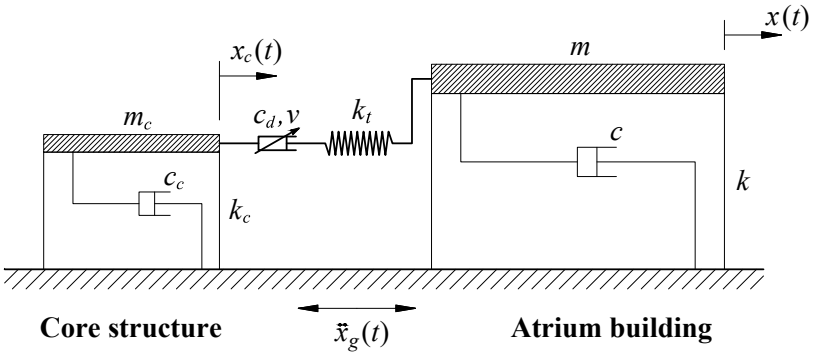

Figure 6.3: Analytic model of an atrium building and its core structure connected by a truss-FVD system.

To assess the seismic performance of the proposed truss-FVD system, a simple atrium building and a core structure connected by a truss and a viscous damper in

series is first adopted as the analytic model, as shown in Figure 6.3. In Figure 6.3, m, c, k and $x(t)$ are the mass, damping coefficient, stiffness and horizontal displacement of the atrium building, respectively, while m_c, c_c, k_c and $x_c(t)$ are respectively the mass, damping coefficient, stiffness and horizontal displacement of the core structure; k_t denotes the stiffness of the cantilever truss in the horizontal direction; c_d and ν are the damping coefficient and velocity exponent of the FVD, respectively. The equation of motion of the atrium building and the core structure under an input ground acceleration $\ddot{x}_g(t)$ can be expressed as a second-order differential equation:

$$\mathbf{M_s}\ddot{\mathbf{x}}_\mathbf{s}(t) + \mathbf{C_s}\dot{\mathbf{x}}_\mathbf{s}(t) + \mathbf{K_s}\mathbf{x_s}(t) + \mathbf{F_{d,s}}(t) = -\mathbf{M_s}\mathbf{1}\ddot{x}_g(t) \tag{6.1}$$

where

$\mathbf{M_s} = \begin{bmatrix} m & 0 \\ 0 & m_c \end{bmatrix}$ is the mass matrix of the structural system;

$\mathbf{C_s} = \begin{bmatrix} c & 0 \\ 0 & c_c \end{bmatrix}$ is the damping matrix of the system;

$\mathbf{K_s} = \begin{bmatrix} k & 0 \\ 0 & k_c \end{bmatrix}$ is the stiffness matrix;

$\mathbf{x_s}(t) = \begin{bmatrix} x(t) \\ x_c(t) \end{bmatrix}$ is the story displacement vector relative to the ground;

$\mathbf{F_{d,s}}(t) = \begin{bmatrix} f_d(t) \\ -f_d(t) \end{bmatrix}$ is the damper force vector, $f_d(t)$ is the force in the IMD;

$\mathbf{1} = \begin{bmatrix} 1 \\ 1 \end{bmatrix}$ is a unit vector.

Eq. (6.1) can be numerically solved using different time-history approaches. This study adopts the state-space technique outlined in Section 3.1.1 to compute the structural responses under an input ground acceleration. The state-space expression of Eq. (6.1) is:

$$\dot{\mathbf{z}}_\mathbf{s}(t) = \mathbf{A}\mathbf{z_s}(t) + \mathbf{B}\mathbf{F_{d,s}}(t) + \mathbf{E}\ddot{x}_g(t) \tag{6.2}$$

where

$\mathbf{z_s}(t) = \begin{bmatrix} \mathbf{x_s}(t) \\ \dot{\mathbf{x}}_\mathbf{s}(t) \end{bmatrix}$ is the response vector of the structural system;

$\mathbf{A} = \begin{bmatrix} \mathbf{0} & \mathbf{I} \\ -\mathbf{M_s}^{-1}\mathbf{K_s} & -\mathbf{M_s}^{-1}\mathbf{C_s} \end{bmatrix}$ is the system matrix;

$\mathbf{B} = \begin{bmatrix} \mathbf{0} \\ -\mathbf{M_s}^{-1} \end{bmatrix}$ is the distribution matrix of the damper force;

$\mathbf{E} = \begin{bmatrix} \mathbf{0} \\ -\mathbf{1} \end{bmatrix}$ is the distribution vector of the ground acceleration.

The discrete time-state expression of Eq. (6.2) can be formulated based on the assumptions that the damper force is a constant within two consecutive sampling instants, while the ground acceleration changes linearly:

$$\mathbf{z_s}[\mathrm{k}+1] = \mathbf{A_0}\mathbf{z_s}[\mathrm{k}] + \mathbf{B_0}\mathbf{F_{d,s}}[\mathrm{k}] + \mathbf{E_0}\ddot{x}_g[\mathrm{k}] + \mathbf{E_1}\ddot{x}_g[\mathrm{k}+1] \tag{6.3}$$

where

$\mathbf{A_0} = e^{\mathbf{A}\Delta t}$ is the discrete system matrix;

$\mathbf{B_0} = \mathbf{A}^{-1}(\mathbf{A_0} - \mathbf{I})\mathbf{B}$ is the instant discrete damper force distribution matrix;

$\mathbf{E_0} = [\mathbf{A}^{-1}\mathbf{A_0} + \frac{1}{\Delta t}\mathbf{A}^{-2}(\mathbf{I} - \mathbf{A_0})]\mathbf{E}$ is the instant discrete ground acceleration distribution vector at step [k];

$\mathbf{E_1} = [-\mathbf{A}^{-1} + \frac{1}{\Delta t}\mathbf{A}^{-2}(\mathbf{A_0} - \mathbf{I})]\mathbf{E}$ is the instant discrete ground acceleration distribution vector at step [k + 1].

The structural response-history can be calculated once the damper force vector, $\mathbf{F_{d,s}}(t)$, is computed at each time step. Notably, for the simple structural system shown in Figure 6.3, the relative displacement of the two structures is equal to the total deformation of the truss-damper system, $\Delta(t)$. Therefore, the following kinematic relationship must be satisfied:

$$\Delta(t) = x(t) - x_c(t) = \Delta_d(t) + \Delta_t(t) \tag{6.4}$$

where $\Delta(t)$ is the relative displacement between the two ends of the model, i.e., the total deformation of the truss-IMD system, and $\Delta_d(t)$ and $\Delta_t(t)$ are the deformations of the damper and the cantilever truss, respectively.

6.1.1.1 Force in the truss-FVD system

The damper force vector at step k, $\mathbf{F_{d,s}}[\mathrm{k}]$, can be formed once the damper force $f_d[\mathrm{k}]$ is obtained. In this chapter, the damper force is solved numerically using the fourth-order Runge-Kutta method. Since the truss and FVD are connected in series, as shown in Figure 6.3, the force induced by the damper is equal to the force in the truss. The damper force can thus be expressed as:

$$f_d(t) = k_t\Delta_t(t) = c_d|\dot{\Delta}_d(t)|^{\nu} sgn(\dot{\Delta}_d(t)) \tag{6.5}$$

where $sgn(\cdot)$ denotes the signum function. To calculate the damper force, Eq. (6.5) is first rewritten as:

$$|\dot{\Delta}_d(t)|sgn(\dot{\Delta}_d(t)) = (\frac{k_t}{c_d})^{\frac{1}{\nu}}|\Delta_t(t)|^{\frac{1}{\nu}}sgn(\Delta_t(t)) \tag{6.6}$$

which can be further expressed as:

$$\dot{\Delta}_d(t) = (\frac{k_t}{c_d})^{\frac{1}{\nu}}|\Delta_t(t)|^{\frac{1}{\nu}}sgn(\Delta_t(t)) \tag{6.7}$$

The substitution of the first derivative of Eq. (6.4) into Eq. (6.7) gives the following first-order nonlinear differential equation for the truss deformation:

$$\dot{\Delta}_t(t) = \dot{\Delta}(t) - (\frac{k_t}{c_d})^{\frac{1}{v}}|\Delta_t(t)|^{\frac{1}{v}}sgn(\Delta_t(t)) \tag{6.8}$$

Eq. (6.8) can be discretized and solved numerically following the fourth-order Runge-Kutta method. The discrete time-state function of truss deformation for two consecutive sampling steps [k] and [k + 1] can thus be expressed as:

$$\Delta_t[\mathrm{k}+1] = \Delta_t[\mathrm{k}] + \frac{1}{6}(K_{t1} + 2K_{t2} + 2K_{t3} + K_{t4})\Delta t \tag{6.9}$$

where

$$\begin{cases} K_{t1} = \dot{\Delta}[\mathrm{k}] - (\frac{k_t}{c_d})^{\frac{1}{\nu}}|\Delta_t[\mathrm{k}]|^{\frac{1}{\nu}}sgn(\Delta_t[\mathrm{k}]) \\ K_{t2} = \frac{1}{2}(\dot{\Delta}[\mathrm{k}] + \dot{\Delta}[\mathrm{k}+1]) - (\frac{k_t}{c_d})^{\frac{1}{\nu}}|\Delta_t[\mathrm{k}] + \frac{\Delta t}{2}K_{t1}|^{\frac{1}{\nu}}sgn(\Delta_t[\mathrm{k}] + \frac{\Delta t}{2}K_{t1}) \\ K_{t3} = \frac{1}{2}(\dot{\Delta}[\mathrm{k}] + \dot{\Delta}[\mathrm{k}+1]) - (\frac{k_t}{c_d})^{\frac{1}{\nu}}|\Delta_t[\mathrm{k}] + \frac{\Delta t}{2}K_{t2}|^{\frac{1}{\nu}}sgn(\Delta_t[\mathrm{k}] + \frac{\Delta t}{2}K_{t2}) \\ K_{t4} = \dot{\Delta}[\mathrm{k}+1] - (\frac{k_t}{c_d})^{\frac{1}{\nu}}|\Delta_t[\mathrm{k}] + \Delta t K_{t3}|^{\frac{1}{\nu}}sgn(\Delta_t[\mathrm{k}] + \Delta t K_{t3}) \end{cases} \tag{6.10}$$

Note that Eq. (6.10) assumes the deformation of the truss-FVD system, $\Delta(t)$, changes linearly within each computational time interval. By substituting the truss deformation $\Delta_t[\mathrm{k}+1]$ in Eq. (6.9) into Eq. (6.5), the force in the truss-damper system at sampling step [k + 1] can be obtained:

$$f_d[\mathrm{k}+1] = k_t\Delta_t[\mathrm{k}+1] = k_t\left[\Delta_t[\mathrm{k}] + \frac{1}{6}(K_{t1} + 2K_{t2} + 2K_{t3} + K_{t4})\Delta t\right] \tag{6.11}$$

6.1.2 Performance evaluation of the truss-FVD system

Parametric studies using the analytic model in Figure 6.3 will now be conducted to assess the performance of the truss-FVD system in seismic vibration control of an atrium building, and the effects of truss stiffness and damper nonlinearity on the dynamic performance of the building will be primarily investigated. The following parameters are introduced to facilitate later performance evaluation process:

$$\alpha \equiv \frac{k_t}{k},\ \beta \equiv \frac{c_d}{2m\omega_1},\ \gamma \equiv \frac{k_c}{k},\ \mu \equiv \frac{m_c}{m} \tag{6.12}$$

where α is the truss stiffness ratio, β is the damping ratio of the damper with a unit of $(\mathrm{s/m})^{\nu-1}$, γ is the core structure stiffness ratio, μ is the mass ratio of the core structure, and ω_1 is the natural circular frequency of the atrium building.

To evaluate the effectiveness of a truss-damper system, an interstory drift performance index, defined as the average of root-mean-square value of the interstory drift time-histories of a n-story atrium building, is first adopted:

$$PI_D = \frac{1}{n}\sum_{i=1}^{n} rms\left(\delta_i\right) \quad \text{for a } n\text{-story building} \tag{6.13}$$

where δ_i is the interstory drift time-history of the i-th story of the atrium building. A response reduction ratio, RR_D, is then adopted with the following expression to evaluate the performance improvement:

$$RR_D(\%) = \left(1 - \frac{PI_D}{PI_{D,org}}\right) \times 100 \tag{6.14}$$

where $PI_{D,org}$ is the original performance index of the atrium building without the truss and damper. A larger RR_D represents a more effective design of the system. In addition to the atrium building, to assess the seismic performance of the core structure, a performance index, $PI_{D,c}$, and a response reduction, $RR_{D,c}$, are similarly defined.

The simple system in Figure 6.3 is investigated with the following properties: the natural period, structural mass and structural stiffness of the atrium building are 1 second, 2533 kg and 100 kN/m, respectively. The stiffness ratio γ and mass ratio μ of the core structure are set to 0.1 and 5%, respectively. Selection of the values is based on the assumption that both the mass and stiffness of the core structure are much smaller than those of the atrium building. The inherent damping ratio of both structures are assumed to be 2%, and a zero-mean white-noise acceleration-history is adopted as the input ground excitation.

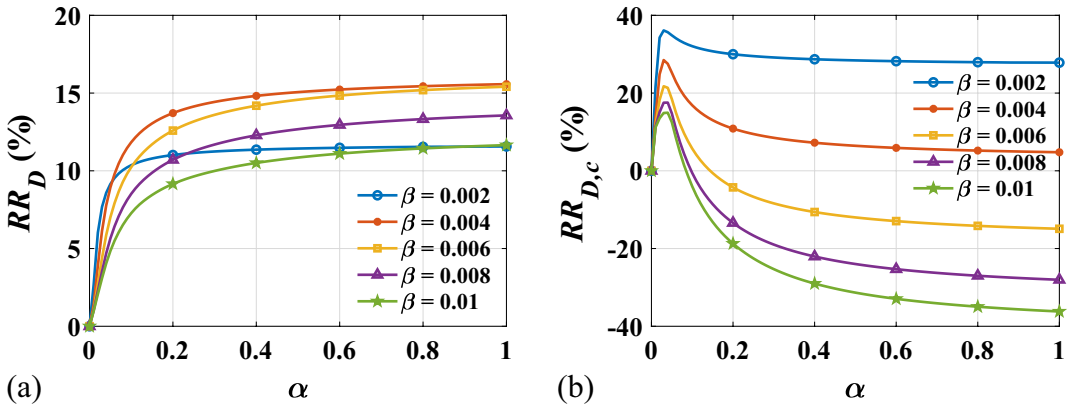

Figure 6.4: Variations of response reduction in story drift with truss stiffness ratio for (a) the atrium building and (b) the core structure under white-noise ($\nu = 0.4$).

The effectiveness of the truss-FVD system on enhancing seismic performance of the atrium building is first investigated. The variations of building response reduction in story drift with truss stiffness ratio for different damper parameters are shown in Figure 6.4. It can be seen from Figure 6.4(a) that, for the preset velocity exponent ($\nu = 0.4$), the response reduction of the atrium building increases rapidly with increasing truss stiffness ratio for small truss stiffness ratio, say $\alpha < 0.2$; when the truss stiffness ratio becomes larger, the response reduction still increases but with a reduced growth rate, indicating that the change in truss stiffness has a small influence on the building performance when stiffness ratio is large, say $\alpha > 0.2$. It can also be seen from Figure 6.4(a) that, for a given truss stiffness ratio, the response reduction may not increase with increasing damping ratio of the viscous damper. For instance, when α equals 0.4, the response reduction increases as β grows from 0.002 to 0.004; as the damping ratio becomes larger, RR_D starts to decrease, indicating there may exist an optimal damping ratio for the set truss stiffness to maximize the structural performance. The story drift response reduction of the core structure, $RR_{D,c}$, versus truss stiffness ratio is plotted in Figure 6.4(b). It can be observed from Figure 6.4(b) that, the response reduction of the core structure is sensitive to the truss stiffness when stiffness ratio is low, say $\alpha < 0.1$. For the examined damping ratios, a sharp increase in the response reduction can be found when truss stiffness ratio is smaller than 0.04, and a peak response reduction can be observed for a given damping ratio. After the peak, the response reduction decreases with increasing truss stiffness ratio.

The variation of story drift response reduction of the atrium building with truss stiffness ratio and damping ratio of the damper for velocity exponent equals 0.4 is shown in Figure 6.5(a). From Figure 6.5(a) it can be seen that, the use of larger truss stiffness and damping coefficient may not improve the performance of the atrium

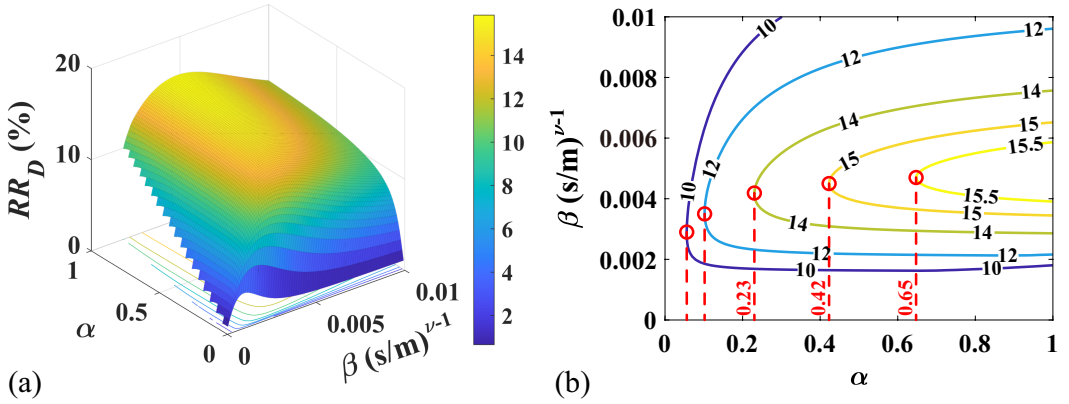

Figure 6.5: (a) Mesh and (b) contour plots of response reduction versus truss stiffness ratio and damping ratio of truss-FVD system for the atrium building under white-noise excitation ($\nu = 0.4$).

building; however, using a larger truss stiffness can generally increase the response reduction when the damper parameters are preset, which agrees with the observation from Figure 6.4(a). A contour plot is shown in Figure 6.5(b). It can be seen from Figure 6.5(b) that, there exists an infinite combination of design parameters to achieve a certain response reduction; however, a minimum truss stiffness ratio will be required, as indicated by the red dashed lines. Therefore, if the stiffness of the truss is predefined, there must exist a maximum achievable response reduction in story drift of the atrium building and a corresponding optimal damping coefficient.

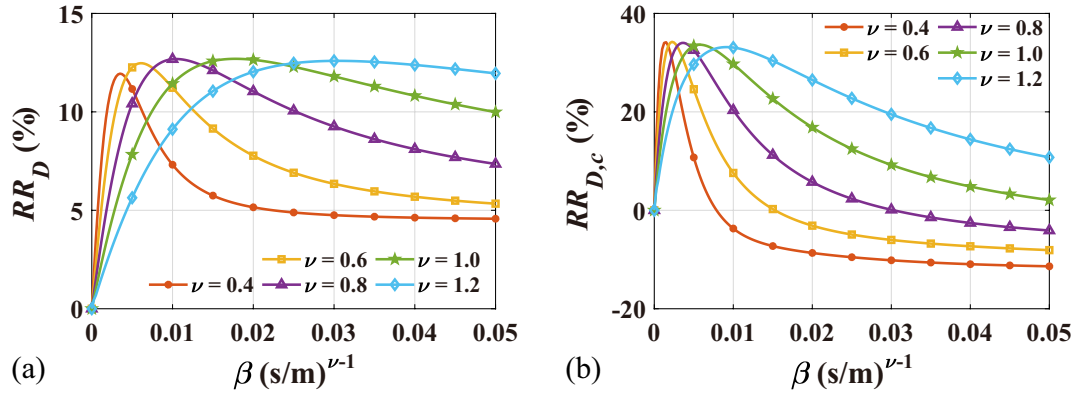

Figure 6.6: Variations of response reductions in story drift with damping ratio for (a) the atrium building (b) the core structure under white-noise excitation ($\alpha = 0.1$).

The effects of damper parameters, i.e., damping ratio and velocity exponent, on the seismic performance of the atrium building are also investigated. Figures 6.6(a) and (b) show response reductions of the atrium building and the core structure against damping ratio of the damper, respectively, when truss stiffness ratio equals 0.1. It can

be seen from Figure 6.6(a) that, for a given set of truss stiffness and velocity exponent, the response reduction of the building first increases with increasing damping ratio and reaches a peak value, and then decreases. It can also be seen that, for the investigated structural system under white-noise excitation, using a larger velocity exponent requires a larger "optimal" damping ratio to achieve a maximum response reduction of the building. However, the magnitudes of $RR_{D,max}$ are fairly close for different velocity exponents. Figure 6.6(b) shows the variations of response reduction of the core structure with damping ratio for different velocity exponents. The curves in Figure 6.6(b) show similar trends to those in Figure 6.6(a). When the damping ratio becomes larger, the response reduction reduces to negative, indicating magnified core structure's response.

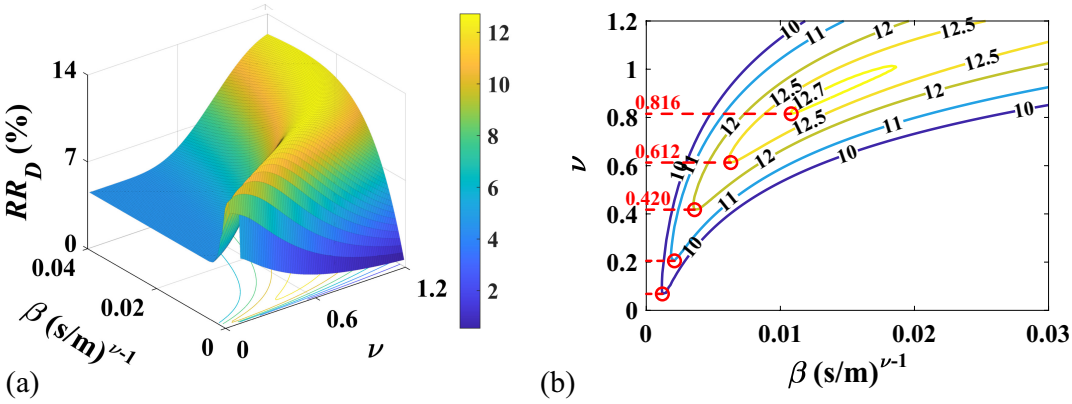

Figure 6.7: (a) Mesh and (b) contour plots of response reduction versus damping ratio and velocity exponent of viscous damper for the atrium building under white-noise excitation ($\alpha = 0.1$).

The variation of the response reduction of the atrium building with damping ratio and velocity exponent of the damper for truss stiffness ratio equals 0.1 is shown in Figure 6.7. It can be seen from Figure 6.7(a) that, using a large damping coefficient may not result in a good performance of the atrium building; a greater value of damping ratio will be required when using a larger velocity exponent to increase the response reduction, which agrees with the observation from Figures 6.6(a) and (c). In general, to achieve a certain response reduction, there exists an infinite combination of damping coefficient and velocity exponent. Figure 6.7(b) shows the contour plot of response reduction of the atrium building for the examined truss stiffness. From Figure 6.7(b) it can be seen that, there seems to exist a global maximum response reduction at velocity exponent about 0.9. When ν is less than 0.9, to achieve a given response reduction, there exists a minimum velocity exponent, as indicated by the dashed lines, and a corresponding minimum required damping ratio.

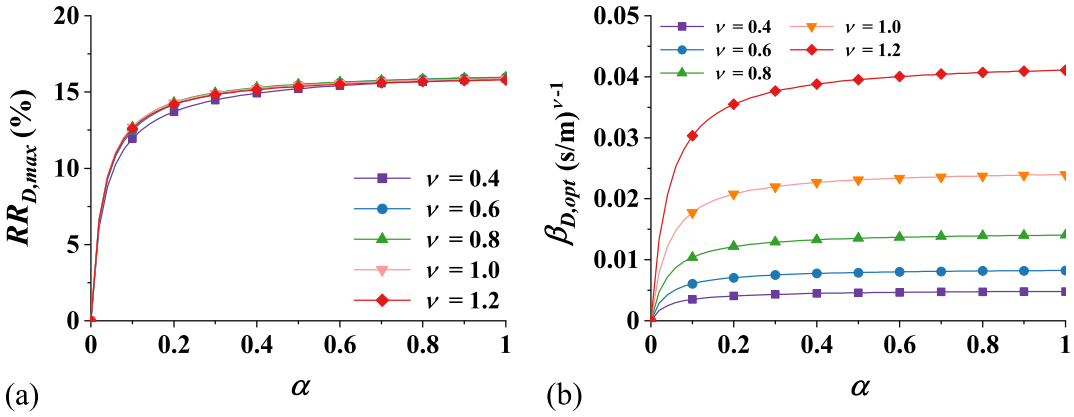

Figure 6.8: (a) Maximum response reduction in story drift and (b) corresponding optimal damping ratio versus truss stiffness ratio for the atrium building under white-noise excitation.

Since the results from Figures 6.5 and 6.6 suggest that for a given truss stiffness, there exist a maximum response reduction of the atrium building and a corresponding optimal damping coefficient, it may be worthwhile to investigate the effect of truss stiffness on the maximum response reduction. Figure 6.8 shows the maximum response reduction $RR_{D,max}$, and the corresponding optimal damping ratios $\beta_{D,opt}$, for truss stiffness ratio ranging from 0 to 1. It can be seen from Figure 6.8(a) that, the $RR_{D,max}$ increases rapidly with truss stiffness in a low stiffness region, say $\alpha < 0.2$, and shows a diminishing return when α becomes larger. It can also be observed from Figure 6.8(a) that for a given stiffness ratio, the maximum response reductions are very close, indicating that the examined velocity exponents have no significant influence on the maximum response reduction of the building if the dampers are optimally designed. Figure 6.8(b) shows the corresponding optimal damping ratios required to achieve the maximum response reductions for different velocity exponents. It can be seen from the figure that, for the same truss stiffness, the use of a smaller velocity exponent reduces the required damping to achieve a maximum response reduction, which agrees with the observation from Figure 6.6(a).

Although the core structure only serves as a supporting element of the proposed truss-damper system during an earthquake, it is nonetheless important to evaluate its dynamic response when equipped with the optimally designed truss-damper systems. Figure 6.9 shows the story drift response reduction of the core structure with the optimal dampers for different truss stiffness ratios. From the figure it can be seen that, as the truss stiffness becomes larger, the response reduction of the core structure $RR_{D,c}$ reduces with a decreasing rate. When the stiffness ratio is larger than around 0.6, there is no performance improvement on the core structure, noting that the

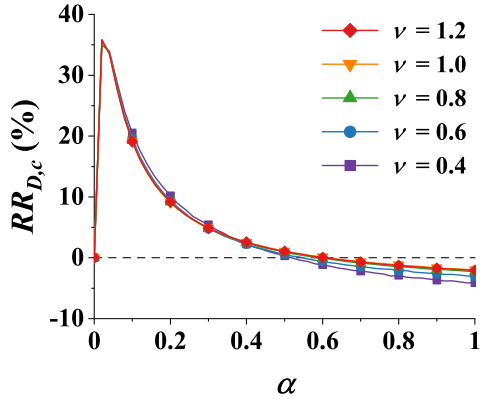

Figure 6.9: Story drift response reductions of the core structure with optimal damper parameters for different truss stiffness.

optimal performance of the atrium building will not be significantly enhanced when the truss stiffness ratio is larger than 0.2.

6.2 A novel truss-IMD system for vibration control of atrium buildings

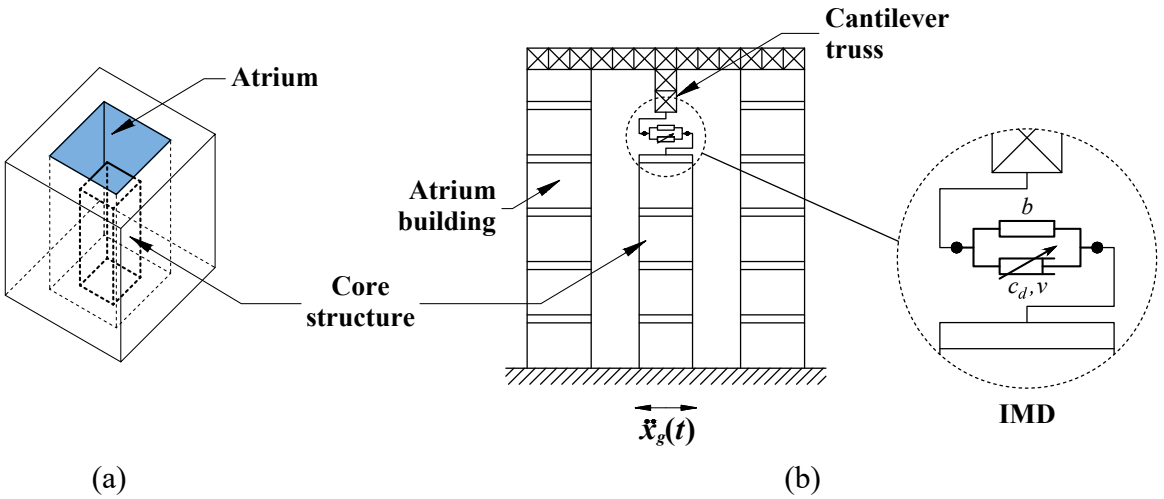

Figure 6.10: (a) A centralized atrium building with a core structure (b) proposed truss-IMD system.

In this section, a nonlinear IMD is incorporated into the proposed truss-damper configuration for seismic energy dissipation of atrium buildings, which utilizes an inerter to improve the performance of a nonlinear viscous damper, as shown in Figure 6.10. An analytic model of an atrium building equipped with a truss-IMD system is established first, and a numerical time-history method is developed to compute the dynamic response of the building under earthquake excitation. Based on the numerical approach, parametric studies are conducted to assess the effectiveness of

the truss-IMD system on mitigating interstory drift response of the atrium building, using first SDOF structural models, followed by a 6-story building. The performance of the truss-IMD system is also compared with the truss-FVD system.

6.2.1 Analytic model of a simple atrium building and a core structure connected by a truss-IMD system

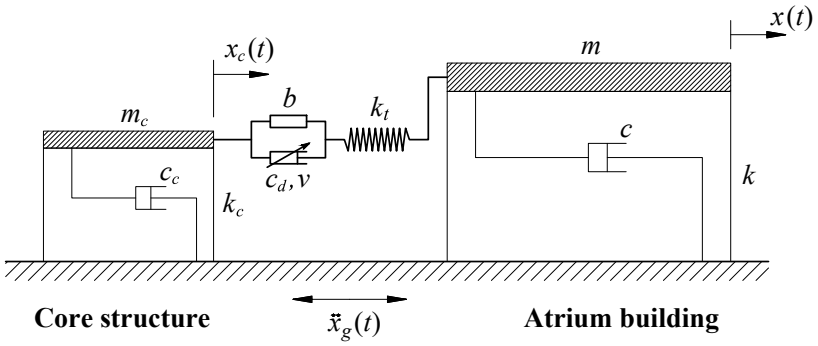

Figure 6.11: Analytic model of an atrium building and its core structure connected by a truss-IMD system.

To evaluate the seismic performance of the proposed truss-IMD system, an analytic model of a simple structural system is adopted, as shown in Figure 6.11, which is similar to the model shown in Figure 6.3, yet the viscous damper is replaced by an inertial mass damper. In Figure 6.11, b, c_d and ν represent the inertance, damping coefficient and velocity exponent of the IMD, respectively. The equation of motion of the atrium building and the core structure under seismic excitation can be expressed as the following second-order differential equation:

$$\mathbf{M_s}\ddot{\mathbf{x}}_\mathbf{s}(t) + \mathbf{C_s}\dot{\mathbf{x}}_\mathbf{s}(t) + \mathbf{K_s}\mathbf{x_s}(t) + \mathbf{F_{d,s}}(t) = -\mathbf{M_s}\mathbf{1}\ddot{x}_g(t) \tag{6.15}$$

Eq. (6.15) is similar to the equation of motion of the structural model studied in Section 6.1.1, thus it can be similarly solved using the state-space procedure and obtain the discrete time-state solution expressed in Eq. (6.3). However, as an inertial mass damper is adopted in the section, the damper force vector of the truss-IMD system, $\mathbf{F_{d,s}}(t)$, should be different from that of the truss-FVD system.

Figure 6.12 shows the hysteretic curves of a nonlinear viscous damper, an inerter, and a nonlinear IMD subjected to a sinusoidal vibration. It can be seen from Figure 6.12 that the force-displacement loop of an ideal IMD is the superposition of the hysteretic curves of the viscous damper and the inerter. Therefore, the damper force

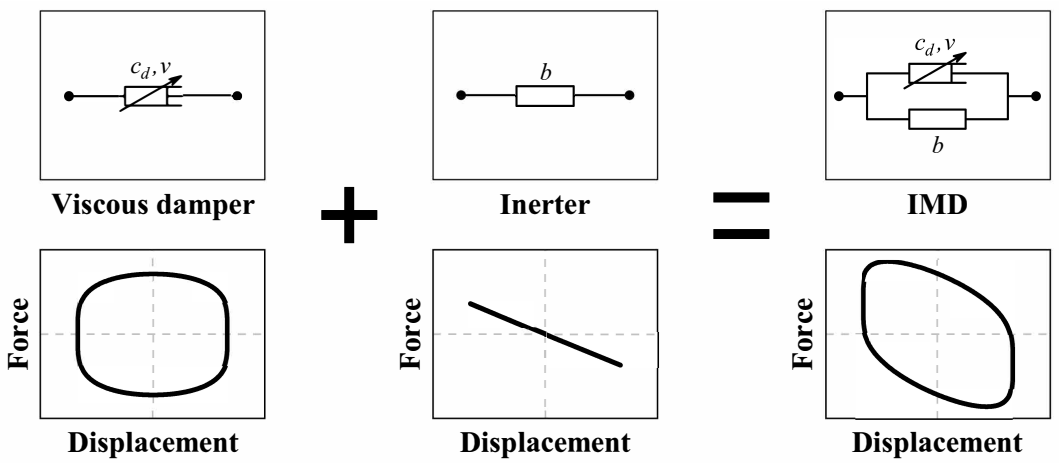

Figure 6.12: Superposition of hysteretic curves of a viscous damper ($\nu = 0.5$) and an inerter.

in an IMD can be expressed as:

$$f_d(t) = c_d|\dot{\Delta}_d(t)|^{\nu} sgn(\dot{\Delta}_d(t)) + b\ddot{\Delta}_d(t) = k_t\Delta_t(t) \tag{6.16}$$

The rearrangement of Eq. (6.16) yields a second-order differential equation:

$$\ddot{\Delta}_d(t) + \frac{c_d}{b}|\dot{\Delta}_d(t)|^{\nu} sgn(\dot{\Delta}_d(t)) - \frac{k_t}{b}\Delta_t(t) = 0 \tag{6.17}$$

The substitution of $\Delta_t(t)$ in Eq. (6.4) into Eq. (6.17) gives the following differential equation:

$$\ddot{\Delta}_d(t) + \frac{c_d}{b}|\dot{\Delta}_d(t)|^{\nu} sgn(\dot{\Delta}_d(t)) + \frac{k_t}{b}\Delta_d(t) = \frac{k_t}{b}\Delta(t) \tag{6.18}$$

From Eq. (6.18) it can be observed that, the response of the IMD, $\Delta_d(t)$, can be found based on the input relative displacement of the truss-IMD system, $\Delta(t)$. Here, $\Delta(t)$ is assumed to change linearly within two adjacent sampling instants, and Eq. (6.18) is treated as an initial value problem at each computational time interval that can be solved piece-wisely :

$$\begin{gathered}\ddot{\Delta}_d(t) + \frac{c_d}{b}|\dot{\Delta}_d(t)|^{\nu} sgn(\dot{\Delta}_d(t)) + \frac{k_t}{b}\Delta_d(t) = \frac{k_t}{b}(\Delta_0 + \frac{\Delta_1 - \Delta_0}{\Delta t}t), \\ \Delta_d(t_0) = \Delta_{d,0},\ \dot{\Delta}_d(t_0) = \dot{\Delta}_{d,0} \\ \Delta(t_0) = \Delta_0,\ \Delta(t_0 + \Delta t) = \Delta_1 \\ \text{for}\ \ t_0 \le t \le t_0 + \Delta t\end{gathered} \tag{6.19}$$

The `ode45` (Shampine and Reichelt 1997) based on the Dormand-Prince (4,5) pair

(Dormand and Prince 1980) is used in this study to solve Eq. (6.19) numerically. The IMD deformation at sampling instant $(\mathrm{k}+1)\Delta t$, namely $\Delta_d[\mathrm{k}+1]$, can be calculated by extracting the numerical solution of the following equation at $t = (\mathrm{k}+1)\Delta t$.

$$\begin{gathered}\ddot{\Delta}_d(t) + \frac{c_d}{b}|\dot{\Delta}_d(t)|^{\nu} sgn(\dot{\Delta}_d(t)) + \frac{k_t}{b}\Delta_d(t) = \frac{k_t}{b}(\Delta[\mathrm{k}] + \frac{\Delta[\mathrm{k}+1] - \Delta[\mathrm{k}]}{\Delta t}t), \\ \Delta_d(0) = \Delta_d[\mathrm{k}],\ \dot{\Delta}_d(0) = \dot{\Delta}_d[\mathrm{k}] \\ \text{for}\ \ \mathrm{k}\Delta t \le t \le (\mathrm{k}+1)\Delta t\end{gathered} \tag{6.20}$$

The substitution of Δ_d[k+1] and Δ[k+1] into Eq. (6.4) gives the truss deformation at time step $[\mathrm{k}+1]$, $\Delta_t[\mathrm{k}+1]$. The control force in the IMD at step $[\mathrm{k}+1]$, $f_d[\mathrm{k}+1]$, can thus be calculated by substituting $\Delta_t[\mathrm{k}+1]$ into Eq. (6.16).

6.2.2 Performance evaluation of the truss-IMD system

Parametric studies using the analytic model in Figure 6.11 will now be conducted to evaluate the effectiveness of the truss-IMD system, focusing primarily on the effects of truss stiffness, damper inertance and nonlinearity. To relate the design variables of the IMD to the properties of the atrium building, in addition to the parameters in Eq. (6.12), a normalized dimensionless inertial mass ratio λ is defined as the ratio of IMD inertance to the story mass of the atrium building:

$$\lambda \equiv \frac{b}{m} \tag{6.21}$$

To evaluate the effectiveness of a truss-IMD system, the performance indices PI_D and $PI_{D,c}$, as well as the corresponding response reductions RR_D and $RR_{D,c}$ are also adopted here. The simple system shown in Figure 6.11 is investigated with the same structural properties as those of the SDOF system studied in Section 6.1.2. The zero-mean white-noise accelerogram is also adopted here as the input ground acceleration.

The effectiveness of truss stiffness on enhancing seismic performance of the atrium building is first investigated. Figure 6.13 shows the story drift response reduction of the building against truss stiffness ratio for different inertial mass ratios, when the damping ratio and the velocity exponent are 0.0015 and 0.4, respectively. It can be seen from Figure 6.13 that, the response reduction generally increases rapidly with increasing truss stiffness at low stiffness region, say $\alpha < 0.1$. As the truss stiffness becomes larger, for λ equals 0.005, 0.04 and 0.05, the response reduction tends towards a diminishing return; for an examined inertial mass ratio between 0.005 and 0.04, the response reduction reaches a peak and decreases afterwards. Moreover,

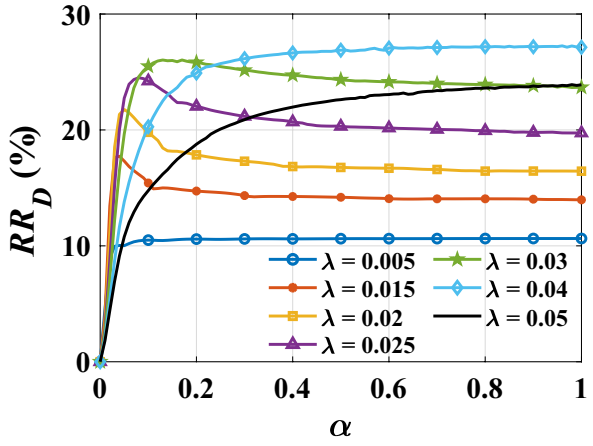

Figure 6.13: Variations of response reduction in story drift with truss stiffness ratio for different inertial mass ratios under white-noise excitation ($\beta = 0.0015$ (s/m)$^{-0.6}$, $\nu = 0.4$).

for a given truss stiffness, using a larger inertial mass ratio may not improve the structural performance. For example, when α equals 0.2, the response reduction increases as λ grows from 0.005 to 0.03; as λ becomes larger, the response reduction starts to decrease, indicating that there may be an optimal inertance to maximize the structural performance for the given truss stiffness.

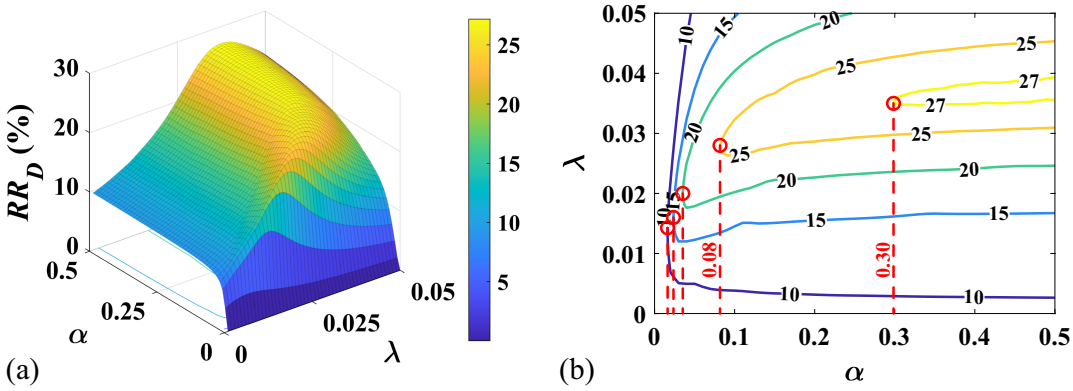

Figure 6.14: (a) Mesh and (b) contour plots of response reduction versus truss stiffness ratio and inertial mass ratio of the truss-IMD system for the atrium building under white-noise excitation ($\beta = 0.0015$, $\nu = 0.4$).

Figures 6.14(a) and (b) show the three-dimensional mesh and contour plots of building response reduction versus the truss stiffness ratio and inertial mass ratio for a given set of damping ratio and velocity exponent, respectively. It can be seen from Figure 6.14(a) that, the use of larger truss stiffness and IMD inertance may not improve the performance of the atrium building, yet using a larger truss stiffness can generally increase the response reduction when the IMD parameters are preset. In

general, for a given truss stiffness, there seems to exist an optimal inertial mass ratio. It can be seen from the contour plot in Figure 6.14(b) that, there exists an infinite combination of design parameters for the truss-IMD system to achieve a specific response reduction; however, a minimum truss stiffness will be required, as indicated by the red dashed lines. For example, to obtain a 25% story drift response reduction, the truss stiffness ratio shall not be smaller than 0.08.

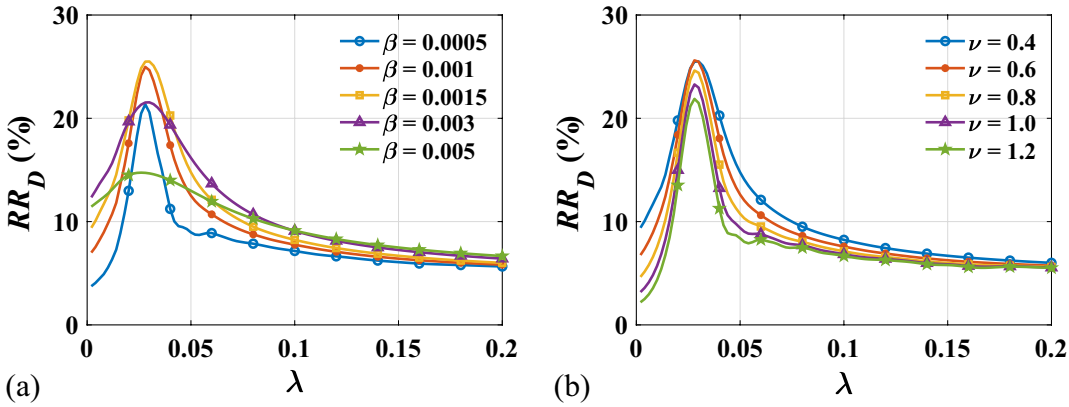

Figure 6.15: Variations of response reductions in story drift with (a) damping ratio ($\alpha = 0.1$, $\nu = 0.4$) and (b) velocity exponent ($\alpha = 0.1$, $\beta = 0.0015$) of the IMD for the atrium building under white-noise excitation.

To study the effect of inertance on dynamic performance of the atrium building, variations of the response reduction with inertial mass ratio for a given truss stiffness are plotted in Figure 6.15, in which Figure 6.15(a) is plotted for a preset velocity exponent, while for Figure 6.15(b) the damping ratio is fixed. It can be seen from Figure 6.15(a) that, all the peak response reductions occur at inertial mass ratio around 0.03, and the use of a larger damping ratio may not necessarily result in a better structural performance. For the examined damping ratios, the peak response reduction increases as β rises from 0.0005 to 0.0015, and it drops when β becomes larger, indicating that there may exist an optimal damping ratio to maximize the response reduction. From Figure 6.15(b) it can be seen that, the peak response reductions for different velocity exponents also converge at inertial mass ratio around 0.03. From the above observations, it may be concluded that for a given truss stiffness, there exists an optimal inertance of the IMD, regardless of the damping ratios and the velocity exponents considered.

Results from Figure 6.15(a) suggest that for a preset velocity exponent, there may exist an optimal damping ratio and a corresponding optimal inertial mass ratio to achieve a maximum response reduction for a given truss stiffness. To verify this speculation, Figure 6.16 is plotted to show the three-dimensional mesh ((a)-(c))

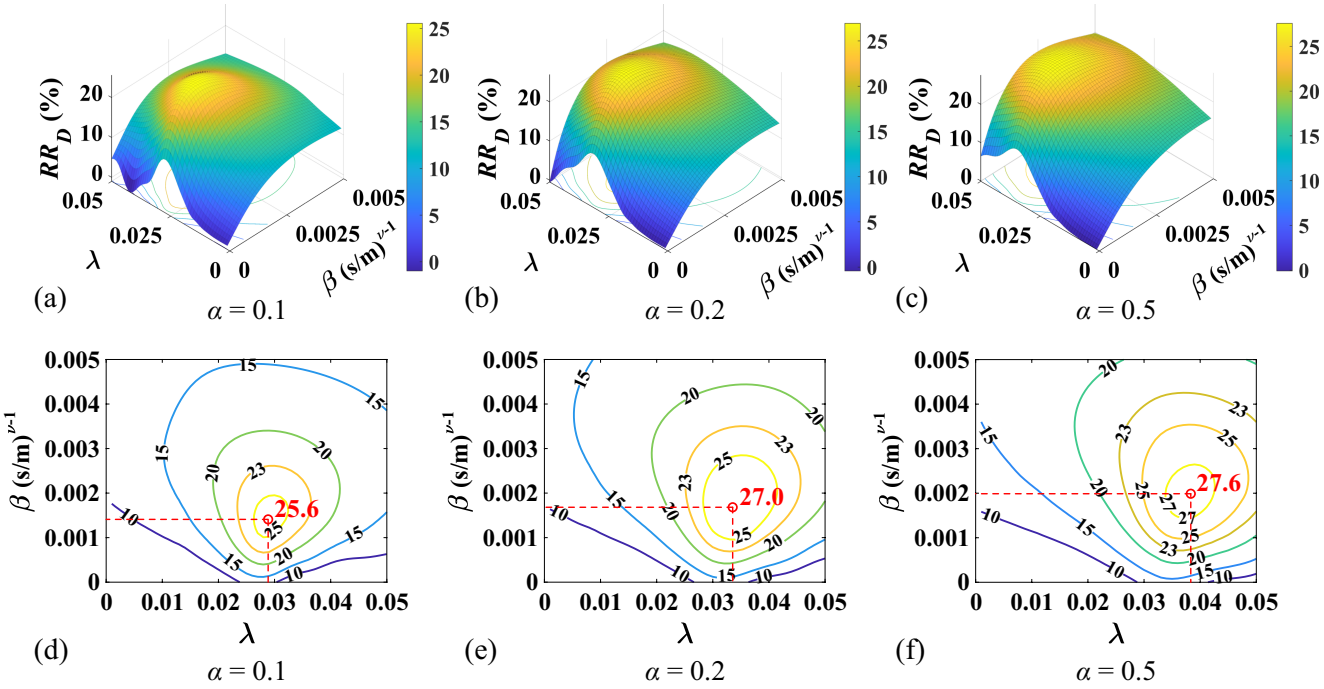

Figure 6.16: Mesh and contour plots of response reduction in story drift versus inertial mass ratio and damping ratio for the atrium building under white-noise excitation (ν = 0.4).

and contour ((d)-(f)) plots of the response reduction RR_D versus the inertial mass ratio λ and the damping ratio β for truss stiffness ratio equals 0.1, 0.2 and 0.5 at velocity exponent equals 0.4. Figures 6.16(a)-(c) show that, the damping ratio and the inertial mass ratio can be combined in numerous ways to achieve a target performance objective; however, for each stiffness ratio, there exists one global maximum response reduction. It can be seen from Figures 6.16(d)-(f) that, as the truss stiffness becomes larger, the maximum achievable response reduction increases, so do the optimal inertial mass ratio and damping ratio of the IMD.

Previous results from Figure 6.16 have shown the existence of a maximum response reduction of the atrium building for a given truss stiffness, to further investigate the relationship between the maximum response reduction and the truss stiffness, the genetic algorithm described in Section 3.3 is used to search for the optimal design parameters of the IMD to maximize response reduction for a given set of stiffness ratio and velocity exponent. Figure 6.17(a) shows the variations of maximum building response reduction with truss stiffness ratio. It can be seen from Figure 6.17(a) that, as stiffness ratio increases, there is a sharp increase in maximum response reduction at small truss stiffness region, say $\alpha < 0.1$, and a diminishing return can be found when truss stiffness becomes larger. Moreover, velocity exponent is noted to have

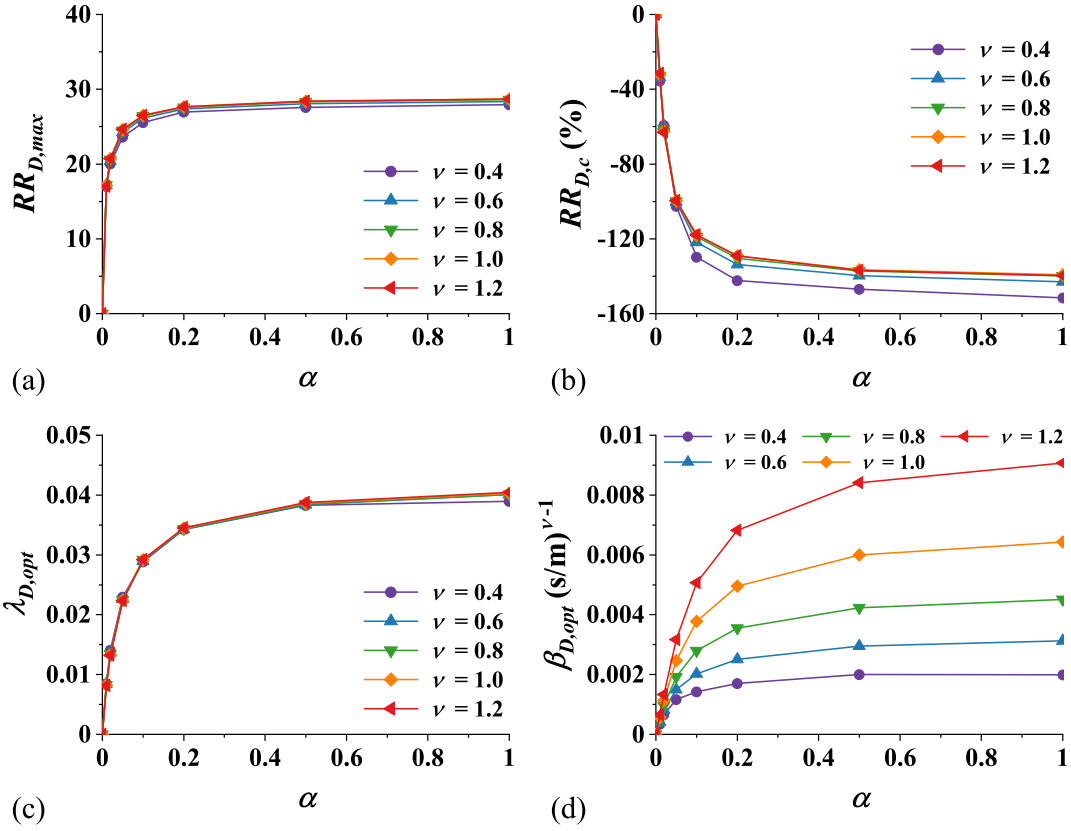

Figure 6.17: (a) Maximum story drift response reduction of the atrium building (b) corresponding response reduction of the core structure (c) optimal inertial mass ratio and (d) optimal damping ratio against truss stiffness ratio under white-noise excitation.

no significant influence on maximum response reduction of the building. It is worth noting that, the curves in Figure 6.17(a) are similar to those in Figure 6.8(a), yet with larger achievable $RR_{D,max}$. For instance, when the truss stiffness ratio equals 0.1, the $RR_{D,max}$ that can be achieved by a truss-FVD system is approximately 12.48%, while the $RR_{D,max}$ for the truss-IMD system is about 26.23%, which shows around 14% difference, indicating that the IMD exhibits better performance than the viscous damper in terms of response reduction in story drift. Figure 6.17(b) shows the response reduction of the core structure when the optimal parameters of the IMD are used. From Figure 6.17(b) it can be seen that, the response reduction in story drift of the core structure, $RR_{D,c}$, decreases rapidly with increasing truss stiffness at small truss stiffness region, say $\alpha < 0.1$, regardless of the magnitude of the velocity exponent. Figures 6.17(c) and (d) show respectively the optimal inertial mass ratio and the optimal damping ratio versus truss stiffness ratio. It can be seen from Figures 6.17(c) and (d) that, for a given truss stiffness, the optimal inertial mass ratios for different velocity exponent are very close, but the optimal damping ratio increases

with increasing velocity exponent.

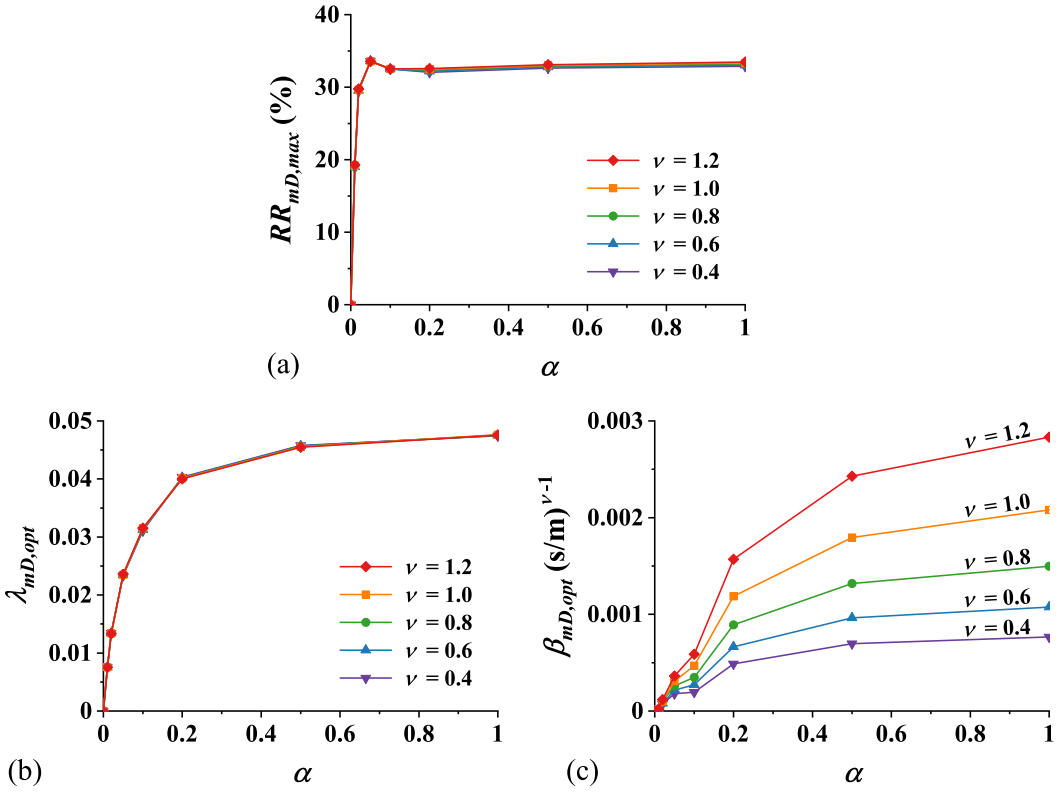

Figure 6.18: (a) Maximum response reduction in peak story drift (b) optimal inertial mass ratio and (c) optimal damping ratio against truss stiffness ratio of the atrium building with a truss-IMD system under white-noise excitation.

In addition to the story drift response reduction ratio RR_D, the performance of the truss-IMD system in mitigating peak response of the atrium building during an earthquake is also evaluated based on the response reduction ratio in peak story drift RR_{mD}, which is defined in Section 5.1.4 (Eq. (5.9)). Figure 6.18 shows the maximum peak story drift response reduction of the building $RR_{mD,max}$ and the corresponding optimal IMD parameters ($\lambda_{mD,opt}$ and $\beta_{mD,opt}$) versus truss stiffness ratio α for different velocity exponents under the white-noise excitation. Note that the examined range of truss stiffness ratio is $0 \leq \alpha \leq 1$, as $RR_{mD,max}$ is found to be very sensitive to the truss stiffness when the stiffness ratio is smaller than 0.1. In general, the curves in Figure 6.18 show similar trends to the corresponding curves in Figure 6.17 for the maximum story drift response reduction, which indicates that in addition to the root-mean-square of story drift, the truss-IMD system can also effectively mitigate the peak drift of the atrium building. From Figure 6.18(a) it can be seen that as the truss stiffness becomes larger, the maximum response reduction in peak story drift reaches a peak at α around 0.05. Moreover, by comparing Figure

6.18(c) with Figure 6.17(d), it can be found that the optimal damping required to minimize the peak story drift of the building are generally smaller than that required to minimize the root-mean-square of story drift for a given truss stiffness ratio.

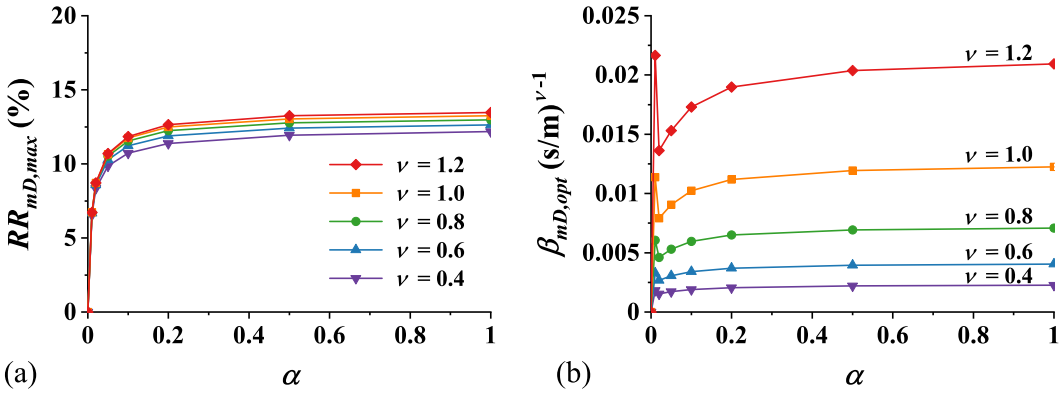

Figure 6.19: (a) Maximum response reduction in peak story drift and (b) optimal damping ratio against truss stiffness ratio of the atrium building with a truss-FVD system under white-noise excitation.

The optimal performance of the truss-FVD system in reducing peak displacement of the atrium building is also evaluated based on the response reduction in peak story drift; the maximum response reductions and the corresponding optimal damping ratios are shown in Figure 6.19. It can be seen from Figure 6.19(a) that the truss-FVD system is also capable of mitigating the peak story drift when it is properly designed; however, by comparing Figure 6.19(a) with Figure 6.18(a) it can be found that, the maximum achievable response reduction of the viscous damper is significantly smaller than that of the inertial mass damper for a given truss stiffness ratio. It can be seen from Figure 6.19(b) that the optimal damping ratio generally increases with the truss stiffness ratio for a preset velocity exponent, yet sharp changes in $\beta_{mD,opt}$ can be observed at α around 0.01 for the examined velocity exponents. These sharp changes in optimal damping ratio may also be due to the fact that the damping required to minimize a peak structural response at different time instants may be quite different, as explained in Section 5.1.4.

6.2.3 Numerical example I: incremental dynamic analysis of a nonlinear simple structural system

To assess capacity and robustness of the proposed truss-IMD system to the uncertainty of ground motion input, incremental dynamic analysis has been carried out for a nonlinear SDOF atrium building under multiple earthquakes with increasing excitation intensities. The nonlinear restoring force-displacement behaviour of the building is assumed to be bilinear, as shown in Figure 5.21, and the mass m, elastic stiffness k_E and post-elastic stiffness k_{PE} of the structure are 2533 kg, 100 kN/m and 10 kN/m, respectively. Noting that the fundamental period of the atrium building based on its elastic stiffness is 1 second. A 2% inherent damping is assigned to the building, and the yielding story drift in the horizontal direction δ_y is set to 2 cm. The core structure is assumed to be a linear elastic structure with a mass ratio of 0.05 and a damping ratio of 2%.

Table 6.1: Seismic design parameters.

Parameters	value
Risk/Occupancy category	II
Importance factor	1
Seismic design category	D
Site class	C
MCE[1] spectral response acceleration parameter at short periods S_S (g)	1.5
MCE spectral response acceleration parameter at period of 1 sec S_1 (g)	0.6
Short period site coefficient F_a	1.2
Long period site coefficient F_v	1.4
Spectral response acceleration parameter at short periods S_{DS} (g)	1.2
Spectral response acceleration parameter at period of 1 sec S_{D1} (g)	0.56
Long-period transition period T_L (s)	12

[1]Maximum Considered Earthquake.

The atrium building may be subjected to ground motions with various vibration properties. In this section, it is assumed that the building is located in downtown San Jose, California, USA, on very dense soil and soft rock that is classified as site class C according to ASCE 7-05 (ASCE 2005). The seismic design parameters used are summarized in Table 6.1 (SEAOC and OSHPD 2022), based on which a design response spectrum of the construction site is produced. Twenty realistic ground motion records were selected from the PEER database, as listed in Table 6.2; these earthquake records were scaled to have a mean spectrum that approximately matches the design spectrum, particularly between periods of $0.2T_1$ and $1.5T_1$, namely 0.2 and 1.5 seconds, as shown in Figure 6.20. For conducting the IDA, the 5% damped spectral acceleration at the structure's fundamental period, $S_a(T_1, 5\%)$, is chosen as

Table 6.2: Selected ground motions used in the numerical example.

Code	Earthquake event	Year	Station	Magnitude	$S_a(T_1, 5\%)$ (g)	PGA (g)
EQ1	Kern County	1952	Santa Barbara Courthouse	7.36	0.86	0.35
EQ2	Kern County	1952	Taft Lincoln School	7.36	0.50	0.39
EQ3	Lytle Creek	1970	Wrightwood - 6074 Park Dr	5.33	0.40	0.61
EQ4	San Fernando	1971	Castaic - Old Ridge Route	6.61	0.38	0.56
EQ5	San Fernando	1971	Palmdale Fire Station	6.61	0.61	0.42
EQ6	Friuli, Italy-01	1976	Tolmezzo	6.50	0.44	0.64
EQ7	Tabas, Iran	1978	Dayhook	7.35	0.44	0.63
EQ8	Coyote Lake	1979	Coyote Lake Dam	5.74	0.38	0.54
EQ9	Coyote Lake	1979	Gilroy Array #6	5.74	0.77	0.56
EQ10	Imperial Valley-06	1979	Cerro Prieto	6.53	0.26	0.42
EQ11	Livermore-01	1980	San Ramon - Eastman Kodak	5.80	0.94	0.53
EQ12	Livermore-02	1980	San Ramon - Eastman Kodak	5.42	0.52	0.58
EQ13	Mammoth Lakes-01	1980	Convict Creek	6.06	0.28	0.67
EQ14	Mammoth Lakes-01	1980	Long Valley Dam	6.06	0.43	0.81
EQ15	Mammoth Lakes-02	1980	Convict Creek	5.69	0.46	0.51
EQ16	Mammoth Lakes-03	1980	Convict Creek	5.91	0.47	0.52
EQ17	Mammoth Lakes-04	1980	Long Valley Dam	5.70	0.42	0.75
EQ18	Mammoth Lakes-06	1980	Convict Creek	5.94	0.50	0.74
EQ19	Mammoth Lakes-06	1980	Long Valley Dam	5.94	0.33	1.20
EQ20	Victoria, Mexico	1980	Cerro Prieto	6.33	0.69	0.63

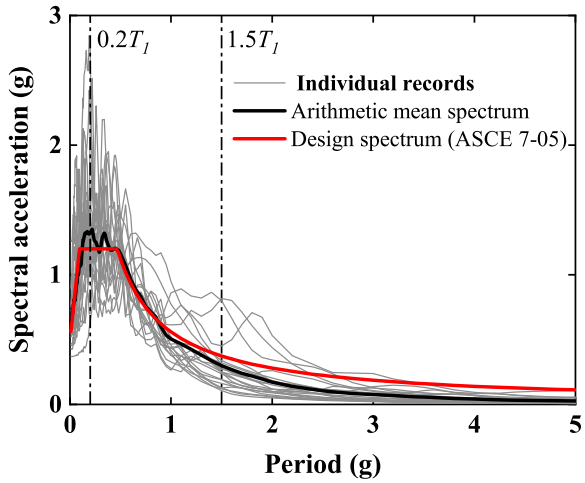

Figure 6.20: Design response spectrum at downtown San Jose (based on parameters in Table 6.1) and acceleration response spectrums of the selected earthquakes.

the intensity measure of a scaled ground acceleration-history. The scaled $S_a(T_1, 5\%)$ for the selected earthquakes are summarized in Table 6.2. In this numerical example, the spectral acceleration considered in the IDA increases from 0 to 2 g with a step size of 0.1 g. A maximum story drift and an average maximum story drift are defined as the damage measures of the structure with the following expressions:

$$\text{Maximum story drift} = max\{max(\delta_1),\ max(\delta_2),\ \ldots,\ max(\delta_{20})\} \tag{6.22}$$

and

$$\text{Average maximum story drift} = \frac{1}{20}\sum_{j=1}^{20} max(\delta_j) \tag{6.23}$$

where δ_j is the story drift time-history of the atrium building under j-th earthquake and $j = 1,\ 2,\ \ldots,\ 20$.

Table 6.3: Optimal damper parameters and response reductions of the atrium building and the core structure under white-noise excitation ($\text{PGA}_{\ddot{x}_g}$= 0.64 g, $\nu = 0.6$).

		Truss-IMD system				Truss-FVD system		
γ	α	λ_{opt} (kg)	β_{opt} (N·(s/m)$^{0.6}$)	$RR_{D,max}$ (%)	$RR_{D,c}$ (%)	β_{opt} (N·(s/m)$^{0.6}$)	$RR_{D,max}$ (%)	$RR_{D,c}$ (%)
0.2	0.2	0.073	0.0062	31.86	-73.32	0.0096	11.54	39.59
0.2	0.5	0.097	0.0084	35.59	-99.80	0.0177	14.76	8.44
0.5	0.5	0.185	0.0191	48.50	-86.38	0.0291	27.56	0.18

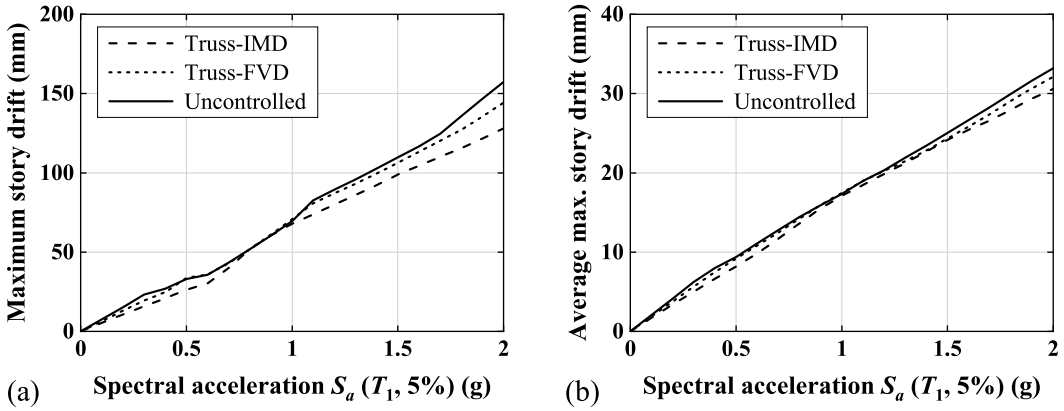

Figure 6.21: IDA curves of (a) maximum story drift (b) average maximum story drift for structure controlled by truss-IMD system, truss-FVD system and for uncontrolled structure under the selected earthquakes ($\gamma = 0.2$, $\alpha = 0.2$).

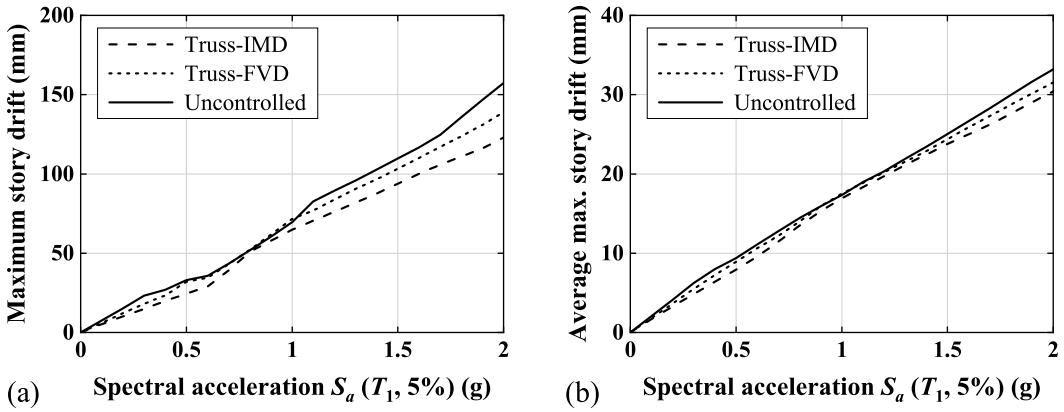

Figure 6.22: IDA curves of (a) maximum story drift (b) average maximum story drift for structure controlled by truss-IMD system, truss-FVD system and for uncontrolled structure under the selected earthquakes ($\gamma = 0.2$, $\alpha = 0.5$).

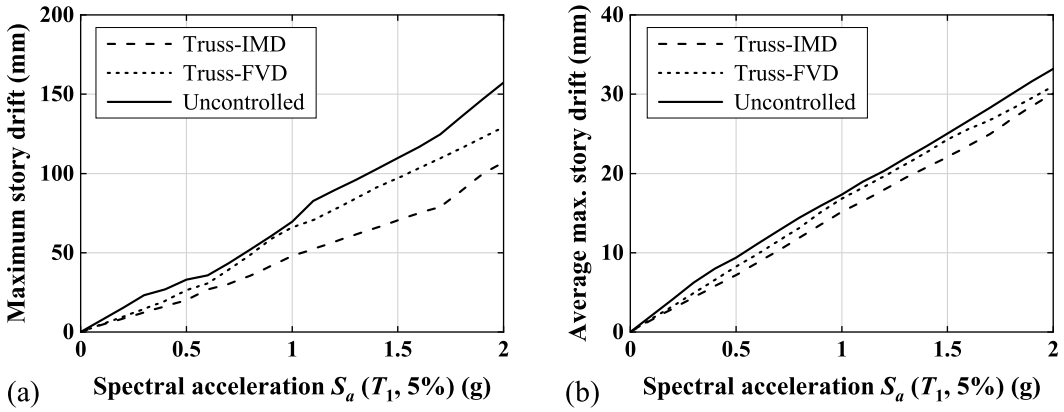

Figure 6.23: IDA curves of (a) maximum story drift (b) average maximum story drift for structure controlled by truss-IMD system, truss-FVD system and for uncontrolled structure under the selected earthquakes ($\gamma = 0.5$, $\alpha = 0.5$).

Figures 6.21, 6.22 and 6.23 show the IDA curves of the atrium building equipped with the optimal truss-damper systems to maximize response reductions in story drift under white-noise for ($\alpha = 0.2$, $\gamma = 0.2$), ($\alpha = 0.5$, $\gamma = 0.2$) and ($\alpha = 0.5$, $\gamma = 0.5$), respectively. The optimal parameters of the dampers, as well as the achievable structural response reductions are summarized in Table 6.3. It can be seen from the figures that, both the FVD and IMD are effectively robust to the stochastic characteristic of the input earthquake excitation, and the truss-IMD system generally outperforms the truss-FVD system in mitigating peak story drift of the building. For the uncontrolled building, a change in slope of the IDA curve of maximum story drift can be found at a spectral acceleration approximately equals 0.3 g, as shown in Figure 6.21(a), indicating the atrium building starts to yield; this slope change seems to be postponed when a truss-damper system is used. For example, Figure

6.22(a) shows the IDA curves for α equals 0.5 and γ equals 0.2, in which the yielding spectral acceleration of the building is postponed to around 0.4 and 0.6 g by the truss-FVD and truss-IMD systems, respectively. It can also be seen from Figures 6.21(a), 6.22(a) and 6.23(a) that, for a given spectral acceleration, the maximum story drift of the building with a truss-damper system generally reduces with increasing stiffness of the truss and core structure, indicating the use of a stiffer truss or a stiffer core structure can further enhance performance of a truss-damper system and alleviate displacement response of the atrium building within the examined excitation intensity range. From Figures 6.21(b), 6.22(b) and 6.23(b) it can be seen that, the truss-IMD system is generally more robust than the truss-FVD system in reducing the average maximum story drift of the building under different ground motions. As the stiffness of the truss and core structure becomes larger, the distance between an IDA curve of the structure with a truss-damper system and the curve of the uncontrolled structure is amplified, indicating more structural response is mitigated by the truss-damper systems.

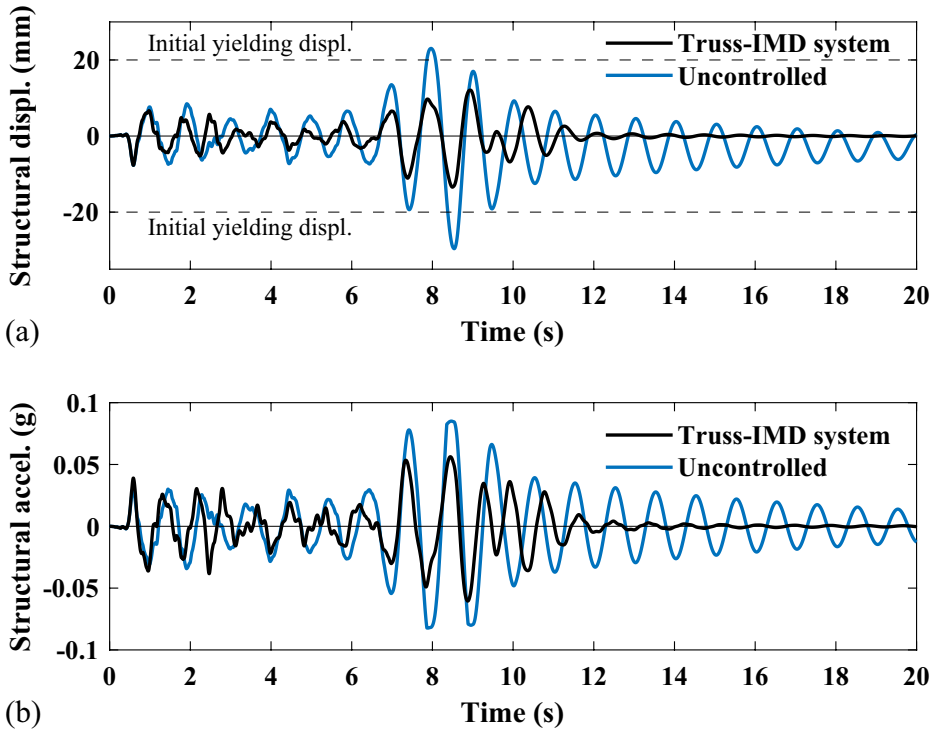

Figure 6.24: (a) Displacement and (b) acceleration time-histories of the uncontrolled atrium building and equipped with the optimal truss-IMD system for $\alpha = 0.5$ and $\gamma = 0.5$ under the EQ2 Kern County earthquake.

To illustrate the seismic behaviour of the nonlinear atrium building with a truss-IMD system, Figure 6.24 is plotted, which shows the displacement and accelera-

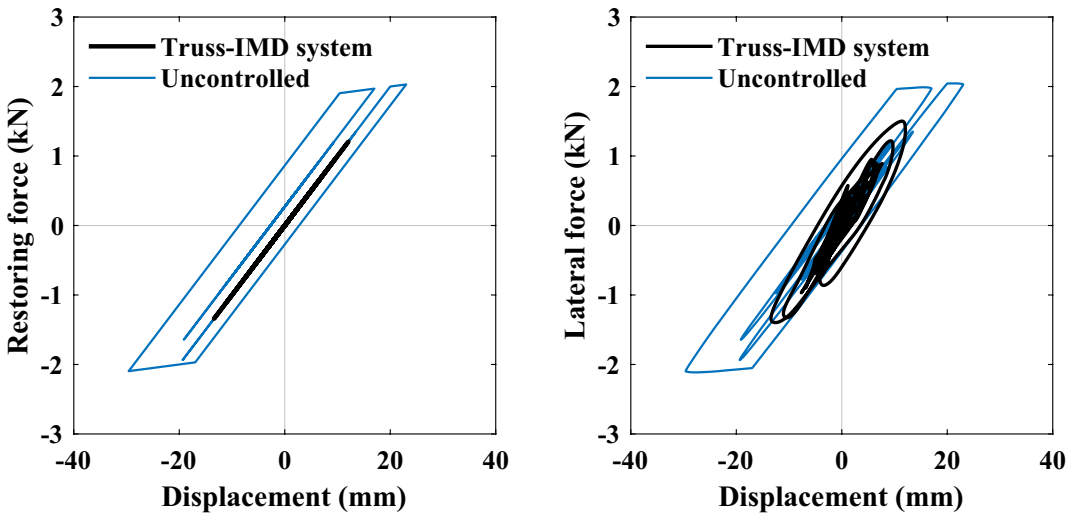

Figure 6.25: (a) Structural restoring force versus displacement (b) total lateral force versus displacement of the uncontrolled atrium building and equipped with the optimal truss-IMD system for $\alpha = 0.5$ and $\gamma = 0.5$ under the EQ2 Kern County earthquake.

tion time-histories of the building under ground motion EQ2, namely the 1952 Kern County earthquake. It can be seen from Figure 6.24(a) that, the lateral displacement of the building with the truss-IMD system is generally smaller than that of the uncontrolled structure, and the horizontal drift of the uncontrolled building reaches the initial yielding displacement when t is around 8 s, which causes inelastic deformation of the structure. However, the building with the truss-IMD system stays within its elastic phase during the earthquake. It can also be seen from Figure 6.24(a) that, after twelve seconds of the time-history, the uncontrolled building still oscillates with large amplitudes and tends not to restore its initial position, i.e., the final displacement of the uncontrolled building after the earthquake will not be zero. However, the vibration amplitude of the building with the truss-IMD system are much smaller than that of the uncontrolled structure, and the lateral structural displacement tends to stabilize to zero, indicating the truss-IMD system can effectively increase the damping of the atrium building and reduce inelastic structural deformation during the earthquake. From Figure 6.24(b) it can be seen that, in general, when equipped with the truss-IMD system, the acceleration response of the building is reduced, and the structure is quickly stabilized after the earthquake due to the additional damping. When $t < 3$ s, the structural acceleration with the truss-IMD system is sometimes larger than that of the uncontrolled structure, which can be attributed to the large damper force generated by the IMD. To further improve the acceleration performance of the building, the damper parameters could be optimized based on a performance

index in story acceleration.

Figure 6.25(a) shows the hysteretic curves of the shear walls that provide restoring force in the horizontal direction for the uncontrolled building and when equipped with the optimal truss-IMD system, and 6.25(b) plots the hysteretic loops of the entire structure. As can be seen from Figure 6.25(a) that, the truss-IMD system can suppress dynamic response of the atrium building and prevent inelastic deformation of the shear wall under the examined earthquake; when equipped with the truss-IMD system, the structure utilizes the supplemental IMD to dissipate a significant amount of input seismic energy, rather than relying only on its damping and inelastic deformations.

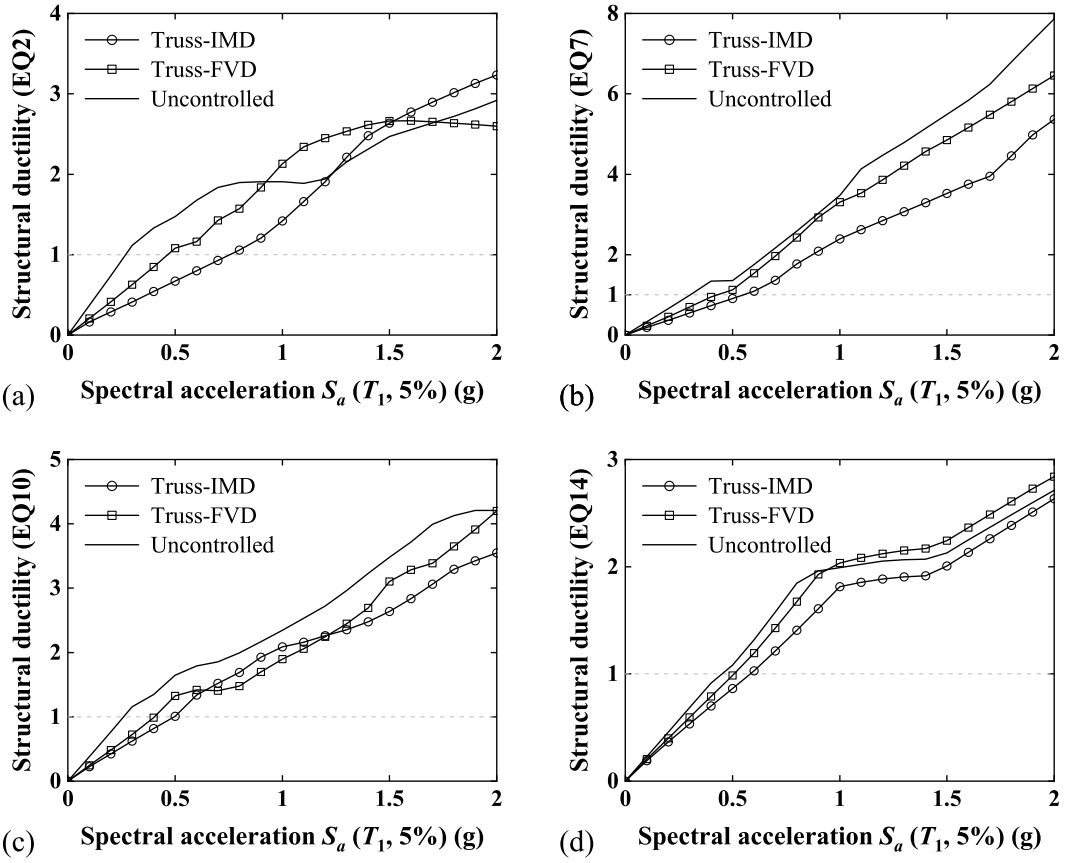

Figure 6.26: Structural ductility of the uncontrolled atrium building and with the optimal truss-damper systems under the (a) EQ2 (b) EQ7 (c) EQ10 and (d) EQ14 earthquakes ($\gamma = 0.5$, $\alpha = 0.5$).

To illustrate the response intensity of the atrium building deforming into its post-elastic range during some intense earthquakes, Figure 6.26 is plotted, which shows the ductility of the building with and without an optimal truss-damper system under earthquakes with progressively increasing spectral acceleration $S_a(T_1, 5\%)$, in which

the ductility factor of the building is defined as:

$$\text{Structural ductility factor} = \frac{\delta_{max}}{\delta_y} \tag{6.24}$$

where δ_{max} and δ_y are the maximum absolute drift and yield drift of the structure, respectively. It can be seen from Figure 6.26 that, the optimal truss-damper systems can generally reduce the structural ductility, and the truss-IMD system outperforms the truss-FVD system at most of the examined excitation intensities. However, it can also be seen from Figures 6.26(a) and (d) that, under the Kern County earthquake (EQ2), the structural ductility is amplified when the building is equipped with a truss-damper system for $S_a(T_1, 5\%)$ larger than 1.2, and under the Mammoth Lakes earthquake (EQ14), the ductility of the building with the truss-FVD system is greater than that of the uncontrolled structure when $S_a(T_1, 5\%)$ is larger than 0.9. These observations suggest that although being effective in most of the examined intensities, the optimal truss-damper systems are not capable of reducing the peak inelastic deformation of the building for all earthquake intensities.

6.2.4 Analytic model of a multi-story atrium building with a truss-IMD system

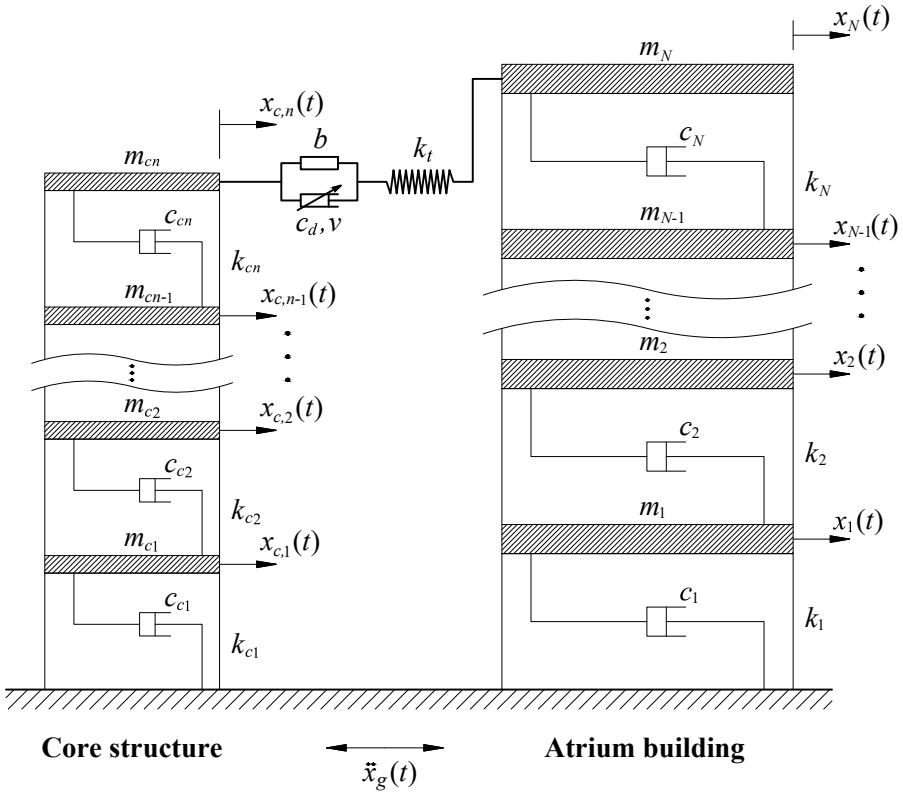

Figure 6.27: Analytic model of a N-story atrium building and a n-story core structure connected by a truss-IMD system.

To compute the response of a multi-story atrium building under earthquake excitation, the simple model in Section 6.2.1 is further extended. The analytic model of a N-story atrium building connected to a n-story core structure using a truss-IMD system is shown in Figure 6.27. The equation of motion of this system can be written as:

$$\mathbf{M}\ddot{\mathbf{x}}(t) + \mathbf{C}\dot{\mathbf{x}}(t) + \mathbf{K}\mathbf{x}(t) + \mathbf{F_d}(t) = -\mathbf{M1}\ddot{x}_g(t) \tag{6.25}$$

where

$\mathbf{M} = \begin{bmatrix} \mathbf{M_a} & \mathbf{0} \\ \mathbf{0} & \mathbf{M_c} \end{bmatrix}$ is the $(N+n) \times (N+n)$ mass matrix of the structural system;

$\mathbf{C} = \begin{bmatrix} \mathbf{C_a} & \mathbf{0} \\ \mathbf{0} & \mathbf{C_c} \end{bmatrix}$ is the $(N+n) \times (N+n)$ damping matrix of the system;

$\mathbf{K} = \begin{bmatrix} \mathbf{K_a} & \mathbf{0} \\ \mathbf{0} & \mathbf{K_c} \end{bmatrix}$ is the $(N+n) \times (N+n)$ stiffness matrix;

$\mathbf{F_d}(t) = \begin{bmatrix} \mathbf{0}_{1\times(N-1)} & f_d(t) & \mathbf{0}_{1\times(n-1)} & -f_d(t) \end{bmatrix}^{\mathbf{T}}$ is the $(N+n) \times 1$ damper force vector;

$\mathbf{x}(t) = \begin{bmatrix} \mathbf{x_a}(t) \\ \mathbf{x_c}(t) \end{bmatrix}$ is the $(N+n) \times 1$ response vector;

$\mathbf{x_a}(t) = \begin{bmatrix} x_1(t) & x_2(t) & \cdots & x_N(t) \end{bmatrix}^{\mathbf{T}}$ is the story displacement vector of the atrium building;

$\mathbf{x_c}(t) = \begin{bmatrix} x_{c,1}(t) & x_{c,2}(t) & \cdots & x_{c,n}(t) \end{bmatrix}^{\mathbf{T}}$ is the story displacement vector of the core structure;

$\mathbf{M_a}$, $\mathbf{C_a}$ and $\mathbf{K_a}$ are the $N \times N$ mass, damping and stiffness matrices of the atrium building, respectively; $\mathbf{M_c}$, $\mathbf{C_c}$ and $\mathbf{K_c}$ are the $n \times n$ mass, damping and stiffness matrices of the core structure, respectively; $\mathbf{1}$ is a $(N+n) \times 1$ unit vector.

The state-space procedure outlined in Section 3.1.1 is adopted to calculate the seismic responses of the MDOF structural system, and the steps outlined in Section 6.2.1 are used to calculate the force in the truss-IMD system. Notably, for a multi-story atrium building, the total deformation of the system $\Delta(t)$ is equal to the relative displacement between the atrium roof and the top of the core structure:

$$\Delta(t) = x_N(t) - x_{c,n}(t) = \Delta_d(t) + \Delta_t(t) \tag{6.26}$$

6.2.5 Numerical example II: a six-story atrium building

A six-story atrium building with a five-story core structure is used to evaluate the performance of the proposed truss-IMD system. The example building has identical story mass and stiffness, i.e., $m_1 = m_2 = \cdots = m_6 = 50 \times 10^3$ kg and $k_1 = k_2 = \cdots = k_6 = 40$ MN/m. The fundamental period of the building is 0.92 second, and a 3% inherent damping is assigned to the building. The core structure is a 5-story elevator tower with equal story mass and stiffness. The story stiffness of the tower is assumed to be 50% and 100% of that of the atrium building (γ equals 0.5 and 1), and the story mass is 5% of that of the building. 2% inherent damping is assigned to the elevator tower, and it is connected to the top of the atrium building by a truss-damper system. The ground motion used in this example is the filtered white-noise following the Kanai-Tajimi model, with a power spectral density function shown in Figure 6.28(a) and an acceleration time-history shown in Figure 6.28(b), which simulates the seismic excitation with an intensity class of 8 on type II site according to the Chinese code for seismic design of buildings (GB50011-2010) (CMC 2010).

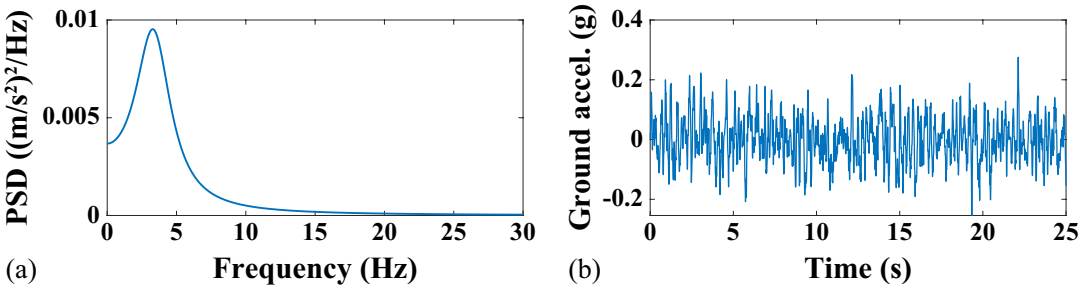

Figure 6.28: (a) Power spectral density function and (b) artificial accelerogram of the Kanai-Tajimi model considered.

Table 6.4: Optimal damper parameters and response reductions of the atrium building and the core structure.

			Truss-IMD system				Truss-FVD system		
ν	γ	α	b_{opt} (kg)	$c_{d,opt}$ (N·(s/m)$^{\nu}$)	$RR_{D,max}$ (%)	$RR_{D,c}$ (%)	$c_{d,opt}$ (N·(s/m)$^{\nu}$)	$RR_{D,max}$ (%)	$RR_{D,c}$ (%)
0.5	0.5	0.1	28526	45624	52.86	-68.08	95391	37.57	6.90
		0.2	33296	60727	55.01	-79.71	117630	42.32	-7.70
		0.5	37487	73460	56.70	-90.81	136935	45.70	-20.72
		1	39432	79636	57.28	-95.61	144620	46.91	-25.91
		2	40148	83822	57.59	-97.89	148892	47.53	-28.77
0.5	1	0.1	33520	64487	55.75	-156.00	123458	42.82	-57.69
		0.2	42658	93590	58.95	-187.31	163914	49.24	-94.50
		0.5	47446	128901	61.68	-200.55	207355	54.14	-132.24
		1	51249	145361	62.78	-214.38	227758	56.01	-149.52
		2	53205	156164	63.33	-222.46	240991	57.00	-160.28
1	0.5	0.1	28028	89952	52.99	-62.19	238517	36.98	7.53
		0.2	33765	128118	55.30	-75.48	311371	41.67	-8.80
		0.5	38676	167473	57.00	-86.33	379698	45.18	-23.46
		1	40639	185232	57.60	-90.45	408880	46.48	-29.42
		2	41482	197390	57.94	-92.63	425172	47.16	-32.66
1	1	0.1	34764	136777	56.03	-153.00	326475	42.67	-58.77
		0.2	44398	227264	59.36	-180.13	472648	49.41	-99.27
		0.5	53407	348771	62.06	-208.08	639092	54.64	-139.61
		1	57021	417152	63.11	-220.60	718796	56.64	-157.40
		2	58692	461850	63.67	-227.62	765168	57.70	-167.36

To further evaluate the performance of the truss-IMD system, dynamic responses of the atrium building equipped with a truss-IMD system and a truss-FVD system are compared. The damper parameters of the two systems are optimized for maximizing interstory drift performance of the building for different truss stiffness ratio (i.e., α equals 0.1, 0.2, 0.5, 1 and 2, where α here is defined as the ratio of the truss stiffness

k_t to first story stiffness of the building k_1). Table 6.4 summarizes the optimal design parameters of the two truss-damper systems, and the response reductions of the building and the core structure for different velocity exponents (0.5 and 1). From the table it can be seen that for both systems, the optimal damper parameters and the maximum response reductions increase with increasing truss stiffness, while the response reductions of the core structure decrease with increasing truss stiffness. As compared to the truss-FVD system, the optimal damping coefficients required from the truss-IMD system are smaller, but the maximum response reductions are generally larger, by 6-16%. Importantly, the maximum response reduction of the atrium building with the truss-FVD system at α equals 2 are still smaller than that with the truss-IMD system at α equals 0.2 for the examined velocity exponents, indicating the superior performance of the truss-IMD system. It is also worth noting that, the maximum achievable response reduction of the building increases as the core structure stiffness ratio γ increases from 0.5 to 1.

Figure 6.29 shows the structural response, base shear and damper force time-histories, and the hysteretic loops of the atrium building with two optimal truss-damper systems under the Kanai-Tajimi excitation for core structure stiffness ratio equals 0.5, truss stiffness ratio equals 0.5 and velocity exponent equals 0.5. It can be seen from the figure that, the truss-IMD system exhibits better performance in the examined structural responses, especially in roof displacement, and the damper force provided by the IMD is generally larger than the viscous damper. It can also be seen from the figure that, the area enclosed by the hysteretic loop of the IMD is larger than that of the viscous damper, indicating more seismic energy been dissipated by the truss-IMD system. To illustrate the dynamic responses of the core structure equipped with an optimally designed truss-IMD system, the top story displacement and base shear force time-histories of the core structure are plotted, as shown in Figure 6.30. The core structure story stiffness, truss stiffness and optimal damper parameters are identical to those used in Figure 6.29. It can be seen from Figure 6.30(a) that the roof displacement response of the core structure is amplified during the earthquake, but the base shear force of the core structure is reduced, as can be seen from Figure 6.30(b). As a 56.7% of interstory drift response reduction is achieved by the atrium building, the increased displacement of core structure in Figure 6.30(a) is deemed an acceptable cost to ensure safety of the building; possible damage in core structure caused by the amplified displacement could be repaired after the earthquake.

The two truss-damper systems optimized for the Kanai-Tajimi excitation are also evaluated using realistic ground motions. Five historic strong ground motion records are considered in this example to assess the robustness of the optimal damper de-

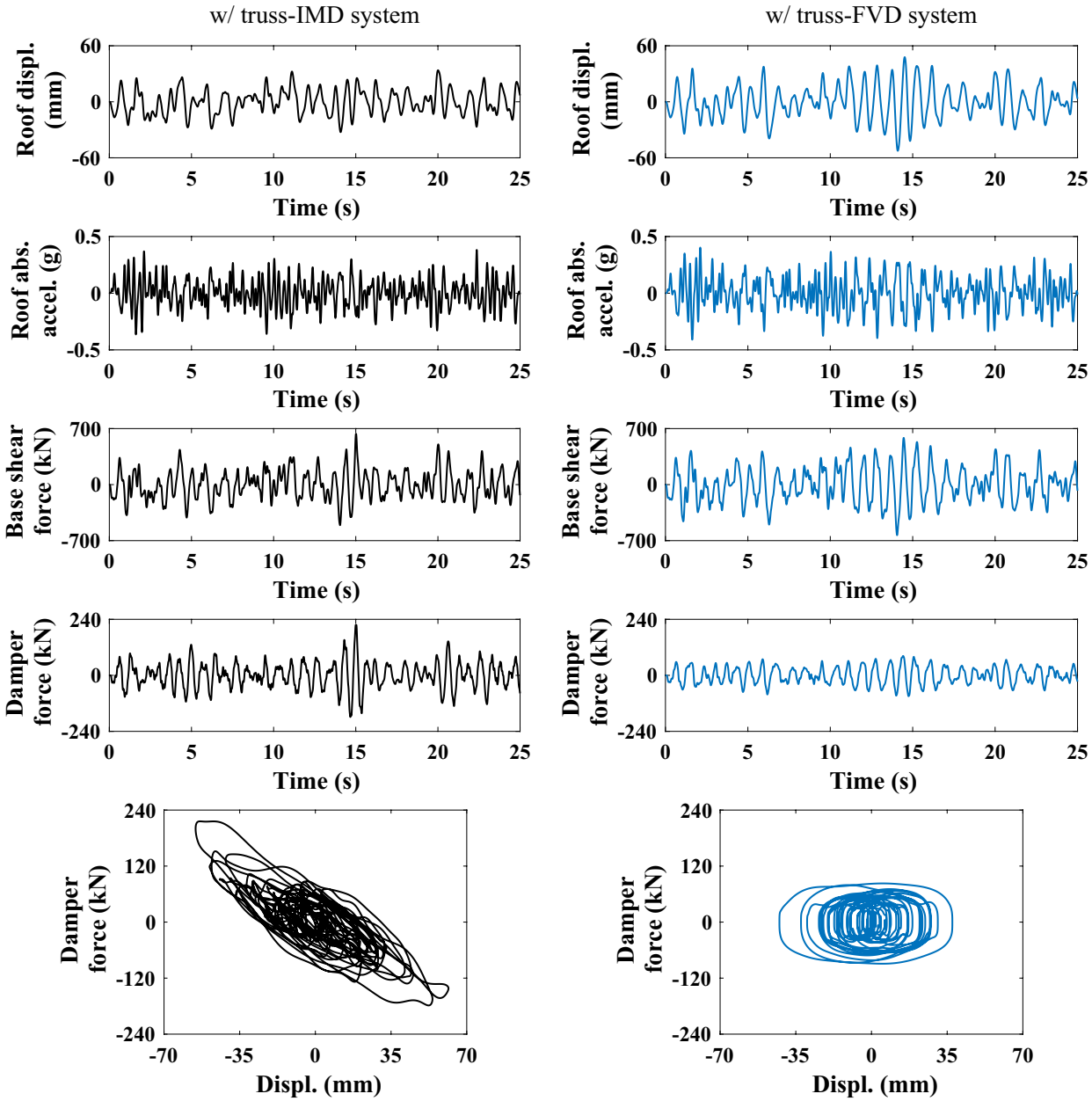

Figure 6.29: Roof story responses, base shear, damper force time-histories of the 6-story building with the optimal damper systems under the Kanai-Tajimi excitation and dampers' hysteretic loops ($\gamma = 0.5$, $\alpha = 0.5$, $\nu = 0.5$).

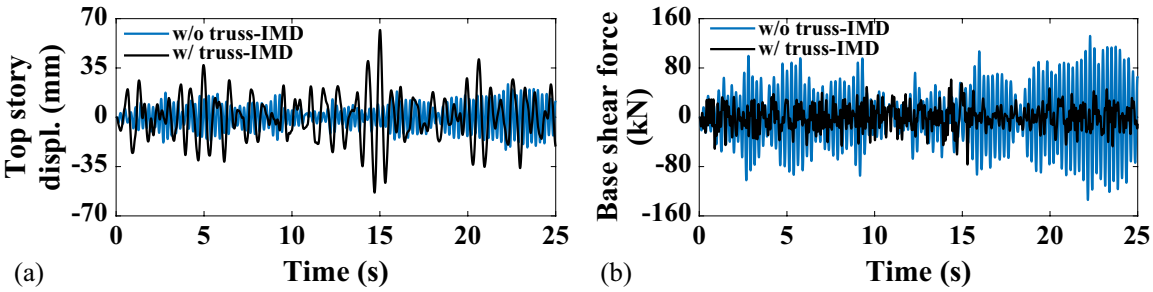

Figure 6.30: Response histories of the core structure with and without an optimal truss-IMD system under the Kanai-Tajimi excitation.

Table 6.5: Realistic earthquake ground motions considered.

Code	Event	Year	Station	Magnitude	Fault type	PGA (g)
EQ1	Imperial Valley	1940	El Centro	6.9	Strike-slip	0.348
EQ2	Imperial Valley	1979	El Centro Array #10	6.5	Strike-slip	0.173
EQ3	Kobe	1995	Kakogawa	6.9	Strike-slip	0.345
EQ4	Northridge	1994	Canoga Park—Topanga Canyon	6.7	Reverse	0.358
EQ5	Kern County	1952	Taft Lincoln School	7.4	Reverse	0.159

signs. The selected earthquakes are summarized in Table 6.5. Figure 6.31 reports the average story displacement, absolute acceleration, interstory drift and story shear force ratios under the five earthquakes, in which the ratios are defined as the ratio of the mean value of a specific structural response with added truss-damper system to that without a truss-damper. For example, the average story displacement ratio is defined as:

$$\text{Average story displacement ratio at } i\text{−th floor} = \frac{1}{5}\sum_{j=1}^{5}\frac{J_{S(i,j)}}{J_{S,org(i,j)}} \tag{6.27}$$

where $J_{S(i,j)}$ and $J_{S,org(i,j)}$ are the mean story displacements of i-th floor under j-th earthquake of the building with and without a truss-damper system, respectively, which are defined as:

$$J_{S(i,j)} = \frac{1}{K_j}\sum_{\kappa=1}^{K_j} abs(x_{(i,j,\kappa)}),\ J_{S,org(i,j)} = \frac{1}{K_j}\sum_{\kappa=1}^{K_j} abs(x_{org(i,j,\kappa)}) \tag{6.28}$$

where K_j is the number of sampling instants of j-th earthquake, $x_{(i,j,\kappa)}$ and $x_{org(i,j,\kappa)}$ are the displacements of i-th floor under j-th earthquake at sampling instant κ for the controlled and uncontrolled building, respectively, and $abs(\cdot)$ is the absolute value function. The average absolute story acceleration, interstory drift and story shear

force ratios have been similarly defined using Eqs. (6.27) and (6.28). These ratios are used to reflect the capability of a truss-damper system in mitigating the overall structural responses during the considered earthquakes, and a response ratio equals 1 indicates no performance improvement. It can be seen from Figure 6.31 that, both the truss-IMD and truss-FVD systems can significantly alleviate the overall responses of the building, and the mean responses generally decrease with increasing truss stiffness. Although both dampers are designed for minimizing the structural interstory drift, the two systems still perform well in reducing the story acceleration and story shear force of the building. It can also be seen from Figure 6.31 that, despite the larger average interstory drift ratio at 5-6th floor, the truss-IMD system in general outperforms the truss-FVD system. In particular, the average story shear force ratios of the truss-IMD system with a truss stiffness ratio of 0.1 are even smaller than those of the truss-FVD system with a stiffness ratio equals 1.

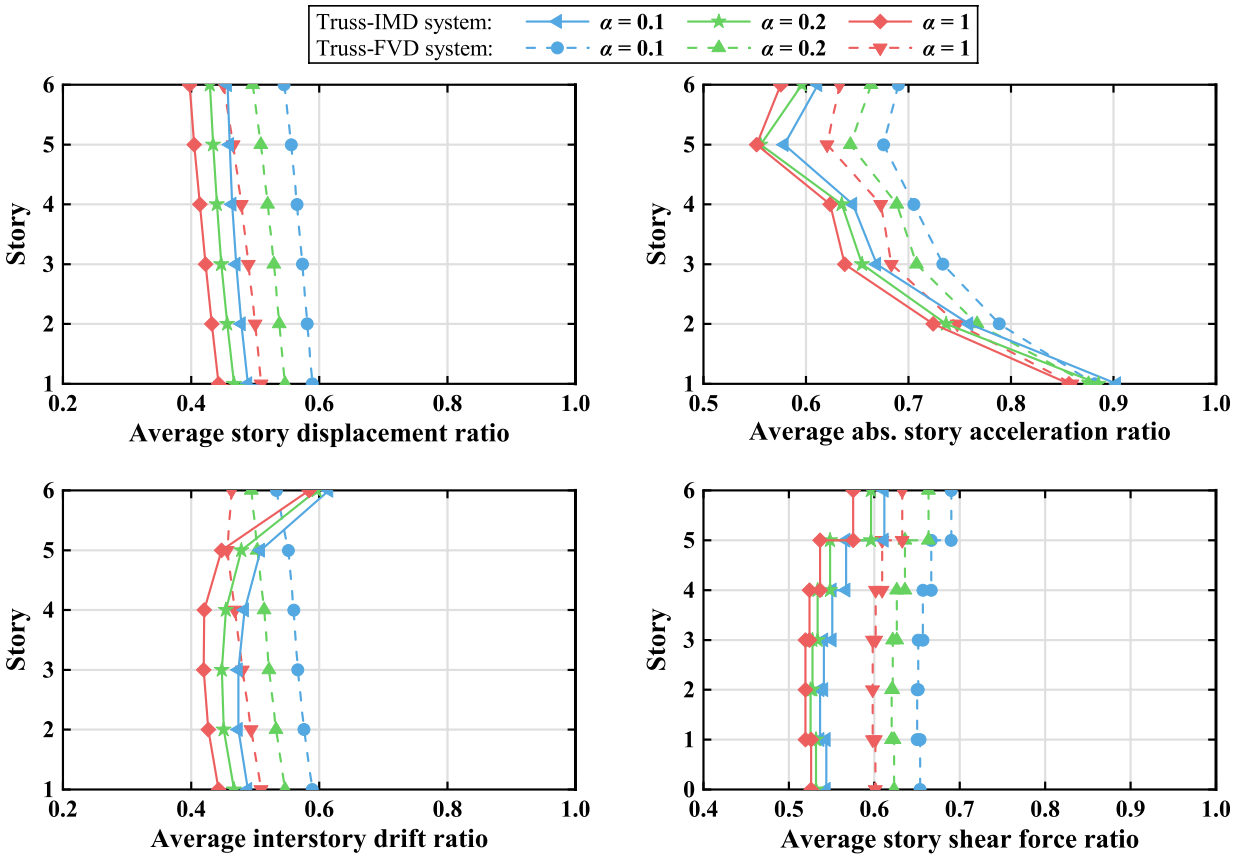

Figure 6.31: Average story response ratios of the atrium building with optimal truss-damper systems under the five earthquakes ($\gamma = 0.5$, $\nu = 0.5$).

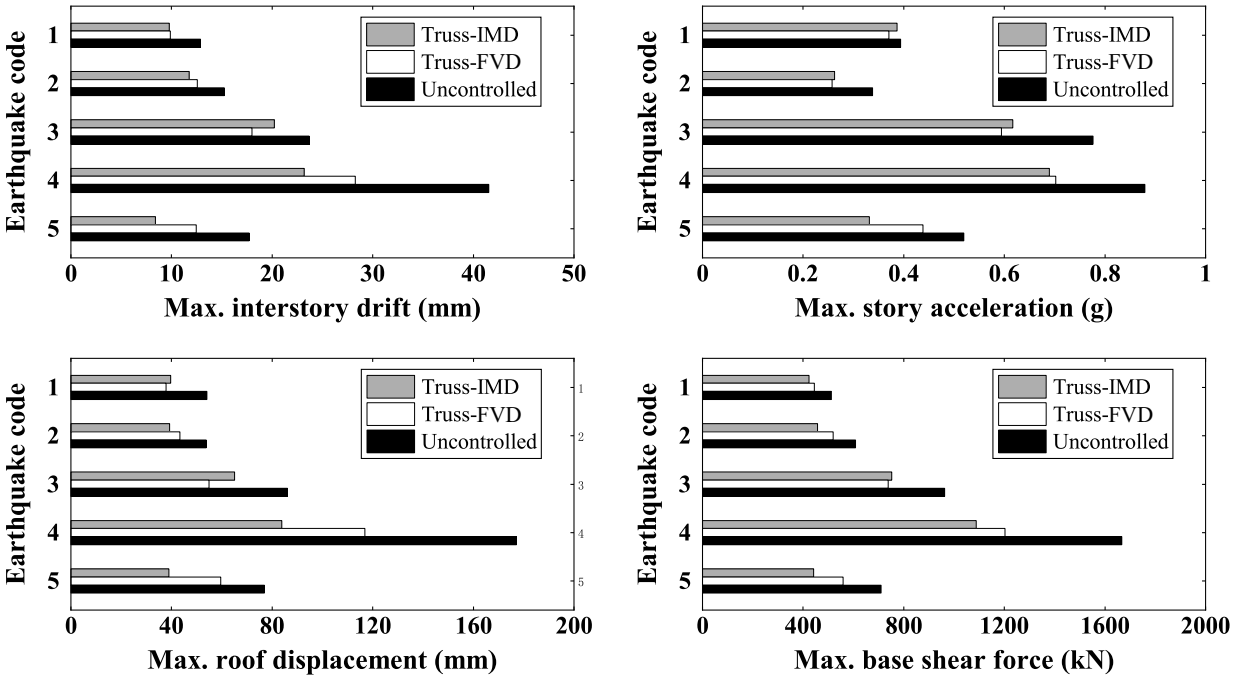

Figure 6.32: Maximum responses of the atrium with optimal truss-damper systems under different earthquakes ($\alpha = 0.1$, $\gamma = 0.5$, $\nu = 0.5$).

The maximum interstory drift, absolute story acceleration, roof displacement and base shear force of the atrium building equipped with an optimal truss-IMD system, an optimal truss-FVD system, and of the uncontrolled building under the five earthquakes are plotted in Figure 6.32 to illustrate the maximum responses and seismic loads of the structure for α equals 0.1, γ equals 0.5 and ν equals 0.5. It can be seen from the figure that, both the truss-IMD and truss-FVD systems can reduce peak responses of the atrium building under different earthquakes, and the maximum structural responses and base shear force of the truss-IMD system are generally smaller than those of the truss-FVD system, although the truss-FVD performs slightly better in earthquake 3 (the Kobe earthquake in 1995).

6.3 Conclusions

A novel truss-damper configuration for vibration control of atrium buildings with a core structure was proposed in this chapter. The effectiveness of a truss-FVD system and a truss-IMD system on mitigating interstory drift response of an atrium building has been numerically evaluated. Results from a simple structural model indicated that the story drift of the atrium building generally decreased with increasing stiffness of the cantilever truss. For a given truss stiffness, there existed an optimal combination of inertance and damping coefficient of the IMD to achieve a best structural performance. Damper nonlinearity was found to have no significant influence

on the maximum building response reduction and the optimal inertance, yet the use of a smaller velocity exponent reduced the optimal damping coefficient for a given truss stiffness. Results from a six-story atrium building showed that the maximum structural response reduction with a truss-IMD system was larger than that with a truss-FVD system, and the damping required from the IMD was smaller. When both damper systems were optimally designed, the IMD was general more effective than the conventional viscous damper. Incremental dynamic analysis has also been conducted on a nonlinear SDOF structural system to evaluate the robustness of the truss-damper systems to the uncertainty of the earthquake excitation input. The proposed truss-damper configuration was shown to be an effective energy dissipation scheme for seismic vibration control of atrium buildings.

Chapter 7 A simplified model for a truss-IMD system and a core structure

In the previous chapter, a truss-damper configuration was introduced for seismic vibration control of an atrium building with an internal core structure, in which the core structure has been simulated as a MODF system. Since the core structure can also be a purpose-built truss structure, of which the structural mass and damping are relatively small compared to the main building, in this chapter, a simplified model that combines a truss-IMD system and a core structure is proposed. The effect of lateral stiffness of the core structure on the seismic performance of the atrium building will be further investigated. A multi-objective optimization approach is developed for the simplified model to minimize the peak interstory drift and story acceleration simultaneously when subjected to a set of different earthquakes, which is achieved by finding the Pareto optimal solutions of a predefined multi-objective optimization problem with discrete fitness functions of the structural responses using a controlled elitist genetic algorithm.

7.1 Analytic model of an atrium building with a simplified truss-IMD-core structure system

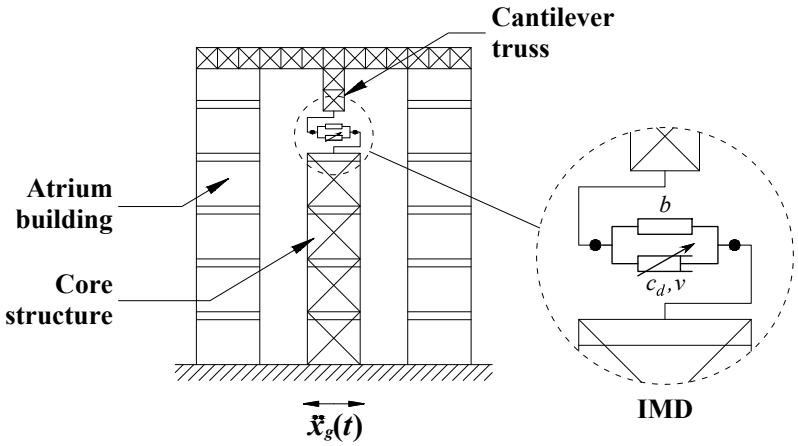

Figure 7.1: Atrium building with a truss-IMD-core structure system.

Figure 7.1 shows the truss-IMD configuration proposed in this study and the core structure connecting the roof of the atrium building to the ground. The core structure in Figure 7.1 is assumed to be a purpose-built truss structure, of which the structural mass and damping are relatively small compared to the main building and could be neglected in the analysis. Therefore, a simplified truss-IMD-core structure

system is proposed for dynamic analysis of an atrium building controlled by a truss-IMD system, in which the core structure is idealized as a spring element with a stiffness coefficient k_c, with the mass and damping been neglected for simplification. The structural system shown in Figure 7.2(a) is thus adopted as the analytic model of a N-story atrium building equipped with a truss-IMD-core structure system, in which m_i, c_i and k_i (i = 1, 2, ..., N) denote the story mass, damping and stiffness coefficients, respectively, b, c_d and ν denote the inertance, damping coefficient and velocity exponent of the IMD, respectively, and k_t is the stiffness of the truss in the horizontal direction.

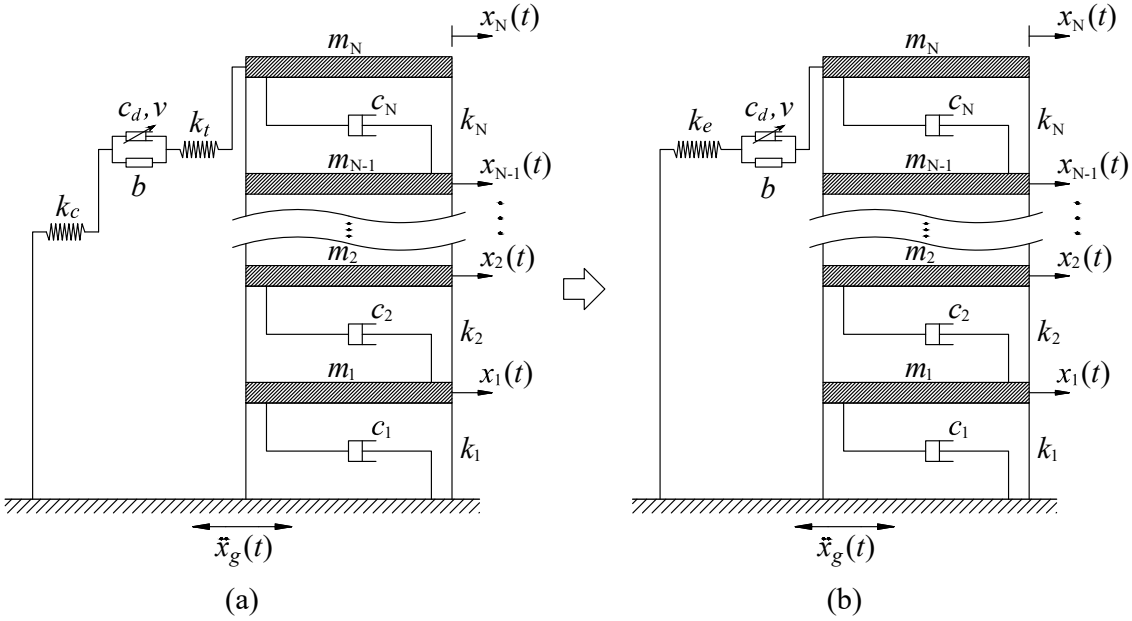

Figure 7.2: (a) Analytic model of an atrium building with a simplified truss-IMD-core structure system and (b) an equivalent model.

The relative displacement between the atrium building and the core structure will transmit to the IMD through the truss. It can be seen from Figure 7.2(a) that, since the core structure has been idealized as a spring and it is in series with the truss, the core structure and the truss can be represented by a spring with an equivalent stiffness coefficient of k_e, as shown in Figure 7.2(b), where:

$$\frac{1}{k_e} = \frac{1}{k_c} + \frac{1}{k_t} \tag{7.1}$$

The effect of the lateral stiffness of the truss and core structure can thus be investigated through an evaluation of the equivalent stiffness of the spring. Importantly, as the IMD and the equivalent spring are arranged in series, the following kinematic

condition must be satisfied:

$$\Delta(t) = \Delta_d(t) + \Delta_e(t) \tag{7.2}$$

where $\Delta(t)$ is the total deformation of the spring and IMD system, $\Delta_d(t)$ and $\Delta_e(t)$ are the deformations of the IMD and the equivalent spring, respectively.

7.1.1 Dynamic response of the atrium building

The equation of motion of the atrium building in Figure 7.2(b) under seismic excitation can be represented by a second-order differential equation:

$$\mathbf{M}\ddot{\mathbf{x}}(t) + \mathbf{C}\dot{\mathbf{x}}(t) + \mathbf{K}\mathbf{x}(t) + \mathbf{F_d}(t) = -\mathbf{M1}\ddot{x}_g(t) \tag{7.3}$$

where $\mathbf{M}$, $\mathbf{C}$ and $\mathbf{K}$ are the N $\times$ N mass, inherent damping, and stiffness matrices of the atrium building, respectively, $x(t)$ is the N$\times$1 response vector of the building, $\mathbf{1}$ is a N $\times$ 1 influence vector with each element equal to unity, and $\ddot{x}_g(t)$ is the horizontal ground acceleration. The damper force vector, $\mathbf{F_d}(t)$, is a N $\times$ 1 vector with the following expression:

$$\mathbf{F_d}(t) = \begin{bmatrix} \mathbf{0}_{(\mathrm{N}-1)\times 1} \\ f_d(t) \end{bmatrix} \tag{7.4}$$

where $f_d(t)$ is the force in the IMD. The equation of motion in Eq. (7.3) can be solved numerically using the state-space technique outlined in Section 3.1.1 to compute the dynamic response of the building during an earthquake input $\ddot{x}_g(t)$. The response-history can be obtained once the damper force $f_d(t)$ is calculated at each computational time instant. The damper force in the IMD can be expressed as:

$$f_d(t) = c_d|\dot{\Delta}_d(t)|^{\nu} sgn(\dot{\Delta}_d(t)) + b\ddot{\Delta}_d(t) = k_e\Delta_e(t) \tag{7.5}$$

To calculate the damper force at each sampling instant, Eq. (7.5) is first rewritten as:

$$\ddot{\Delta}_d(t) + \frac{c_d}{b}|\dot{\Delta}_d(t)|^{\nu} sgn(\dot{\Delta}_d(t)) = \frac{k_e}{b}\Delta_e(t) \tag{7.6}$$

The substitution of Eq. (7.2) into Eq. (7.6) yields:

$$\ddot{\Delta}_d(t) + \frac{c_d}{b}|\dot{\Delta}_d(t)|^{\nu} sgn(\dot{\Delta}_d(t)) + \frac{k_e}{b}\Delta_d(t) = \frac{k_e}{b}\Delta(t) \tag{7.7}$$

The total deformation of the equivalent spring and IMD, $\Delta(t)$, is equal to the roof displacement of the atrium building $x_{\mathrm{N}}(t)$. It can be seen from Eq. (7.7) that the damper deformation $\Delta_d(t)$ can be calculated from an input $\Delta(t)$ (or $x_{\mathrm{N}}(t)$). In this section, similar to the approach outlined in Section 6.2.1, it is assumed that the roof displacement changes linearly between two consecutive sampling instants and Eq. (7.7) becomes an initial value problem at each computational time interval:

$$\begin{gathered}\ddot{\Delta}_d(t) + \frac{c_d}{b}|\dot{\Delta}_d(t)|^{\nu} sgn(\dot{\Delta}_d(t)) + \frac{k_e}{b}\Delta_d(t) = \frac{k_e}{b}(\Delta_0 + \frac{\Delta_1 - \Delta_0}{\Delta t}t), \\ \Delta_d(t_0) = \Delta_{d,0},\ \dot{\Delta}_d(t_0) = \dot{\Delta}_{d,0} \\ \Delta(t_0) = \Delta_0,\ \Delta(t_0 + \Delta t) = \Delta_1 \\ \text{for}\ \ t_0 \le t \le t_0 + \Delta t\end{gathered} \tag{7.8}$$

The roof displacements of the building at two adjacent time steps, $x_{\mathrm{N}}[\mathrm{k}]$ and $x_{\mathrm{N}}[\mathrm{k}+1]$, can be calculated from the structural responses, which are respectively equal to the total deformations of the spring and IMD system at these steps, $\Delta[\mathrm{k}]$ and $\Delta[\mathrm{k}+1]$. Therefore, Eq. (7.8) becomes:

$$\begin{gathered}\ddot{\Delta}_d(t) + \frac{c_d}{b}|\dot{\Delta}_d(t)|^{\nu} sgn(\dot{\Delta}_d(t)) + \frac{k_e}{b}\Delta_d(t) = \frac{k_e}{b}(\Delta[\mathrm{k}] + \frac{\Delta[\mathrm{k}+1] - \Delta[\mathrm{k}]}{\Delta t}t), \\ \Delta_d(0) = \Delta_d[\mathrm{k}],\ \dot{\Delta}_d(0) = \dot{\Delta}_d[\mathrm{k}] \\ \text{for}\quad \mathrm{k}\Delta t \le t \le (\mathrm{k}+1)\Delta t\end{gathered} \tag{7.9}$$

`ode45` based on the explicit Runge-Kutta (4, 5) pair of Dormand and Prince (1980) is also adopted here to solve Eq. (7.9) between two adjacent computational time instants. The next step damper deformation, $\Delta_d[\mathrm{k}+1]$, can be calculated by extracting the numerical solution at $t = (\mathrm{k}+1)\Delta t$. Noting that the substitution of $\Delta_d[\mathrm{k}+1]$ into Eq. (7.2) gives the spring deformation $\Delta_e[\mathrm{k}+1]$. Therefore, the next step damper force $f_d[\mathrm{k}+1]$ can be calculated from either the IMD deformation or the spring deformation using Eq. (7.5).

7.2 Performance assessment of a SDOF atrium building with a simplified truss-IMD-core structure system

To evaluate the effect of the equivalent stiffness of the truss and core structure on dynamic performance of the atrium building, parametric studies will first be conducted using a SDOF model, i.e., a single-story atrium building controlled by a simplified truss-IMD-core structure system. The improved structural performance after the installation of the simplified control system will be assessed based on response reductions in terms of interstory drift and story acceleration of the atrium building.

7.2.1 Minimization of story drift

The performance of an atrium building under seismic excitation is first assessed based on the structural interstory drifts. The performance index PI_D and the corresponding response reduction for interstory drift RR_D defined in Section 6.1.2 are adopted in this section. The equivalent model in Figure 7.2(b) is used to assess the performance of the simplified truss-IMD-core structure system. The simplified control system has four design variables, namely k_e, b, c_d and ν, indicating the stiffness, inertance, damping and nonlinearity of the system, respectively. The first three variables are related to the building properties with three new parameters to facilitate later performance evaluation process:

$$\eta \equiv \frac{k_e}{k_1}, \lambda \equiv \frac{b}{M_1}, \beta \equiv \frac{c_d}{2M_1\omega_1} \tag{7.10}$$

where η is the stiffness ratio of the equivalent spring, λ and β are the inertial mass ratio and damping ratio of the IMD, respectively, k_1 is the first story stiffness of the building, M_1 and ω_1 are the modal mass and natural circular frequency of the first vibration mode of the building, respectively. Notably, η and λ are dimensionless parameters, while β has a unit of $(\text{s/m})^{\nu-1}$.

A SDOF structural model is first considered to assess the effectiveness of the simplified control system. The investigated model has the following properties: structural mass $m = 2533$ kg, structural lateral stiffness $k = 100$ kN/m and inherent damping ratio $\xi = 2\%$. A white-noise acceleration time-history with a zero-mean is adopted to be the ground excitation input of the building model.

Figure 7.3 shows the variations of the story drift response reduction of the atrium building with the stiffness ratio of the equivalent spring and the damping ratio of the IMD for different velocity exponents. From the mesh plots it can be seen that, for a given inertial mass ratio of the IMD, the response reduction generally increases with increasing equivalent stiffness ratio and damping ratio. However, it can also be seen

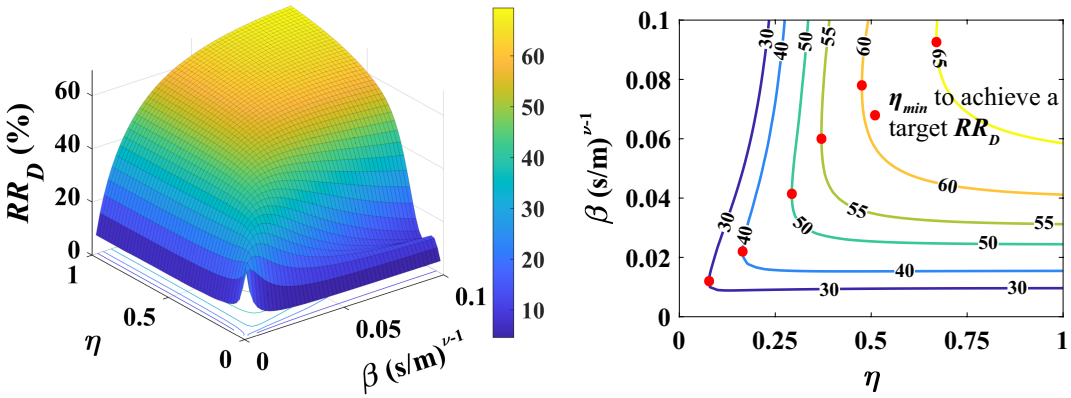

(a) Mesh and contour plots for ν equals 0.6.

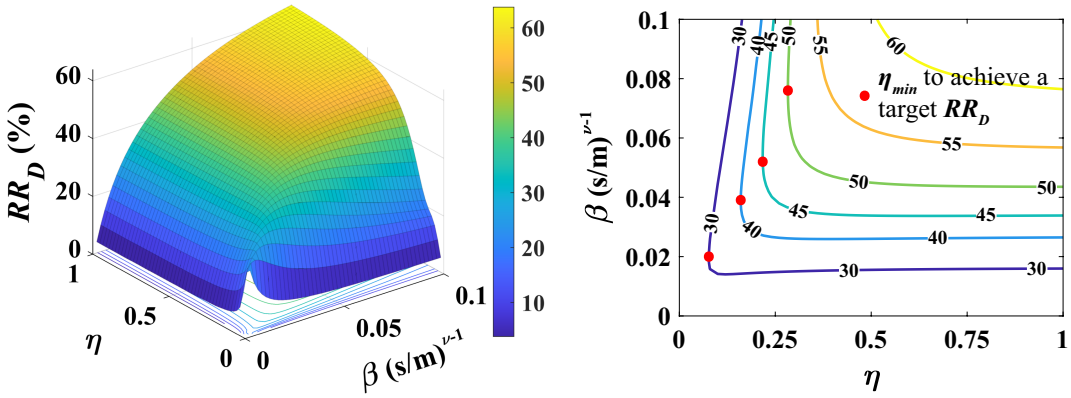

(b) Mesh and contour plots for ν equals 0.8.

Figure 7.3: Three-dimensional mesh plots and contour plots of story drift response reduction versus equivalent stiffness ratio and IMD damping ratio ($\lambda = 0.02$).

that using a larger damping ratio may not result in a greater response reduction, and there exists an optimal damping ratio to maximize the story drift performance for a given equivalent stiffness k_e. A red dot in the contour plots indicates a minimum equivalent stiffness ratio of the truss and core structure, η_{min}, and the corresponding "optimal" damping ratio of the IMD, that are required to achieve a target response reduction. As the target RR_D increases, the required minimum stiffness ratio and "optimal" damping ratio also increase.

Figure 7.4 shows the variations of response reduction in story drift with inertial mass ratio and damping ratio of the IMD for equivalent stiffness ratios of 0.1, 0.2 and 0.5. It can be seen from the figure that, for a given equivalent stiffness of the truss and core structure, there is an optimal combination of inertial mass ratio and damping ratio for the atrium building to achieve a global maximum response reduction. Here, the optimal combination is defined as the optimal design parameters of the IMD for a given stiffness ratio. It can be observed from Figures 7.4(d), (e) and (f) that,

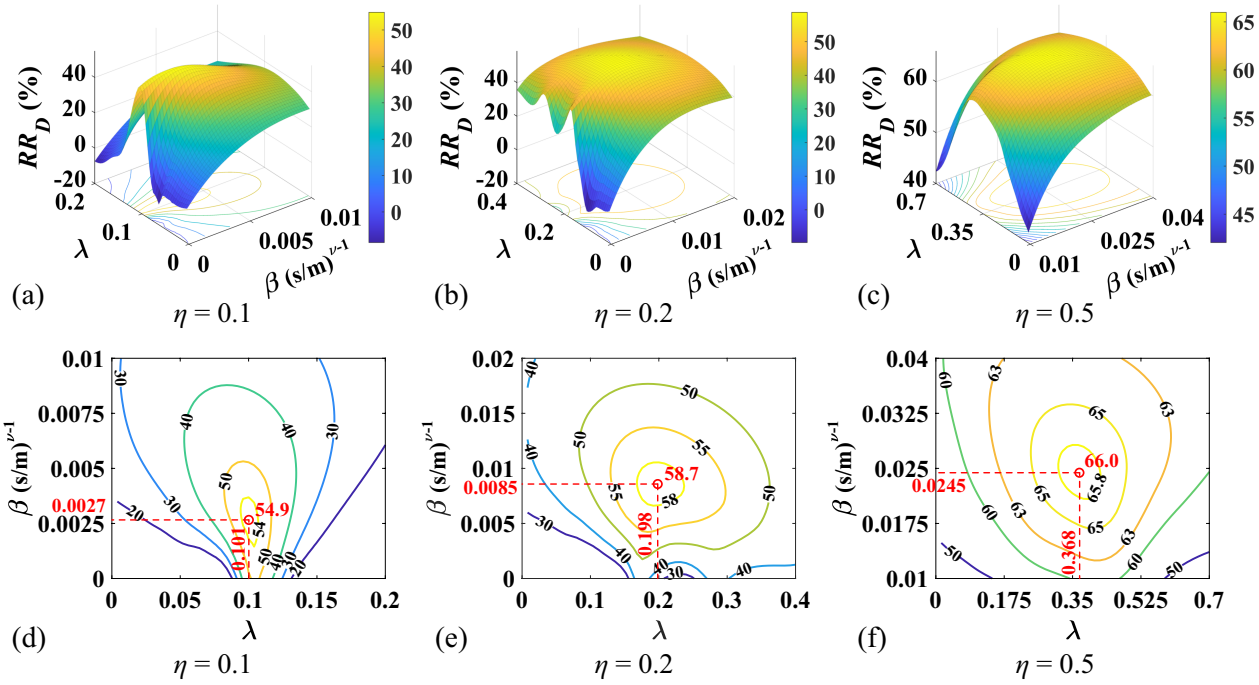

Figure 7.4: Mesh and contour plots of story drift response reduction versus inertial mass ratio and damping ratio of the IMD for different equivalent stiffness ratios ($\nu = 0.4$).

the maximum achievable response reduction of the building increases with increasing equivalent stiffness of the truss and core structure, so do the optimal inertial mass ratio and damping ratio of the IMD.

The maximum story drift response reductions of the atrium building, and the corresponding optimal design parameters of the IMD for different velocity exponents are plotted in Figure 7.5. The optimal parameters are obtained using the genetic algorithm described in Section 3.3 by setting the story drift response reduction as the objective function. It can be seen from Figure 7.5(a) that the maximum response reduction increases rapidly with increasing equivalent stiffness when η is smaller than 0.1; when η becomes larger, the increasing rate of $RR_{D,max}$ reduces significantly. This growth pattern of $RR_{D,max}$ is noted regardless of the magnitude of the velocity exponent, indicating the nonlinearity of IMD has no significant influence on the optimal performance of the truss-IMD system, which agrees with the observations made in Section 6.2.2. From Figures 7.5(b) and (c) it can be seen that, the optimal inertance and damping coefficient of the IMD also increase with the equivalent stiffness; however, for a given stiffness ratio, the optimal inertial mass ratios are similar for different velocity exponents, while a greater amount of optimal damping will be required when using a larger velocity exponent. It can also be seen from Figure 7.5(c)

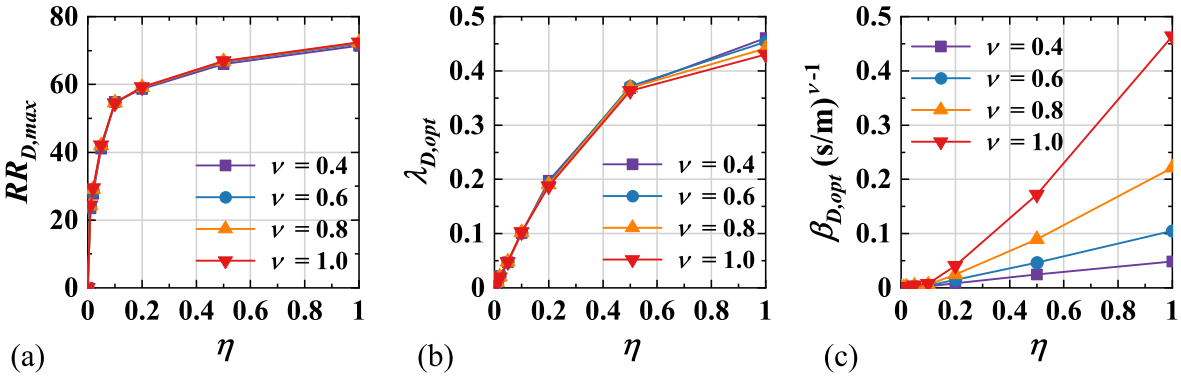

Figure 7.5: (a) Maximum response reductions in story drift, (b) corresponding optimal inertial mass ratios and (c) optimal damping ratios for the atrium building under white-noise excitation.

that the value of the optimal damping coefficient for a given equivalent stiffness increases with the velocity exponent, and for the examined range of equivalent stiffness, the growth rate of the optimal damping ratio increases with increasing stiffness ratio. Moreover, it can be seen from Figure 7.5(a) that when η equals 0.1, the $RR_{D,max}$ is already around 55%, and a further increase in the equivalent stiffness will not result in a significant increase in the $RR_{D,max}$, yet it will cost large amounts of inertance and damping from the IMD, as shown in Figures 7.5(b) and (c).

7.2.2 Minimization of story acceleration

In addition to the performance index in interstory drift, the story acceleration index PI_A and the corresponding response reduction RR_A are also adopted to evaluate the overall seismic performance of the atrium building, as defined in Eqs. (3.13) and (3.15) in Section 3.2.1. Based on the response reduction in story acceleration, the effectiveness of the truss-IMD-core structure system on enhancing acceleration-related performance of the building is assessed using the same SDOF structural model described in Section 7.2.1.

Figure 7.6 shows the three-dimensional mesh plots and contour plots of the response reduction in story acceleration RR_A against the equivalent stiffness ratio and the damping ratio of the IMD for velocity exponent equals 0.6 and 0.8. Similar to RR_D, the story acceleration response reduction also increases with increasing equivalent stiffness ratio. However, it can be seen from the mesh plot in Figure 7.6(a) that, as both η and β become larger, RR_A does not necessarily increase, indicating an excessively large damping will deteriorate acceleration performance of the atrium building. A minimum equivalent stiffness will also be required to achieve a target story acceleration response reduction, as shown in the contour plots, and this

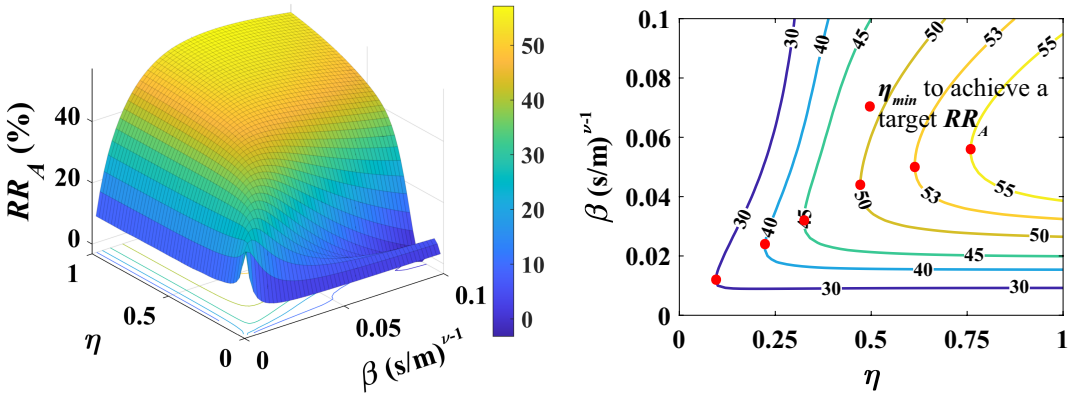

(a) Mesh and contour plots for ν equals 0.6.

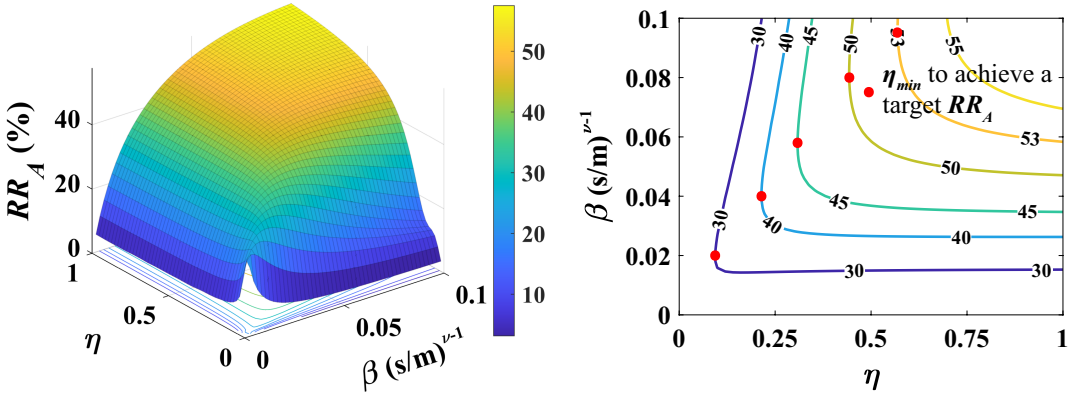

(b) Mesh and contour plots for ν equals 0.8.

Figure 7.6: Three-dimensional mesh plots and contour plots of story acceleration response reduction versus equivalent stiffness ratio and IMD damping ratio (λ = 0.02).

minimum stiffness and the corresponding "optimal" damping ratio are also noted to increase with the response reduction desired.

An optimal combination of the inertance and damping of the IMD also exists to achieve a maximum response reduction in story acceleration $RR_{A,max}$ for a given equivalent stiffness, as shown in Figure 7.7. The optimal inertial mass ratio and damping ratio are also noted to increase with increasing equivalent stiffness. However, it can be seen from Figures 7.7(d), (e) and (f) that, for a given equivalent stiffness ratio, the optimal IMD design variables required to achieve a maximum response reduction in story acceleration are generally smaller than those parameters showing in Figure 7.4 for maximizing the story drift response reduction, which indicates that the optimal IMD parameters for the story drift performance may be too large for the story acceleration performance of the atrium building, namely, optimize one performance may deteriorate the other.

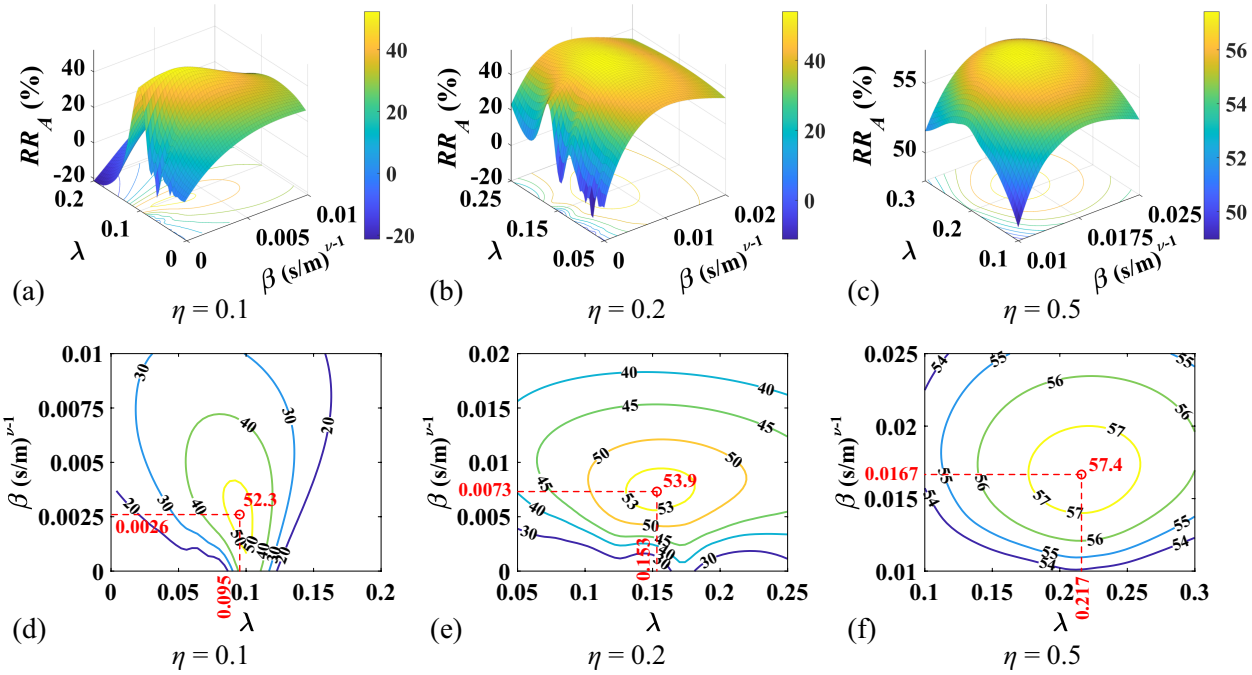

Figure 7.7: Mesh and contour plots of story acceleration response reduction versus inertial mass ratio and damping ratio of the IMD for different equivalent stiffness ratios ($\nu = 0.4$).

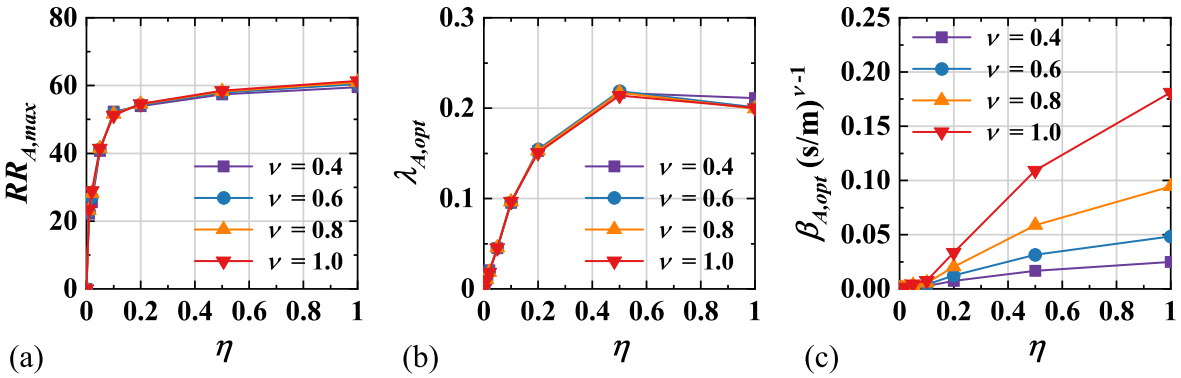

Figure 7.8: (a) Maximum response reductions in story acceleration, (b) corresponding optimal inertial mass ratios and (c) optimal damping ratios for the atrium building under white-noise excitation.

Figure 7.8 shows the achievable maximum story acceleration response reductions of the atrium building, and the corresponding optimal inertial mass ratios and damping ratios, against the equivalent stiffness ratio for different velocity exponents. Similar to the maximum story drift response reduction, $RR_{A,max}$ increases sharply when $\eta < 0.1$ and tends towards a diminishing return, as can be seen from Figure 7.8(a). However, in terms of the optimal IMD inertance, for the examined range of η, unlike $\lambda_{D,opt}$ that increases continuously with η, $\lambda_{A,opt}$ stops growing when $\eta > 0.5$. More-

over, it can be observed from Figures 7.8(a) and (b) that the optimal inertance and damping for story acceleration are generally smaller than those for maximizing the story drift performance.

7.3 Multi-objective optimal design of a truss-IMD system

To further assess the effectiveness of the proposed truss-IMD system on mitigating seismic response of atrium buildings, a six-story shear-type building is considered with the following properties: the story mass and stiffness of the building are identical for all floors, namely, $m_1 = m_2 = \cdots = m_6 = 50 \times 10^3$ kg and $k_1 = k_2 = \cdots = k_6 = 40$ MN/m; the fundamental period of the structure T_1 is 0.92 second. A 3% inherent damping is assigned to the building, and a truss-IMD system is used to connect the roof with a core structure. The building is designated occupancy category II based on ASCE 7-05 (ASCE 2005), and it is assumed to locate in downtown Los Angeles in California, USA, on stiff soil that is classified as site class D. The seismic design parameters considered are summarized in Table 7.1. A controlled elitist genetic algorithm developed based on the NSGA-II (Deb et al. 2002) will be used to solve a multi-objective optimization problem that is defined to minimize the interstory drift and story acceleration of the building simultaneously. The description of the multi-objective optimization algorithm can be found in Section 3.3.

Table 7.1: Seismic design parameters.

Parameters	value
Risk/Occupancy category	II
Importance factor	1
Seismic design category	D
Site class	D
MCE[1] spectral response acceleration parameter at short periods S_S (g)	1.947
MCE spectral response acceleration parameter at period of 1 sec S_1 (g)	0.733
Short period site coefficient F_a	1
Long period site coefficient F_v	1.5
Spectral response acceleration parameter at short periods S_{DS} (g)	1.298
Spectral response acceleration parameter at period of 1 sec S_{D1} (g)	0.733
Long-period transition period T_L (s)	8

[1]Maximum Considered Earthquake.

7.3.1 Optimization problem formulation

A practical design problem in structural engineering often requires multiple performance objectives to be satisfied simultaneously; for instance, minimizing interstory drift and story acceleration at the same time. However, the improvement of a performance objective may lead to degrading of others. To solve such a design problem,

multi-objective optimization shall be implemented, which can output the Pareto front for satisfying different combinations of the performance objectives. Notably, any solution lies on the Pareto front of a multi-objective optimization problem is deemed an acceptable solution, as none of the solutions can be identified as the "best" one, namely, none of the solution dominates. In this study, a controlled elitist genetic algorithm based on NSGA-II (Deb et al. 2002) that has been introduced in Section 3.3 is adopted to solve the multi-objective optimization problems.

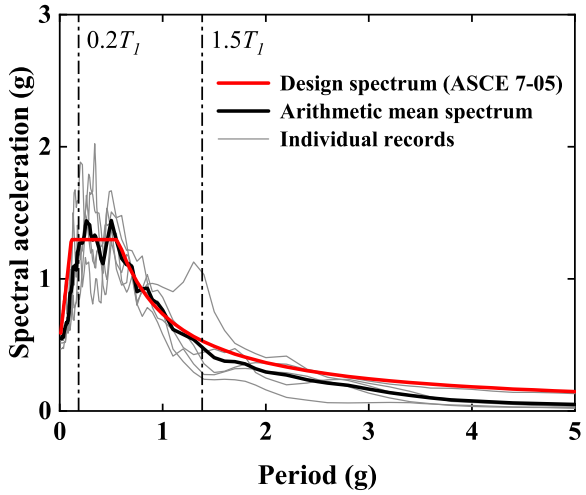

Figure 7.9: Design response spectrum at downtown Los Angeles (based on parameters in Table 7.1) and acceleration response spectrums of the selected earthquakes.

The optimal design present here aims at finding the combinations of IMD inertance and damping coefficient to minimize structural responses in interstory drift and story absolute acceleration simultaneously under multiple earthquake inputs, for a given equivalent stiffness of the truss and core structure. To achieve the optimal design, an optimization problem is first formulated as:

$$\begin{aligned} Find: \quad & \lambda_{opt} \text{ and } \beta_{opt} \\ Minimize: \quad & f_1 = max\left(\frac{PI_D(j)}{PI_{D,org}(j)}\right) \\ & f_2 = max\left(\frac{PI_A(j)}{PI_{A,org}(j)}\right) \\ & j = 1,\ 2,\ ...,\ \mathrm{w} \end{aligned} \tag{7.11}$$

where λ_{opt} and β_{opt} are the optimal solutions (design parameters) of the formulated problem, f_1 and f_2 are the fitness functions for interstory drift and story acceleration of the building, respectively, and w is the total number of earthquakes considered. Noting that a larger ratio of $PI_D(j)$ to $PI_{D,org}(j)$ (or $PI_A(j)$ to $PI_{A,org}(j)$) represents

a larger structural response under the j-th earthquake.

7.3.2 Numerical analyses and discussion

In this numerical example, five ground motion records were selected for design and analysis of the example building. These ground motions were scaled to have a mean response spectrum that approximately matches the design response spectrum of the construction site, especially between periods of $0.2T_1$ and $1.5T_1$, as illustrated in Figure 7.9. The design spectrum is computed based on the parameters listed in Table 7.1 per ASCE 7-05 (ASCE 2005). The selected earthquake events are summarized in Table 7.2.

Table 7.2: Selected ground motions used in the numerical example.

Code	Earthquake event	Year	Station	Magnitude	PGA (g)	Scale factor
EQ1	Imperial Valley-02	1940	El Centro Array #9	6.95	0.48	1.83
EQ2	Managua, Nicaragua-01	1972	Managua - ESSO	6.24	0.60	1.79
EQ3	Coyote Lake	1979	Gilroy Array #4	5.74	0.53	2.29
EQ4	Imperial Valley-06	1979	EC County Center FF	6.53	0.47	2.21
EQ5	Corinth, Greece	1981	Corinth	6.60	0.53	2.33

The inertial mass damper installed in between the building roof and the core structure has been designed for minimizing the interstory drift and story absolute acceleration simultaneously under the selected earthquakes, through solving the multi-objective problem formulated in Eq. (7.11) using the controlled elitist GA. In this study, the size of population and the maximum number of generations of the genetic algorithm are set to 60 and 50, respectively, and a constant mutation probability of 0.02 is used. For a given equivalent stiffness, all the parameter combinations lie on the Pareto front are deemed optimal solutions for the optimization problem, denoted as λ_{opt} and β_{opt} for the optimal inertial mass ratios and damping ratios, respectively. Although the upper and lower bounds of the two parameters have no significant influence on the optimal solutions if being included, to increase the convergence rate of the algorithm, the upper and lower bounds for both the inertial mass ratio and damping ratio have been set to 0.1 (for β the unit is $(\mathrm{s/m})^{0.5}$) and 0, respectively, for η equals 0.5 and ν equals 0.5. These bounds were decided through trial-and-error to ensure the inclusion of optimal solutions. As can be seen from Table 7.3, the optimal design variables are within the decided bounds.

Table 7.3: Optimal design parameters of the IMD ($\eta = 0.5$, $\nu = 0.5$).

Optimal parameter combinations of IMD	λ_{opt}	β_{opt} (s/m)$^{0.5}$
Combo 1	0.0473	0.0471
Combo 2	0.0398	0.0397
Combo 3	0.0381	0.0342

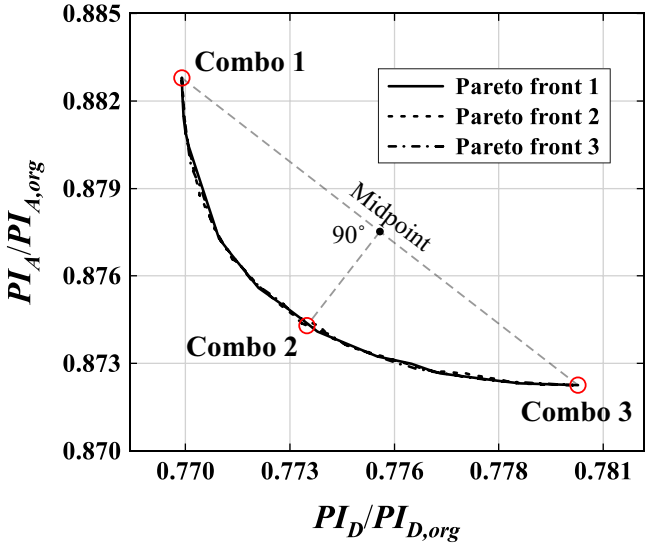

Figure 7.10: Pareto fronts of the multi-objective optimization problem for the atrium building under the selected earthquakes ($\eta = 0.5$, $\nu = 0.5$).

To ensure accuracy of the optimal solutions, the design problem has been solved several times using the genetic algorithm. Figure 7.10 shows the Pareto optimal solutions computed from three different runs of the algorithm for η equals 0.5 and ν equals 0.5. It can be seen from the figure that the three Pareto fronts generally match with each other, and there exist multiple combinations of the ratios of performance indices in interstory drift and story acceleration that can be achieved by the truss-IMD system. All these combinations are considered as optimal solutions to design the IMD, and designers of the atrium building can select desired combinations according to the design requirements. Here, the performances of a combination that minimizes the interstory drift, denoted as "Combo 1", a combination minimizing the the story acceleration, denoted as "Combo 3", and a "Combo 2" lies between the combinations 1 and 3, are compared in this study. The location of Combo 2 is determined from a perpendicular extending from the midpoint of a line that connects Combo 1 and Combo 3, as shown in Figure 7.10, and the optimal design parameters of the three combinations are listed in Table 7.3. To evaluate the effectiveness of the truss-IMD systems with these optimal parameter combinations, the mean structural

responses and the average base shear force of the building under the five earthquakes are summarized in Table 7.4. It can be seen from the table that all of the three parameter combinations can significantly alleviate the examined structural responses. When equipped with the truss-IMD systems, the mean values of interstory drift, story displacement, story acceleration and base shear force are reduced by around 45%, 35%, 27% and 36%, respectively (these percentages show the average response reductions of the three combinations). It can also be observed from Table 7.4 that the IMD system with parameter Combo 1 mitigates more structural interstory drift and story displacement among the three combinations, while Combo 3 performs better in reducing base shear force of the building under the five earthquakes.

Table 7.4: Mean responses of the atrium building with different parameter combinations under selected ground motions ($\eta = 0.5$, $\nu = 0.5$).

Parameter combinations	Interstory drift (mm)	Story displ. (mm)	Story accel. (m/s^2)	Base shear (kN)
Uncontrolled	1.04	3.51	0.44	55.52
Combo 1	0.55	2.17	0.32	36.47
Combo 2	0.57	2.29	0.32	35.31
Combo 3	0.59	2.40	0.32	34.88

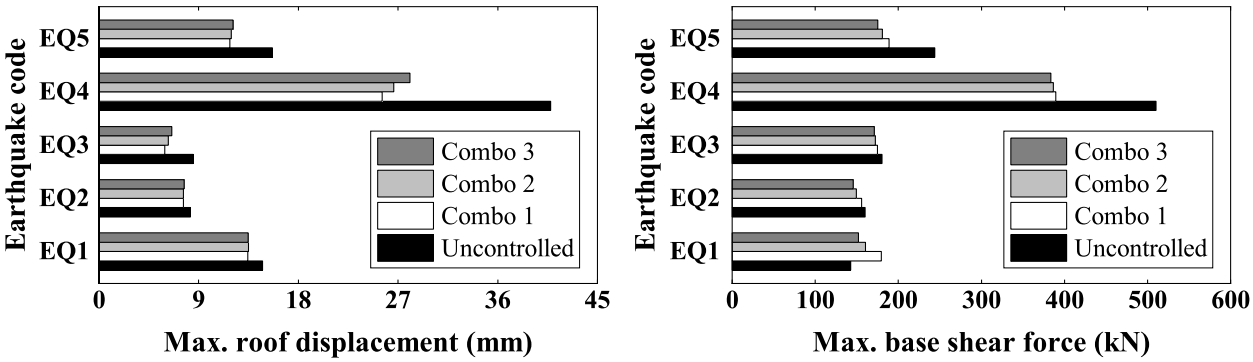

Figure 7.11: Maximum roof displacements and base shear forces of the atrium building under different earthquakes.

Figure 7.11 shows the maximum roof displacement and base shear force of the atrium building with the optimal truss-IMD-core structure systems and the uncontrolled structure under the five selected earthquakes. From the figure it can be observed that the maximum roof displacements of the controlled building with parameter Combo 1 are generally smaller than those with the other two parameter combinations, and the truss-IMD system with parameter Combo 3 outperformed

those with Combo 1 and Combo 2 in reducing the peak base shear forces. However, as root-mean-square of the responses are used as the performance indices, and five earthquakes have been considered in the optimizations, not all of the optimal combinations can reduce the maximum response of the building. For example, the maximum base shear force under the EQ1 excitation is amplified with the optimal IMD systems. To further illustrate the seismic behaviour of the atrium building with an optimal truss-IMD-core structure system, the time-histories of story displacement and absolute acceleration of the first, fourth and sixth floors with parameter Combo 2 under the EQ5 Corinth earthquake are plotted, as shown in Figure 7.12. As can be seen, the supplemental control system can effectively mitigate the overall structural responses of the building during the earthquake.

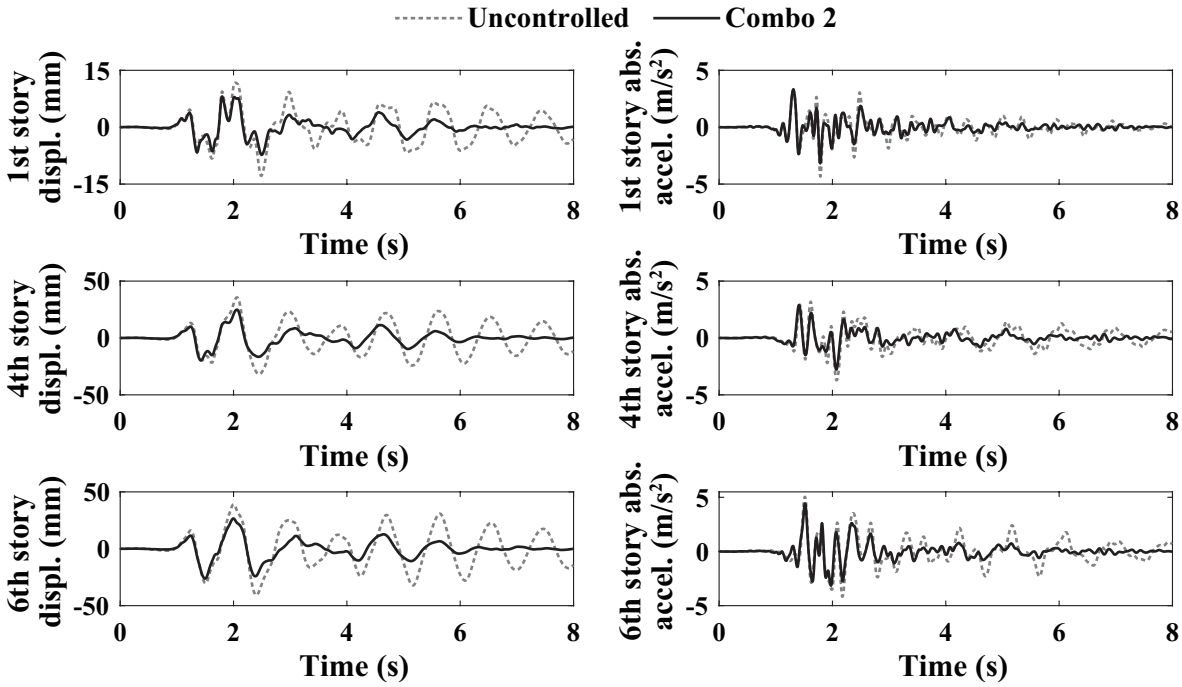

Figure 7.12: Story displacement and acceleration time-histories of the uncontrolled building and with the parameter Combo 2 IMD system under the EQ5 Corinth earthquake.

7.4 Conclusions

This chapter further evaluated the performance of the truss-IMD system in mitigating seismic response of atrium buildings using a simplified model for the truss-IMD system and the core structure. In addition to the response reduction in interstory drift, a story acceleration response reduction index was adopted to assess the effectiveness of the proposed system on suppressing structural accelerations of the building.

Results from the parametric studies on a simple structure showed that the dynamic performance of the atrium building generally improved with an increasing equivalent stiffness of the cantilever truss and the core structure, and a minimum equivalent stiffness was required to achieve a target response reduction of the building. For a preset damper nonlinearity, the inertance and damping coefficient of the IMD can also be optimally determined to maximize a response reduction for a given equivalent stiffness. A multi-objective optimization approach has been developed for the truss-IMD system to minimize the structural interstory drift and story acceleration simultaneously under multiple earthquake inputs. The optimization results of a 6-story building suggested good performance of the optimal truss-IMD systems designed based on the developed approach, e.g., the mean responses in interstory drift and base shear force of the building were reduced by around 45% and 36% respectively when equipped with the optimal control systems, and the maximum responses in roof displacement and base shear force were also alleviated by the optimal systems.

Chapter 8 Conclusions and future research

8.1 Conclusions

Passive energy dissipation devices such as fluid viscous dampers are frequently adopted in seismic vibration control of civil engineering structures. This thesis investigated the effectiveness of the fluid vicious damper and an inertial mass damper with nonlinear damping characteristic on improving seismic performance of building structures, when the devices are installed in conjunction with supporting elements. Different numerical approaches include state-space technique and Runge-Kutta methods were adopted to compute the dynamic response-histories of structures with different damper systems, and the correctness and feasibility of a numerical time-history approach developed for a nonlinear damper-brace system were evaluated in Chapter 4. The effects of brace stiffness and nonlinearity of the viscous dampers on the seismic performance of a building were investigated in Chapter 5 through parametric studies, and an optimization approach for the damper-brace systems was developed. In addition to the damper-brace assembly for conventional frame buildings without a large internal open space, a truss-damper configuration was proposed in Chapter 6, which is specifically for the vibration mitigation of atrium buildings. The thesis also introduced a simplified model for a truss-IMD-core structure system in Chapter 7, and a multi-objective optimization approach for the simplified system was also presented to minimize structural interstory drift and story acceleration of an atrium building simultaneously. The following important observations have been made from the investigations of different damper systems:

1. There exists an infinite combination of design parameters for a damper-brace system, or a truss-damper system, to achieve a specific response reduction of a building, yet a minimum stiffness of the supporting elements will be required to obtain the desired performance. For a given stiffness of the supporting elements, the damper parameters can be optimally determined to maximize the response reduction of the building, as shown in Chapters 5, 6, and 7.

2. The structural performance can generally be improved as the stiffness of the supporting elements increases; however, a large stiffness is not necessary for a building to achieve an acceptable performance level, as a diminishing return can generally be observed in the maximum response reductions of the structure as the support stiffness becomes larger, as shown in Chapters 5, 6, and 7.

3. The velocity exponent of FVDs and IMDs has a significant influence on the seismic performance of a building for given damping coefficients of the FVDs, or preset inertances and damping coefficients of the IMDs. However, the damper nonlinearity generally has an insignificant effect on the maximum response reductions of the structure, as shown in Chapters 5 and 6; the velocity exponent also has no significant influence on the optimal inertance of the IMD, as shown in Chapters 6 and 7.

4. In a linear structural system, if the intensity of ground excitation is uniformly changed, the original optimal linear dampers still exhibit their best performance, yet the optimal nonlinear dampers may no longer be the optimal ones. However, compared with linear viscous dampers, the nonlinear ones with a velocity exponent smaller than unity is capable of reducing peak damper force while achieving a similar structural response reduction, as shown in Chapter 5.

5. The use of the optimal dampers for maximizing displacement-based response reductions may not obtain a desirable acceleration-based response reduction of a building, and an increase in displacement-related performance may be at the expense of deteriorations in structural acceleration and base shear performances, as shown in Chapter 5. However, multi-objective optimization allows one to select the design parameters to achieve performance objectives in displacement and acceleration simultaneously, as shown in Chapter 7.

6. For a given set of damper nonlinearity and truss stiffness, there exists an optimal combination of inertance and damping coefficient for the truss-IMD system to maximize a response reduction of an atrium building, as shown in Chapter 6.

7. The proposed truss-damper configuration is effective in the mitigation of dynamic response of atrium buildings, and the optimal truss-IMD system generally outperforms the optimal truss-FVD system in suppressing structural responses in story displacement, acceleration, interstory drift and story shear force, as shown in Chapter 6.

8. For the truss-damper configuration, the core structure stiffness also has a great influence on the seismic performance of an atrium building, and the maximum response reduction of the building could be enhanced by using a larger equivalent stiffness of the truss and core structure, followed by an optimization of the damper parameters, as shown in Chapter 7.

The thesis makes several contributions to the literature. First, this study investi-

gated the influences of supporting element stiffness and damper nonlinearity on the effectiveness of fluid viscous damper and inertial mass damper in mitigating seismic response of building structures, especially when optimal performance of a building was reached. Second, a novel truss-damper configuration was proposed in this study that can achieve an effective vibration control of atrium-type buildings during earthquakes. Third, whereas much research analysed the nonlinear dampers based on equivalent linearization approaches, this study explicitly dealt with the damper nonlinearity in the analysis of different damper systems, especially for the truss-IMD system, which yielded results that enable one to gain new insight into the dynamic behaviours of the nonlinear dampers with supporting elements. Finally, this study presented approaches to achieve robust designs of the brace-damper and truss-damper assemblies in building structures, which could facilitate the design and application of such "supporting element-damper" configurations in practical projects.

8.2 Future research

In addition to the topics investigated in this thesis, several research problems related to the passive energy dissipation systems still need to be addressed and warrant future exploration:

- Inerter shows high potential in upgrading conventional seismic control systems, while the real application of inerters in civil engineering is rather limited. Further investigations are still required in (i) inerter-based seismic control systems for specific types of civil structures (e.g., offshore structures) and (ii) practical applications of the inerter-based seismic control technology.

- Evaluating the extent of damage suffered by a structure and by its structural components under seismic loads is an important topic in the framework of performance-based design, yet few works have been reported on the damage assessment of a building or a certain structural component with an inerter-based control system (e.g., an IMD). Further investigations on this topic are warranted.

- The thesis adopted Chevron braces as the supporting elements of FVDs. Approaches that incorporate the stiffness of different brace components in more complicate brace configurations, such as toggle braces and scissor-jack braces, into the design of different types of dampers should be developed to facilitate practical design of the damper-brace systems.

- Unlike a negative stiffness device that exhibits a constant stiffness coefficient during its operation, the force-displacement relationship of an inerter has a neg-

ative slope that changes with excitation frequency. Therefore, it is worthwhile to conduct further investigations on the dynamic behaviour of IMDs at different excitation frequencies and develop new strategies to control the large damper forces that may be possibly induced.

- Experimental work is required to validate the proposed analytic models and numerical approaches, especially for the IMD systems. Cyclic element tests should be performed on the damper-brace assembly and the truss-damper systems to verify the assumptions made in their rheological behaviours, and the numerical simulation approaches should be further evaluated by shaking table tests with white-noise and realistic earthquake excitation.

List of publications

- Li, S., Chen, Y.-T., Li, B. and Wah, W. S. L. (2022), 'Seismic vibration control of atrium buildings using a truss-nonlinear inertial mass damper system', *International Journal of Structural Stability and Dynamics* **22**(14), 2250164.

- Li, S. and Chen, Y.-T., Seismic response mitigation of atrium buildings with truss-IMD system, *17th East Asia-Pacific Conference on Structural Engineering and Construction*, Singapore, 27 June 2022.

- Li, S. and Chen, Y.-T., A novel truss-damper configuration for seismic control of atrium buildings, *13th International Conference on Structural Safety and Reliability*, Shanghai, China, 13 September 2022.

- Li, S., Chen, Y.-T., Chai, Y. H. and Li, B. (2021), 'Effects of brace stiffness and nonlinearity of viscous dampers on seismic performance of structures', *International Journal of Structural Stability and Dynamics* **21**(13), 2150188.

- Li, S. and Chen, Y.-T., Seismic design of shear-type buildings with Maxwell model-based nonlinear damper-brace systems, *17th World Conference on Earthquake Engineering*, Sendai, Japan, 27 September 2021.

Bibliography

Akcelyan, S., Lignos, D. G., Hikino, T. and Nakashima, M. (2016), 'Evaluation of simplified and state-of-the-art analysis procedures for steel frame buildings equipped with supplemental damping devices based on E-Defense full-scale shake table tests', *Journal of Structural Engineering, ASCE* **142**(6), 04016024.

Aldea, S., Bazaez, R., Astroza, R. and Hernandez, F. (2021), 'Seismic fragility assessment of Chilean skewed highway bridges', *Engineering Structures* **249**, 113300.

Alembagheri, M. and Ghaemian, M. (2013), 'Damage assessment of a concrete arch dam through nonlinear incremental dynamic analysis', *Soil Dynamics and Earthquake Engineering* **44**, 127–137.

Alhaddad, W., Halabi, Y., Xu, H. and Lei, H. (2020), 'A comprehensive introduction to outrigger and belt-truss system in skyscrapers', *Structures* **27**, 989–998.

Ali Sadeghian, M., Yang, J., er Wang, X. and Wang, F. (2021), 'Novel adaptive tuned viscous inertance damper (ATVID) with adjustable inertance and damping for structural vibration control', *Structures* **29**, 814–822.

Altieri, D., Tubaldi, E., De Angelis, M., Patelli, E. and Dall'Asta, A. (2018), 'Reliability-based optimal design of nonlinear viscous dampers for the seismic protection of structural systems', *Bulletin of Earthquake Engineering* **16**(2), 963–982.

Asadpour, G., Asadi, P. and Hajirasouliha, I. (2022), 'A new modified stochastic linearization technique to analyze structures with nonlinear fluid viscous dampers', *Journal of Vibration and Control* **28**, 2746–2761.

ASCE (2000), *Prestandard and commentary for the seismic rehabilitation of buildings, FEMA 356*, American Society of Civil Engineers, Reston, Virginia, USA.

ASCE (2005), *Minimum design loads for buildings and other structures, ASCE/SEI 7-05*, American Society of Civil Engineers, Reston, Virginia, USA.

ASCE (2017), *Minimum design loads and associated criteria for buildings and other structures, ASCE/SEI 7-16*, American Society of Civil Engineers, Reston, Virginia, USA.

Bahnasy, A. and Lavan, O. (2013), Linear or nonlinear fluid viscous dampers? A seismic point of view, *in* 'Proceedings of Structures Congress 2013', Pittsburgh, Pennsylvania, USA, pp. 2253–2264.

Bakhshinezhad, S. and Mohebbi, M. (2020), 'Multi-objective optimal design of semi-active fluid viscous dampers for nonlinear structures using NSGA-II', *Structures* **24**, 678–689.

Beg, A. H. and Islam, M. Z. (2016), Advantages and limitations of genetic algorithms for clustering records, *in* 'Proceedings of IEEE 11th Conference on Industrial Electronics and Applications', Hefei, China, pp. 2478–2483.

Bekdaş, G. and Nigdeli, S. (2011), 'Estimating optimum parameters of tuned mass dampers using harmony search', *Engineering Structures* **33**(9), 2716–2723.

Bekdaş, G., Nigdeli, S. and Yang, X. (2018), 'A novel bat algorithm based optimum tuning of mass dampers for improving the seismic safety of structures', *Engineering Structures* **159**, 89–98.

Bharti, S., Dumne, S. and Shrimali, M. (2010), 'Seismic response analysis of adjacent buildings connected with MR dampers', *Engineering Structures* **32**(8), 2122–2133.

Bigdeli, K., Hare, W., Nutini, J. and Tesfamariam, S. (2016), 'Optimizing damper connectors for adjacent buildings', *Optimization and Engineering* **17**(1), 47–75.

Cao, L. and Li, C. (2022), 'A high performance hybrid passive base-isolated system', *Structural Control and Health Monitoring* **29**(3), e2887.

Cash, J. R. and Karp, A. H. (1990), 'A variable order Runge-Kutta method for initial value problems with rapidly varying right-hand sides', *ACM Transactions on Mathematical Software* **16**(3), 201–222.

Castaldo, P. and De Iuliis, M. (2014), 'Optimal integrated seismic design of structural and viscoelastic bracing-damper systems', *Earthquake Engineering and Structural Dynamics* **43**(12), 1809–1827.

Chen, L., Sun, L. and Nagarajaiah, S. (2015), 'Cable with discrete negative stiffness device and viscous damper: Passive realization and general characteristics', *Smart Structures and Systems* **15**(3), 627–643.

Chen, M. Z. and Hu, Y. (2019), *Inerter and its application in vibration control systems*, 1st edn, Springer, Singapore.

Chen, Y.-T. and Chai, Y. (2011), 'Effects of brace stiffness on performance of structures with supplemental Maxwell model-based brace-damper systems', *Earthquake Engineering and Structural Dynamics* **40**(1), 75–92.

Chopra, A. (2012), *Dynamics of structures: theory and applications to earthquake engineering*, 4th edn, Prentice Hall, Upper Saddle River, New Jersey, USA.

CMC (2010), *Code for seismic design of buildings (GB50011-2010) [in Chinese]*, China Ministry of Construction, Beijing, China.

Constantinou, M., Soong, T. and Dargush, G. (1998), *Passive energy dissipation systems for structural design and retrofit*, Multidisciplinary Center for Earthquake Engineering Research, State University of New York at Buffalo, New York, USA.

Constantinou, M. and Symans, M. (1992), Experimental and analytical investigation of seismic response of structures with supplemental fluid viscous dampers, Technical Report NCEER-92-0032, National Center for Earthquake Engineering Research, State University of New York at Buffalo, New York, USA.

Constantinou, M. and Symans, M. (1993), 'Experimental study of seismic response of buildings with supplemental fluid dampers', *The Structural Design of Tall Buildings* **2**(2), 93–132.

Craig, R. and Kurdila, A. (2006), *Fundamentals of structural dynamics*, 2nd edn, John Wiley and Sons, Hoboken, New Jersey, USA.

Dai, W., Shi, B., Yang, J., Zhu, X. and Li, T. (2022), 'Enhanced suppression of longitudinal vibration transmission in propulsion shaft system using nonlinear tuned mass damper inerter', *Journal of Vibration and Control* pp. 1–11.

Daryan, A. S. and Palizi, S. (2020), 'New plastic analysis procedure for collapse prediction of braced frames by means of genetic algorithm', *Journal of Structural Engineering, ASCE* **146**(1), 04019168.

De Angelis, M., Giaralis, A., Petrini, F. and Pietrosanti, D. (2019), 'Optimal tuning and assessment of inertial dampers with grounded inerter for vibration control of seismically excited base-isolated systems', *Engineering Structures* **196**, 109250.

De Domenico, D., Deastra, P., Ricciardi, G., Sims, N. D. and Wagg, D. J. (2019), 'Novel fluid inerter based tuned mass dampers for optimised structural control of base-isolated buildings', *Journal of the Franklin Institute* **356**(14), 7626–7649.

De Domenico, D., Qiao, H., Wang, Q., Zhu, Z. and Marano, G. (2020), 'Optimal design and seismic performance of multi-tuned mass damper inerter (MTMDI) applied to adjacent high-rise buildings', *The Structural Design of Tall and Special Buildings* **29**(14), e1781.

De Domenico, D. and Ricciardi, G. (2018), 'Improved stochastic linearization technique for structures with nonlinear viscous dampers', *Soil Dynamics and Earthquake Engineering* **113**, 415–419.

De Domenico, D. and Ricciardi, G. (2019), 'Earthquake protection of structures with nonlinear viscous dampers optimized through an energy-based stochastic approach', *Engineering Structures* **179**, 523–539.

Deastra, P., Wagg, D., Sims, N. and Akbar, M. (2020), 'Tuned inerter dampers with linear hysteretic damping', *Earthquake Engineering and Structural Dynamics* **49**(12), 1216–1235.

Deb, K. (2001), *Multi-objective optimization using evolutionary algorithms*, 1st edn, John Wiley and Sons, Chichester, UK.

Deb, K., Pratap, A., Agarwal, S. and Meyarivan, T. (2002), 'A fast and elitist multiobjective genetic algorithm: NSGA-II', *IEEE Transactions on Evolutionary Computation* **6**(2), 182–197.

Del Gobbo, G. M., Williams, M. S. and Blakeborough, A. (2018), 'Comparing fluid viscous damper placement methods considering total-building seismic performance', *Earthquake Engineering and Structural Dynamics* **47**(14), 2864–2886.

De Domenico, D. and Ricciardi, G. (2018), 'An enhanced base isolation system equipped with optimal tuned mass damper inerter (TMDI)', *Earthquake Engineering and Structural Dynamics* **47**(5), 1169–1192.

Di, F., Chen, L. and Sun, L. (2021), 'Optimal design of dampers for multi-mode cable vibration control based on genetic algorithm', *International Journal of Structural Stability and Dynamics* **21**(4), 2150058.

Di Paola, M., La Mendola, L. and Navarra, G. (2007), 'Stochastic seismic analysis of structures with nonlinear viscous dampers', *Journal of Structural Engineering, ASCE* **133**(10), 1475–1478.

Di Paola, M. and Navarra, G. (2009), 'Stochastic seismic analysis of MDOF structures with nonlinear viscous dampers', *Structural Control and Health Monitoring* **16**(3), 303–318.

Diotallevi, P., Landi, L. and Dellavalle, A. (2012), 'A methodology for the direct assessment of the damping ratio of structures equipped with nonlinear viscous dampers', *Journal of Earthquake Engineering* **16**(3), 350–373.

Djerouni, S., Abdeddaim, M., Elias, S. and Rupakhety, R. (2021), 'Optimum double mass tuned damper inerter for control of structure subjected to ground motions', *Journal of Building Engineering* **44**, 103259.

Dong, Z., Chronopoulos, D. and Yang, J. (2021), 'Enhancement of wave damping for metamaterial beam structures with embedded inerter-based configurations', *Applied Acoustics* **178**, 108013.

Dong, Z., Shi, B., Yang, J. and Li, T. (2022), 'Suppression of vibration transmission in coupled systems with an inerter-based nonlinear joint', *Nonlinear Dynamics* **107**, 1637–1662.

Dong, Z., Yang, J., Zhu, C., Chronopoulos, D. and Li, T. (2022), 'Energy flow and performance evaluation of inerter-based vibration isolators mounted on finite and infinite flexible foundation structures', *Advances in Mechanical Engineering* **14**(1), 1–15.

Dormand, J. and Prince, P. (1980), 'A family of embedded Runge-Kutta formulae', *Journal of Computational and Applied Mathematics* **6**(1), 19–26.

Driscoll, M. (2013), *Model making for architects*, 1st edn, Crowood Press, Wilshire, UK.

Duan, N., Wu, Y., Sun, X.-M. and Zhong, C. (2021), 'Vibration control of conveying fluid pipe based on inerter enhanced nonlinear energy sink', *IEEE Transactions on Circuits and Systems I: Regular Papers* **68**(4), 1610–1623.

Etedali, S. and Rakhshani, H. (2018), 'Optimum design of tuned mass dampers using multi-objective cuckoo search for buildings under seismic excitations', *Alexandria Engineering Journal* **57**(4), 3205–3218.

Fu, K., Li, Q., Fan, S., Li, T., Huang, T. and Luo, Y. (2020), Spark and dask performance analysis based on arl image library, *in* 'Big Data in Astronomy', Elsevier, pp. 325–345.

Fu, Y. and Kasai, K. (1998), 'Comparative study of frames using viscoelastic and viscous dampers', *Journal of Structural Engineering, ASCE* **124**(5), 513–522.

Fujita, K., Kasagi, M., Lang, Z.-Q., Penfei, G. and Takewaki, I. (2014), 'Optimal placement and design of nonlinear dampers for building structures in the frequency domain', *Earthquakes and Structures* **7**(6), 1025–1044.

Fujita, K., Moustafa, A. and Takewaki, I. (2010), 'Optimal placement of visco-elastic dampers and supporting members under variable critical excitations', *Earthquakes and Structures* **1**(1), 43–67.

Gembicki, F. and Haimes, Y. Y. (1975), 'Approach to performance and sensitivity multiobjective optimization: The goal attainment method', *IEEE Transactions on Automatic Control* **20**(6), 769–771.

Gen, M. and Cheng, R. (1999), *Genetic algorithms and engineering optimization*, 1st edn, John Wiley and Sons, New York, USA.

Ghasemof, A., Mirtaheri, M. and Karami Mohammadi, R. (2022), 'Multi-objective optimization for probabilistic performance-based design of buildings using FEMA P-58 methodology', *Engineering Structures* **254**, 113856.

Gonzalez-Buelga, A., Clare, L., Neild, S., Burrow, S. and Inman, D. (2015), 'An electromagnetic vibration absorber with harvesting and tuning capabilities', *Structural Control and Health Monitoring* **22**(11), 1359–1372.

Gönen, S. and Soyöz, S. (2021), 'Seismic analysis of a masonry arch bridge using multiple methodologies', *Engineering Structures* **226**, 111354.

Han, S. W. and Chopra, A. K. (2006), 'Approximate incremental dynamic analysis using the modal pushover analysis procedure', *Earthquake Engineering and Structural Dynamics* **35**(15), 1853–1873.

Hatada, T., Kobori, T., Ishida, M. and Niwa, N. (2000), 'Dynamic analysis of structures with Maxwell model', *Earthquake Engineering and Structural Dynamics* **29**(2), 159–176.

Holland, J. H. (1962), 'Outline for a logical theory of adaptive systems', *Journal of the ACM* **9**(3), 297–314.

Hu, Y. and Chen, M. Z. (2015), 'Performance evaluation for inerter-based dynamic vibration absorbers', *International Journal of Mechanical Sciences* **99**, 297–307.

Hu, Y., Chen, M. Z., Shu, Z. and Huang, L. (2015), 'Analysis and optimisation for inerter-based isolators via fixed-point theory and algebraic solution', *Journal of Sound and Vibration* **346**, 17–36.

Huang, H. (2009), 'Efficiency of the motion amplification device with viscous dampers and its application in high-rise buildings', *Earthquake Engineering and Engineering Vibration* **8**, 521–536.

Hung, W. (2003), 'Architectural aspects of atrium', *International Journal on Engineering Performance-Based Fire Codes* **5**(4), 131–137.

Hussain, S. and Oosthuizen, P. H. (2012), 'Numerical investigations of buoyancy-driven natural ventilation in a simple atrium building and its effect on the thermal comfort conditions', *Applied Thermal Engineering* **40**, 358–372.

Hwang, J., Huang, Y. and Hung, Y. (2005), 'Analytical and experimental study of Toggle-Brace-Damper systems', *Journal of Structural Engineering, ASCE* **131**(7), 1035–1043.

Hwang, J.-S., Kim, J. and Kim, Y.-M. (2007), 'Rotational inertia dampers with toggle bracing for vibration control of a building structure', *Engineering Structures* **29**(6), 1201–1208.

Høgsberg, J. (2011), 'The role of negative stiffness in semi-active control of magneto-rheological dampers', *Structural Control and Health Monitoring* **18**(3), 289–304.

Ibarra, L., Medina, R. and Krawinkler, H. (2005), 'Hysteretic models that incorporate strength and stiffness deterioration', *Earthquake Engineering and Structural Dynamics* **34**(12), 1489–1511.

Idels, O. and Lavan, O. (2021), 'Performance-based seismic retrofitting of frame structures using negative stiffness devices and fluid viscous dampers via optimization', *Earthquake Engineering and Structural Dynamics* **50**(12), 3116–3137.

IEM (2004), *General rule for performance-based seismic design of buildings (CECS160:2004) [in Chinese]*, Institute of Engineering Mechanics, CEA, Beijing, China.

Iemura, H. and Pradono, M. H. (2005), 'Simple algorithm for semi-active seismic response control of cable-stayed bridges', *Earthquake Engineering and Structural Dynamics* **34**(4-5), 409–423.

Ikago, K., Saito, K. and Inoue, N. (2012), 'Seismic control of single-degree-of-freedom structure using tuned viscous mass damper', *Earthquake Engineering and Structural Dynamics* **41**(3), 453–474.

Ismail, A. (2001), Training and optimization of product unit neural networks, Master's thesis, University of Pretoria, Hatfield, South Africa.

Javidialesaadi, A. and Wierschem, N. E. (2019), 'An inerter-enhanced nonlinear energy sink', *Mechanical Systems and Signal Processing* **129**, 449–454.

Ji, X., Zhang, J., Ikago, K., Chakraborty, S. and Kanno, H. (2021), 'Tuned viscous mass damper (TVMD) coupled wall system for enhancing seismic performance of high-rise buildings', *Engineering Structures* **240**, 112307.

John, E. and Wagg, D. (2019), 'Design and testing of a frictionless mechanical inerter device using living-hinges', *Journal of the Franklin Institute* **356**(14), 7650–7668.

Kanai, K. (1960), An empirical formula for the spectrum of strong earthquake motion, *in* 'Proceedings of 2nd World Conference on Earthquake Engineering', Tokyo, Japan, pp. 1541–1551.

Kandemir-Mazanoglu, E. C. and Mazanoglu, K. (2017), 'An optimization study for viscous dampers between adjacent buildings', *Mechanical Systems and Signal Processing* **89**, 88–96.

Katoch, S., Chauhan, S. S. and Kumar, V. (2021), 'A review on genetic algorithm: past, present, and future', *Multimedia Tools and Applications* **80**(8), 8091–8126.

Kaveh, A., Farzam, M. F., Jalali, H. H. and Maroofiazar, R. (2020), 'Robust optimum design of a tuned mass damper inerter', *Acta Mechanica* **231**, 3871–3896.

Kenny (2014), 'A shopping mall within the petronas twin towers', `https://holidaysinmalaysia.org/kuala-lumpur/suria-klcc/` [Accessed January 31, 2021].

Kim, C., Oh, H., Jung, B. C. and Moon, S. J. (2022), 'Optimal sensor placement to detect ruptures in pipeline systems subject to uncertainty using an Adam-mutated genetic algorithm', *Structural Health Monitoring* **21**(5), 2354–2369.

Kitayama, S. and Constantinou, M. (2018), 'Seismic performance of buildings with viscous damping systems designed by the procedures of ASCE/SEI 7-16', *Journal of Structural Engineering, ASCE* **144**(6), 04018050.

Kutta, M. W. (1901), 'Beitrag zur näherungsweisen integration totaler differentialgleichungen', *Zeitschrift für Mathematik und Physik* **46**, 435–453.

Lai, J.-W. and Mahin, S. A. (2015), 'Strongback system: a way to reduce damage concentration in steel-braced frames', *Journal of Structural Engineering, ASCE* **141**(9), 04014223.

Landi, L., Fabbri, O. and Diotallevi, P. P. (2014), 'A two-step direct method for estimating the seismic response of nonlinear structures equipped with nonlinear viscous dampers', *Earthquake Engineering and Structural Dynamics* **43**(11), 1641–1659.

Lang, Z., Guo, P. and Takewaki, I. (2013), 'Output frequency response function based design of additional nonlinear viscous dampers for vibration control of multi-degree-of-freedom systems', *Journal of Sound and Vibration* **332**(19), 4461–4481.

Lavan, O. (2015), 'Optimal design of viscous dampers and their supporting members for the seismic retrofitting of 3D irregular frame structures', *Journal of Structural Engineering, ASCE* **141**(11).

Lavan, O. and Levy, R. (2005), 'Optimal design of supplemental viscous dampers for irregular shear-frames in the presence of yielding', *Earthquake Engineering and Structural Dynamics* **34**(8), 889–907.

Lavan, O. and Levy, R. (2006), 'Optimal design of supplemental viscous dampers for linear framed structures', *Earthquake Engineering and Structural Dynamics* **35**(3), 337–356.

Lazar, I., Neild, S. and Wagg, D. (2014), 'Using an inerter-based device for structural vibration suppression', *Earthquake Engineering and Structural Dynamics* **43**(8), 1129–1147.

Lee, C., Chen, Y.-T., Chung, L. and Wang, Y. (2006), 'Optimal design theories and applications of tuned mass dampers', *Engineering Structures* **28**(1), 43–53.

Lee, S.-H., Min, K.-W., Hwang, J.-S. and Kim, J. (2004), 'Evaluation of equivalent damping ratio of a structure with added dampers', *Engineering Structures* **26**(3), 335–346.

Leng, J., Buonopane, S. G. and Schafer, B. W. (2020), 'Incremental dynamic analysis and FEMA P695 seismic performance evaluation of a cold-formed steel–framed building with gravity framing and architectural sheathing', *Earthquake Engineering and Structural Dynamics* **49**(4), 394–412.

Leung, A., Zhang, H., Cheng, C. and Lee, Y. (2008), 'Particle swarm optimization of TMD by non-stationary base excitation during earthquake', *Earthquake Engineering and Structural Dynamics* **37**(9), 1223–1246.

Levy, R. and Lavan, O. (2009), 'Quantitative comparison of optimization approaches for the design of supplemental damping in earthquake engineering practice', *Journal of Structural Engineering, ASCE* **135**(3), 321–325.

Li, C., Chang, K., Cao, L. and Huang, Y. (2021), 'Performance of a nonlinear hybrid base isolation system under the ground motions', *Soil Dynamics and Earthquake Engineering* **143**, 106589.

Li, C., Liang, M., Wang, Y. and Dong, Y. (2012), 'Vibration suppression using two-terminal flywheel. Part I: Modeling and characterization', *Journal of Vibration and Control* **18**(8), 1096–1105.

Li, H., Liu, M. and Ou, J. (2008), 'Negative stiffness characteristics of active and semi-active control systems for stay cables', *Structural Control and Health Monitoring* **15**(2), 120–142.

Li, S., Chen, Y.-T., Chai, Y. H. and Li, B. (2021), 'Effects of brace stiffness and nonlinearity of viscous dampers on seismic performance of structures', *International Journal of Structural Stability and Dynamics* **21**(13), 2150188.

Li, Y., Jiang, J. Z. and Neild, S. (2017), 'Inerter-based configurations for main-landing-gear shimmy suppression', *Journal of Aircraft* **54**(2), 684–693.

Lin, R., Liang, Z., Soong, T. and Zhang, R. (1988), An experimental study of seismic structural response with added viscoelastic dampers, Technical Report NCEER-88-0018, National Center for Earthquake Engineering Research, State University of New York at Buffalo, New York, USA.

Lin, W. and Chopra, A. (2002), 'Earthquake response of elastic SDF systems with non-linear fluid viscous dampers', *Earthquake Engineering and Structural Dynamics* **31**(9), 1623–1642.

Lin, Y. Y., Chang, K. C. and Chen, C. Y. (2008), 'Direct displacement-based design for seismic retrofit of existing buildings using nonlinear viscous dampers', *Bulletin of Earthquake Engineering* **6**(3), 535–552.

Lindfield, G. and Penny, J. (2019), *Numerical methods using MATLAB*, 4th edn, Academic Press, San Diego, California, USA.

Liu, Y., Wu, J. and Donà, M. (2018), 'Effectiveness of fluid-viscous dampers for improved seismic performance of inter-storey isolated buildings', *Engineering Structures* **169**, 276–292.

Liu, Y., Yang, J., Yi, X. and Chronopoulos, D. (2022), 'Enhanced suppression of low-frequency vibration transmission in metamaterials with linear and nonlinear inerters', *Journal of Applied Physics* **131**(10), 105103.

Londoño, J., Neild, S. and Wagg, D. (2013), 'A noniterative design procedure for supplemental brace-damper systems in single-degree-of-freedom systems', *Earthquake Engineering and Structural Dynamics* **42**(15), 2361–2367.

Londoño, J., Wagg, D. and Neild, S. (2014), 'Supporting brace sizing in structures with added linear viscous fluid dampers: A filter design solution', *Earthquake Engineering and Structural Dynamics* **43**(13), 1999–2013.

Losanno, D., Londoño, J., Zinno, S. and Serino, G. (2018), 'Effective damping and frequencies of viscous damper braced structures considering the supports flexibility', *Computers and Structures* **207**, 121–131.

Losanno, D., Spizzuoco, M. and Serino, G. (2015), 'An optimal design procedure for a simple frame equipped with elastic-deformable dissipative braces', *Engineering Structures* **101**, 677–697.

Losanno, D., Spizzuoco, M. and Serino, G. (2019), 'Design and retrofit of multi-story frames with elastic-deformable viscous damping braces', *Journal of Earthquake Engineering* **23**(9), 1441–1464.

Lu, L., Duan, Y.-F., Spencer Jr, B. F., Lu, X. and Zhou, Y. (2017), 'Inertial mass damper for mitigating cable vibration', *Structural Control and Health Monitoring* **24**(10), e1986.

Lu, L., Xu, J., Zhou, Y., Lu, W. and Spencer, B. F. (2021), 'Viscous inertial mass damper (VIMD) for seismic responses control of the coupled adjacent buildings', *Engineering Structures* **233**, 111876.

Ma, R., Bi, K. and Hao, H. (2019), 'A novel rotational inertia damper for heave motion suppression of semisubmersible platform in the shallow sea', *Structural Control and Health Monitoring* **26**(7), e2368.

Ma, R., Bi, K. and Hao, H. (2020), 'Heave motion mitigation of semi-submersible platform using inerter-based vibration isolation system (IVIS)', *Engineering Structures* **219**, 110833.

Ma, R., Bi, K. and Hao, H. (2021*a*), 'Inerter-based structural vibration control: a state-of-the-art review', *Engineering Structures* **243**, 112655.

Ma, R., Bi, K. and Hao, H. (2021*b*), 'A novel rotational inertia damper for amplifying fluid resistance: Experiment and mechanical model', *Mechanical Systems and Signal Processing* **149**, 107313.

Marian, L. and Giaralis, A. (2014), 'Optimal design of a novel tuned mass-damper–inerter (TMDI) passive vibration control configuration for stochastically support-excited structural systems', *Probabilistic Engineering Mechanics* **38**, 156–164.

Marian, L. and Giaralis, A. (2017), 'The tuned mass-damper-inerter for harmonic vibrations suppression, attached mass reduction, and energy harvesting', *Smart Structures and Systems* **19**(6), 665–678.

Martinez-Rodrigo, M. and Romero, M. (2003), 'An optimum retrofit strategy for moment resisting frames with nonlinear viscous dampers for seismic applications', *Engineering Structures* **25**(7), 913–925.

MathWorks (2021), 'Choose an ODE solver', `https://www.mathworks.com/help/matlab/math/choose-an-ode-solver.html?searchHighlight=ode%20suite&s_tid=srchtitle_ode%20suite_2` [Accessed December 6, 2021].

McNamara, R. J., Huang, C. D. and Wan, V. (2000), Viscous-damper with motion amplification device for high rise building applications, *in* 'Proceedings of Structures Congress 2000: Advanced Technology in Structural Engineering', Philadelphia, Pennsylvania, USA, pp. 1–10.

Meirovitch, L. (1990), *Dynamics and control of structures*, 1st edn, John Wiley and Sons, Hoboken, New Jersey, USA.

Miari, M. and Jankowski, R. (2022), 'Incremental dynamic analysis and fragility assessment of buildings founded on different soil types experiencing structural pounding during earthquakes', *Engineering Structures* **252**, 113118.

Mishra, S., Sahoo, S. and Das, M. (2017), 'Genetic algorithm: an efficient tool for global optimization', *Advances in Computational Sciences and Technology* **10**(8), 2201–2211.

Mohsenin, M. and Hu, J. (2015), 'Assessing daylight performance in atrium buildings by using climate based daylight modeling', *Solar Energy* **119**, 553–560.

Moradpour, S. and Dehestani, M. (2019), 'Optimal DDBD procedure for designing steel structures with nonlinear fluid viscous dampers', *Structures* **22**, 154–174.

Moraes, F. d. H., Silveira, M. and Gonçalves, P. J. P. (2018), 'On the dynamics of a vibration isolator with geometrically nonlinear inerter', *Nonlinear Dynamics* **93**, 1325–1340.

Moslehi Tabar, A. (2019), 'Linearization of seismic response of structures equipped with nonlinear viscous dampers using perturbation technique', *Engineering Structures* **184**, 459–468.

Moslehi Tabar, A. and De Domenico, D. (2020), 'Nonlinear response spectrum analysis of structures equipped with nonlinear power law viscous dampers', *Engineering Structures* **219**, 110857.

Nagarajaiah, S. and Sen, D. (2020), 'Apparent-weakening by adaptive passive stiffness shaping along the height of multistory building using negative stiffness devices and dampers for seismic protection', *Engineering Structures* **220**, 110754.

Nakamura, Y., Fukukita, A., Tamura, K., Yamazaki, I., Matsuoka, T., Hiramoto, K. and Sunakoda, K. (2014), 'Seismic response control using electromagnetic inertial mass dampers', *Earthquake Engineering and Structural Dynamics* **43**(4), 507–527.

Newmark, N. M. (1959), 'A method of computation for structural dynamics', *Journal of the Engineering Mechanics Division* **85**(3), 67–94.

Ou, J. and Li, H. (2010), 'Analysis of capability for semi-active or passive damping systems to achieve the performance of active control systems', *Structural Control and Health Monitoring* **17**(7), 778–794.

Ou, J., Long, X. and Li, Q. (2007), 'Seismic response analysis of structures with velocity-dependent dampers', *Journal of Constructional Steel Research* **63**(5), 628–638.

Palermo, M., Laghi, V., Gasparini, G. and Trombetti, T. (2018), 'Coupled response of frame structures connected to a strongback', *Journal of Structural Engineering, ASCE* **144**(9), 04018148.

Palermo, M., Silvestri, S., Landi, L., Gasparini, G. and Trombetti, T. (2018), 'A "direct five-step procedure" for the preliminary seismic design of buildings with added viscous dampers', *Engineering Structures* **173**, 933–950.

Papageorgiou, C., Houghton, N. E. and Smith, M. C. (2009), 'Experimental testing and analysis of inerter devices', *Journal of Dynamic Systems, Measurement, and Control* **131**(1), 011001.

Papageorgiou, C. and Smith, M. C. (2005), Laboratory experimental testing of inerters, *in* 'Proceedings of the 44th IEEE Conference on Decision and Control', Seville, Spain, pp. 3351–3356.

Park, J., Kim, J. and Min, K. (2004), 'Optimal design of added viscoelastic dampers and supporting braces', *Earthquake Engineering and Structural Dynamics* **33**(4), 465–484.

Parulekar, Y. and Reddy, G. (2009), 'Passive response control systems for seismic response reduction: A state-of-the-art review', *International Journal of Structural Stability and Dynamics* **9**(1), 151–177.

Pasala, D., Sarlis, A., Nagarajaiah, S., Reinhorn, A., Constantinou, M. and Taylor, D. (2013), 'Adaptive negative stiffness: New structural modification approach for seismic protection', *Journal of Structural Engineering, ASCE* **139**(7), 1112–1123.

Pawlak, Z. M. and Lewandowski, R. (2020), 'The effectiveness of the passive damping system combining the viscoelastic dampers and inerters', *International Journal of Structural Stability and Dynamics* **20**(12), 2050140.

PEER (2022), 'Pacific earthquake engineering research center ground motion database', `https://ngawest2.berkeley.edu/site` [Accessed June 1, 2022].

Petrini, F., Giaralis, A. and Wang, Z. (2020), 'Optimal tuned mass-damper-inerter (TMDI) design in wind-excited tall buildings for occupants' comfort serviceability performance and energy harvesting', *Engineering Structures* **204**, 109904.

Pietrosanti, D., De Angelis, M. and Basili, M. (2017), 'Optimal design and performance evaluation of systems with tuned mass damper inerter (TMDI)', *Earthquake Engineering and Structural Dynamics* **46**(8), 1367–1388.

Pietrosanti, D., De Angelis, M. and Giaralis, A. (2020), 'Experimental study and numerical modeling of nonlinear dynamic response of SDOF system equipped with tuned mass damper inerter (TMDI) tested on shaking table under harmonic excitation', *International Journal of Mechanical Sciences* **184**, 105762.

Pollini, N., Lavan, O. and Amir, O. (2017), 'Minimum-cost optimization of nonlinear fluid viscous dampers and their supporting members for seismic retrofitting', *Earthquake Engineering and Structural Dynamics* **46**(12), 1941–1961.

Pollini, N., Lavan, O. and Amir, O. (2018), 'Optimization-based minimum-cost seismic retrofitting of hysteretic frames with nonlinear fluid viscous dampers', *Earthquake Engineering and Structural Dynamics* **47**(15), 2985–3005.

Praime construction (2015), 'Avia park', `https://www.praimecons.ru/en/avia-park-2/` [Accessed January 31, 2021].

Preumont, A. (2011), *Vibration control of active structures*, 3rd edn, Springer, Dordrecht, Netherlands.

Ramirez, O., Constantinou, M., Kircher, C., Whittaker, A., Johnson, M., Gomez, J. and Chrysostomou, C. (2001), Development and evaluation of simplified procedures of analysis and design for structures with passive energy dissipation systems, Technical Report MCEER-00-0010, Multidisciplinary Center for Earthquake Engineering Research, State University of New York at Buffalo, New York, USA.

Reinhorn, A., Li, C. and Constantinou, M. (1995), Experimental and analytical investigation of seismic retrofit of structures with supplemental damping, part 1: Fluid viscous damping devices, Technical Report NCEER-95-0001, National Center for Earthquake Engineering Research, State University of New York at Buffalo, New York, USA.

Roque, J., Oliveira, D., Ferreira, T. and Lourenço, P. (2019), 'Nonlinear dynamic analysis for safety assessment of heritage buildings: church of Santa Maria de Belém', *Journal of Structural Engineering, ASCE* **145**(12), 04019153.

Runge, C. D. T. (1895), 'Ueber die numerische auflösung von differentialgleichungen', *Mathematische Annalen* **46**(2), 167–178.

Sadek, F., Mohraz, B. and Riley, M. A. (2000), 'Linear procedures for structures with velocity-dependent dampers', *Journal of Structural Engineering, ASCE* **126**(8), 887–895.

Saitoh, M. (2012), 'On the performance of gyro-mass devices for displacement mitigation in base isolation systems', *Structural Control and Health Monitoring* **19**(2), 246–259.

SEAOC and OSHPD (2022), 'Seismic design maps (by Structural Engineers Association of California and California Office of Statewide Health Planning and Development)', `https://www.seismicmaps.org/` [Accessed June 1, 2022].

Shabbir, F. and Omenzetter, P. (2016), 'Model updating using genetic algorithms with sequential niche technique', *Engineering Structures* **120**, 166–182.

Shampine, L. F. and Reichelt, M. W. (1997), 'The MATLAB ODE suite', *SIAM Journal on Scientific Computing* **18**(1), 1–22.

Shen, H., Zhang, R., Weng, D., Ge, Q., Wang, C. and Islam, M. M. (2020), 'Design method of structural retrofitting using viscous dampers based on elastic–plastic response reduction curve', *Engineering Structures* **208**, 109917.

Shen, W., Long, Z., Wang, H. and Zhu, H. (2021), 'Power analysis of SDOF structures with tuned inerter dampers subjected to earthquake ground motions', *ASCE-ASME Journal of Risk and Uncertainty in Engineering Systems, Part B: Mechanical Engineering* **7**(1), 010907.

Shen, W., Niyitangamahoro, A., Feng, Z. and Zhu, H. (2019), 'Tuned inerter dampers for civil structures subjected to earthquake ground motions: optimum design and seismic performance', *Engineering Structures* **198**, 109470.

Shen, Y., Chen, L., Yang, X., Shi, D. and Yang, J. (2016), 'Improved design of dynamic vibration absorber by using the inerter and its application in vehicle suspension', *Journal of Sound and Vibration* **361**, 148–158.

Shi, B., Dai, W. and Yang, J. (2022), 'Performance analysis of a nonlinear inerter-based vibration isolator with inerter embedded in a linkage mechanism', *Nonlinear Dynamics* **109**, 419–442.

Shi, X. and Zhu, S. (2019), 'A comparative study of vibration isolation performance using negative stiffness and inerter dampers', *Journal of the Franklin Institute* **356**(14), 7922–7946.

Shin, H. and Singh, M. (2014), 'Minimum failure cost-based energy dissipation system designs for buildings in three seismic regions, part II: Application to viscous dampers', *Engineering Structures* **74**, 275–282.

Shinozuka, M. and Deodatis, G. (1991), 'Simulation of stochastic processes by spectral representation', *Applied Mechanics Reviews* **44**(4), 191–204.

Silvestri, S., Gasparini, G. and Trombetti, T. (2010), 'A five-step procedure for the dimensioning of viscous dampers to be inserted in building structures', *Journal of Earthquake Engineering* **14**(3), 417–447.

Silvestri, S. and Trombetti, T. (2007), 'Physical and numerical approaches for the optimal insertion of seismic viscous dampers in shear-type structures', *Journal of Earthquake Engineering* **11**(5), 787–828.

Singh, M. and Moreschi, L. (2002), 'Optimal placement of dampers for passive response control', *Earthquake Engineering and Structural Dynamics* **31**(4), 955–976.

Singh, M., Verma, N. and Moreschi, L. (2003), 'Seismic analysis and design with Maxwell dampers', *Journal of Engineering Mechanics* **129**(3), 273–282.

Skinner, R., Kelly, J. and Heine, A. (1974), 'Hysteretic dampers for earthquake-resistant structures', *Earthquake Engineering and Structural Dynamics* **3**(3), 287–296.

Smith, M. C. (2002), 'Synthesis of mechanical networks: the inerter', *IEEE Transactions on Automatic Control* **47**(10), 1648–1662.

Smith, M. C. and Wang, F.-C. (2003), Performance benefits in passive vehicle suspensions employing inerters, *in* 'Proceedings of the 42nd IEEE Conference on Decision and Control', Maui, Hawii, USA, pp. 2258–2263.

Smith, R. J. and Willford, M. R. (2007), 'The damped outrigger concept for tall buildings', *The Structural Design of Tall and Special Buildings* **16**(4), 501–517.

Soleimani, S., Aziminejad, A. and Moghadam, A. (2018), 'Approximate two-component incremental dynamic analysis using a bidirectional energy-based pushover procedure', *Engineering Structures* **157**, 86–95.

Soong, T. and Dargush, G. (1997), *Passive energy dissipation system in structural engineering*, 1st edn, John Wiley and Sons, Chichester, UK.

Soong, T. and Spencer Jr, B. (2002), 'Supplemental energy dissipation: state-of-the-art and state-of-the-practice', *Engineering Structures* **24**(3), 243–259.

Soysal, B. F., Binici, B. and Arici, Y. (2016), 'Investigation of the relationship of seismic intensity measures and the accumulation of damage on concrete gravity dams using incremental dynamic analysis', *Earthquake Engineering and Structural Dynamics* **45**(5), 719–737.

Symans, M., Charney, F., Whittaker, A., Constantinou, M., Kircher, C., Johnson, M. and McNamara, R. (2008), 'Energy dissipation systems for seismic applications: current practice and recent developments', *Journal of Structural Engineering, ASCE* **134**(1), 3–21.

Symans, M. and Constantinou, M. (1998), 'Passive fluid viscous damping systems for seismic energy dissipation', *Journal of Earthquake Technology* **35**(4), 185–206.

Tajimi, H. (1960), A statistical method of determining the maximum response of a building structure during an earthquake, *in* 'Proceedings of 2nd World Conference on Earthquake Engineering', Tokyo, Japan, pp. 781–797.

Takewaki, I. (1997), 'Optimal damper placement for minimum transfer functions', *Earthquake Engineering and Structural Dynamics* **26**(11), 1113–1124.

Takewaki, I. and Yoshitomi, S. (1998), 'Effects of support stiffnesses on optimal damper placement for a planar building frame', *The Structural Design of Tall Buildings* **7**(4), 323–336.

Talley, P. C., Javidialesaadi, A., Wierschem, N. E. and Denavit, M. D. (2021), 'Evaluation of steel building structures with inerter-based dampers under seismic loading', *Engineering Structures* **242**, 112488.

Tavakolinia, M. and Ch. Basim, M. (2021), 'Performance-based optimum tuning of tuned mass dampers on steel moment frames for seismic applications using the endurance time method', *Earthquake Engineering and Structural Dynamics* **50**(13), 3646–3669.

Taylor, D. (2013), *History, design, and applications of fluid dampers in structural engineering*, Taylor Devices, Inc., Available: https://www.taylordevices.com/custom/pdf/tech-papers/68-HistoryDesignApplication.pdf [Accessed June 16, 2019].

Terenzi, G. (1999), 'Dynamics of SDOF systems with nonlinear viscous damping', *Journal of Engineering Mechanics* **125**(8), 956–963.

Tsopelas, P., Okamoto, S., Constantinou, M., Ozaki, D. and Fujii, S. (1994), NCEER-Taisei corporation research program on sliding seismic isolation systems for bridges: experimental and analytical study of systems consisting of sliding bearings, rubber restoring force devices and fluid dampers, Technical Report NCEER-94-0002, National Center for Earthquake Engineering Research, State University of New York at Buffalo, New York, USA.

Tubaldi, E. and Kougioumtzoglou, I. (2015), 'Nonstationary stochastic response of structural systems equipped with nonlinear viscous dampers under seismic excitation', *Earthquake Engineering and Structural Dynamics* **44**(1), 121–138.

Vamvatsikos, D. (2011), 'Performing incremental dynamic analysis in parallel', *Computers and Structures* **89**(1), 170–180.

Vamvatsikos, D. and Cornell, C. A. (2002), 'Incremental dynamic analysis', *Earthquake Engineering and Structural Dynamics* **31**(3), 491–514.

Viola, E. and Guidi, F. (2009), 'Influence of the supporting braces on the dynamic control of buildings with added viscous dampers', *Structural Control and Health Monitoring* **16**(3), 267–286.

Walsh, K. K., Sallar, G., Haftman, J. T. and Steinberg, E. P. (2021), 'Resetting passive stiffness damper with passive negative stiffness device for seismic protection of structures', *Structural Control and Health Monitoring* **28**(8), e2774.

Wang, F.-C., Hong, M.-F. and Lin, T.-C. (2011), 'Designing and testing a hydraulic inerter', *Proc. the Institution of Mechanical Engineers, Part C: Journal of Mechanical Engineering Science* **225**(1), 66–72.

Wang, Q., Tian, H., Qiao, H., Tiwari, N. D. and Wang, Q. (2021), 'Wind-induced vibration control and parametric optimization of connected high-rise buildings with tuned liquid-column-damper–inerter', *Engineering Structures* **226**, 111352.

Wilson, E. L., Farhoomand, I. and Bathe, K. J. (1972), 'Nonlinear dynamic analysis of complex structures', *Earthquake Engineering and Structural Dynamics* **1**(3), 241–252.

Wu, Q., Feng, H., Xiao, S., Zhu, H. and Bai, X. (2020), 'Passive control analysis and design of twin-tower structure with chassis', *International Journal of Structural Stability and Dynamics* **20**(6), 2040010.

Xie, Y., Zhang, J. and Xi, W. (2018), 'Effectiveness evaluation and optimal design of nonlinear viscous dampers for inelastic structures under pulse-type ground motions', *Earthquake Engineering and Structural Dynamics* **47**(14), 2802–2820.

Yaghmaei-Sabegh, S., Jafari-Koucheh, E. and Ebrahimi-Aghabagher, M. (2020), 'Estimating the seismic response of nonlinear structures equipped with nonlinear viscous damper subjected to pulse-like ground records', *Structures* **28**, 1915–1923.

Yang, J. (2016), 'Force transmissibility and vibration power flow behaviour of inerter-based vibration isolators', *Journal of Physics: Conference Series* **744**, 012234.

Yang, J., Jiang, J. Z. and Neild, S. A. (2020), 'Dynamic analysis and performance evaluation of nonlinear inerter-based vibration isolators', *Nonlinear Dynamics* **99**, 1823–1839.

Yang, J., Jiang, J. Z., Zhu, X. and Chen, H. (2017), 'Performance of a dual-stage inerter-based vibration isolator', *Procedia Engineering* **199**, 1822–1827.

Yang, J. N., Long, F. X. and Wong, D. (1988), 'Optimal control of nonlinear structures', *Journal of Applied Mechanics* **55**(4), 931–938.

Zacharenaki, A., Fragiadakis, M., Assimaki, D. and Papadrakakis, M. (2014), 'Bias assessment in incremental dynamic analysis due to record scaling', *Soil Dynamics and Earthquake Engineering* **67**, 158–168.

Zadeh, L. A. (1963), 'Optimality and non-scalar-valued performance criteria', *IEEE Transactions on Automatic Control* **8**(1), 59–60.

Zhang, J. and Xi, W. (2012), Optimal nonlinear damping for inelastic structures using dimensional analysis, *in* 'Proceedings of 20th Analysis and Computation Specialty Conference', Chicago, Illinois, USA, pp. 97–106.

Zhang, Y.-W., Lu, Y.-N., Zhang, W., Teng, Y.-Y., Yang, H.-X., Yang, T.-Z. and Chen, L.-Q. (2019), 'Nonlinear energy sink with inerter', *Mechanical Systems and Signal Processing* **125**, 52–64.

Zhao, Z., Zhang, R., Jiang, Y. and Pan, C. (2019), 'A tuned liquid inerter system for vibration control', *International Journal of Mechanical Sciences* **164**, 105171.

Zheng, L. and Zhang, X. (2017), *Modeling and analysis of modern fluid problems*, Mathematics in Science and Engineering, 1st edn, Academic Press, San Diego, California, USA.

Zhou, P., Liu, M. and Li, H. (2020), 'A passive negative stiffness damper in series with a flexible support: Theoretical and experimental study', *Structural Control and Health Monitoring* **27**(9), e2594.

Zhou, Y., Lu, X., Weng, D. and Zhang, R. (2012), 'A practical design method for reinforced concrete structures with viscous dampers', *Engineering Structures* **39**, 187–198.

Zhu, C., Yang, J. and Rudd, C. (2021), 'Vibration transmission and power flow of laminated composite plates with inerter-based suppression configurations', *International Journal of Mechanical Sciences* **190**, 106012.

Zuo, H., Bi, K. and Hao, H. (2020), 'A state-of-the-art review on the vibration mitigation of wind turbines', *Renewable and Sustainable Energy Reviews* **121**, 109710.